THE UNIVERSITY OF CHICAGO

MOLECULAR SIMULATIONS OF POLY[N]CATENANES

A DISSERTATION SUBMITTED TO
THE FACULTY OF THE PRITZKER SCHOOL OF MOLECULAR ENGINEERING
IN CANDIDACY FOR THE DEGREE OF
DOCTOR OF PHILOSOPHY

BY
PHILLIP M. RAUSCHER

CHICAGO, ILLINOIS
JUNE 2020

CONTENTS

LIST OF FIGURES

LIST OF TABLES

ACKNOWLEDGMENTS

I am deeply indebted to my advisors, Profs. Stuart J. Rowan and Juan J. de Pablo for their extraordinary mentorship and support. I could not have asked for better advisors. I have also had the privilege of working with many exceptional colleagues, including (in no particular order): Dr. Qiong Wu, Dr. Forrest S. Etheridge, Dr. Katie M. Herbert, Dr. Lucas Antony, Dr. Emre Sevgen, Prof. Yamil J. Colón, Prof. Michael A. Webb, Prof. Nicholas E. Jackson, Dr. Alec S. Bowen, Dr. Benjamin W. Rawe, Viviana Palacio-Betancur, Joshua Moller, Marissa T. Tranquilli, Jerald E. Hertzog, Laura F. Hart, Dr. Artem M. Rumyantsev, Dr. Heyi Liang, Dr. Daniel R. Reid, Dr. Phwey S. "Danny" Gil, Brian Keene, Dr. Marat Andreev, Dr. Abhinendra Singh, Dr. Deborah K. Schneiderman, Dr. Jeffrey M. Ting, Prof. Samanvaya Srivastava, Prof. Blair K. Brettmann, Prof. Amanda B. Marciel, Harrison Paul, James H. Lettow, Cody Bezik, Chuqiao "Elise" Chen, Dr. Ashley Z. Guo, Dr. Yu Kambe, Dr. Philip J. Griffin, Prof. Vivek Sharma, Prof. Marcus Müller, Prof. Alexander R. Klotz, and Beatrice W. Soh. Special thanks to Viviana Palacio-Betancur for help with several figures and to the staff of the PME for their assistance, especially Heather Crews, Rovana Popoff, David Taylor, Lisa Abston, and Maria Rubio.

I wish to thank Profs. Matthew V. Tirrell and Vincenzo Vitelli for serving on my committee and offering many helpful suggestions during my candidacy and beyond. Over the course of my graduate studies, I been extremely fortunate to participate in several collaborative efforts with outstanding professors at other institutions. In particular, I have benefited greatly from the mentorship of Profs. Kenneth S. Schweizer and Hans Christian Öttinger. I also gratefully acknowledge the National Science Foundation for their financial support through the award of a Graduate Research Fellowship.

This work would never have been completed without the support of my parents, Jamie and Steven Rauscher, and my wife, Rachel.

PERMISSIONS

Portions of this dissertation have been reproduced in whole or in part from a number of previously published works, all of which I co-authored. The relevant credits and permissions are listed below.

Chapters 1 & 2 - Reproduced in part from [Wu, Q.; Rauscher, P.M.; Lang, X.; Wojtecki, R.J.; de Pablo, J.J.; Hore, M.J.A.; Rowan, S.J. Poly[n]catenanes: Synthesis of molecular interlocked chains. *Science* **358**, 1434-1439 (2017)]. Reprinted with permission from AAAS. https://doi.org/10.1126/science.aap7675.

Chapter 3 - Reproduced in part with permission from [Rauscher, P.M.; Rowan, S.J.; de Pablo, J.J. Topological Effects in Isolated Poly[n]catenanes: Molecular Dynamics Simulations and Rouse Mode Analysis *ACS Macro Letters* **7**, 938-943 (2018)]. Copyright 2018 American Chemical Society. https://doi.org/10.1021/acsmacrolett.8b00393.

Chapters 1 & 5 - Reproduced in part with permission from [Rauscher, P.M.; Schweizer, K.S.; Rowan, S.J.; de Pablo, J.J. Thermodynamics and Structure of Poly[n]catenane Melts *Macromolecules* **53**, 3390-3408 (2020)]. Copyright 2020 American Chemical Society. https://doi.org/10.1021/acs.macromol.9b02706.

Chapters 1 & 6 - Partly reproduced from [Rauscher, P.M.; Schweizer, K.S.; Rowan, S.J.; de Pablo, J.J. Dynamics of Poly[n]catenane Melts *The Journal of Chemical Physics* Accepted (2020)] with the permission of AIP Publishing.

ABSTRACT

The remarkable properties and processability of polymers have made them ubiquitous in our lives in the form of products, technologies, foods, medical devices, and more. These giant molecules have also presented many scientific challenges which have been met with a diverse array of elegant theories over the past century. Today, polymer scientists and engineers turn their attention to ever more sophisticated macromolecules in search of new frontiers in polymer physics and new solutions to modern technological needs. Some of the most intriguing avenues of research center on mechanically-interlocked polymers (MIPs), which contain complex and permanent topological interactions in the form of mechanical bonds. Topological interactions (or constraints), such as entanglements, are crucial in determining the properties of polymeric materials with practical implications in many industrial processes. Owing to the unique and long-lived nature of the mechanical bond, certain systems of MIPs have been found to exhibit a host of unusual material properties including excellent toughness and resilience, which has made them promising candidates for a variety of technological applications, ultimately leading to their recent commercialization as scratch-resistance coatings.

Despite the promise of MIPs, scientists and engineers must still contend with many challenges in applying these polymers to new technologies. In addition to the well-known synthetic difficulties associated with crafting new MIP architectures, researchers are also faced with a relative dearth of knowledge concerning the material properties of MIP systems, both in the basic phenomenology and the underlying physics. This is especially apparent in the case of poly[n]catenanes - polymers which consist entirely of interlocking ring molecules. Such systems have been targeted by chemists for many decades and were recently synthesized for the first time, but their mechanical and dynamical properties remain largely unexplored.

This dissertation alleviates some of these difficulties by using molecular simulations to examine the physics of poly[n]catenanes. To begin, the force-extension behavior of the polymers is studied with atomistic resolution and the results are found to agree very well with

dynamic light scattering experiments. To access longer length and time scales, coarse-grained models are then used to study poly[n]catenane structure and dynamics in good solvent conditions. It is found that topological interactions greatly slow the dynamics of the system at short and intermediate length scales in a manner similar to entanglement in linear polymer systems. Next, the effect of hydrodynamic interactions in catenated polymers is considered using both theory and simulation and we find that the symmetries of ring molecules greatly simplify the physical situation and the effects of topology and hydrodynamics may be considered as roughly independent. Large scale molecular dynamics simulations are then used to study poly[n]catenanes in the melt. It is found that the mechanical bonds cause large reductions in the pressure and lead to complex polymer conformations that resist interchain entanglement. Despite the lack of such entanglements, the dynamics of poly[n]catenane melts are extremely rich, although some qualitative features can be explained by a simply, analytically solvable model. Most strikingly, the viscosity exhibits a non-monotonic dependence on the ring size, with larger rings (i.e. bigger polymers) leading to *lower* viscosities up to a critical ring size, above which the trend reverses and the viscosity increases with ring size as expected. To conclude, implications for chemical synthesis and materials design are discussed and directions for future research are proposed.

CHAPTER 1

INTRODUCTION AND BACKGROUND

1.1 Mechanically Interlocking Polymers

Over the past century, polymeric materials have been produced and applied at an astounding scale, becoming integral parts of our lives. As polymer engineers have shifted their focus to modern scientific and technological challenges, they have developed increasingly sophisticated macromolecular architectures for the purpose. Indeed, aside from chemical composition, polymer architecture has the largest effect on the material properties of polymer systems. For instance, even the "simple" modification of joining the ends of an ordinary linear polymer to form a loop results in dramatically different properties [1–4]. As a result, the synthesis and characterization of exotic architectures has been a major part of polymer science for several decades and remains an active area of research [5]. For instance, in addition to the cyclic/ring polymers mentioned above, researchers have also examined dendimers [6, 7], star polymers and miktoarms [8, 9], combs and bottlebrushes [10–12], and more. As polymer science rises to meet new societal and technological challenges, the design and development of new architectures will no doubt play a vital role.

Taking polymer architecture a step further, mechanically interlocked polymers (MIPs) have seen enormous growth in preparation and study over the last few decades. Unlike the other architectures discussed above, these polymers contain multiple components connected by one or more mechanical bonds, which are a form of permanent topological interaction [13]. Such mechanically-bound components are not covalently joined to each other, but cannot be separated without breaking a covalent bond. Mechanical bonds allow for many more degrees of freedom than covalent linkages and different components of the same molecule can be engineered to perform concerted motions relative to one another, allowing for the design of molecular machines [14]. The most commonly synthesized MIPs are polyrotaxanes

[15], which typically consist of rings (or macrocycles) threaded on a polymer "axle." The materials made from these polymers exhibit excellent toughness and recoverability [16, 17] and have even been commercialized as anti-scratch coatings [16].

The success of polyrotaxanes can be attributed to their relatively facile synthesis. Much more challenging is the synthesis of polycatenanes [18], which are polymers containing interlocking macrocycles. However, these polymers have great potential as they can contain enormous numbers of mechanical bonds. For instance, poly[n]catenanes are composed entirely of interlocking rings, with no covalent attachments in the polymer backbone, leading to the highest concentration of mechanical bonds possible. This novel polymer architecture was recently synthesized for the first time [19] and is depicted in Figure 1.1. For many decades, researchers had speculated that poly[n]catenanes would exhibit a variety of unusual behaviors [17, 18, 20]. In particular, it had been suggested that poly[n]catenanes could exhibit "high loss modulus, rapid stress relaxation, and low activation energy for viscous flow" [20]. While such potential properties motivated many chemists to target polycatenanes synthetically [17], to date no rheological studies have been carried out to confirm such claims and only a few theoretical or computational studies have been conducted [21, 22]. As a result, the static and dynamic properties of poly[n]catenanes are not known at this time. As poly[n]catenane synthesis remains an active area of research, a better understanding of the properties of these polymers will help chemists design and target the most promising candidates for new materials. On the other hand, mechanical bonds represent permanent and well-defined topological interactions, which have been actively studied in polymer physics for many decades, making the behaviors of poly[n]catenanes a topic of fundamental physical interest. This dissertation describes the results of molecular simulations of poly[n]catenanes in solution and in the melt state.

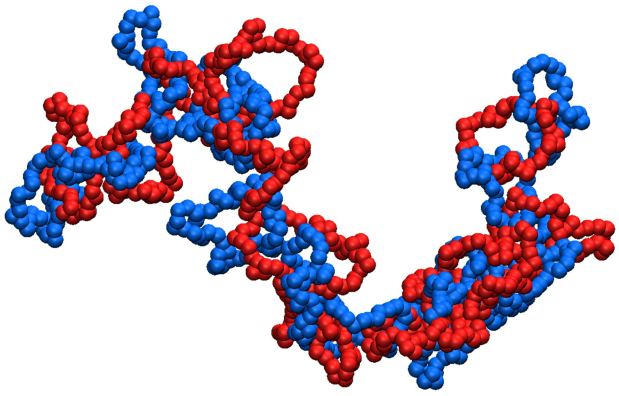

Figure 1.1: Visualization of a simulated poly[n]catenane. Alternating rings are colored differently to more easily discern the interlocking structure.

1.2 Topological Interactions in Polymer Systems

Polymer liquids are often dominated by topological interactions, which arise because chains cannot pass through one another [13]. In linear polymer systems, these topological constraints do not greatly affect small chains since the interactions are transient and the relevant time and length scales are quite short. However, for systems of long chains, the polymers are severely restricted in their motion by their neighbors. These restrictions greatly increase polymer relaxation times, and dramatically alter diffusion and rheological behavior [13, 23]. Over the past few decades, many theories have attempted to explain and predict the effects of topological interactions in linear polymer systems, for instance the phenomenological tube/reptation [24–29], and slip-link [30–35] models, or more fundamental force-level theories [36–39].

Despite these impressive effects on dynamical behavior, linear polymers do not show any meaningful changes in melt structure or chain conformations associated with the onset of entanglement, either at the intra- or inter-molecular level, as shown by experiment [40–42] and simulation [23, 43, 44]. Thus, the topological interactions do not disallow any chain or sys-

tem configurations, but instead prevent certain dynamical paths between them. To connect structure and dynamics, many authors have attempted to formulate microscopic definitions of an "entanglement" so that molecular simulations could be used to unambiguously identify such topological interactions and analyze their statistics and dynamics [45–54]. However, researchers have yet to reach consensus about how entanglements should be defined and what kinds of relative chain conformations constitute them. On account of these challenges, linear polymers and their topological interactions remain an active subject of research.

Non-concatenated (unlinked) ring polymers present an entirely distinct challenge since topological interactions manifest themselves very differently in these systems. For example, linear polymers do not show changes in structural features, including scaling of radius of gyration, R_g, due to entanglement, as mentioned above. However, at intermediate molecular weight, ring polymers in the melt appeared to scale in size according to $R_g \sim N^{2/5}$ in early work, owing to the topological interactions [1, 55–60]. However, more recent studies have demonstrated that this is not a true scaling regime but rather a crossover between ideal scaling at small N, $R_g \sim N^{1/2}$, and collapsed, globule-like scaling at large N, $R_g \sim N^{1/3}$ [59, 61–63]. The topological interactions also affect the dynamics in a unique way in ring polymer melts. Although the diffusion constants scale similarly to those of entangled linear polymers: $D \sim N^{-a}$ with $a \approx 1.9 - 2.3$ (a major puzzle) [60–62, 64], the stress relaxation modulus shows no rubbery plateau and polymer relaxation times scale much more slowly than those of entangled linear polymers, suggesting a decoupling of internal and center-of-mass dynamics [63–68].

These differences between linear and ring polymer systems can be attributed to the fact that the topological interactions are quite different in the two systems. While linear polymers can interpenetrate each other freely, ring polymers cannot, as they must remain non-concatenated, prohibiting certain configurations. As a result, the topological interactions affect both structure and dynamics in ring polymer systems, as opposed to linear polymer

systems in which only dynamics are impacted. This kind of non-concatenation constraint has been studied theoretically for quite a long time using topological invariants such as the Gauss linking number [69, 70]. For instance, these constraints are known to lead to a positive second virial coefficient, even when excluded volume interactions disappear [71–73]. Based on this observation, ring polymer melts should exhibit topological contributions to thermodynamic quantities such as the pressure, but these effects have not yet been observed [64].

Ring polymers melts and solutions also behave uniquely in non-equilibrium scenarios, exhibiting thickening in weak extensional flows as a result of long-lived inter-ring threadings in the form of "reef knots" [74, 75]; these systems even show glass-like dynamics on the macromolecular scale under certain conditions [76–78]. In blends of ring and linear polymers, the linear chains can thread the rings, leading to an entirely different set of rheological responses [79–81]. Although the aforementioned ring polymer systems exhibit significant threading of the rings by neighboring polymers, there are no true topological (or otherwise permanent) concatenations or links, so nearby molecules will eventually diffuse away from one another (glassy dynamics notwithstanding).

Catenated ring polymers represent yet another form of topological constraint, and have been a fixture in the biophysics literature for many decades [71, 82–84]. However, the mechanical and dynamical properties of such systems have not been characterized as extensively as those polymer systems described previously. Nevertheless, some theoretical and computational work has indeed been devoted to the topic. For instance Otto and Vilgis [85, 86] examined the elasticity of large (asymptotic) linked Gaussian ring polymers (i.e. polymeric [2]catenanes) and found that when segments on opposite rings are stretched to a distance $R > R_{g,r}$ where $R_{g,r}$ is the size of a single ring, the free energy scales as $F \sim R^4$, much faster than an ordinary Gaussian linear or ring polymer, which exhibits scaling of $F \sim R^2$ [87]. Such behavior was not apparent in recent simulations [88], but this may be due to the

presence of excluded volume interactions or insufficient polymer size. Polymeric [2]catenanes have also been studied in the melt using a lattice model by Rane and Mattice [89], but those authors focused on fairly small, stiff rings and did not characterize the dynamics beyond the mean-squared displacement of monomers at short times/distances. Moreover, lattice-based models such as the one used in that work (and others) are known to introduce artifacts into the dynamics of catenated polymers [90], making the results difficult to interpret.

More complex interlocking systems systems have also been studied. For instance, Vilgis and Otto [91] used scaling arguments to study the elasticity of catenated networks, also known as Olympic gels, finding two distinct regimes. At small deformations, the free energy is predicted to be linear in the deformation, λ, therefore having constant modulus, unlike a typical polymer network [87]. However, at large deformations, the free energy is expected to scale as $F \sim \lambda^{5/2}$, exhibiting significant strain-hardening. Unfortunately, the synthesis and characterization of such materials is difficult so these results have not yet been tested either by experiment or simulation.

Based on the discussion above, we expect topological interactions to play a key role in the properties and dynamics of poly[n]catenane materials, as the molecules contain a large number of interacting and interlocked ring polymers. In fact, even a single, isolated poly[n]catenane possesses a great many topological constraints, both between mutually linked and un-linked macrocycles. Meanwhile, in dense melt states, intermolecular interactions will also become important and the overall linear character of the polymer and its potential for interchain entanglement may also play a a role.

1.3 Properties of Poly[n]catenanes

Poly[n]catenanes have only recently been synthesized for the first time, so the physical characterization of the systems is still in its infancy; in fact, this is the topic of Chapter 2. As a result, existing literature on poly[n]catenanes has leveraged theory and simulation rather

than experiment. There are a limited number of such works and all of them have focused on isolated poly[n]catenanes, typically under good solvent conditions. The polymers were first studied using an athermal lattice-based Monte Carlo method by Pakula and Jeszka [22], who examined a variety of ring sizes and chain lengths. The end-to-end vector in poly[n]catenanes was found to obey Gaussian statistics, indicating that the chains could be "renormalized" to ordinary linear polymers at large length scales; this conclusion was further supported by later theoretical work of Brereton [21]. Pakula and Jeszka also showed that poly[n]catenane radius of gyration and end-to-end distance obey the same scaling relations, $R_g \sim R_e \sim (nm)^\nu$, as ordinary linear polymers in good solvent conditions ($\nu \approx 0.588 \approx 3/5$) and the data for polymer dimensions collapse to a master curve when normalized by the size of the individual rings. However, this observation has been challenged by a more recent simulation study by Ahmadian Dehaghani *et al.* [92] who used a continuum molecular dynamics method to show that $R_g \sim m^\mu n^\nu$ with $\nu \approx 3/5$ and $\mu \approx 0.658$; this result was rationalized using a Flory-type theory. Those authors also observed that poly[n]catenanes exhibit a higher θ-temperature than linear or ring polymers; it is suspected that the threading segments act as additional "points of attraction," for the macrocycles, allowing more facile chain collapse. Other authors [93] have also examined poly[n]catenanes by molecular simulations, extending the chain lengths up to $n = 100$ rings. These extremely long poly[n]catenanes showed highly unusual structural properties, including unexpected scaling behavior and large, long-lived orientational correlations along the chain. However, the simulation times appear to be short relative to the relaxation times of the polymers (and in some cases only half as long) so the results may be complicated by inadequate sampling.

Although the structural features of poly[n]catenanes have been only sparingly studied, the dynamical properties are an even greater mystery. For instance, although Pakula and Jeszka [22] did indeed examine monomer displacements, orientational relaxation times, and diffusion coefficients of poly[n]catenanes, these properties were only characterized in detail

for systems with very small ring sizes (comparable to the lattice spacing in their model). As mentioned in the previous section, this is known to cause dynamical artifacts [90] and indeed the polymer center-of-mass diffusion coefficients do not follow a $1/N$ dependence, despite the absence of intermolecular and/or hydrodynamic interactions. These issues make it difficult to draw meaningful conclusions concerning poly[n]catenane dynamics. More recently, Kanaeda and Deguchi [94] simulated linear and cyclic catenanes including hydrodynamic interactions via Brownian dynamics. However, only the diffusion constant and radius of gyration were examined and the results were not compared to non-concatenated systems in any detail, so the effect of the topological linking on these properties is unknown. Other authors have also studied poly[n]catenane dynamics by molecular simulations, but only as a test system for a mode analysis method; the properties of the polymers themselves were not discussed [95].

Clearly, the structural and dynamical characteristics of poly[n]catenanes are not well understood at this time, even at the single-molecule level, and the polymers remain completely unstudied in the melt. Now that the synthesis of poly[n]catenanes has finally been achieved, it is important to understand the properties of these molecules and how they may be controlled and engineered at the molecular level. Since poly[n]catenanes are still difficult to synthesis and study, molecular simulations are an excellent tool for the task.

1.4 Outline

The remainder of this dissertation is organized as follows. In Chapter 2, we describe the synthesis and physical properties of poly[n]catenanes and use detailed molecular dynamics simulations to interpret the observations. Chapter 3 then uses a coarse-grained molecular model to study the structure and dynamics of isolated poly[n]catenanes and how these properties are affected by ring size and segment stiffness. In Chapter 4, use theory and simulation to study the effect of hydrodynamics interactions on the dynamics of interlocked polymers. Chapters 5 and 6 use large scale molecular dynamics simulations to characterize

the structure and dynamics, respectively, of poly[n]catenanes in the melt. We conclude by reflecting on the future of the field and avenues for further research.

CHAPTER 2

ATOMISTIC CHARACTERIZATION OF POLY[*N*]CATENANES

2.1 Introduction

As discussed in the Introduction, the structure of a poly[n]catenane can be considered the molecular equivalent of a macroscopic chain, which retains its flexibility no matter the stiffness of its components on account of the unique topology. Such structures allow access to both high strength and excellent flexibility and several authors have suggested that poly[n]catenanes could exhibit a large loss modulus and a low activation energy for flow, and could potentially act as outstanding energy damping materials and/or elastomers with excellent toughness and stimuli-responsive mechanical properties [18, 20]. Although chemists have targeted poly[n]catenanes for many decades, until recently, no successful synthesis had been achieved and therefore little was actually known about their properties, despite ample speculation. In this chapter, we describe the synthesis and some physical properties of poly[n]catenanes which were recently reported by our group [19] and represent a major advance in the preparation of mechanically interlocked polymers. Furthermore, we develop an all-atom molecular model of the polymers and use molecular dynamics simulations to study the force-extension and diffusive behaviors of the polymers, comparing the results with experiment. Since this dissertation focuses primarily on the physics of these novel polymers, only a cursory discussion of the chemical synthesis will be offered; a comprehensive account can be found in the original publication [19].

2.2 Poly[*n*]catenane Synthesis and Properties

The synthesis of poly[n]catenanes is a major challenge. Before the work of Wu *et al.* [19], the confirmed synthesis of this molecular topology for a relatively high molecular weight had yet to be reported. Most of the prior work on polycatenanes has focused on poly[2]catenanes

in which [2]catenane moieties are incorporated into the backbone of conventional polymers [20, 96–102], poly/oligocatenanes with unclearly-defined architectures [103, 104], and polymeric [2]catenanes (i.e. two interlocked cyclic polymers) [105]. These materials have afforded insights into the potentially interesting properties of MIPs. For example, poly[2]catenanes have shown conformational flexibility along the polymer chain in solution (indicated by a shorter Kuhn segment length than the length of its [2]catenane moiety) [20] and temperature-dependent motion of the rings in solution [98] or in bulk materials [101]. It is worthwhile pointing out that poly[2]catenanes (shown in Figure 2.1a) have covalent linking groups along the backbone, in addition to the topological bonds, which can limit the degree of rotation of the ring component. Poly[n]catenanes, on the other hand, are linked solely by topological bonds allowing full rotational mobility of every ring (with sufficient ring size) and, as such, more conformational freedom. One of the most successful attempts to access oligo[n]catenanes with at least seven interlocked rings was recently achieved via the ring-opening polymerization of metallo-[2]catenanes by Meijer, Di Stefano and their coworkers [104]. However, the specific architecture of the product (i.e., linear, branched, etc.) could not be clearly defined. Prior to 2017, the longest interlocked molecular chain with clearly defined structure was a linear [5]catenane (olympiadane) reported by Stoddart and coworkers [106] and, more recently, by Iwamoto *et al.* [107], both via stepwise approaches. Stoddart and coworkers have also used a similar strategy to access a branched [7]catenane [108]. These step-wise strategies, however, are not efficient methodologies for the synthesis of long chain poly[n]catenanes. One key challenge in the synthesis of poly[n]catenanes is the conflicting reaction conditions for accessing macrocycles (requiring low concentration) and polymers (requiring high concentration). Takata, Kihara and coworkers proposed an elegant solution to this conflict by converting a bridged poly[2]catenane into poly[n]catenane [100], but to date there is no report of a poly[n]catenane synthesized via this route.

The synthetic strategy toward poly[n]catenanes outlined herein, illustrated in Figure 2.1b,

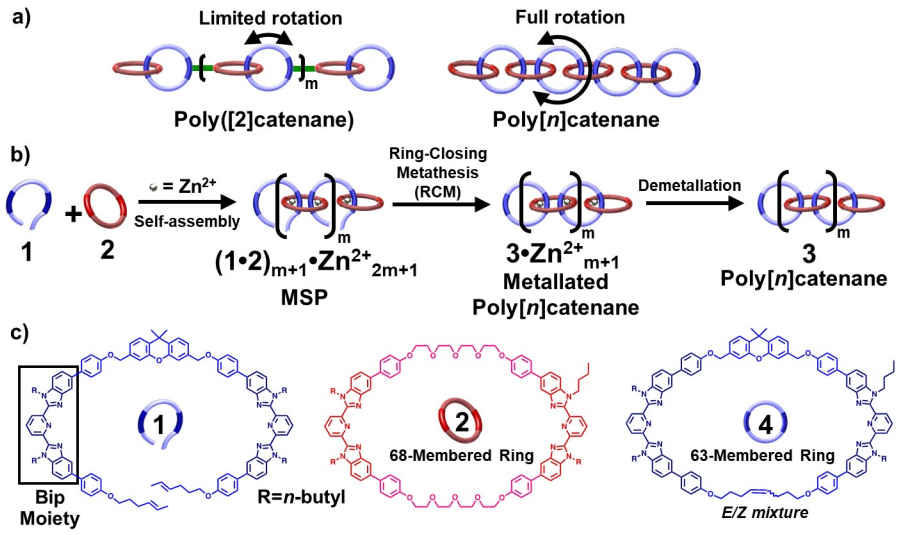

Figure 2.1: Poly[n]catenanes and their synthesis. a) Comparison of ring mobility in poly[2]catenanes and poly[n]catenanes, b) Synthesis of poly[n]catenane **3** via assembly of **1** and **2** into a metallosupramolecular polymer (MSP), followed by ring-closing and demetallation, c) Structure of thread **1** and macrocycles **2** and **4**; the box highlights the structure of the Bip moiety.

decouples the above-mentioned conflicting synthetic requirements through the pre-assembly of a metallosupramolecular polymer (MSP) as a template, followed by an efficient ring-closing reaction and demetallation. Pioneered by Sauvage, metal-ligand coordination has been one of the most successful synthetic routes toward mechanically interlocked (small) molecules (MIMs) [109–112]. The terdentate ligand, 2,6-bis(N-alkyl-benzimidazolyl)pyridine (Bip, Figure 2.1c), which binds transition metal ions such as Zn^{2+} or Fe^{2+} in a 2:1 stoichiometry, was chosen as it has already been shown to access a wide range of functional metallosupramolecular polymers that exhibit photo-healing [113], stimuli-responsive [114], shape memory [115] and actuation [116] properties. Furthermore, we have recently shown that [3]catenanes can be accessed via a near quantitative ring-closing reaction of a pseudo[3]rotaxane assembled from a monotopic Bip-containing macrocycle, Zn^{2+}, and a ditopic thread (**1** with R = hexyl, see Figure 2.1), in a ratio of 2:2:1 [112].

Building on these studies, we targeted the MSP assembly of the rationally designed 68-

membered ditopic Bip-macrocycle **2** with the threading molecule **1** and the subsequent ring closing of **1** (Figure 2.1c). Upon the addition of two equivalents of Zn^{2+} to the 1:1 mixture of **1** and **2**, the components self-assembled into the alternating supramolecular copolymer (Figure 2.1b). The alternation is a consequence of the principle of maximal site occupancy [117]: two Bip moieties in the same (or different) macrocycle **2** cannot bind the same Zn^{2+} ion; therefore, each Bip unit in **2** must form a 2:1 Bip:Zn^{2+} ion complex with a Bip unit in **1** in order to maximize enthalpic gain. The formation of an MSP was confirmed by Diffusion-Ordered Spectroscopy (DOSY). The large binding constant ($> 10^6 M^{-1}$ in acetonitrile) between Bip and Zn^{2+} [118] maintains the MSP under the relatively dilute conditions required to favor the ring closing reaction (although cyclic MSPs should be favored under very dilute conditions). The ring-closing metathesis (RCM) reaction showed excellent olefin conversion at 2.5 mM (with respect to **1**), and the resulting reaction mixture could be readily demetallated with tetrabutylammonium hydroxide. The synthesis of a mixture of cyclic, linear, and branched poly[n]catenanes in approximately 80% yield was confirmed by a combination of size exclusion chromatography, light scattering measurements, mass spectrometry, and nuclear magnetic resonance spectroscopy. The details of the purification and characterization of the reaction products are outside the scope of this work, but may be found in ref. [19].

It is known that catenanes prepared via metal templating exhibit metallo-responsive behavior [119] and, as such, the metallo stimuli-responsive properties of these poly[n]catenanes were investigated in the bulk and in solution, by measuring the glass transition temperature, T_g (by differential scanning calorimetry, DSC), and the hydordynamic radius, R_h (with dynamic light scattering, DLS), respectively. In particular, a sample/fraction of poly[n]catenanes, **3c**, believed to be predominantly linear in overall architecture, was analyzed closely. In the bulk, the T_g of fraction **3c** was found to be 97°C, compared to 137°C for **5**, a chemically similar linear (covalent) polymer of **1** formed by acyclic diene metathesis

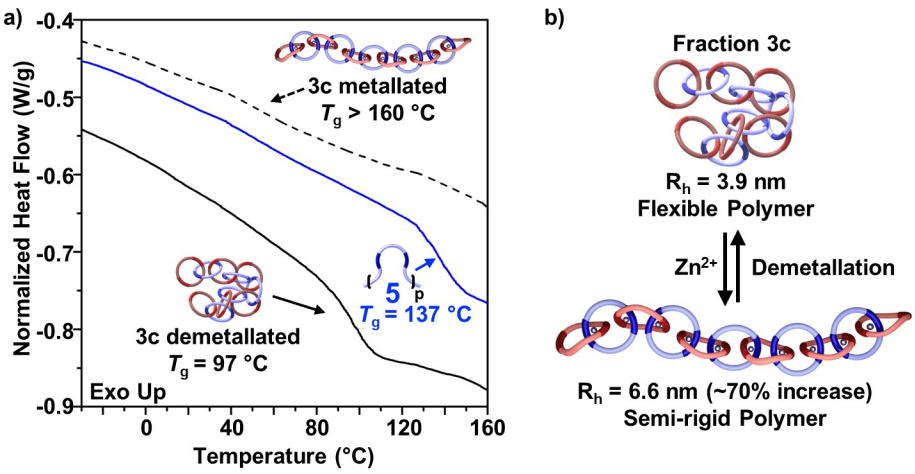

Figure 2.2: Some physical properties of polycatenanes. a) DSC data for linear poly[n]catenane (fraction **3c**) in the metallated and demetallated state compared with data for ADMET polymer **5** (T_g calculated by half-height midpoint). b) Illustration of the metallo-responsive conformational change of a linear poly[n]catenane between flexible and semi-flexible structures as indicated by change in hydrodynamic radius, R_h.

(ADMET) polymerization (Figure 2.2a). In general, polymers with greater segmental motion show lower T_g, which is consistent with the more facile conformational motions expected in the poly[n]catenane backbones. Metallation with Zn^{2+} locks these conformational motions as the Bip-Zn^{2+} complexes reform, significantly reducing the flexibility of poly[n]catenanes; as such, no T_g is observed upon heating up to 160°C for the metallated polymers. This result suggests that addition of Zn^{2+} ions into poly[n]catenanes induces a switch from a highly flexible polymer to a rigid one. In solution (with 1,1,2,2-tetrachloroethane, TCE, as solvent), fraction **3c** showed a significant ($\sim 70\%$) increase in R_h from 3.9 nm to 6.6 nm, upon addition of Zn^{2+} as seen in Figure 2.2b. However, the increase is not as large as might be expected if the metallated polymer were truly rigid. In order to understand this behavior, we must examine the polymers in greater detail, using atomistic molecular dynamics simulations. To do so, we first develop a molecular model for the various components within the polymers, and then conduct *in silico* experiments to probe the quantities of interest. In particular, we wish to determine R_h for metallated, linear poly[n]catenanes to compare with the DLS

experiments described above to confirm that a sample of primarily linear poly[n]catenane has indeed been successfully isolated. These efforts are described in the following sections.

2.3 Simulation Details and Molecular Model

All simulations in this chapter were conducted with the GROMACS [120, 121] molecular dynamics package. The OPLS-AA force field [122–126] was used with a 1.2 nm cutoff radius for Coulombic and Lennard-Jones interactions. Mean-field tail corrections to the energy and pressure were included to account for the cutoff of the short-range non-bonded interactions [127]. Long-range electrostatics were calculated using the particle mesh Ewald (PME) algorithm [128, 129] with a Fourier grid spacing of 0.16 nm. For production simulations, a constant temperature of 293.15 K was maintained using the Nosé-Hoover thermostat algorithm [130, 131] with a time constant of 0.5 ps; the catenanes (macrocycles and metal ions) and solvent (TCE and counterions) were coupled separately to the heat bath. Where applicable, a constant pressure of 1 bar was maintained using the Parrinello-Rahman pressure coupling algorithm [132] with a time constant of 2.0 ps and a compressibility of $6.5 \times 10^{-5}\text{bar}^{-1}$, which is the room-temperature compressibility of the solvent [133, 134]. The LINCS algorithm [135, 136] was used to constrain all bonds and allowed the use of a 2 fs time step using a leapfrog integrator [137]. Periodic boundary conditions were applied in all directions. The rigorous development of a complete force field for the system in question is outside the scope of this work. As mentioned above, we instead use the well-known OPLS-AA force field and make small modifications and additions as needed to describe the system components in a first-order approximation. In particular, additional parametrization was necessary for the macrocycles, solvent, and metal ions.

The macrocycles **1** and **2** within poly[n]catenanes can be thought of as two extended Bip molecules connected by two linking groups. These linkers (oligoethylene glycol, xanthene, and an unsaturated alkane) can be easily described using existing OPLS atom types and

parameters. However, to our knowledge, the Bip moieties have not been parametrized in the context of the OPLS-AA force field. The atoms types, charges, and bonded parameters were therefore taken by analogy with existing OPLS atom types found in benzene [122], imidazole [123], and pyridine [124]. However, a dihedral potential for rotation around the bi-aryl pyridine-benzimidazole bond was not available. Since rotation around this bond greatly changes the shape of the Bip molecule - switching from a "V"-shape to a linear conformation as shown in Figure 2.3 - a small parametrization effort was required. In addition, partial charges were unavailable for $N1$-substituted imidazoles, which necessitated additional efforts.

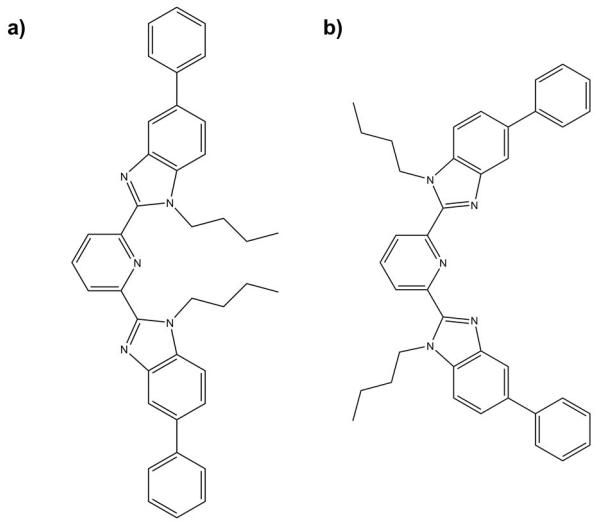

Figure 2.3: a) Linear and b) "V"-shaped conformers of the extended Bip ligand. Rotation around the central bi-aryl bonds allows for transitions between the two states.

Following previous work by the developers of the force field [126], we use quantum mechanical calculations to determine the bi-aryl torsional energetics of two model molecules, **6** and **7**, shown in Figure 2.4. All quantum mechanical calculations were performed using the Gaussian09 software [138]. The molecules had their geometries optimized at dihedral angles ranging from 0° to 180° in increments of 10° at the MP2(full)/6-311G(d,p) level [139]. Single point energies were calculated at each of the resulting configurations at the MP2(full)/aug-cc-pVTZ level of theory [140]. The results for **6** were compared to the torsional energies obtained from a dihedral scan conducted in GROMACS using the classical

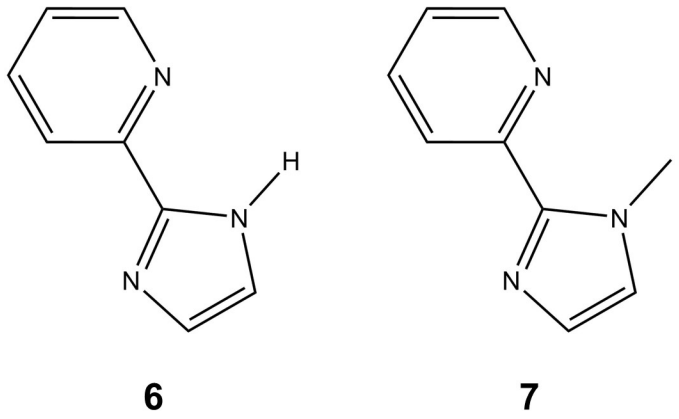

Figure 2.4: Model molecules used for quantum mechanics calculations to parametrize the Bip ligand

force field with the default OPLS parameters and no biaryl torsion potential. The dihedral torsion parameters were updated iteratively until the root-mean-square error between classical and quantum values was minimized, having a final value of 0.049 kcal/mol. The resulting parameters were assumed to be transferable to **7** as well as the full Bip moiety. To determine the partial charges on the alkyl-substituted imidazole, the dihedral potential derived above was applied to **7** and the partial charges on the imidazole $N1$ and methyl C atoms were varied until error between the classical and quantum mechanical torsional energies was minimized. The methyl hydrogens were assumed to have charge $+0.06e$ (similar to aliphatic hydrogens in amines for OPLS) and the remaining partial charges were unchanged. Upon requiring charge neutrality, the optimization is reduced to a one-parameter minimization of the root mean-squared error, the resulting value being 0.48 kcal/mol. Figure 2.5 shows the quantum and classical torsion energy profiles for each of the model molecules.

The partial charges and torsional potentials derived from the model molecules were then applied to the Bip moiety and the two macrocycles in an additive fashion consistent with the OPLS-AA force field. Coordinate files for the macrocycles were created using the PRODRG tool [141] and the GROMACS [120, 121] tools were then used to create topology files, which were checked and edited manually to account for the results of the fitting procedure above.

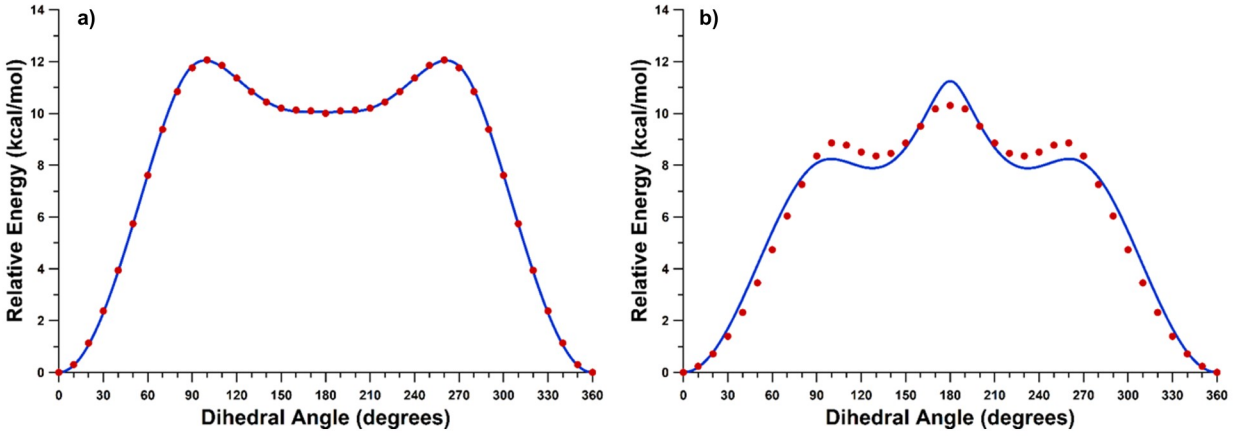

Figure 2.5: Bi-aryl torsional energy profiles for the model molecules a) **6** and b) **7**. Red points show the results from quantum chemistry calculations; blue lines show the results from classical force field calculations.

The alkene segment in the macrocycle **4** was initialized in the E configuration; there are no other stereocenters in either macrocycle. The Visual Molecular Dynamics (VMD) software [142] was used to arrange macrocycles into an interlocking structure. It is important to note that these efforts are not to be taken as a highly detailed or accurate parametrization of the Bip molecule, only the simplest possible treatment to describe the energetics of the most important degrees of freedom in the molecule.

1,1,2,2-tetrachlorethane (TCE) was used in the DLS experiments described in the previous section and is therefore the desired solvent for these simulations. Although the DLS experiments used deuterated TCE, for simplicity this detail will be omitted here. While the molecule was part of a recent benchmarking effort for the OPLS-AA force field [134], the resulting the dielectric constant (a critically important solvent property) is only $\sim 50\%$ of the experimental value. To improve the quality of the solvent model, the partial charges were treated as variable parameters to achieve agreement with experiment, in the spirit of the OPLS force field; the partial charges are expected to have a large impact on the dielectric without altering the structural properties of the liquid (e.g. density, compressibility, etc.) which are well-reproduced by the previous study. The partial charges shown in Table 2.1

were found to reproduce a variety of experimental quantities very well. In particular, excellent agreement is observed for the previously troublesome dielectric constant. All calculated properties of the updated TCE model are reported and compared to experimental values in Table 2.2. 95% confidence intervals are reported for each property. For the density and heat of vaporization, standard errors were obtained by block-averaging error analysis. For the dielectric constant, thermal expansion coefficient, and isothermal compressibility, the simulation trajectory (15 ns in total) was divided into fifteen 1.0 ns intervals and analyzed independently. The resulting data were averaged to obtain a mean value and the associated confidence intervals. The fluid viscosity was calculated by analyzing the transverse current autocorrelation functions (TCAFs) as described by Palmer [143], which can be performed out-of-the-box in GROMACS. The confidence interval for the viscosity was determined from the variance in the fit of the wave-vector-dependent viscosities. The updated charges for TCE were used in all catenane simulations.

Table 2.1: Partial charges for 1,1,2,2-tetrachloroethane.

Atom	**Charge** (e)
C	0.122
Cl	-0.135
H	0.06

Table 2.2: Experimental and simulated properties of 1,1,2,2-tetrachloroethane at 293.15K (unless otherwise indicated). Uncertainties are provided as 95% confidence intervals as described in the main text.

Property	**Exp. Value**	**Sim. Value**	**Refs.**
Density (g/L)	1594.2	1611.1 ± 0.5	[144]
Dielectric Constant	$8.1 - 8.5$	8.33 ± 0.54	[145, 146]
Thermal Expansion Coef. (0.001/K)	0.96 (298.15K)	1.01 ± 0.03	[134, 147]
Isothermal Compressibility (1/GPa)	0.65	0.61 ± 0.02	[134]
Heat of Vaporization (kJ/mol)	47.17	47.52 ± 0.92	[148]
Shear Viscosity (cP)	1.77	1.12 ± 0.15	[149]

The Zn^{2+} ion is used experimentally to metallate the catenane molecules by binding to two Bip ligands and must therefore be modeled in the simulations. Metal-ion complexes have been extensively studied in molecular simulations and a wide range of models has been developed, offering a variety of features and complexities [150]. A detailed parametrization of the Bip-Zn^{2+} complex is outside the scope of this work, so a simple yet generally accurate description is chosen for the Zn^{2+} ion: the non-bonded model of Stote and Karplus [151] based on electrostatics and the Lennard-Jones potential. To evaluate the performance of this model, the structural properties of the Bip-Zn^{2+}-Bip complex obtained from simulations in vacuum at low temperature are compared to crystallographic data [152]. For simplicity, a methyl-substituting Bip (Figure 2.1c with R = Me) was used in these simulations. A comparison of the N-Zn bond lengths and N-Zn-N angles is shown in Table 2.3 and the agreement is satisfactory. However, it is worth noting that no efforts were made to validate the strength of the metal-ligand interaction, only the basic structural characteristics. Experimentally, the Zn^{2+} ions are added as a salt with two bistriflimide counterions which are known to be non-coordinating molecules and as such do not interfere with the Bip-Zn^{2+} complex. However, this behavior is not well-described by classical MD simulations and the counterions are able to displace the Bip ligand. Following previous work in ionic liquids [153–155] and polymer electrolytes [156–158], the partial charges on all ionic species were scaled down to improve ion separation. To determine the minimum necessary charge reduction, several simulations were conducted on solvated complexes; Cl^- was chosen as the counterion for simplicity. A scaling factor of 0.6 was sufficient to prevent direct coordination between the metal and the counterions and to maintain the integrity of the Bip-Zn^{2+} complex. Thus, partial charges of $+1.2e$ and $-0.6e$ were used for Zn^{2+} and Cl^- ions in all catenane simulations.

Table 2.3: Some key structural parameters for the Bip-Zn^{2+} complex determined from experiment [152] and simulation. Values were averaged over identical bonds/angles within the complex. Pyr = Pyridine Nitrogen, Im = Imidazole Nitrogen, Zn = Zinc ion. For the angles listed, there is additional indication if the angle connects Nitrogen atoms on the same or different Bip molecules.

	Bonds/Angles	**Experiment**	**Simulation**
Bonds	Zn-Pyr	2.14 Å	2.09 Å
	Zn-Im	2.15 Å	2.15 Å
Angles	Pyr-Zn-Pyr (different Bip)	168.8°	174.8 °
	Im-Zn-Im (same Bip)	149.0°	151.8 °
	Im-Zn-Im (different Bip)	94.1°	93.3 °
	Pyr-Zn-Im (same Bip)	74.6°	76.1 °
	Pyr-Zn-Im (different Bip)	105.5°	103.9 °

2.4 Simulated Properties of Metallated Poly[n]catenanes

Since the poly[n]catenanes synthesized experimentally have average degree of polymerization (i.e. number of rings) in the range of 11-12 and each ring is approximately 2.5 nm in diameter, full atomistic simulations of even a single polymer would require many millions of atoms, which is computationally impractical. Therefore, we must employ more sophisticated methods to evaluate the properties of the polymers by examining much smaller systems. The quantity of immediate interest is the hydrodynamic radius, R_h, which is related to the diffusion coefficient by the Stokes-Einstein equation:

$$R_h = \frac{k_B T}{6\pi\eta D} \tag{2.1}$$

where η is the solvent viscosity and D the diffusion coefficient. Although various approximations exist for R_h based solely on structural information, the rigorous definition relies on dynamical information found in the diffusion coefficient. Fortunately, for polymers, one expects measures of molecular size such as R_h and the end-to-end distance, R_e,to exhibit

similar scaling [87, 159], so that the ratio between the two values should be relatively constant when the number of macrocycles is varied. Thus, if we have measurements of R_h and R_e for a small poly[n]catenane and an estimate of R_e for a larger one, we can obtain an accurate estimate of R_h for the latter. Still, we must be able to estimate R_e for poly[n]catenanes of arbitrary size, which can be done through various analytical formulas [87] if certain physical parameters of the polymer are known, such as the persistence length and contour length. Such quantities can be determined from a force-extension experiment which can be performed *in silico*.

First, we determine R_h and R_e for a small metallated poly[n]catenane with $n = 4$ to find the ratio between the two values. R_e was calculated by evaluating the average distance between metal ions bound to the Bip moieties at the chain ends. As discussed below, a number of independent simulations were run for the system; the distribution of mean end-to-end distances from each trajectory was used to compute R_e and the associated 95% confidence interval, with the result $R_e = 7.25 \pm 0.33$ nm. Strictly speaking, this is not a *true* end-to-end distance since a terminal Bip ligand will extend beyond the metal's position in the direction of the contour length. However, this value can be directly compared to the force-extension simulations detailed below since the equivalent measure of molecule size in that system is simply the box length. R_h was calculated from Eq. 2.1 where the diffusion coefficient, D, is obtained from the mean squared displacement $\langle \Delta R^2 \rangle$ of the polymer center-of-mass using the Einstein relation:

$$\langle \Delta R^2 \rangle = 6Dt + C \tag{2.2}$$

where t is time, and C is a constant of integration. When determining the diffusion coefficient from molecular dynamics simulations, it is crucial to obtain multiple independent samples, especially for macromolecules [160]. Accordingly, 20 independent simulations of 25 ns each were conducted for the system. The first 5 ns were discarded as equilibration time and the

squared displacements of the catenane center-of-mass from each trajectory were calculated, averaging over all initial conditions. To estimate error, each trajectory was independently fit to Eq. 2.2 and the resulting sample of diffusion coefficients was used to calculate a mean and 95% confidence interval.

Following similar work on the diffusion of oligomeric species [161], a number of corrections must be made to the raw value of D for accurate analysis. First, the change in viscosity due to the presence of the solutes must be accounted for. This is done in an approximate manner by calculating the volume fraction of the non-TCE molecules and using the Einstein equation:

$$\eta = \eta_s(1 + 2.5\phi) \tag{2.3}$$

where η_s is the viscosity of the pure solvent and ϕ is the volume fraction of the solutes (catenane, metal, and counterions). Since the volume fraction of the solute is very small (~ 0.0029), the resulting correction to the viscosity is less than 1%. Second, a correction for finite size effects must be added; this correction accounts for long-range hydrodynamic interactions between solutes in different periodic images as described by Yeh and Hummer [162]:

$$D_0 = D + \frac{2.837292 k_B T}{6\pi\eta L} \tag{2.4}$$

where η is the viscosity of the solution, L is the box length (assuming a cubic box), and D_0 is the corrected diffusion coefficient. Finally, it is important to recognize that the viscosities of liquids are often poorly captured by classical molecular dynamics simulations, which alters the diffusive behavior of the systems. For instance, the viscosity of TIP4P water is only about half of the experimental value [143]. To correct for this in the present system, all diffusion constants were scaled by the ratio of simulated to experimental viscosities of the pure solvents, 1.12 cP/1.77 cP = 0.633. The corrected diffusion coefficient from Eq. 2.4 was then substituted into Eq. 2.1 along with the experimental viscosity to obtain the hydrody-

namic radius. Error was determined by standard propagation of uncertainty in the diffusion coefficient and the viscosity. The corrected diffusion coefficient of the metallated [4]catenane was found to be $(0.033 \pm 0.010) \times 10^{-5}\text{cm}^2/\text{s}$, resulting in a hydrodynamic radius, R_h, of 2.44 ± 0.36 nm. The mean end-to-end distance was $R_e = 7.25 \pm 0.33$ nm, resulting in a ratio $R_h/R_e \approx 0.34 \pm 0.05$.

Having obtained an estimate of the ratio between R_h and R_e, we now use a force-extension experiment to find to the persistence and contour lengths of poly[n]catenanes, so that R_h may be estimated for polymers of arbitrary number of rings, n. To determine the force-extension properties of poly[n]catenanes, a metallated [8]catenane was stretched and oriented along the z-axis and connected to itself through the periodic boundary conditions of the simulation cell. After solvating with TCE molecules and equilibrating the system, the box length in the z-direction was systematically varied in a series of simulations while the box dimensions in the x- and y-directions were chosen so as to maintain the equilibrium density at 1 bar. Production simulations at each box length were run for a total of 200 ns. Since the solvent is a simple liquid, all extra stress in the system must arise from the tension on the chain. Thus the force, f is written:

$$f = L_x L_y \left(\frac{P_{xx} + P_{yy}}{2} - P_{zz} \right) \tag{2.5}$$

where L_x and L_y are the box dimensions in the x- and y-directions, respectively, and $P_{\alpha\beta}$ is the $\alpha\beta$ component of the pressure tensor, which is readily available in simulations through the virial theorem [127]. Meanwhile, the extension is simply the box length in the z-direction.

An illustration of the simulations and the resulting force-extension behavior of the metallated [8]catenane are shown in Figure 2.6a. Due to its relatively small size, this model system is only valid for fairly large forces. This is because the forced periodicity of the polymer places a constraint on the available conformations such that the end-to-end vector must lie principally along the z-axis with only small transverse fluctuations. By contrast, a real

polymer will have an average end-to-end distance of zero in any given direction. However, when subjected to a large force on the chain ends, the polymer backbone will indeed lie approximately along the vector of that force as the end-to-end distance becomes comparable to the contour length. As an example, a tension force of ∼10 pN is sufficient to extend a double-stranded DNA molecule to >95% of its contour length [163]. In this high-force regime, the periodic [8]catenane becomes a more accurate model of the system. Accordingly, only data points having average tensions >10 pN were included when comparing to theoretical models.

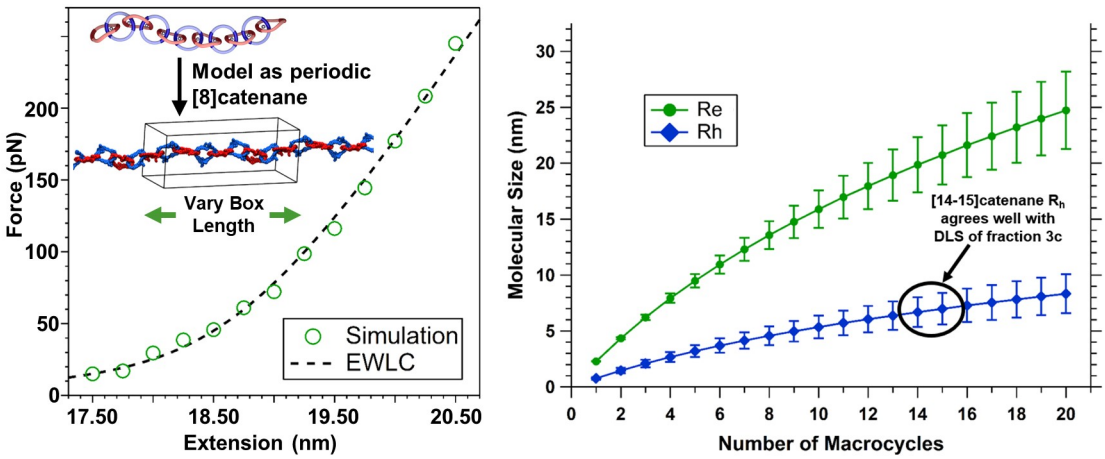

Figure 2.6: a) Illustration of the force-extension simulations and the resulting data. Green circles indicate simulation data (size of data point includes error) and the black line is a fit to the EWLC model, Eq. 2.6. b) Estimated end-to-end distance, R_e and hydrodynamic radius, R_h, obtained from the paramters of the EWLC fit in a); the results agree well with DLS experiments.

The simulated values can be well-fit by a high-force interpolation [164] of the extensible worm-like chain (EWLC) model given by Eq. 2.6:

$$x = L_n \left[1 - \frac{1}{2} \left(\frac{k_B T}{l_p f} \right)^{1/2} + \frac{f}{E} \right] \tag{2.6}$$

where x is the end-to-end distance in the direction of the force, L_n is the contour length of a poly[n]catenane, f is the force on the chain, l_p is the persistence length, and E is the

stretch modulus. Non-linear least squares fitting was used to obtain the values of $L_n(= L_8)$, l_p, and E for the metallated [8]catenane with relative weights of data points given by the standard error in the tension from each simulation, as determined from block-averaging error analysis. To generate statistics for the fitting parameters, a bootstrap method was used. Each trajectory was block-averaged over 1 ns intervals to generate a population of pseudo-independent values. A bootstrap sample was taken for each box length and the resulting means were fit to Eq. 2.6. The process was repeated 10,000 times to generate distributions for the parameters, which were used to determine means and 95% confidence intervals. The persistence length showed a skewed distribution and is therefore reported as the median and a symmetric interval containing 95% of the observed values. The resulting fit parameters are: $L_8 = 19.22 \pm 0.23$ nm, $l_p = 7.46 \pm 2.88$ nm, and $E = 2630 \pm 280$ pN/nm. Dividing the counter length by the number of macrocycles gives a per-macrocycle contribution to the contour length of $l = 2.40 \pm 0.03$ nm (ignoring differences between the macrocycles **2** and **4**). This value is considerably smaller than the persistence length, which indicates that the linear metallated catenanes obtained experimentally ($n = 8 - 27$) are semi-flexible polymers with contour length $L_n \approx 2.5 - 8\ l_p$, not rigid rods as has been expected before. With these parameters, the end-to-end distance, R_e can be calculated for arbitrary n using worm-like chain (WLC) statistics [87]:

$$R_e^2 = 2 l_p L_n \left[1 - \frac{l_p}{L_n}\left(1 - e^{-L_n/l_p}\right)\right] \tag{2.7}$$

Error in R_e was estimated by randomly sampling the set of EWLC parameters determined above. It is worth noting that the predicted value of R_e for $n = 4$ is ∼9% larger than the value found from the simulation of the metallated [4]catenane detailed above. This is likely due to end effects: the reported persistence length only applies to portions of the chain in which each macrocycle has two topological bonds, whereas the chain ends have just one. To reduce the influence of these end effects, the [2]catenane defined by the inner rings of the

[4]catenane can be studied. The predicted R_e for this system differs by only ∼4.5% compared to the observed value. In general, end effects will become less important as the number of macrocycles increases so the EWLC parameters reported here should be more accurate for larger polymers.

Applying the ratio R_h/R_e found earlier, R_h is calculated by simple multiplication. Figure 2.6b shows the resulting values as a function of n. To determine if the fraction **3c** is indeed mostly linear, we compare our results to the earlier DLS experiments, which showed an average R_h of 6.66 nm. Since the magnitude of DLS signal is proportional to the square of molecular weight of the scatterers, this value does not correspond to the number-averaged DP of 11-12, but instead to the weight-squared averaged DP of 14-15, which was determined from Gel Permeation Chromatography with Multi-Angle Light Scattering (GPC-MALS) [165]. The R_h value predicted for catenanes of this size from our simulations is 6.89 ± 1.38 nm, in good agreement with the experimental value, suggesting that sample **3c** is indeed predominantly linear.

Our simulations can also be used to study the origin of the flexibility in metallated poly[n]catenanes. To study the relative flexibility of the two different types of macrocycles, the distances between neighboring metal ions along the chain were analyzed. Each pair of adjacent ions is connected by either macrocycle **2** or **4** so that the fluctuations in the associated distances, d_2 vs. d_4, provide a simple measure of macrocycle flexibility. For the [4]catenane studied above, only the internal rings were considered so as not to include end effects. Due to the presence of the TEG segments used as linker groups, **2** is expected to be more flexible than **4**, which has a rigid xanthene linker. This is indeed the case in the [4]catenane system: both distances show a unimodal distribution as seen in Figusre 2.7a, but d_2 shows larger absolute and relative fluctuations compared to d_4 as measured by the standard deviations of $\sigma_2 = 0.21$ nm and $\sigma_4 = 0.11$ nm. Furthermore, **2** is extended more easily under tension. Figure 2.7b shows d_2 and d_4 as a function of box length for the pe-

riodic [8]catenane with standard deviations σ_2 and σ_4 represented by shaded regions. The macrocycle **2** experiences larger fluctuations in size as well as larger relative and absolute extensions compared to **4**. At large extensions, the mean length of **2** becomes longer than that of **4** in a reversal of the equilibrium observation. In summary, metallated poly[n]catenanes are similar to extensible worm-like chains, whose flexibility is related to the linker groups in the constituent macrocycles.

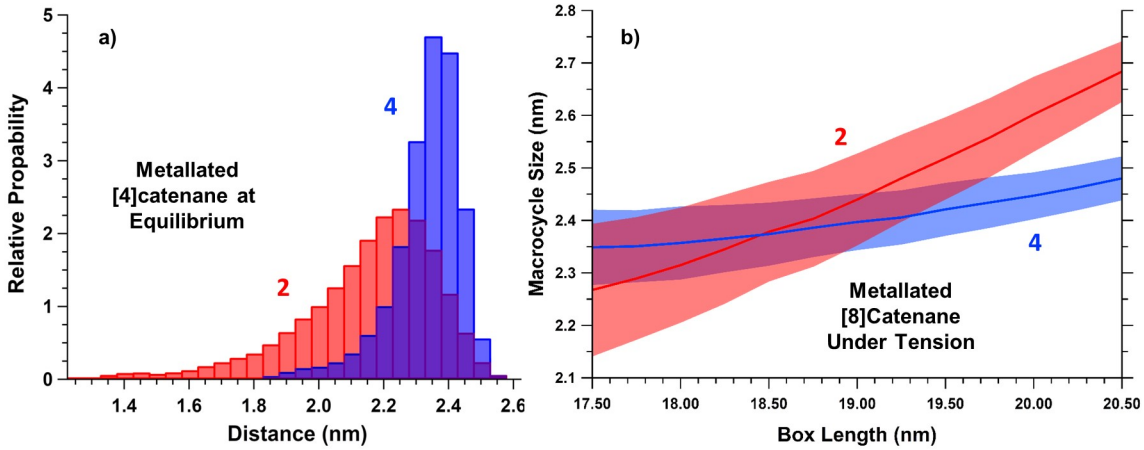

Figure 2.7: a) Relative probability of inter-metal distances for macrocycles **2** (red) and **4** (blue) within a metallated [4]catenane at equilibrium. b) Inter-metal distances for macrocycles **2** (red) and **4** (blue) in a periodic, metallated [8]catenane as a function of box length (extension). The lines show mean values while the shaded areas show the associated standard deviations.

2.5 Discussion and Conclusions

The combination of experiments and atomistic simulations detailed in this chapter helped confirm the first synthesis of high-molecular weight linear poly[n]catenanes [19], which had been sought after by chemists for many decades without success. Furthermore, the force-extension and metallo-responsive behaviors of the polymers were examined, again with a combination of simulation and experiment. Despite these achievements, many difficulties remain, particularly in regard to physical characterization. For instance, even non-metallated

poly[n]catenanes have very high T_g's and form powders at room temperature, rather than films, prohibiting rheological measurements in the bulk. Such measurements could potentially be performed on concentrated solutions, but the available solvents have very low viscosities and boiling points, again making such experiments practically challenging. Small angle neutron scattering (SANS) experiments were performed on poly[n]catenanes but the measured signal was quite weak due to low scattering contrast with the solvent. Meanwhile, quasi-elastic neutron scattering (QENS) experiments showed no significant dynamics up to temperatures of 230°C, above which the alkene groups in **4** become labile, potentially leading to undesirable chemical reactions.

There are also difficulties in simulating such systems with atomistic detail. In particular, the simulations described in this chapter focus only on metallated poly[n]catenanes, in which the Bip-Zn^{2+} complexes significantly reduce the conformational freedom of the polymers. In the absence of the metal ions, longer and more detailed simulations are required to obtain accurate averages. However, such sampling is computationally expensive since the simulated metal-free poly[n]catenanes exhibit ubiquitous $\pi - \pi$ stacking interactions, whose dynamics are too slow to access with conventional molecular dynamics methods. To circumvent this issue, we attempted advanced sampling techniques, such as replica exchange with solute-tempering (REST) [166, 167]; the sampling of the systems improved, but still suffered from large statistical error and required enormous computational resources for even modest results.

To address the challenges above, synthetic chemists are exploring new chemistries which may provide avenues to low-T_g poly[n]catenanes whose physical and rheological properties can be more easily characterized. In the meantime, to understand the novel properties associated with this unique architecture and to guide synthetic efforts, physicists have turned to coarse-grained simulations of poly[n]catenanes, which sacrifice chemical details but provide enormous computational savings. Indeed, chemically-agnostic coarse-grained molecular models have become workhorses in polymer physics over the last 40 years and continue

to provide valuable insight into polymer structure and dynamics. The remaining chapters of this dissertation will focus on using such coarse-grained models to study the physics of poly[n]catenanes.

CHAPTER 3

POLY[*N*]CATENANES AS ISOLATED POLYMERS

3.1 Introduction

As discussed in the Introduction, many unique dynamical properties of polymeric materials depend on molecular architecture and topological interactions [13, 168]. As a result, even a single poly[n]catenane may have highly unusual properties since the polymers are dominated by mechanical bonds, rather than traditional covalent linkages. Mechanical bonds have long been recognized as an important class of topological interactions and have even been used to identify and characterize entanglements between linear polymers [54, 69, 70]. Therefore, one may expect poly[n]catenanes to exhibit topological interactions not only between chains (as in linear polymers), but also between neighboring macrocycles, perhaps offering access to new dynamical and rheological regimes. With the goal of understanding this new architecture, in this chapter, molecular dynamics (MD) simulations were conducted on single, isolated poly[n]catenane molecules (comparable to dilute solution, good solvent conditions), and the results were compared to those of traditional linear and cyclic polymers. To tackle the problem, we quantify the structure and dynamics at various length scales using a Rouse mode analysis [169], which is sensitive to topological interactions in polymeric systems [80, 170–176]. The Rouse theory is the simplest model of polymer dynamics and forms the basis for many more sophisticated treatments, making it a natural starting point.

3.2 Simulation Methods

To simulate polymers in good solvent conditions, the model of Kremer and Grest [23] is adopted for all molecules, including linear and cyclic polymers as well as macrocycles within poly[n]catenanes. This model precludes chain crossings, enforcing topological restrictions, which makes it suitable for MIPs. All beads have mass μ, diameter σ, and interact with one

another via a purely-repulsive Lennard-Jones (LJ) potential:

$$U(r) = 4\epsilon \left[\left(\frac{\sigma}{r}\right)^{12} - \left(\frac{\sigma}{r}\right)^{6} + \frac{1}{4} \right] \tag{3.1}$$

where r is the separation distance between the two beads and the interaction is cut off at $r_c = 2^{1/6}\sigma$. Neighboring beads within covalently-bound segments are connected to one another with a finitely extensible non-linear elastic (FENE) potential:

$$U_{FENE}(r) = -\frac{1}{2} k R_0^2 \ln \left[1 - \left(\frac{r}{R_0}\right)^2 \right] \tag{3.2}$$

with the maximum separation $R_0 = 1.5\sigma$ and stretching constant $k = 30\epsilon$. To alter chain stiffness, a cosine bond-angle bending potential was used with the form:

$$U_{bend}(\theta) = k_\theta \left(1 + \cos\theta\right) \tag{3.3}$$

where θ is the angle between adjacent bonds in the molecules, and the bending constant k_θ is an adjustable parameter used to study flexible ($k_\theta = 0.0$), semi-flexible ($k_\theta = 1.5$), and rigid ($k_\theta = 10.0$) chain segments. The simulation cell was a large cubic box with edge length much longer than the end-to-end distance of the polymers studied and the molecules were allowed to drift freely. Equations of motion were integrated for 10^9 production time steps using a velocity-Verlet algorithm [127] and a time step of 0.005τ where $\tau = \sigma\left(\mu/\epsilon\right)^{1/2}$ is the Lennard-Jones unit of time. All relaxation times (rates) are reported in terms of $\tau\,(1/\tau)$. Constant temperature and the effect of solvent fluctuations were included through the use of a Langevin heat bath with temperature $T = \epsilon/k_B$ and damping constant $\gamma = 0.5\tau^{-1}$. All simulations were conducted using the GPU-accelerated, Python-wrapped MD engine DASH [177]. Particle coordinates were harvested every 200 time steps (1.0τ) for analysis. To analyze the rapid relaxations of individual macrocycles and small ring/linear polymers,

shorter simulations of 2×10^7 time steps were performed and particle coordinates were harvested every 25 time steps (0.125τ). To ensure adequate sampling of the three longest Rouse modes in the poly[n]catenanes, 10-20 independent simulations of 10^9 time steps were performed for ring sizes of m = 10, 15, 20, and 30, calculating the Rouse modes on-the-fly every 2000 time-steps.

In this chapter (and those that follow), n denotes the number of macrocycles within a poly[n]catenane, m denotes the number of beads in a covalently continuous molecule (i.e. a free polymer or a macrocycle within a poly[n]catenane), and N is the total number of beads in a polymer. For linear and cyclic polymers, $m = N$; for poly[n]catenanes, $N = m \times n$. Poly[n]catenanes were simulated with $n = 25$ macrocycles (comparable to the largest molecules synthesized [19]) with the number of beads-per-ring m = 10, 15, 20, or 30; a [5]catenane (i.e. a poly[n]catenane with $n = 5$) having $m = 100$ was also considered. These poly[n]catenanes have total number of beads, N = 250, 375, 500, 750, and 500, respectively. Macrocycles are labeled by an index i, with $i = 1$ referring to an arbitrarily chosen chain end. Ring polymers with $N = m = 30$ and 100 were also simulated and the structure and dynamics were compared to those of macrocycles within poly[n]catenanes.

Since we wish to compare the conformations and dynamics of poly[n]catenanes with those of linear polymers, suitable linear analogues must be identified. An analysis of polymers with identical molecular weight, N, results in linear chains with much greater contour length and overall size than their poly[n]catenane counterparts, setting up a somewhat unbalanced comparison. To identify more appropriate linear analogues, *effective* monomers were defined for linear chains as the centers-of-mass of segments of m_{eff} beads, such that the mean bond length between effective monomers matches the mean inter-macrocycle distance (or mechanical bond length) of the targeted poly[n]catenane. Accordingly, the linear polymer analogue for a poly[n]catenane with n macrocycles will have n effective monomers, and total number of beads $N = n \times m_{\text{eff}}$, where m_{eff} depends on the particular macrocycle

size m. Using this method, the poly[n]catenanes and linear analogues will have roughly the same contour length, so that differences in relaxation spectra are primarily related to the underlying molecular topology. For poly[n]catenanes with $n = 25$ and $m = 10$, 20, and 30, linear analogues have $m_{\text{eff}} = 3$,6, and 9, and $N = 75$, 150, and 225, respectively. No suitable linear analogue could be defined for poly[n]catenanes with $m = 15$. Figure 3.1 depicts some of the molecules studied in this chapter.

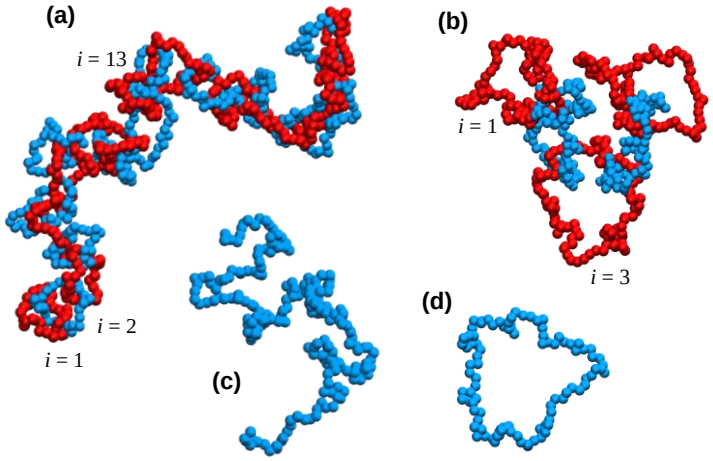

Figure 3.1: Visualization of some of the polymers studied: (a) poly[n]catenane with number of rings $n = 25$, macrocycle size $m = 30$, total size $N = 750$; (b) poly[n]catenane, $n = 5$, $m = 100$, $N = 500$; (c) linear polymer, $N = m = 225$; (d) ring polymer, $N = m = 100$. Macrocycles are indexed by position along the chain, i.

3.3 Rouse Theory and Mode Analysis

In recent years, several computational studies [170–174, 176] have examined the dynamics of polymer melts and blends using a Rouse mode analysis [169]. A detailed derivation of the Rouse model can be found in Appendix A.4, but the main points will be recapitulated here. In the Rouse model, the macromolecule is represented by N beads connected to their neighbors by harmonic springs. The bead coordinates can be transformed into a series of

normal (i.e. statistically independent) modes, $\boldsymbol{X}_p$, with mode numbers $0 \leq p \leq N-1$. For the special case of linear polymers, the p^{th} mode roughly represents motions of sub-chains of N/p beads. The quantity N/p therefore defines a length scale along the polymer backbone, with low mode numbers corresponding to large length scales and vice versa. Note that the longest (or "zeroth") mode corresponds to the polymer center-of-mass and its dynamics will be ignored in this chapter. The mean squared mode amplitudes $\langle X_p^2 \rangle$ carry information about the polymer structure while the mode auto-correlation functions (ACFs) contain dynamical information at the specified length scale. In particular, the normalized ACFs can be described by a stretched exponential, $\langle \boldsymbol{X}_p(0) \cdot \boldsymbol{X}_p(t) \rangle / \langle X_p^2 \rangle \approx \exp\left[-\left(t/\tau_p\right)^{\beta_p} \right]$. The exponent β_p characterizes the distribution of relaxation times, with $\beta_p = 1$ indicating simple exponential decay and smaller values corresponding to broader distributions. Values $\beta_p > 1$ may be observed owing to inertial effects. Note, however, that $\beta_p \neq 1$ does not necessarily imply coupling between modes. Integrating the ACFs yields effective relaxation times for each mode, τ_p^{eff}, which are used to calculate the effective relaxation rate, $W_p^{\text{eff}} \equiv 1/(\lambda_p \tau_p^{\text{eff}})$, where λ_p is an eigenvalue associated with the mode transformation.

For ideal chains, both W_p^{eff} and β_p should be independent of mode number, i.e. they should not vary with the length scale, N/p. However, recent computational studies using both coarse-grained and all-atom models have shown that W_p^{eff} and β_p do in fact depend on mode number and are correlated with entanglement effects [170–172]. For instance, Kalathi *et al.* [170] showed that both W_p^{eff} and β_p decrease dramatically as N/p approaches N_e, the entanglement length. Hsu and Kremer [172] confirmed these results, demonstrating that the effective relaxation time exhibits two scaling regimes, revealing the crossover from Rouse to reptation dynamics. Throughout this chapter, we will refer to such concomitant reductions in W_p^{eff} and β_p as the "entanglement-like effect" (not to be conflated with other signatures of entangled dynamics). In contrast, when chain crossings are allowed (eliminating entanglement), β_p is relatively constant, while W_p^{eff} increases modestly at higher modes,

the latter being attributed to local correlations between monomers [170]. Similar results have been observed in all-atom simulations of unentangled melts of linear poly(ethylene-alt-propylene) [173] and cyclic polyethylene [174]. Rouse modes are also sensitive to topological interactions in blends of cyclic and linear polymers: Tsalikis *et al.* [80, 175] showed that slow relaxation modes emerge when linear chains thread ring polymers and Papadopoulos *et al.* [176] found that this threading is accompanied by a decrease in W_p^{eff} of the rings at low mode number. In light of these findings, a Rouse mode analysis provides a useful starting point to study the dynamics of poly[n]catenanes, since these molecules contain permanent topological interactions in the mechanical bonds. Note that there are no other relevant topological interactions since the poly[n]catenanes studied here are too short to self-entangle.

Two different sets of Rouse modes are calculated here to account for the unique structure of poly[n]catenanes. The first set, denoted $\boldsymbol{X}_q$, describes the individual macrocycles within the poly[n]catenanes, and the coordinates of beads within a single macrocycle are used as monomer positions for the calculation, as in an ordinary analysis [174]. For ring molecules such as these, these modes are defined according to:

$$\boldsymbol{X}_q = \begin{cases} \left(\frac{2}{m}\right)^{1/2} \sum_{i=1}^{m} \boldsymbol{R}_i \cos\left(\frac{q\pi i}{m}\right) & \text{for} \quad q = 2, 4, ..., \frac{m}{2} - 2 \\ \left(\frac{2}{N}\right)^{1/2} \sum_{i=1}^{m} \boldsymbol{R}_i \sin\left(\frac{q\pi i}{m}\right) & \text{for} \quad q = 2, 4, ..., \frac{m}{2} - 2 \\ \left(\frac{1}{m}\right)^{1/2} \sum_{i=1}^{m} \boldsymbol{R}_i \left(-1\right)^i & \text{for} \quad q = \frac{m}{2} \end{cases} \tag{3.4}$$

where $\boldsymbol{R}_i$ is the position of monomer i within the ring (the specific indexing is arbitrary). Note that the third row of Eq. 3.4 does not apply for odd m. Associated with these modes are a set of eigenvalues:

$$\lambda_q = 4 \sin^2\left(\frac{q\pi}{2m}\right) \tag{3.5}$$

These results are equivalent to those given by Ceriotti *et al.* [178] for the thermostatting of ring polymers in path integral molecular dynamics. A detailed presentation of the Rouse theory for ring polymers can be found in [174]. The cosine and sine modes can be related to one another by a shift in the indexing of the monomers (although not necessarily by an integer value). However, just as the choice of the "initial" versus "final" chain end in linear polymers is arbitrary, the indexing in a ring polymer is also arbitrary. Therefore, by symmetry arguments, it will not affect the averages of any quantities related to the Rouse modes, including the ACFs. Thus, only a single mode is considered for each value of q; in analogy with the coordinate transformation for linear chains (see below), the cosine transformation is chosen (first line of Eq. 3.4). For these ring modes, the length scale of relaxation is *absolute* in that it corresponds to a particular number of beads (m/q).

The second set of modes, denoted $\boldsymbol{X}_p$, describes entire poly[n]catenane molecules in terms of the macrocycle centers-of-mass, $\boldsymbol{R}_{i,cm}$. These modes are defined:

$$\boldsymbol{X}_p = \left(\frac{2}{n}\right)^{1/2} \sum_{i=1}^{n} \boldsymbol{R}_{i,cm} \cos\left[\frac{p\pi}{n}\left(i - \frac{1}{2}\right)\right] \qquad \text{for} \qquad p = 1, 2, ..., n-1 \tag{3.6}$$

$$\tag{3.7}$$

with eigenvalues:

$$\lambda_p = 4\sin^2\left(\frac{p\pi}{2n}\right) \tag{3.8}$$

Note that the form of Eq. 3.7 is identical to that of the Rouse modes for ordinary linear polymers [170], but with ring centers-of-mass taken as the *effective* monomer positions. In this case, the relaxation length scale is *relative*, since it corresponds to a particular number of macrocycles (n/p), which may comprise different numbers of beads depending on m. Note that when calculating the Rouse modes for linear polymers, Eq. 3.7 is used in two different manners. When comparing the results to those of the individual rings/macrocycles, the unaltered bead positions, $\boldsymbol{R}_i$ are used and the modes are denoted $\boldsymbol{X}_q$ with an associated

length scale m/q where $m = N$ and $1 \leq q \leq m-1$. When comparing the results to those of the overall poly[n]catenanes, the centers-of-mass of the *effective* monomers are used and the modes are denoted $\boldsymbol{X}_p$ with an associated length scale n/p where $n = N/m_{\text{eff}}$.

A key aspect of the Rouse theory is that the modes are statistically independent [13, 169]. This orthogonality allows one to interpret mode relaxations as dynamical processes with well-defined length scales (e.g. m/q or n/p) and enables the calculation of various material functions, such as shear stress relaxation modulus and dynamic structure factor. However, if there exist significant cross-correlations between modes, such analyses are invalid and the Rouse modes no longer have a straight-forward physical interpretation. Therefore, it is important to assess whether or not the Rouse modes are indeed orthogonal in our systems. This is particularly important since some authors have found significant cross-correlations at high mode number for entangled melts of linear polymers i.e. in the presence of topological interactions [179]. Following previous authors [180, 181], we assess the orthogonality using a normalized correlation product:

$$\chi_{p,p'} = \frac{\left|\langle \boldsymbol{X}_p \cdot \boldsymbol{X}_{p'} \rangle\right|}{\sqrt{\langle X_p^2 \rangle \langle X_{p'}^2 \rangle}} \tag{3.9}$$

which takes on a value of unity for $p = p'$ and zero for $p \neq p'$ if the modes are indeed orthogonal. We compute these quantities for both sets of Rouse modes considered; the subscripts q and p represent the ring-like and linear-like modes, respectively. For the modes of individual rings within pol[n]catenanes, the longet mode $q = 2$ shows some coupling with the others, with the largest correlations reaching $\chi_{q,q'} \approx 0.1$. However, since the amplitudes of the lower modes are much larger than the rest, the sum total of *un*-normalized cross-correlations is still two orders of magnitude smaller than the self correlation in the low-q regime, so these couplings are not likely to affect the relaxation behavior meaningfully in the region of interest. Figure 3.2 shows the cross-correlations (Eq. 3.9) between macrocycle

modes in the form of a heat map for poly[n]catenanes with $m = 30$ and $m = 100$ beads per macrocycle.

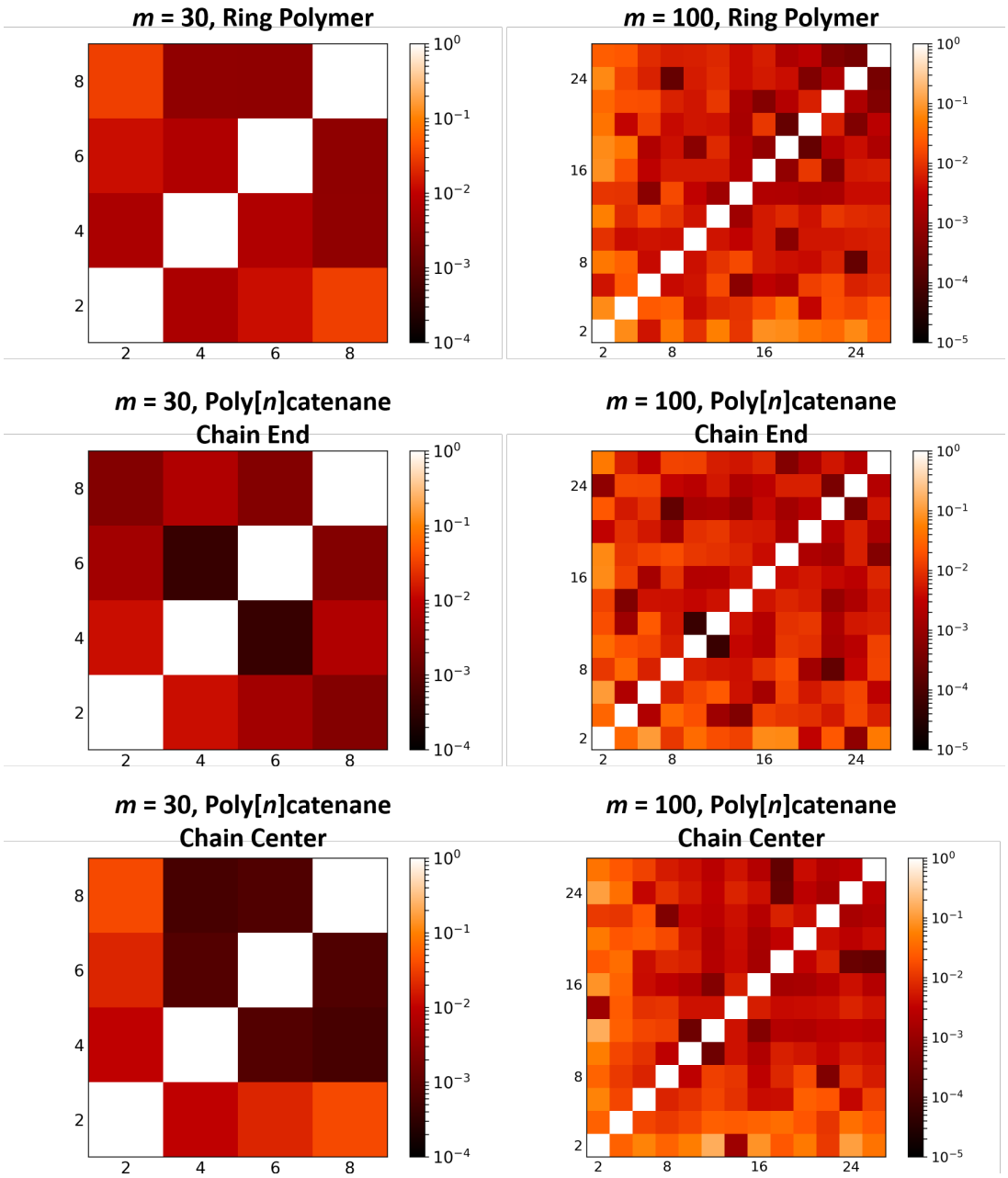

Figure 3.2: Normalized cross-correlations between Rouse modes for macrocycles within poly-[n]catenanes.

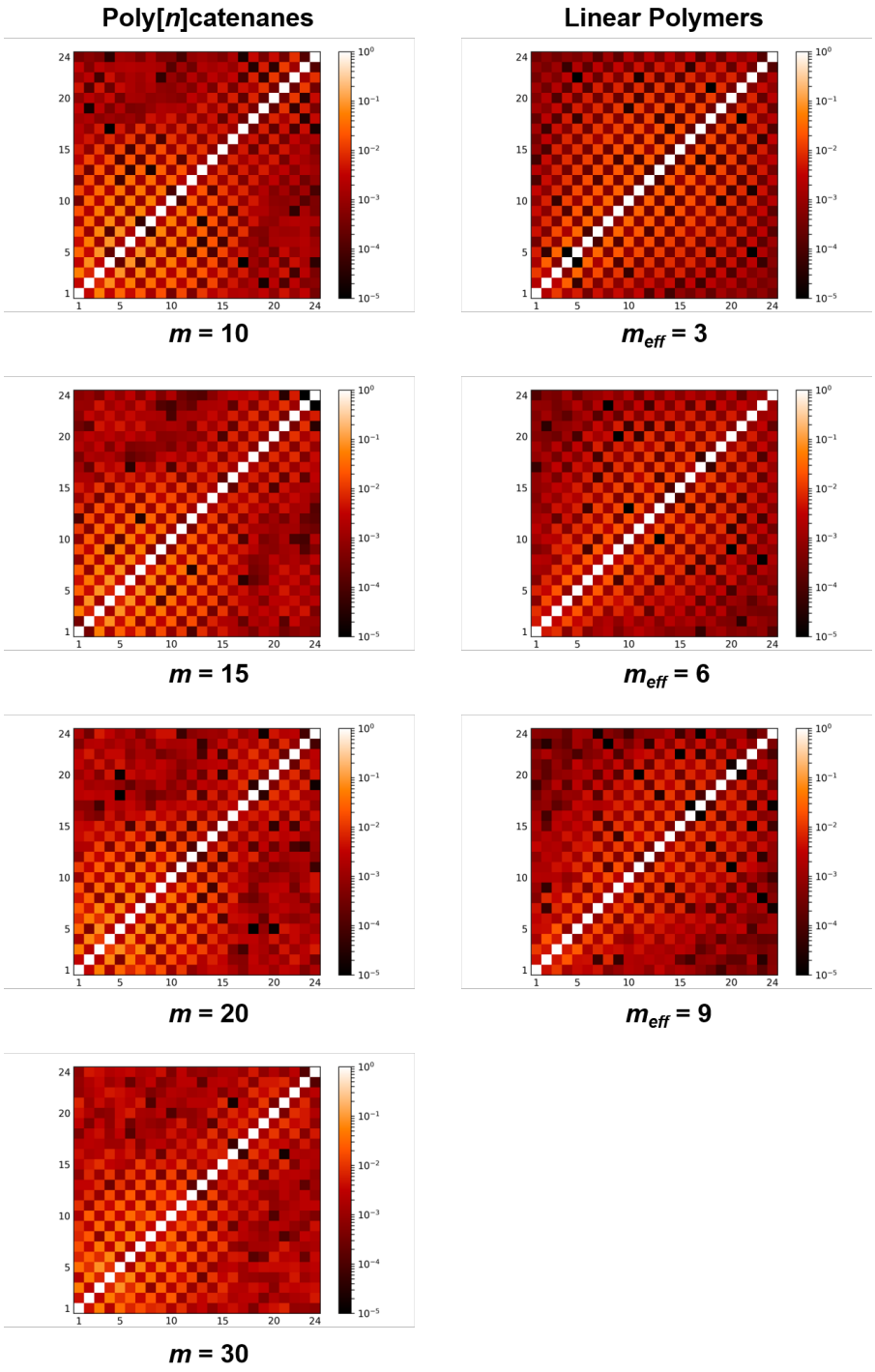

Figure 3.3: Normalized cross-correlations between Rouse modes of poly[n]catenanes and linear polymers.

For the second set of Rouse modes, corresponding to the entire poly[n]catenane chain or a linear analogue, we observe non-zero coupling between pairs of modes with both even or both odd mode numbers. The same trend has been observed in the literature [179–181] and results in a checker-board pattern in the resulting cross-correlation heat map (Figure 3.3). In agreement with the literature results, the cross-correlations are always at least 1-2 orders of magnitude smaller than the self-correlation, suggesting that the Rouse modes are indeed orthogonal to within reasonable approximation. In general, poly[n]catenanes of all ring sizes exhibit slightly larger couplings at low mode number than do the linear analogues. However, at higher mode number, the couplings are suppressed and the modes become *more* orthogonal; this is clearly seen in the resulting correlation heat map, which shows much more yellow/orange coloring in the lower left (low mode number) than in the upper right (high mode number). So while the Rouse analysis is indeed applicable to the entire polymer, the results will be particularly meaningful at high mode number, which is where the most unusual dynamics are observed, as discussed later on. In summary, both sets of modes are orthogonal to within good approximation, ensuring that we obtain meaningful dynamical information at well-defined length scales in our analysis. Before continuing, we note that cross-correlations between different rings or between ring and chain type modes vanish identically by symmetry considerations. These symmetries will be discussed more fully in Chapters 4 and 6.

3.4 Static Properties of Poly[n]catenanes

Here we present a few selected static properties of poly[n]catenanes and their linear counterparts. Since this chapter focuses primarily on the dynamical behaviors, we discuss only those properties which are useful for understanding and interpreting the dynamics. Further analysis of the structural characteristics of these polymers in solution has previously been performed by Pakula and Jeszka [22] and more recently by Ahmadian Dehaghani *et al.* [92]. Table 3.1 shows various elementary quantities including mean segment length between ef-

fective monomers/macrocycles (b), radius of gyration (R_g), and end-to-end distance (R_e) for poly[n]catenanes and linear counterparts. Although mean effective bond lengths differ by at most 2% between architectures, linear polymers have smaller end-to-end distance and radius of gyration, which is probably caused by local chain swelling and excluded volume effects. By design, macrocycles and the effective monomers in linear analogues have the same segmental volume (b^3), but the macrocycles contain many more beads ($m > 3 \times m_{\text{eff}}$). Because of this increased bead density, one may expect poly[n]catenanes to be more strongly impacted by excluded volume and therefore stiffer than linear polymers. This leads to physically larger/longer molecules, which slows down the large length-scale dynamics; in the next section, this expectation is borne out as linear chains tend to relax 50-80% faster than poly[n]catenanes at the lowest modes.

Table 3.1: Static Properties of Selected Poly[n]catenanes and Linear Analogues

Property	**Poly[n]catenane**	**Linear Polymer**
N	250	75
m or m_{eff}	10	3
$b(\sigma)$	1.87	1.90
$\langle R_g^2 \rangle^{1/2}$	7.74	6.25
$\langle R_e^2 \rangle^{1/2}$	19.8	16.0
N	500	150
m or m_{eff}	20	6
$b(\sigma)$	2.93	3.00
$\langle R_g^2 \rangle^{1/2}$	11.5	9.62
$\langle R_e^2 \rangle^{1/2}$	29.4	24.4
N	750	225
m or m_{eff}	30	9
$b(\sigma)$	3.73	3.70
$\langle R_g^2 \rangle^{1/2}$	14.5	12.4
$\langle R_e^2 \rangle^{1/2}$	36.6	31.6

To understand local chain structure, two additional quantities are calculated: the mean-

squared amplitudes of the Rouse modes and the mean-squared internal distances between effective monomers. Physically, these quantities both represent the size of sub-chains, but are calculated according to different means. For ideal chains, the Rouse mode amplitudes are given by [13]:

$$\langle X_p^2 \rangle = \frac{3k_B T}{k\lambda_p} = \frac{b^2}{\lambda_p} \tag{3.10}$$

where k is the spring constant between neighboring beads. For chains with excluded volume effects, the following scaling relation holds in the asymptotic limit [181]:

$$\lambda_p \langle X_p^2 \rangle \sim \left(\frac{N}{p}\right)^{2\nu-1} \tag{3.11}$$

where ν is the Flory exponent. The scaled amplitudes for poly[n]catenanes and linear analogues as a function of n/p are shown in Figure 3.4. In all cases, there is a positive slope at the largest length scales which suggests that the chains are not long enough to reach the asymptotic limit and are therefore in some intermediate or crossover regime. The values for poly[n]catenanes generally span a wider range than linear counterparts, indicating that they are subject to greater local stiffness effects. The linear polymers also appear to level off more quickly at higher values of n/p, while the poly[n]catenanes seem slower to reach their asymptotic limit.

The scaled Rouse mode amplitudes for individual macrocycles within poly[n]catenanes, $\lambda_q X_q^2$ can also be calculated and compared to free ring polymers as well as linear polymers as a function of length scale, m/q. The results for macrocycles of size $m = 30$ and $m = 100$ are shown in Figure 3.5 and the results are qualitatively similar. At high mode numbers (short length scales), the mode amplitudes vary according to the number of threadings, with poly[n]catenane chain centers having the lowest amplitudes, followed by chain ends, and then free polymers. In this regime, the dependence on m/q is identical for all systems. At the lowest mode, however, the situation is reversed, with all three cyclic systems having

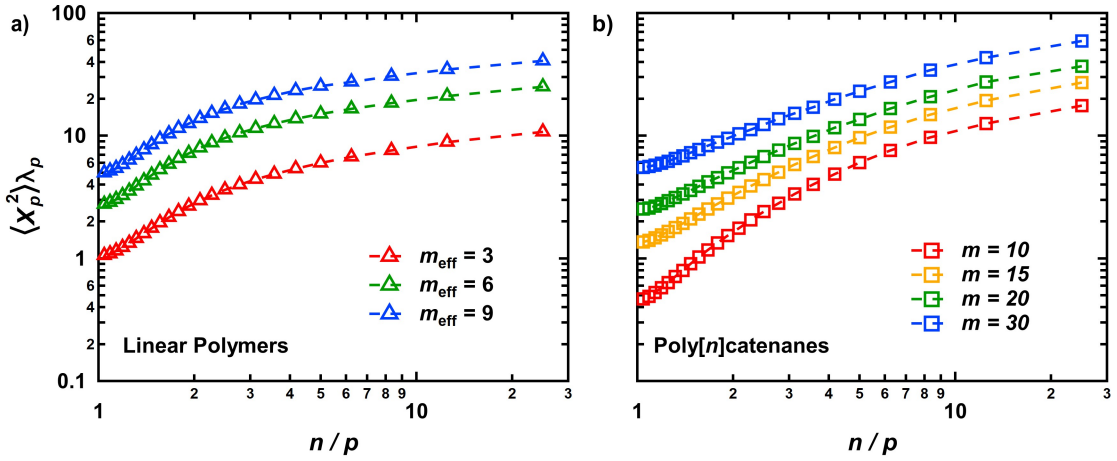

Figure 3.4: Scaled Rouse mode amplitudes for a) linear polymers and b) poly[n]catenanes.

amplitudes larger than the linear polymer. Furthermore, the magnitude of the modes now increases with increased threading, contrary to the situation at high mode number. These data suggest that ring polymers and catenane macrocycles are expanded at large length scales compared to linear chains, and that the mechanical bonds magnify the effect.

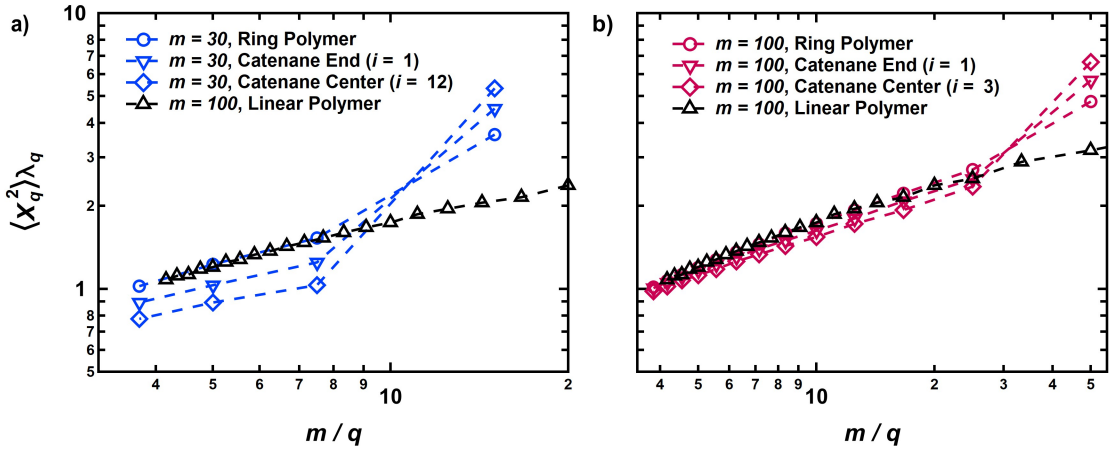

Figure 3.5: Scaled Rouse mode amplitudes for macrocycles within poly[n]catenanes with a) $m = 30$, and b) $m = 100$, compared to linear and ring polymers.

The mean-square internal distances between effective monomers are another set of data which describe the internal structure of polymer chains. They are qualitatively similar to the Rouse mode amplitudes in that they quantify the size of sub-chains within the molecule.

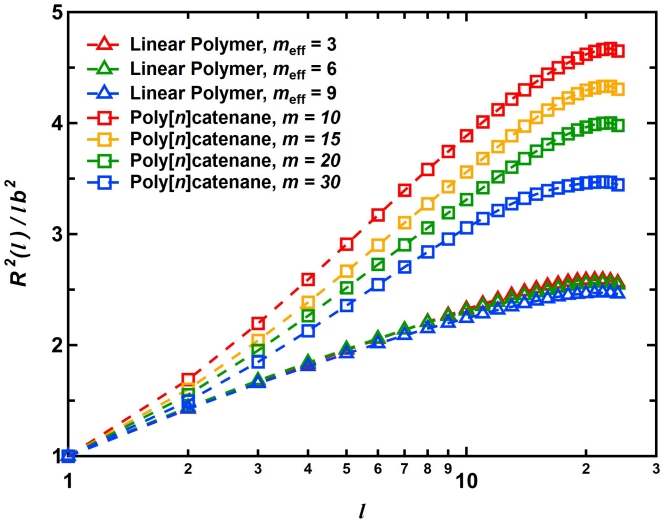

Figure 3.6: Normalized mean square internal distances for poly[n]catenanes and linear polymers.

For a polymer with n effective monomers, these data are calculated according to:

$$R^2(l) = \frac{1}{n-l} \sum_{i=1}^{n-l} \left\langle (\boldsymbol{R}_{i+l} - \boldsymbol{R}_i)^2 \right\rangle \tag{3.12}$$

where $l > 0$, $\boldsymbol{R}_i$ is the position of effective monomer i, and the brackets $\langle ... \rangle$ indicate an ensemble average. The quantity $R^2(l)$ is typically divided by l so that ideal random walk statistics correspond to a constant value; to compare the data for various ring and effective monomer sizes, we will also normalize the distances by the mean square bond lengths, b^2. Figure 3.6 shows these data for linear polymers and poly[n]catenanes. As expected, all polymers are locally swollen at short length scales, showing increasing values before leveling off at higher l. However, it is clear from this data that linear polymers are considerably *less* expanded than poly[n]catenanes, which is presumably a consequence of the lower bead density within each segment volume. For poly[n]catenanes, smaller macrocycles lead to greater relative swelling, which would indicate enhanced excluded volume effects at short length scales and greater overall stiffness, consistent with the observations from the Rouse

mode amplitudes. The transition to "ideal" statistics at $l \sim 20$ rings in the poly[n]catenanes is likely the result of increased flexibility/mobility at the chain ends. These data also support the conclusion that these polymers are not large enough to reach the asymptotic scaling limit. Beyond these features, there are no other glaring anomalies associated with poly[n]catenane structure at any length scale (so far as effective monomers are concerned). Indeed, differences in scaling behavior or theta point observed by other authors are quite subtle [92]. Therefore, one would expect the dynamical properties at short length scales to be consistent with those of an ordinary polymer with excluded volume. However, as described in the next section, there are *qualitative* differences in dynamics at short length scales between poly[n]catenanes and linear polymers, and such differences cannot be understood in terms of the static scaling properties discussed above, which are qualitatively *similar* for all architectures considered.

3.5 Dynamics of Poly[n]catenanes

The relaxation dynamics of the first set of Rouse modes described above have been calculated for macrocycles of size $m = 30$ and $m = 100$ within poly[n]catenanes of $n = 25$ and $n = 5$ total rings, respectively. The macrocycles at the chain end ($i = 1$) and chain center ($i \approx n/2$) are considered separately since they have different numbers of threadings, which greatly affects the dynamics [80, 175, 176]. Figure 3.7 compares the results to linear and non-catenated ring polymers. At high mode number, W_q^{eff} is independent of polymer topology as all spectra converge. However, at low mode number, W_q^{eff} decreases substantially as topological restrictions are added: linear chains relax fastest, followed by ring polymers, poly[n]catenane chain ends, and poly[n]catenane chain centers. This result agrees well with recent work on blends of cyclic and linear polymers [176]. Interestingly, the largest decrease in W_q^{eff} occurs at the longest modes, regardless of the macrocycle size, m. This indicates that the mechanical bond slows dynamics at a length scale relative to the macrocycle itself, rather than at some absolute length scale (i.e. some specific number of beads). β_q also

decreases with increased threading for the longest modes (Table 3.2); such concomitant reductions in W_q^{eff} and β_q are reminiscent of the entanglement-like effect in linear polymer melts described baove [170–172], suggesting that this effect may be related to topological interactions quite generally, rather than just the specific case of linear polymers in melts or concentrated solutions.

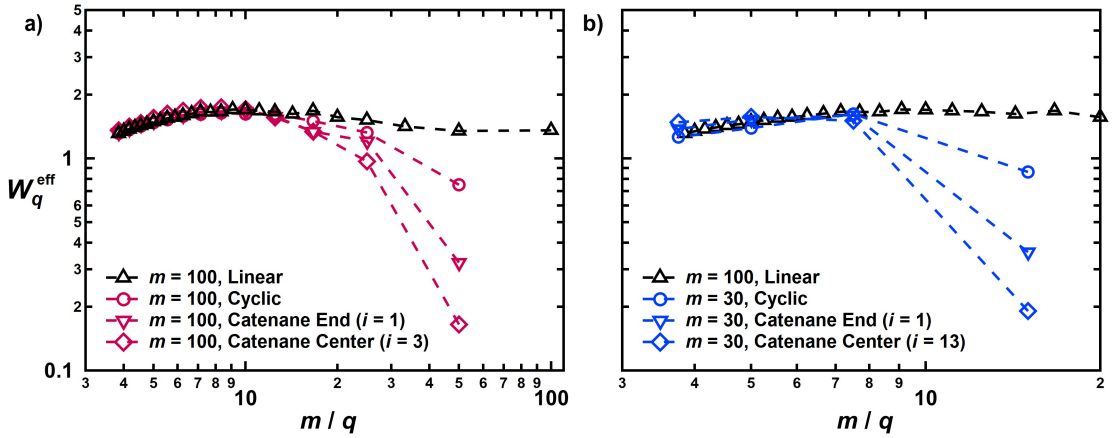

Figure 3.7: Mode-dependent relaxation rates for poly[n]catenane macrocycles at the chain center (diamonds) and chain ends(downward triangles) as a function of length scale compared to linear and ring polymers: a) $m = 100$, b) $m = 30$.

Table 3.2: Rouse mode stretching exponents, β_q, of various polymer architectures ($m = 100$) as determined from the first Rouse mode analysis described in the main text.

Architecture	$q = 2$	$q = 4$	$q = 6$
Linear Polymer	0.94	0.96	1.05
Ring Polymer	0.90	0.95	0.99
Poly[n]catenane Chain End ($i = 1$)	0.76	0.87	0.90
Poly[n]catenane Chain Center ($i = 3$)	0.69	0.77	0.85

To describe the overall dynamics of poly[n]catenane molecules, the relaxation dynamics of the second set of Rouse modes described above, $\boldsymbol{X}_p$, were also calculated. A represen-

tative subset of Rouse mode ACFs with stretched exponential fits is shown in Figure 3.8. We begin by considering the effect of macrocycle size, m; as the ring size is decreased, the number of mechanical bonds, $n-1$, increases relative to the total molecular weight, nm, so the effects of topological interactions should be magnified. Figure 3.9 compares W_p^{eff} for poly[n]catenanes with $n = 25$ and $m = 10$, 15, 20, and 30 as a function of n/p. Unsurprisingly, W_p^{eff} for all modes increases with decreasing ring size, which is expected since smaller ring sizes lead to smaller polymers. To compare the spectra on more equal footing, we introduce a theoretically-informed scaling procedure that accounts for: (i) effective drag on the macrocycles, (ii) effective segment length, and (iii) excluded volume effects, as described below.

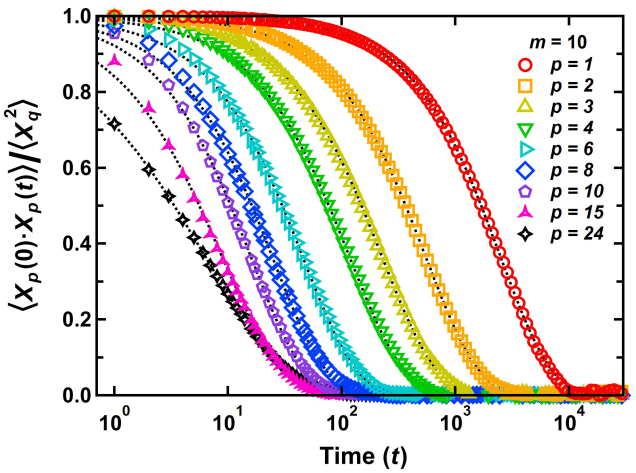

Figure 3.8: A representative subset of normalized Rouse mode ACFs for poly[n]catenanes with $n = 25$ and $m = 10$. Points are simulation data and dotted lines are fits to a stretched exponential.

To start, we leverage the fact that for ideal polymers, the relaxation rates should be inversely proportional to the segment size, b^2, and the drag coefficient, ζ:

$$W = \frac{1}{\lambda_p \tau_p} = \frac{3k_B T}{\zeta b^2} \tag{3.13}$$

where we have used the fact $\tau_p = \zeta b^2 / 3k_B T \lambda_p$ [13, 170]. This relationship suggests that

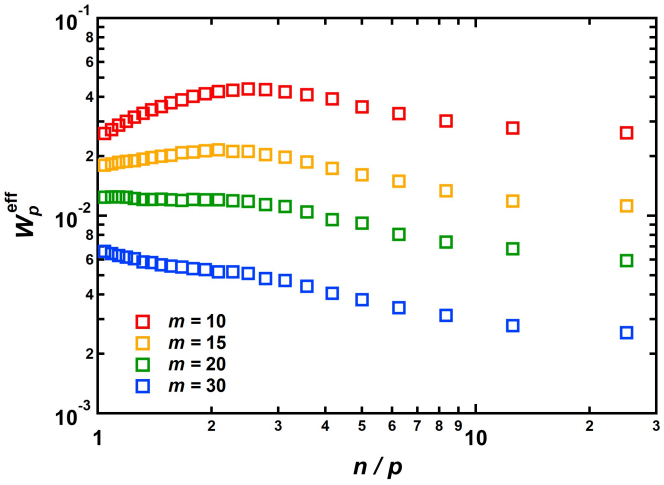

Figure 3.9: Mode-dependent relaxation rates for poly[n]catenanes with various ring sizes.

multiplying W_p^{eff} by b^2 and ζ (or quantities directly proportional to them) would allow for comparisons between polymers of different molecular weight and monomer size. In a Langevin dynamics simulation, the drag coefficient for a given molecule will be directly proportional to the number of beads in the molecule so that the monomeric drag is proportional to either m or m_{eff} for poly[n]catenanes and linear polymers, respectively. Meanwhile, mean values of b^2 can be obtained directly from simulation trajectories. Accordingly, a scaled relaxation rate is defined by $mb^2W_p^{\text{eff}}$ where m and b^2 depend on the architecture in question. Applying this formula to the relaxation rates for poly[n]catenanes, the spectra are now much more comparable, as shown in Figure 3.10). However, two features are immediately apparent: (i) the curves show a dependence on p at low mode numbers, suggesting that they do not obey ideal Rouse dynamics, and (ii) the relaxation rates increase monotonically with the size of the effective monomer. Both of these observations may be understood in terms of excluded volume effects, which can be included using a dynamical scaling argument.

To begin this scaling argument, a similar analysis by Doi and Edwards [13] is summarized. In the Rouse theory, the longest relaxation time for a linear polymer of N segments, τ_N, is

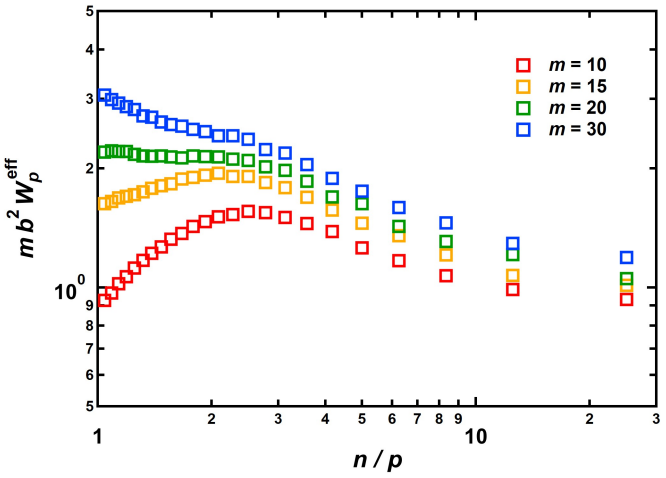

Figure 3.10: Relaxation spectra for poly[n]catenanes with various ring sizes scaled by ring molecular weight and mean squared bond length.

given by:

$$\tau_N \sim \frac{\zeta b^2 N^2}{k_B T} \tag{3.14}$$

Using dimensional analysis, an expression can be crafted which contains the same physical quantities as Eq. 3.14, but assumes no particular dependence on N, so that it may be applied to non-ideal or non-linear polymers:

$$\tau_N \sim \frac{\zeta b^2}{k_B T} f(N) \tag{3.15}$$

The fraction has units of time, while the function $f(N)$ is dimensionless. By lumping together groups of κ segments, the following scaling transformation is introduced:

$$N \to N/\kappa \qquad b \to \kappa^{\nu} b \qquad \zeta \to \kappa \zeta \tag{3.16}$$

where ν is the Flory scaling exponent. Since the relaxation time must be unaffected by the

scaling (i.e. independent of κ), insertion of Eq. 3.16 into Eq. 3.15 yields the form of $f(N)$:

$$\tau_N \sim f(N) \sim N^{2\nu+1} \tag{3.17}$$

This result was first noted by de Gennes [182] and confirmed by simulations [183, 184] some time ago. Now roughly speaking, the p^{th} Rouse mode describes relaxations of segments of N/p beads in linear (or linear-like) polymers. In keeping with the self-similar nature of polymers, it is assumed that Eq. 3.17 also holds for sub-chains, so that the Rouse relaxation times may be written as:

$$\tau_p \sim \left(\frac{N}{p}\right)^{2\nu+1} \tag{3.18}$$

This same approximate scaling has been proposed before by Panja and Barkema [181]. For small p, the eigenvalues for linear polymers, Eq. 3.8, are approximated as $\lambda_p \sim (p/N)^2$. This relation, along with Eqs. 3.13 and 3.18, indicates that the relaxation rates scale as

$$W \sim \left(\frac{N}{p}\right)^{1-2\nu} \tag{3.19}$$

in the small-p range. By analogy, since $\nu > 1/2$ in a good solvent, W will decrease with n/p for poly[n]catenanes, which is indeed observed in Figure 3.10.

One may use similar arguments to understand why the scaled relaxation rates increase as the effective monomer size increases. Consider the density of beads within the effective monomer or macrocycle, $\rho \sim m/b^3$. Since $b \sim m^\nu$ with $\nu \approx 3/5$, this density decreases with increasing m in a good solvent. Smaller bead densities allow for greater overlap between effective monomers or macrocycles, which reduces the relative importance of excluded volume effects, leading to faster dynamics in analogy with Eq. 3.17. To quantitatively account for this effect, the dynamical scaling argument is used again, for now considering only linear polymers. In particular, for ordinary linear polymers, it is clear that the relaxation time for a given chain segment should not depend on the level of discretization, i.e. m_{eff}. For

now, it is assumed that this asos holds for poly[n]catenanes, i.e. for a given total molecular weight $N = nm$, the associated relaxation times should not depend on the "discretization" m; we will return to this point later. Although the level of discretization should not matter, just such a dependence is introduced into the relaxation rates W_p^{eff} through the eigenvalues λ_p, since different discretizations yield different values of $n = N/m$ and therefore different eigenvalues. Furthermore, the values of ζ and b^2 also depend on m as already discussed. To understand the effect of this discretization, consider a chain (or sub-chain) of N monomers with a relaxation time τ_N which obeys Eq. 3.18. For a given effective monomer size m, one may write:

$$\frac{n}{p} = \frac{N}{p}\frac{1}{m} \tag{3.20}$$

which represents the number of effective monomers in the segment for a given discretization. Using Eqs. 3.13, 3.18, 3.20, along with the small-p approximation for λ_p and the relation $b \sim m^{\nu}$, one finds:

$$m\langle b^2\rangle W_p^{\text{eff}} \sim \left(\frac{N}{pm}\right)^{1-2\nu} \tag{3.21}$$

In good solvents, the scaling exponent will be greater than 1/2, so that the scaled relaxation rates $mb^2W_p^{\text{eff}}$ increase monotonically with m, which is indeed the observed behavior in Figure 3.10. Eq. 3.21 indicates that one may correct the relaxation spectra $mb^2W_p^{\text{eff}}$ by multiplying the values by the denominator of the right-hand side of Eq. 3.21. The final result is:

$$W_p^{\text{scale}} = m^{2-2\nu} \times b^2 \times W_p^{\text{eff}} \tag{3.22}$$

For large length scales (low mode number), the resulting spectra should collapse onto a master curve. This representation accounts for excluded volume effects introduced by the effective monomer size, allowing for comparisons between polymers with different effective monomer or macrocycle sizes. However, this approach cannot be expected to yield perfect agreement in all scenarios. In particular, for any real polymer chain, the effective value

of the scaling exponent will be non-constant at low molecular weight, which will introduce discrepancies into the results; however, such errors do not appear to be very large in the present circumstances as the scaling procedure turns out to be quite successful, as seen below.

Many of the assumptions invoked in the above argument are not obviously valid for poly[n]catenanes, in which the number of beads in an effective monomer (i.e. macrocycle), m, has a true physical meaning and is not simply a parameter of the analysis, as is m_{eff} in the case of linear polymers. In general, the scaling behaviors of poly[n]catenanes will be quite complicated. One can immediately envision *at least* two different types of scaling: a familiar one involving changes in the number of rings, and a new one involving changes in the *size* of the rings. In fact, Ahmadian Dehaghani *et al.* [92] recently demonstrated two such exponents and found that their values are *not* identical. In general, the second scaling exponent will violate self-similarity, thus precluding any straightforward scaling analysis. For instance, it would be unreasonable to assume *a priori* that a [100]catenane with $m = 5$ will relax on the same time scale as a [5]catenane with $m = 100$ just because they have the same molecular weight. Such an assumption becomes even more dubious when entanglement-like effects are considered.

However, the simulations conducted here indicate that for reasonably large catenane segments, the relaxation times are not strongly dependent on the size of the macrocycles, provided that the molecular weights are comparable. For example, when $n = 25$, the values of τ_1^{eff} for $m = 10$ and τ_3^{eff} for $m = 30$ both describe relaxations of $\sim$250 beads and differ by only $\sim$8%. As one might expect, the longer of the relaxation times corresponds to the system with the smaller macrocycles, i.e. the one with the greater density of mechanical bonds. Perhaps for the macrocycle and catenane sizes studied here, the polymer can be thought of as a homogeneous coil of beads, allowing one to neglect the local structure of the chain at large length scales. In this picture, the two varieties of scaling discussed above are effectively the same. Naturally, in the limits of either very large or very small macrocycles,

this behavior would not hold.

To proceed, we fit the values of b to a power law in m, finding that $\nu \approx 0.658$ in this range of ring sizes, somewhat larger than the ordinary good-solvent value and in surprisingly good agreement with a similar exponent studied by Ahmadian Dehaghani *et al.* [92], who found a value of 0.65 ± 0.02. However, this agreement may be fortuitous as the rings considered here are rather small and may therefore be subject to local stiffness and finite size effects. The scaled relaxation spectra are then calculated according to:

$$W_p^{\text{scale}} = m^{0.684} b^2 W_p^{\text{eff}} \tag{3.23}$$

With this scaling procedure in hand, the dynamics of catenanes with different macrocycle sizes can be properly compared to study the effect of the mechanical bond.

Using the scaling procedure developed above, the various poly[n]catenane spectra collapse onto a master curve at long length scales, as shown in Figure 3.11. However, on the length scale of about three macrocycles ($n/p \sim 3$), *smaller* ring sizes lead to *slower* dynamics, with the effect growing as n/p approaches unity. The exact opposite trend is found in linear polymers, as discussed later (and also observed in ref. [170]). In order to put this unusual result in context, it is worthwhile to comment on the physical significance of the scaling procedure formulated earlier and the limits of its interpretation. The excluded volume arguments used above are only truly valid in the large-scale asymptotic limit and even then are merely approximations. As discussed in the previous section, the poly[n]catenanes studied here are not large enough to reach this regime, at least in terms of static properties. While the connection between static and dynamic scaling is a subtle issue, it can be safely assumed that these polymers (and indeed their linear analogues) are in a crossover regime and therefore do not have a well-defined value of the scaling exponent, ν, which can be formally applied to a dynamical scaling analysis. Therefore, the excluded volume arguments, whose correctness is evidenced only by their ability to converge the spectra, should not be taken as

important results in this chapter. However, this does not affect the key findings of the present study: if the effects of excluded volume were completely ignored and the spectra were only scaled according to segment size and monomer drag, the qualitative differences associated with decreasing ring size would still be apparent, as demonstrated by Figure 3.10. In fact, if we have eschewed *any* theoretical basis for scaling the spectra and had simply shifted or normalized them in an *ad hoc* manner, the same conclusions would have been reached. The scaling procedure therefore represents only a means to rationalize the *quantitative* differences between the spectra of poly[n]catenanes with various ring sizes, but it does not impact the *qualitative* distinctions, which are the key findings.

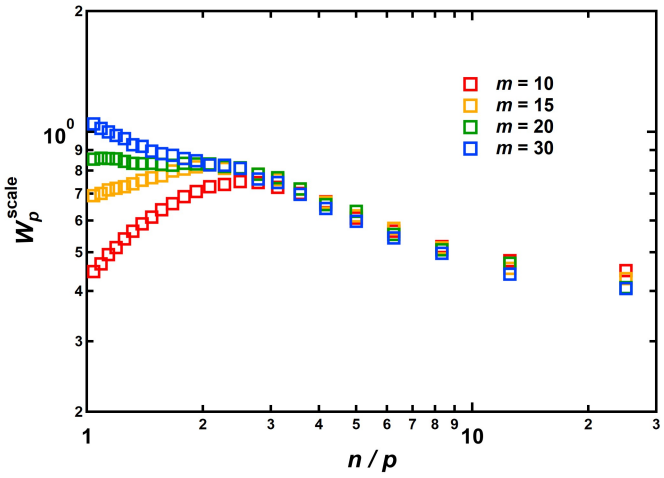

Figure 3.11: Scaled relaxation spectra for poly[n]catenanes with various ring sizes.

It must also be emphasized that the n/p dependencies at high mode numbers (short length scales) could *not* be expected merely on the basis of non-asymptotic behavior. For a swollen polymer chain, the effective spring constant between segments is increased, leading to faster dynamics. This effect can be easily seen in the case of linear polymers: various static properties (see Figs. 3.4 and 3.6) show that the chains are swollen at small length scales and accordingly show accelerated dynamics in this regime (see Figure 3.12 below and [170]). One could account for these local stiffness effects by recognizing that (in the ideal

case) both the Rouse relaxation time and the mean-squared mode amplitudes are inversely proportional to the effective spring constant, suggesting that the quantity $W_p^{\text{eff}}\lambda_p\langle X_p^2\rangle$ (an effective mobility) should be constant for all modes. Based on common scaling relations, this result should also hold in the large-length scale limit for chains with excluded volume. This sort of analysis combining static and dynamic simulation results has been attempted by many researchers [173, 179, 185–188] with mixed results. In particular, Colmenero and coworkers [173, 187, 188] have repeatedly shown that local stiffness *cannot* explain the deviations from ideal behavior at high mode number and a mode-dependent friction coefficient must be introduced. A similar observation was made in polymer melts and glasses employing the same molecular model used here [186]. However, it is unclear what physical factors influence this effective friction and in what way, precluding further analysis. But even if such a procedure were applied, it would not affect the results presented here. As discussed above, poly[n]catenanes are swollen at short length scales, as seen through the static properties (Figs. 3.4 and 3.6). However, the relaxation rates do *not* show an upturn at high mode number as the linear polymers do. In fact, for the smallest ring sizes $m = 10$ and 15, the relaxation rates actually *decrease* at the shortest length scales, where the chains are the *most* swollen and should therefore be *most* accelerated! Therefore, applying this kind of analysis would only emphasize the differences between the various poly[n]catenanes at short length scales. In summary, even though these poly[n]catenanes are in a crossover scaling regime (i.e. not in the asymptotic limit), this cannot explain the differences in relaxation behavior which occur at small length scales along the polymer backbone.

Interestingly, β_p also decreases markedly along with W_p^{eff}, consistent with the entanglement-like effect observed above in individual macrocycles within poly[n]catenanes and in linear polymer melts. However, this entanglement-like effect occurs at short length scales in poly[n]catenanes, while ordinary linear polymers are only subject to entanglements at relatively long length scales. These data will be discussed in more detail later on. Interestingly,

some systems exhibit an overlap between the two sets of Rouse modes. For instance, the shortest overall modes in poly[n]catenanes with $m = 30$ relax considerably faster than the longest modes of the constituent macrocycles, suggesting that poly[n]catenane melts and glasses may exhibit interesting dynamical responses in these regimes.

At this point it is helpful to compare the dynamics of poly[n]catenanes with their linear analogues. A naive, direct comparison of the relaxation rates indicates that linear polymers relax far faster than poly[n]catenanes, as shown in Figure 3.12a. However, this is not a meaningful comparison as the effective monomers in poly[n]catenanes have many more beads and therefore experience much great friction. To compare the two architectures more appropriately, we again revisit the scaling procedure detailed above. The arguments presented above allow one to correct for excluded volume effects for both linear polymers and poly[n]catenanes separately, but they do not readily indicate a basis for comparing the two species to one another. Indeed, this analysis is based on the fact that molecules with the same architecture and molecular weight must relax on the same time scale, no matter the level of discretization or coarse-graining. However, this does not hold across polymer architectures: poly[n]catenanes relax much faster than linear polymers of the same molecular weight. This is not a particularly interesting result since the poly[n]catenanes are far smaller in size than the linear polymers and therefore *should* relax faster. It is for this reason that linear polymers and poly[n]catenanes are compared on the basis of segment length and monomer mass. In practical terms, we consider only the quantity $mb^2W_p^{\text{eff}}$, with the understanding that poly[n]catenanes possess greater excluded volume effects than their linear counterparts, and that these effects are not controlled for. This limitation is unimportant. As demonstrated above, any scaling arguments used to account for excluded volume effects will result merely in a vertical shift of the spectra, which does not change the *qualitative* character of the data. Indeed, the key findings which we are about to present are the qualitative differences in dynamics associated with the novel poly[n]catenane architecture.

At low mode number, $mb^2W_p^{\text{eff}}$ for poly[n]catenanes with $m = 30$ is roughly 50-80% of W_p^{eff} for the linear analogue ($m_{\text{eff}} = 9$), as shown in Figure 3.12a, in agreement with our expectation of more pronounced excluded volume effects. However, at higher modes, linear polymers show an increase in W_p^{eff}, attributed to local correlations [170], while catenanes exhibit the entanglement-like effect instead, which slows dynamics and widens the gap between the architectures. This behavior is observed for all ring sizes: Figure 3.12b shows the ratio of linear/catenane $mb^2W_p^{\text{eff}}$ as a function of n/p for various poly[n]catenane/linear analogue pairs. At low mode number, the ratio is relatively constant at a factor of 1-2. However, it increases sharply starting at $n/p \sim 3$, where the entanglement-like effect emerges in poly[n]catenanes and dominates the behavior.

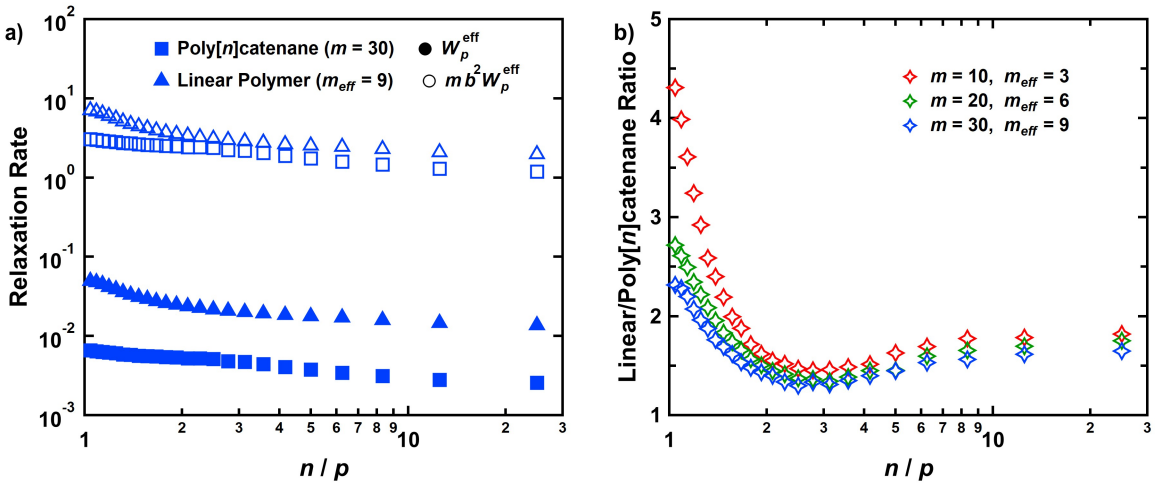

Figure 3.12: a) Raw and scaled relaxation spectra for poly[n]catenane ($n = 25, m = 30$) compared to its linear analogue ($N = 225, n = 25, m_{\text{eff}} = 9$). b) Ratio of scaled relaxation rates $mb^2W_p^{\text{eff}}$ for poly[n]catenanes and linear analogues.

In linear polymer melts, the stretching exponents β_p decrease to ~ 0.5 at length scales comparable to the entanglement length, N_e, indicating that topological interactions are correlated with a broadening of relaxation times [170–172]. A similar trend is observed in poly[n]catenanes, but at relatively short length scales: β_p exhibits a shoulder at $n/p \approx 3$ and then decreases dramatically as n/p approaches unity, as shown in Figure 3.13. Interestingly,

this decrease occurs at the *relative* length scale of $n/p \approx 3$ for all m. These results are in direct contrast to those for linear polymers, which show an increase in β_p at small length scales, which is attributed to inertial effects. As expected, this upturn is sensitive to m_{eff}, as it always occurs at the same *absolute* length scale of ∼10 beads, which corresponds to a difference value of n/p depending on m_{eff}. If this dependence is removed by plotting the exponents β_p as a function of $n/p \times m_{\text{eff}}$, all data collapse onto a master curve as shown in Figure 3.14. These observations are consistent with the above results for individual macrocycles: the effect of the mechanical bond is manifested at a length scale relative to the macrocycles (no matter their size), rather than at some absolute number of beads. This suggests that the entanglement-like effect is a general feature of the mechanical bond that distinguishes it from traditional covalent linkages. This result is also suggestive as it indicates that correlated local motions along the polymer backbone are interrupted by the mechanical bond. Such motions are a mechanism of phonon transport in solids, which is why stretched/oriented polymer melts exhibit anisotropic thermal conductivity [189, 190]. Therefore, one may expect that stretched poly[n]catenane systems would *not* posses such anisotropy, or that it would be considerably mitigated, since no continuous covalently bonded path connects one chain end to the other.

Finally, the effect of segmental stiffness is examined by strengthening the angle-bending potential between neighboring covalent bonds, Eq. 3.3. The results are shown in Figure 3.15. As stiffness is increased, the (unscaled) W_p^{eff} for linear chains is greatly reduced at low modes, but remains mostly unperturbed at higher modes. This is not surprising, since the additional stiffness increases the size of the polymers while also increasing the spring constant between effective monomers, leading to slower dynamics at low modes and faster dynamics at high ones. In contrast, W_p^{eff} for poly[n]catenanes is only moderately reduced at low modes, but more so at high modes. This may be understood in qualitative terms: just as a steel chain is highly flexible in spite of its rigid links, stiff molecular segments will not greatly affect

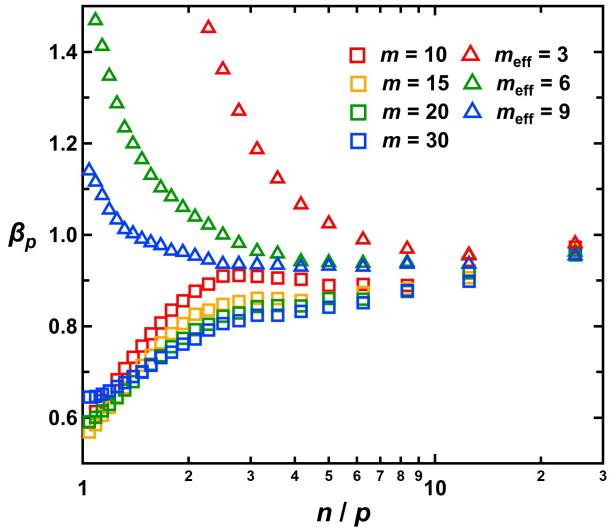

Figure 3.13: Stretching exponents, β_p, vs. n/p for poly[n]catenanes (squares) and linear polymers (triangles).

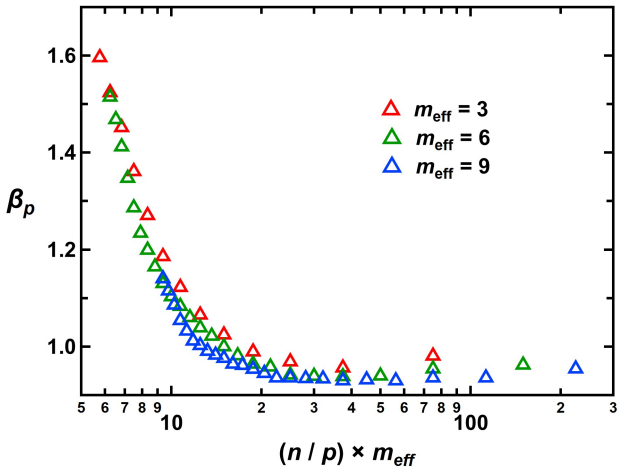

Figure 3.14: Stretching exponents, β_p, for linear polymers as a function of absolute length scale (i.e., a specific number of beads).

the large-scale mobility in poly[n]catenanes. However, at short length scales, the topological interactions may be exacerbated by the stiffness, leading to slower dynamics at higher modes.

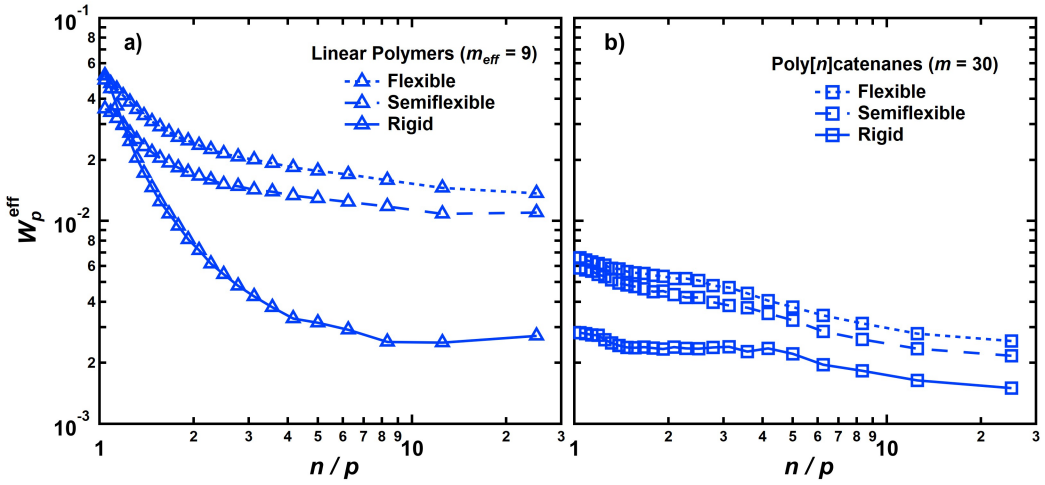

Figure 3.15: Unscaled relaxation spectra for a) linear polymers ($m_{\text{eff}} = 9$), and b) poly[n]-catenanes ($m = 30$), with varying segmental stiffness.

3.6 Discussion and Conclusions

At present, there are limited data on poly[n]catenane dynamics [19], so comparison with experiment is not possible. However, since the Rouse modes studied here are orthogonal to good approximation, they can be used to compute various experimental quantities, such as shear relaxation modulus and dynamic structure factor [13]. The former could be measured by rheological experiments on poly[n]catenane solutions; since the largest effects are found at short length scales, high frequencies and/or low temperatures may be required. Meanwhile, dynamic structure factor can be measured by neutron scattering experiments. In particular, dynamics of individual rings could be probed by introducing labelled macrocycles during poly[n]catenane synthesis. As in the rheological measurements, the large wave-vector regime is likely to be of greatest interest.

The results presented in this chapter highlight the complex dynamics introduced by mechanical bonds. Since these bonds represent permanent and well-defined topological interactions, it seems fitting that the qualitative character of the dynamics is similar to that of entangled linear polymer melts, which also experience such constraints, albeit transiently.

Nevertheless, such a connection is by no means obvious must account for deep physics in the systems. Indeed, the properties of interlocked ring polymers remain an active and challenging field of research, but despite the interest over many decades, the results presented in this chapter represent one of only very few investigations of the dynamics of such systems. Clearly, further research is warranted, given the unusual and exciting nature of the results. In particular, more realistic scenarios must be considered, for instance, systems with hydrodynamic and/or intermolecular interactions. These are the topics of the subsequent chapters of this dissertation.

CHAPTER 4

HYDRODYNAMIC INTERACTIONS IN LINKED POLYMERS

4.1 Introduction

In the previous chapter, we studied the dynamics of poly[n]catenanes in good solvent conditions. Although the behavior of the polymers was remarkable and complex, those studies neglected the dynamical effects of the solvent. In solution, polymers are subject to solvent-mediated hydrodynamic interactions (HI), which introduce long-ranged correlations into segmental motion and significantly alter the dynamics [13]. In particular, the motion of a polymer segment induces a hydrodynamic flow field in the surrounding solvent. In turn, the flowing solvent exerts drag forces on other polymer segments. Thus, even if two beads/monomers on a given polymer have no *direct* interaction, they still influence each other through the intervening medium. These interactions cause pronounced changes in the dynamics of polymers [13]. For instance, the longest relaxation time of a linear polymer scales as $\tau \sim N^{1+2\nu}$ in the Rouse model, but scales as $\tau \sim N^{3\nu}$ when HI is taken into account. Similarly the diffusion coefficient scales as $D \sim 1/N$ without HI and $D \sim 1/N^{\nu}$ with HI. To obtain an accurate picture of poly[n]catenane dynamics or compare with experiments, such effects must be accounted for.

The interplay between topological and hydrodynamic interactions has been a topic of growing interest in recent years [191], with numerous papers examining the dynamics of both unknotted [192–201] and knotted [202–206] ring polymers in equilibrium and non-equilibrium conditions. However, to the best of our knowledge, only a single study has characterized the dynamics of *linked* rings with HI [94] and even then, only the diffusion coefficient and radius of gyration of small linear and cyclic catenanes was considered. The lack of results in this particular area is perhaps unsurprising: hydrodynamic and topological interactions are both mathematically challenging subjects and simulations involving such effects require

great computational expense. On the other hand, the dynamics of poly[n]catenanes without HI studied in the previous chapter showed pronounced topological effects even within single isolated polymers, motivating further research in this area.

In this chapter, we use theory and Brownian dynamics (BD) simulations to investigate the equilibrium dynamics of topologically linked ring polymers in the presence of hydrodynamic interactions. Theoretically, HI are usually handled by averaging the mobility (or HI) matrix with respect to the steady-state configurational distribution function. We show that any such averaging - even for non-Gaussian polymers and out-of-equilibrium systems - results in a hydrodynamic *decoupling* of the internal relaxations of the rings, allowing the effects of topology and HI to be considered pseudo-independently. We then design efficient Brownian dynamics simulation methods to study large Hopf links (i.e. polymeric [2]catenanes) in equilibrium and test the theoretical results. From a fundamental perspective, these results demonstrate how symmetries in topologically complex systems can greatly simplify the physics of the situation. From a practical point of view, these concepts can be used to efficiently and accurately simulate large topologically linked systems such as kinetoplasts [207], Olympic gels [208], and poly[n]catenanes with HI.

4.2 Theory

Consider a group of n topologically linked ring polymers with m interacting Brownian particles on each ring, thus having total number of particles $N = n \times m$. We assume that all rings are topologically bound to one another, even if indirectly; that is, we assume that there are no disconnected rings or groups of rings. Using the bead radius a, the thermal energy k_BT, and the bead diffusion time $\tau_0 = 6\pi\eta a^3/k_BT$ (with η the solvent viscosity) as the units of length, energy, and time, respectively, the dynamics of the particles at equilibrium

are described by the dimensionless Langevin equation [209]:

$$\frac{d\boldsymbol{R}}{dt} = -\boldsymbol{H} \cdot \frac{\partial U}{\partial \boldsymbol{R}} + \sqrt{2}\boldsymbol{B} \cdot d\boldsymbol{W} \tag{4.1}$$

where $\boldsymbol{R}$ is a vector of particle positions, $\boldsymbol{H}$ is the $N \times N$ mobility or hydrodynamic interaction (HI) matrix whose elements $\boldsymbol{H}_{ij}$ are tensors that describe the direction-dependent hydrodynamic coupling between beads i and j, U is the system interaction potential, $d\boldsymbol{W}$ is an increment of the Wiener process, and $\boldsymbol{B}\boldsymbol{B}^T = \boldsymbol{H}$. Normally, a divergence term of the form $\partial/\partial\boldsymbol{R} \cdot \boldsymbol{H}$ is included in Eq 4.1, but this will be neglected throughout this work as it vanishes due to solvent incompressibility for many commonly employed forms of $\boldsymbol{H}_{ij}$ (e.g. Oseen-Burgers [209], Rotne-Prager-Yamakawa [210, 211], and Zylka-Öttinger [212] tensors).

Eq. 4.1 represents a set of coupled, non-linear equations since both the mobility matrix and the forces ($-\partial U/\partial \boldsymbol{R}$) depend on the particle positions. To make the dynamics of bead-spring polymers tractable, Zimm [213] replaced the mobility matrix by its equilibrium average: $\boldsymbol{H} \rightarrow \langle \boldsymbol{H} \rangle_{\text{eq}}$. The success of these so-called "pre-averaged" hydrodynamics inspired the closely related "consistently-averaged" HI approach in non-equilibrium conditions [214–216] and more recently the iterative averaging method of Sing and coworkers for computer simulations [193]. Following this well established method, we will consider the equilibrium average of the mobility matrix and study the resulting dynamics.

To begin, we establish a useful indexing convention: the vector $\boldsymbol{R}$ is broken up into chunks of size m, each of which represents the position of the beads within a single ring, denoted $\boldsymbol{R}^\alpha$ with $1 \leq \alpha \leq n$. Following this convention, $\boldsymbol{H}$ may be written as a $n \times n$ block matrix with each $m \times m$ block $\boldsymbol{H}^{\alpha\beta}$ representing the hydrodynamic coupling between the beads on rings α and β. The diagonal blocks represent the coupling between beads on the same ring polymer, while the off-diagonal blocks represent the coupling between beads on different rings; for all blocks, the symmetry of $\boldsymbol{H}$ implies $\boldsymbol{H}^{\alpha\beta} = (\boldsymbol{H}^{\beta\alpha})^T$.

We now consider the equilibrium average of the mobility matrix, $\langle \boldsymbol{H} \rangle$ (the subscript "eq"

has been dropped for brevity). The form of the averaged blocks $\langle \boldsymbol{H} \rangle^{\alpha\beta}$ is constrained by the symmetry of the system: all particles within ring polymers are statistically identical. In other words, since our choice of the "first" bead in a ring is completely arbitrary, each of the rows in a given $m \times m$ block will be identical to the others except for a shift in indices. In mathematical terms, the blocks $\langle \boldsymbol{H} \rangle^{\alpha\beta}$ are circulant matrices. This fact was used by Liu and Öttinger [217] to calculate the dynamics of bead-spring ring polymers with pre-averaged hydrodynamics analytically and exactly. This is possible since all circulant matrices have a known set of eigenvectors, which are given by the Fourier modes:

$$\boldsymbol{\omega}_q = \frac{\boldsymbol{\delta}}{\sqrt{m}} \left(1, w_q, w_q^2, ..., w_q^{m-1}\right) \tag{4.2}$$

where $\boldsymbol{\delta}$ is the identity tensor, $0 \leq q \leq m-1$, $w_q = \exp(2\pi i q/m)$ and $i = \sqrt{-1}$.

The off-diagonal blocks $\langle \boldsymbol{H} \rangle^{\alpha\beta} (\alpha \neq \beta)$ possess even greater symmetry. Since the average must not depend on the specific indexing of *either* ring, all elements must be equal. Thus, the off-diagonal blocks have the form:

$$\langle \boldsymbol{H} \rangle^{\alpha\beta} = \frac{\boldsymbol{h}_0^{\alpha\beta}}{m} \begin{bmatrix} 1 & 1 & \dots & \\ 1 & 1 & & \\ \vdots & & \ddots & \\ & & & 1 \end{bmatrix} \equiv \frac{\boldsymbol{h}_0^{\alpha\beta}}{m} \mathbf{1} \tag{4.3}$$

where the (isotropic) tensor $\boldsymbol{h}_0^{\alpha\beta}$ in general depends on which pair of rings is being considered (i.e. on α and β) and we have defined the $m \times m$ "ones" matrix $\mathbf{1}$ in the second equality. The factor of $1/m$ has been incuded for normalization later on.

Having determined the form of $\langle \boldsymbol{H} \rangle$, we can now diagonalize each of its blocks. In particular, if we denote by $\boldsymbol{\omega}$ the $m \times m$ matrix whose columns are given by Eq. 4.2, we can

construct the orthonormal transformation:

$$\boldsymbol{\Omega} = \begin{bmatrix} \boldsymbol{\omega} & 0 & \dots & \\ 0 & \boldsymbol{\omega} & & \\ \vdots & & \ddots & \\ & & & \boldsymbol{\omega} \end{bmatrix} \tag{4.4}$$

which has the properties $\boldsymbol{\Omega}\boldsymbol{\Omega}^\dagger = \boldsymbol{\Omega}^\dagger\boldsymbol{\Omega} = \boldsymbol{I}$, where $\boldsymbol{I}$ is the identity matrix. We now wish to apply this transformation to Eq. 4.1.

Before continuing, it is important to make a key observation. The Fourier modes Eq. 4.2, are physically equivalent to the Rouse modes for ring polymers discussed in the previous chapter. For ring α, we have $\boldsymbol{X}^\alpha = \boldsymbol{\omega}^\dagger \boldsymbol{R}^\alpha$. Accordingly, the mode $q = 0$ corresponds to the ring center-of-mass while the modes $q > 0$ describe the internal configuration of the polymers. This fact will be crucial for the physical interpretation of the dynamics later on.

Substituting the averaged HI matrix into Eq. 4.1 and applying the transformation Eq. 4.4, we have:

$$\frac{d\boldsymbol{X}}{dt} = -\widehat{\boldsymbol{H}} \cdot \frac{\partial U}{\partial \boldsymbol{X}} + \sqrt{2}\widehat{\boldsymbol{B}} \cdot d\boldsymbol{Z} \tag{4.5}$$

where $\widehat{\boldsymbol{H}} = \boldsymbol{\Omega}^\dagger \langle \boldsymbol{H} \rangle \boldsymbol{\Omega}$, $\widehat{\boldsymbol{B}} = \boldsymbol{\Omega}^\dagger \langle \boldsymbol{B} \rangle \boldsymbol{\Omega}$, and $d\boldsymbol{Z} = \boldsymbol{\Omega}^\dagger d\boldsymbol{W}$. The fluctuation-dissipation theorem $\boldsymbol{B}\boldsymbol{B}^T = \boldsymbol{H}$ and the orthonormal character of $\boldsymbol{\Omega}$ imply that $\widehat{\boldsymbol{B}}\widehat{\boldsymbol{B}}^T = \widehat{\boldsymbol{H}}$. Note that despite the fact that $\boldsymbol{\Omega}$ is complex, the matrix $\widehat{\boldsymbol{H}}$ (and therefore $\widehat{\boldsymbol{B}}$) is real and symmetric owing to the symmetry and positive-definiteness of $\boldsymbol{H}$ and the circulant character of each of its blocks.

We now consider explicitly the form of $\widehat{\boldsymbol{H}}$, which inherits the block structure of $\boldsymbol{H}$. The diagonal blocks $\widehat{\boldsymbol{H}}^{\alpha\alpha}$ are themselves diagonal with elements given by the eigenvalues of the matrices $\langle \boldsymbol{H} \rangle^{\alpha\alpha}$, which are denoted $\boldsymbol{h}_q^{\alpha\alpha}$ with $0 \leq q \leq m-1$. This result indicates that in the pre-averaging approximation, the various internal modes of the rings do not hydrodynamically couple to one another; this is the key insight in the work of Liu and Öttinger [217]. The result implies that correlated motions between modes arise only through

the forces in the pre-averaged approximation.

Now to determine the form of the off-diagonal blocks, we evaluate the product:

$$\boldsymbol{\omega}^T \mathbf{1} \boldsymbol{\omega} = m\boldsymbol{\delta} \begin{bmatrix} 1 & 0 & \dots & \\ 0 & 0 & & \\ \vdots & & \ddots & \\ & & & 0 \end{bmatrix} \equiv m\boldsymbol{\delta}\boldsymbol{C} \tag{4.6}$$

where we have defined the "corner" matrix $\boldsymbol{C}$. Using the results Eq. 4.3 and Eq. 4.6, the matrix $\widehat{\boldsymbol{H}}$ has the form:

$$\widehat{\boldsymbol{H}} = \begin{bmatrix} \widehat{\boldsymbol{H}}^{11} & \boldsymbol{h}_0^{12}\boldsymbol{C} & \dots & \\ \boldsymbol{h}_0^{12}\boldsymbol{C} & \widehat{\boldsymbol{H}}^{22} & & \\ \vdots & & \ddots & \\ & & & \widehat{\boldsymbol{H}}^{nn} \end{bmatrix} \tag{4.7}$$

We again emphasize that the on-diagonal blocks $\widehat{\boldsymbol{H}}^{\alpha\alpha}$ are diagonal. Furthermore, the matrix $\widehat{\boldsymbol{B}}$ can be written in a similar manner (see Section A.1) with diagonal on-diagonal blocks $\widehat{\boldsymbol{B}}^{\alpha\alpha}$ having non-zero entries $\boldsymbol{b}_q^{\alpha\alpha}$ $(0 \leq q \leq m-1)$ and off-diagonal blocks $\boldsymbol{b}_0^{\alpha\beta}\boldsymbol{C}$. From Eq. 4.7, the elements of the off-diagonal matrices, which represent HI between modes on different rings, all vanish except those which describe coupling between the "zeroth" modes. But as discussed above, these modes simply correspond to the polymer centers-of-mass. In light of this result, the equation of motion Eq. 4.5 can be separated into two equations: one for the center-of-mass modes $\boldsymbol{X}_0^\alpha$ and another for the internal modes, $\boldsymbol{X}_q^\alpha$ $(q > 0)$ as follows:

$$\frac{d\boldsymbol{X}_0^\alpha}{dt} = \sum_{\beta=1}^{n} \left\{ -\boldsymbol{h}_0^{\alpha\beta} \frac{\partial U}{\partial \boldsymbol{X}_0^\beta} + \sqrt{2}\boldsymbol{b}_0^{\alpha\beta} d\boldsymbol{Z}_0^\beta \right\} \tag{4.8a}$$

$$\frac{d\boldsymbol{X}_q^\alpha}{dt} = -\boldsymbol{h}_q^{\alpha\alpha} \frac{\partial U}{\partial \boldsymbol{X}_q^\alpha} + \sqrt{2}\boldsymbol{b}_q^{\alpha\alpha} d\boldsymbol{Z}_q^\alpha \tag{4.8b}$$

Thus, by a combination of pre-averaging the HI and choosing a suitable coordinate basis,

the set of nm coupled vector equations Eq. 4.1 has been reduced to n coupled equations and $n(m-1)$ (hydrodynamically) independent ones.

We now discuss the physical meaning of this result. According to Eq. 4.8b, the internal modes of the rings ($q > 0$) are *hydrodynamically decoupled* from one another: the only *direct* hydrodynamic coupling between rings occurs at the coarse center-of-mass level, Eq. 4.8a. A similar decoupling of the Rouse modes for isolated linear polymers is a well-known approximation [13, 218], but here, the decoupling is *exact* (within the averaging approximation) and applies to multiple interacting polymers. Of course, the dynamics of the rings will still be coupled through the forces ($-\partial U/\partial \boldsymbol{X}$), but anomalies in these interactions for linked rings are primarily topological; hydrodynamic contributions are higher-order effects (see below). This result is also striking as it does not require that the average be taken over the equilibrium distribution. Indeed, the hydrodynamic decoupling was obtained purely on the basis of the symmetries within the rings, which are still present even in non-ideal (non-Gaussian) polymers or in non-equilibrium conditions. In such cases, Eqs. 4.8 still hold, but with generally anisotropic tensors $\boldsymbol{h}^{\alpha\beta}$ and $\boldsymbol{b}^{\alpha\beta}$. Along similar lines, the precise details of the topological linking do not affect the result, which should therefore hold for arbitrary linking complexity.

In light of these results, HI and topology can only act cooperatively on ring dynamics via three possible mechanisms. First, the values $\boldsymbol{h}_q^{\alpha\alpha}$ may be altered by topological constraints as such constraints modify the configurational distribution functions of the rings. Second, the deviations of $\boldsymbol{h}_q^{\alpha\alpha}$ from the freely-draining value, $\boldsymbol{\delta}$, affect the *non-local-in-time* force-force correlations between modes/segments which are themselves sensitive to topological interactions, thereby influencing the dynamics. Third, the same force correlations mentioned above are affected by the dynamics of the ring centers-of-mass, which still experience HI. The first mechanism is quantitatively negligible, at least for relatively simple links, as discussed later on, so is not likely to be important. Meanwhile, the latter two are *indirect* (or higher-

order) effects in that they describe how the force on a given mode is affected by changes in the dynamics of *other* modes at *earlier* times. Therefore, these effects are expected to be fairly small. As a result, topology and HI are approximately independent and do not act cooperatively to influence the dynamics. If this were case, the dynamical consequences of topological linking would be comparable for systems both with and without HI. In the remainder of this chapter, we develop and apply BD simulation algorithms to test this result. Before continuing, we note that although the theory presented above and methods presented below were developed in the context of linked ring polymers, they apply equally to isolated (i.e. unlinked) or knotted ring polymers. However, no such theory can be developed for linear chains as they have only discrete (head-to-tail) symmetry, rather than the continuous symmetry of rings.

Starting from Eqs. 4.8, it is possible to formulate an efficient scheme for BD simulations of topologically linked polymer systems which includes the three mechanisms of HI-topology coupling described above. This method is presented in Algorithm 1. The forces are calculated in the real-space representation (as interaction potentials are typically expressed in terms of particle positions) while the particle positions are updated in the Fourier mode representation, i.e. using Eqs. 4.8. The advantage of such an approach is that the cumbersome calculations of the matrix-vector products $\boldsymbol{H} \cdot \partial U/\partial \boldsymbol{R}$ and $\boldsymbol{B} \cdot d\boldsymbol{W}$ required for integrating Eq. 4.1 ($\mathcal{O}(N^2)$ operations, even with pre-averaging) are no longer required in integrating Eqs. 4.8, in which such calculations are only necessary for the center-of-mass modes as only these modes are (directly) hydrodynamic coupled. Thus, the bead position update is split into a $\mathcal{O}(N)$ operation for modes $q > 0$ and a $\mathcal{O}(n^2)$ operation for modes $q = 0$. Of course, one must constantly transform back-and-forth between the real-space and Fourier-space representations, but by leveraging fast Fourier transform (FFT) packages, the complexity of these operations is reduced to $\mathcal{O}(nm \log m)$. As a result, for large rings (i.e. large m), this algorithm provides substantial improvements in computational performance

compared to typical conformationally-averaged simulations.

Algorithm 1 Pre-averaged HI

1: Calculate forces on each bead, $-\partial U/\partial \boldsymbol{R}$.
2: Transform $\boldsymbol{R}$ and $-\partial U/\partial \boldsymbol{R}$ to the Fourier-mode space representations $\boldsymbol{X}$,$-\partial U/\partial \boldsymbol{X}$ by FFT.
3: Calculate/apply displacements for modes $q > 0$ independently, leveraging the diagonal character of $\widehat{\boldsymbol{H}}^{\alpha\alpha}$.
4: Calculate/apply displacements of modes $q = 0$ including the hydrodynamic interaction between them as prescribed by $\widehat{\boldsymbol{H}}$ and $\widehat{\boldsymbol{B}}$.
5: Transform $\boldsymbol{X}$ back to the real space representation, $\boldsymbol{R}$ by inverse FFT.

For systems with large conformational fluctuations, averaged hydrodynamic interactions may not provide qualitatively correct results. However, it is possible to modify Algorithm 1 such that some information regarding time-dependent structural variation is preserved; this modification is presented in Algorithm 2. At each time step, the time-dependent HI matrix $\boldsymbol{H}(t)$ is calculated and each of the on-diagonal blocks $\boldsymbol{H}^{\alpha\alpha}(t)$ is averaged along its diagonals such that it becomes circulant. Then, the off-diagonal blocks $\boldsymbol{H}^{\alpha\beta}(t)$ ($\alpha \neq \beta$) are averaged over all elements to obtain the form of Eq. 4.3. Moving to the Fourier space, the time-dependent matrix $\widehat{\boldsymbol{H}}(t)$ will have the form of Eq. 4.7 and $\widehat{\boldsymbol{B}}(t)$ may be computed with complexity $\mathcal{O}(nm) + \mathcal{O}(n^3)$, as described in Section A.1. The remainder of the algorithm is identical to Algorithm 1. In general, the inter-ring couplings $\boldsymbol{h}_0^{\alpha\beta}$ and the intra-ring eigenvalues $\boldsymbol{h}_q^{\alpha\alpha}$ will not be isotropic tensors. However, as discussed before, this anisotropy does not invalidate the hydrodynamic decoupling found in Eqs. 4.8, which relies only on the symmetries of the rings themselves.

Unlike the pre-averaged matrix $\langle \boldsymbol{H} \rangle$, the time-dependent "instantaneously-averaged" HI matrix $\widehat{\boldsymbol{H}}(t)$ still contains some information regarding the instantaneous polymer conformation at various length scales at a given moment in time and may therefore capture some effects of conformational fluctuations with minimal computational expense. As an added bonus, the equilibrium-averaged HI matrix $\langle \boldsymbol{H} \rangle$ need not be known prior to running a simulation. These advantages make Algorithm 2 particularly well-suited to non-equilibrium BD

Algorithm 2 Instantaneously-Averaged HI

1: Calculate forces on each bead, $-\partial U/\partial \boldsymbol{R}$.
2: Calculate the full time/configuration-dependent HI matrix, $\boldsymbol{H}(t)$.
3: Average each of the off-diagonal blocks, $\boldsymbol{H}^{\alpha\beta}$ ($\alpha \neq \beta$), over all elements to calculate the quantities $m\boldsymbol{h}_0^{\alpha\beta}$ appearing in (7).
4: Average each of the on-diagonal blocks, $\boldsymbol{H}^{\alpha\alpha}$, along their diagonals so that the blocks become circulant.
5: Obtain the time-dependent eigenvalues of $\boldsymbol{H}^{\alpha\alpha}(t)$ by FFT and combine with the results of Step 3 above to construct the time-dependent version of (7), $\widehat{\boldsymbol{H}}(t)$.
6: Calculate $\widehat{\boldsymbol{B}}$, leveraging the symmetries of $\widehat{\boldsymbol{H}}$.
7: Transform $\boldsymbol{R}$ and $-\partial U/\partial \boldsymbol{R}$ to the Fourier-mode space representations $\boldsymbol{X}$,$-\partial U/\partial \boldsymbol{X}$ by FFT.
8: Calculate/apply displacements of modes $q = 0$ including the hydrodynamic interaction between them as prescribed by $\widehat{\boldsymbol{H}}$ and $\widehat{\boldsymbol{B}}$ (eq 8a).
9: Calculate/apply displacements for modes $q > 0$ independently, using the diagonal character of $\widehat{\boldsymbol{H}}^{\alpha\alpha}(t)$ (eq. 8b).
10: Transform $\boldsymbol{X}$ back to the real space representation, $\boldsymbol{R}$, by inverse FFT.

simulations.

4.3 Brownian Dynamics Simulations

In the remainder of this chapter, we apply the two algorithms developed above to study the dynamics of topologically linked polymers and test the decoupling predictions. We have conducted BD simulations of unlinks ($n = 1$) and Hopf links ($n = 2$) in equilibrium conditions, employing a commonly-used molecular model with a vanishing excluded volume parameter [192, 219]. We consider ring sizes of $m = 16$, 32, 48, 64, 96, 128, 256, and 512. The ring polymers are modeled as a series of Lennard-Jones particles connected by harmonic bonds. The bonded energy has the form:

$$U_{\text{bond}} = \sum_{\alpha=1}^{n} \sum_{i=1}^{m} \frac{k}{2} \left(|\boldsymbol{R}_i^{\alpha} - \boldsymbol{R}_{(i+1)\%m}^{\alpha}| - R_0 \right)^2 \tag{4.9}$$

where $\boldsymbol{R}_j^\alpha$ is the position of bead j on ring α and the modulo operator ensures ring closure. The bond strength is chosen as $k = 200$ and the equilibrium length as $R_0 = 2$. To enforce topological constraints, nearby beads also interact via a Lennard-Jones potential, whose energy is written:

$$U_{\mathrm{LJ}} = \sum_{j>i}^{N} \epsilon \left[\left(\frac{R_m}{R_{ij}} \right)^{12} - 2 \left(\frac{R_m}{R_{ij}} \right)^{6} \right] \tag{4.10}$$

where R_{ij} is the distance between beads i and j and the sum extends over all pairs of beads in the system. Following previous literature, we choose $R_m = 2$ and $\epsilon = 0.314$ and truncate the interaction at a distance of 4.454. These parameters lead to a vanishing excluded volume parameter, i.e. akin to a theta solution. Of course, topological restrictions alter the theta point in real ring polymers [92, 220] and even lead to excluded-volume type scaling for large ring sizes [221]. Nevertheless, the polymers studied here do indeed obey ideal scaling, as discussed later on.

For the hydrodynamic interaction tensors $\boldsymbol{H}_{ij}$, the Rotne-Prager-Yamakawa tensor [210, 211] is used:

$$\boldsymbol{H}_{ij} = \begin{cases} \boldsymbol{\delta}, & i = j \\ \dfrac{3}{4R_{ij}} \left[\left(1 + \dfrac{2}{3R_{ij}^2} \right) \boldsymbol{\delta} + \left(1 - \dfrac{2}{R_{ij}^2} \right) \dfrac{\boldsymbol{R}_{ij}\boldsymbol{R}_{ij}}{R_{ij}^2} \right], & i \neq j, R_{ij} \geq 2 \\ \left(1 - \dfrac{9R_{ij}}{32} \right) \boldsymbol{\delta} + \dfrac{3}{32} \dfrac{\boldsymbol{R}_{ij}\boldsymbol{R}_{ij}}{R_{ij}}, & i \neq j, R_{ij} < 2 \end{cases} \tag{4.11}$$

where $\boldsymbol{R}_{ij} = \boldsymbol{R}_i - \boldsymbol{R}_j$, $R_{ij} = |\boldsymbol{R}_{ij}|$ and $\boldsymbol{\delta}$ is the identity tensor.

We integrate the equations of motion with a timestep of $\delta t = 10^{-3}\tau_0$ by the Euler method. For the simulations using Algorithm 1, long freely-draining simulations are first conducted to determine $\langle \boldsymbol{H} \rangle$, which is then processed into an isotropic, block-circulant form

in accordance with the symmetries discussed above and then used to calculate $\widehat{\boldsymbol{H}}$ and $\widehat{\boldsymbol{B}}$ (see Section A.1). In the course of this calculation, we obtain the coefficients $\boldsymbol{h}_q^{\alpha\alpha}$ appearing in Eq. 4.8b and find that these values differ only slightly between topologies and that these differences are reduced as m increases. For instance, the values of $\boldsymbol{h}_1^{\alpha\alpha}$ generally experience the largest changes, but differ by less than 3% for $m > 64$. When using Algorithm 2, the HI matrix is updated every 50 to 1000 timesteps. This update interval appears to have no effect on our results.

For comparison, we have conducted additional simulations with fully fluctuating (non-averaged) HI. In these simulations, Eq. 4.1 is integrated by a first-order predictor-corrector scheme with a timestep of $\delta t = 2.5 \times 10^{-3}\tau_0$ and the matrix $\boldsymbol{B}$ is calculated by Cholesky decomposition of $\boldsymbol{H}$ every other step. Such simulations are computationally expensive are therefore not possible for the larger rings studied here. For statistical analysis, sixteen independent simulations were conducted for each system with each algorithm.

4.4 Dynamics of Linked Ring Polymers

Here, we focus on the long-time, large-length-scale dynamical properties and determine how topological linking and HI affect these quantities. In particular, we examine the longest relaxation times of the individual rings (τ, determined from the autocorrelation function of the lowest Rouse mode) and the diffusion coefficient of the whole polymer assembly (D, determined by linear regression on the center-of-mass mean-squared displacement) with the goal of understanding how these quantities are affected by the topological linkage. These data are shown in Figure 4.1. We begin by assessing the validity of the pre-averaging approximation, i.e. the degree to which Algorithms 1 and 2 reproduce the correct dynamical quantities. At small m, the pre-averaging and instantaneous averaging algorithms show considerable deviations in the relaxation times compared to the full BD simulations. However, as m increases, these deviations are reduced and are only about 10% by the time $m = 96$, comparable to the

statistical uncertainty in the results. In general, the diffusion constants show better agreement, exhibiting differences of only 5 - 10 % throughout the range of m values. Despite these differences, all data show roughly the same scaling behavior, as discussed below. Moreover, the results for pre-averaged and instantaneously-averaged HI are in excellent quantitative agreement, suggesting that large length scale conformational fluctuations are not important for the equilibrium dynamics.

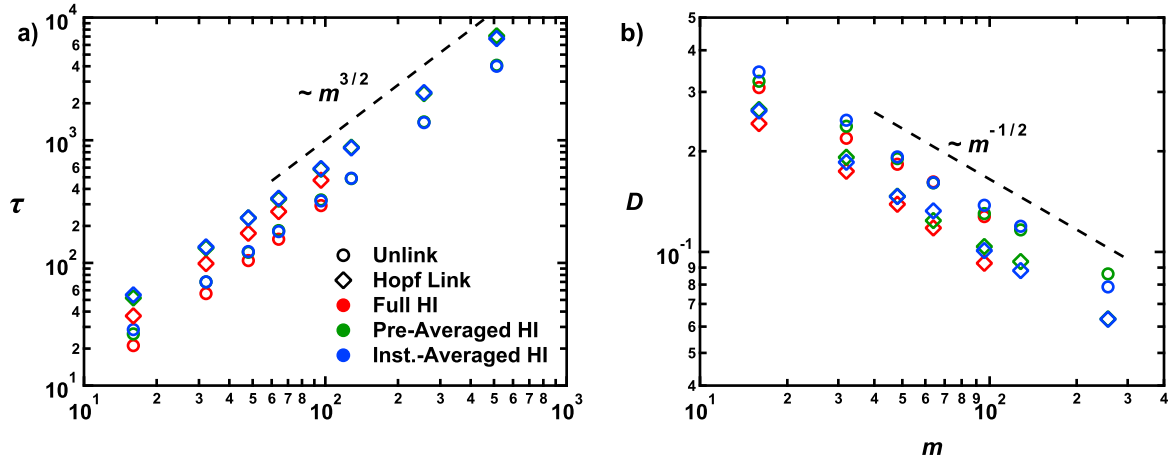

Figure 4.1: a) Longest ring relaxation times, τ, and b) diffusion coefficients, D, for linked and unlinked ring polymers as a function of ring size, m. Error bars are approximately the size of the data points.

Zimm theory predicts that the dynamical quantities presented here scale as $\tau \sim R_{g,r}^3$ and $D \sim R_g^{-1}$ [13] where R_g is the polymer radius of gyration and $R_{g,r}$ is the radius of gyration of an individual ring (for unlinked rings, the latter two quantities are identical). Since our molecular model has a vanishing excluded volume parameter, we expect $R_g \sim R_{g,r} \sim m^{1/2}$; the observed scaling exponents are slightly larger, which is not unexpected as ring polymers exhibit lower θ-temperatures than linear polymers on account of their topological constraints, as mentioned above. Since these deviations are rather small, we still expect to observe (roughly) $D \sim m^{-1/2}$ and $\tau \sim m^{3/2}$ in our simulations. This is indeed the case for all algorithms used, as shown in Figure 4.1.

As in previous simulation studies, the relaxation times of the rings are increased by the

presence of threading segments [222, 223]. However, this is not an unusual result since topological linking also causes the rings to swell relative to the unlinked state [92, 222, 224], which should increase the relaxation times according to the Zimm theory predictions above. Meanwhile, the increased mass and overall size of the Hopf links compared to the unlinks will naturally cause smaller diffusion coefficients, which is indeed observed in the simulations. To understand whether the topology-dependent dynamical properties are simply the result of changes in ring size, we introduce the *effective* mobilities defined by $\mu_\tau(\mathcal{T}) \equiv R_{g,r}^3/\tau$ and $\mu_D(\mathcal{T}) \equiv (R_g D)^{-1}$ where $\mathcal{T}$ is the topological state of the rings, either unlinks, $\mathcal{U}$, of Hopf links, $\mathcal{H}$. According to the scaling predictions above, these mobilities should be independent of m, but may still depend on $\mathcal{T}$. To more clearly quantify such topological effects, we consider the ratios of the effective mobilities, $\mu_\tau(\mathcal{H})/\mu_\tau(\mathcal{U})$ and $\mu_D(\mathcal{H})/\mu_D(\mathcal{U})$. In this way, we isolate the dynamical effects which are solely topological in nature. In a similar manner, we also wish to assess whether or not topological effects are manifested differently in the presence of HI; the theory of Section 4.2 implies that the two are largely independent. To do so, we note that in the absence of HI, relaxation times scale as $\tau \sim mR_{g,r}^2$ [13], suggesting an effective mobility $\mu_0(\mathcal{T}) \equiv mR_{g,r}^2/\tau$; as above, the ratio of this mobility for Hopf and unlinks is considered. Note that any effective mobility calculated from the diffusion constant in freely-draining systems is not a meaningful quantity as these systems have $D = 1/N$ identically, regardless of polymer architecture or topology.

The ratios between effective mobilities, dubbed *relative* mobilities, are shown in Figure 4.2. The relative mobility calculated from the diffusion coefficient is approximately unity for all algorithms and all ring sizes, suggesting that the overall diffusion of the polymer is controlled entirely by its size, so topology and HI couple only insofar as topological constraints affect the ring/polymer dimensions. However, the relative mobility calculated from ring relaxation times shows reductions of $\sim 41\%$ in the absence of HI due to topological effects, in qualitative agreement with previous results [222, 223]. In the presence of full HI, the relative

mobility is decreased just $\sim 26\%$, suggesting that there is indeed some coupling between topology and HI. Nevertheless, the modesty of this difference is notable given how dramatically both HI and topology alter polymer dynamics. Furthermore, when the higher-order *indirect* coupling is included through the pre- and instantaneously-averaged HI simulations, much of this discrepancy is eliminated, with relative mobilities reduced by $\sim 33\%$, further supporting the conclusion that topological interactions and HI are roughly independent effects. Finally, we note that these data are essentially independent of m, indicating that the result is broadly applicable.

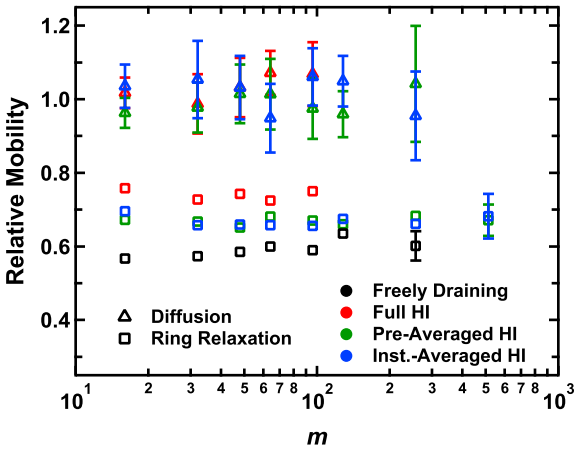

Figure 4.2: Relative mobility of Hopf links and un-links as calculated from either the diffusion coefficient or the ring relaxation times (see main text for details). Statistical uncertainties for the ring relaxation data (squares) are roughly the size of the data points.

The small difference between the relative mobility for averaged vs. full HI represents the *direct* coupling of topology and HI. One potential mechanism for this coupling is offered by the observation that HI effectively "shields" segments from the viscous drag forces of the solvent. By necessity, any averaging procedure assumes that all segments on a given ring share the same local hydrodynamic environment. The data in Figure 4.1 suggest that this approximation leads to some quantitative differences even in the case of unlinked polymers. This heterogeneous environment breaks the symmetry of the rings such that the modes are not truly hydrodynamically decoupled. These errors are likely exacerbated in linked

polymers: when a segment threads a ring, it is surrounded by beads on the threaded ring, which shield the segment from solvent drag. Segments on the other side of the ring, which are farther away from the linked polymer are not as strongly protected. This may explain why the simulations with averaged HI have slightly poorer agreement for linked vs. unlinked rings (see Figure 4.1). Since the two topologies are affected differently, the relative mobility is altered. Nevertheless, these relative mobilities are still quite close to one another, differing by just $\sim 10\%$, thus validating the theoretical result that topological interactions and HI are pseudo-independent.

4.5 Conclusions

This chapter represents the first step in the study of the dynamics of catenaned polymer systems in solution. We have shown that by leveraging the symmetries inherent in ring polymers, the effects of topology and HI may be considered roughly independently. Furthermore, we developed efficient Brownian dynamics algorithms which allow *in silico* access to large interlocking polymer systems and long time scales. We are now in a position to pose and answer a wide array of questions about catenated polymers and poly[n]catenanes, both in equilibrium and non-equilibrium conditions. For instance, we may study the properties of these molecules in shear and extensional flows, under the influence of molecular activity, in varying solvent conditions, etc. We can also apply these methods to study more complex interlocked materials, such as kinetoplasts [207] and Olympic gels [208]. More generally, we anticipate that additional problems in the physics of topologically linked polymers will be simplified by considering the high degrees of symmetry in such systems.

CHAPTER 5

THERMODYNAMICS AND STRUCTURE OF POLY[*N*]CATENANE MELTS

5.1 Introduction

The efforts of the previous chapters have all focused on isolated polymers. However, as pointed out in the introduction, intermolecular interactions become increasingly important in the melt state, which is of interest for poly[n]catenanes as it contains the highest possible density of mechanical bonds. In this chapter and the next, we turn our attention to simulations of poly[n]catenane melts and find a wide array of exciting results.

As mentioned in the Introduction, poly[n]catenanes are completely unstudied in the melt. However, the behavior of linear and ring polymers in the melt (discussed in the Introduction) combined with the properties of these polymers in solution (previous chapters) suggest a number of questions: (1) Does the mechanical bond contribute to the stress/pressure and other thermodynamic quantities, (2) is it possible to further quantify how the topological bond impacts macrocycle conformations, (3) how does ring size affect the conformation and scaling of catenanes, (4) how do intermolecular interactions and the unusual intramolecular conformational structure affect poly[n]catenane melt packing correlations, (5) what is the interplay between intra- and inter-molecular topological interactions, and (6) at what point is inter-chain entanglement important in poly[n]catenane systems? This chapter endeavors to answer the above questions (and others) by performing extensive molecular dynamics simulations of poly[n]catenane melts. Both the degree of polymerization (i.e. the number of links), n, and the ring size, m, are varied and the results are compared to linear polymer and unlinked ring ($n = 1$) melts. Since many different systems have been simulated, it is a challenge to present the entirety of the data in a clear and concise manner. Therefore, this chapter will be representative and illustrative, rather than exhaustive.

5.2 Simulation Methods

As in Chapter 3, the Kremer-Grest (KG) model [23] is employed. All macrocycles in all catenanes are composed of identical beads of mass μ which interact with one another via a shifted Lennard-Jones (LJ) potential (Eq. 3.1). Covalent bonds within ring molecules are enforced by a finitely-extensible nonlinear elastic (FENE) potential (Eq. 3.2) where parameter values of $k = 30\epsilon/\sigma^2$ and $R_0 = 1.5\sigma$ are chosen. No bond angle bending potential is applied, so the ring molecules are fully flexible. These interaction potentials along with the indicated parameters have been shown to prevent chain crossings [23], which is crucial for the simulation of interlocking polymers. The poly[n]catenanes are held together only by the topological linking, which is specified entirely by the initial configurations of the beads and maintained only by the interaction potentials mentioned above. The velocity-Verlet algorithm was used to integrate the equations of motion with a timestep of $\delta t = 0.01\tau$ where $\tau = (\mu\sigma^2/\epsilon)^{1/2}$ is the LJ unit of time. The simulations are conducted at a number density of $\rho 0.85\sigma^{-3}$ and a temperature of $T = 1.0\epsilon/k_B$, maintained via a Langevin thermostat with a drag coefficient of $\Gamma = 0.5\mu/\tau$. All results are reported in reduced LJ units. Simulations were conducted with the GPU-accelerated MD engine DASH [177].

The systems studied here contain a total number of poly[n]catenane molecules of $\mathcal{N} = 100-500$, with the number of rings in each polymer, n, varied between $n = 1, 2, 3, 5, 7, 10, 15$, 20, and 25. For each chain length, catenanes with a number of beads-per-ring, m, varied between $m = 15, 20, 30$ and 50, are considered. Thus, the total molecular weight, $N = nm$, ranges from 15 to $1,250$. Note that these ring sizes are considerably smaller than the entanglement length of the KG model ($N_e \approx 85$) [47] so no significant intermolecular topological compression is expected between the rings [59, 64]. Linear polymer systems with $\mathcal{N} = 500$ and degree of polymerization N varying between $N = 15, 20, 30, 45, 60, 80, 100, 150$, and 175 have also been simulated for comparison. For statistical analysis, five independent

simulations of each system were conducted. Production simulations were run for $10^6 - 10^7\tau$, depending on polymer size. More details concerning the poly[n]catenane and linear polymer systems and the simulation preparation procedures may be found in Appendix A.2, along with quantitative analysis confirming system equilibration.

5.3 Thermodynamic Properties

Topological interactions can affect the pressure in certain polymer systems. For example, in unlinked ring polymers, the topological interactions cause the chains to repel each other weakly [71–73, 225]. In the melt, these interactions should increase the pressure relative to linear polymers, but such an increase has not been observed in simulations of high-MW ring polymer melts [59], likely because such effects are more subtle for these systems. Nevertheless, topological effects may also contribute to the pressure in poly[n]catenane melts, but in the opposite manner. The rings must be linked and are therefore prevented from separating from one another, so they effectively attract each other. Thus, the pressure should decrease as the number (or concentration) of mechanical bonds increases, even if the concentration of covalent bonds does not change. Figure 5.1a shows the pressure as function of the number density of mechanical bonds, defined as:

$$\rho_b \equiv \frac{\mathcal{N}(n-1)}{V} = \rho\frac{n-1}{nm} \tag{5.1}$$

recalling that ρ is the number density of beads in the melt. The pressure is calculated according to the virial theorem:

$$P = \rho k_B T + \frac{1}{3V}\left\langle \sum_{j>i} \boldsymbol{F}_{ij} \cdot \boldsymbol{r}_{ij} \right\rangle \tag{5.2}$$

where V is the system volume, $\boldsymbol{F}_{ij}$ is the force exerted on particle i by particle j, $\boldsymbol{r}_{ij} = \boldsymbol{r}_j - \boldsymbol{r}_i$ is the vector between the particle positions, and the sum runs over all pairs of particles in the system. As expected, the pressure decreases as ρ_b increases, reaching values up to 5% lower than those of ring polymers. In analogy with the virial pressure given above (Eq. 5.2), such decreases typically indicate that more attractive forces are present within the system. The only attractive forces that are specified by the molecular model are the covalent bonds (Eq. 3.2). However, in all cases, each Lennard-Jones bead is bonded to exactly two others, so the concentration of such bonds is constant, irrespective of ρ_b. Also, the beads only interact repulsively via a truncated LJ potential (Eq. 3.1), and therefore cannot lower the pressure unless the particle density is also reduced (and it is not). In general, the Hamiltonian is the same for all systems along with the density and temperature, so any changes in the pressure must be related to changes in the integration limits (rather than the statistical weights) of the partition function, i.e. they must be caused by the topological constraints/bonds. In other words, the mechanical bonds introduce effective (topological) attractions between linked rings, even though the actual forces are purely repulsive; these attractions in turn modify the pressure. Evidently, the topological attraction between linked rings is much stronger than the topological repulsions between non-concatenated rings since pressure increases have not been observed in simulations of non-concatenated ring polymer melts [59]. In any case, such repulsions should not be important for the small rings considered here compared to ordinary excluded volume (i.e. that arising from the finite volume of the beads) since the rings are much smaller than the entanglement length of the KG model, $m < N_e$. For $n > 2$, the pressure decreases linearly with ρ_b, with the largest effects observed for the smallest rings. The dependence on ring size may be related to the fact that the bond length distributions for small rings are more sharply peaked, which would typically lead to stronger effective forces between the macrocycles. However, these distributions lead to potentials of mean force which are highly anharmonic (not shown), precluding any simple interpretation. Since a constant

slope is only observed when $n > 2$, the doubly-threaded rings apparently contribute more strongly to the pressure than the singly-threaded ones.

The potential energy per particle, $u = U/\mathcal{N}N$, also decreases linearly with ρ_b, as shown in Figure 5.1b, but the differences are much smaller than those seen in the pressure, being less than 1% of the value (but still larger than statistical uncertainty). The potential energy is obtained by time-averaging the instantaneous potential energy of the system calculated at regular intervals. In contrast to the pressure, u does not depend strongly on m, which can be rationalized in terms of an equipartition theorem. In a crude sense, the mechanical bond forces the centers-of-mass of two rings to remain close to each other, removing a degree of freedom (without actually altering the Hamiltonian!). On average, this degree of freedom will be associated with some potential energy which depends on the temperature and if the internal degrees of freedom of the rings are not affected, then this energy will not depend on m. Denoting this energy by $A(T)$ and assuming that these degrees of freedom are independent, the change in potential energy associated with adding mechanical bonds to the system, ΔU, will be proportional to the number of mechanical bonds: $\Delta U \approx A(T)\mathcal{N}(n-1)$. Dividing this quantity by $\mathcal{N}N$, the total number of particles, leads to a linear relation between the potential energy and the concentration of mechanical bonds, $\Delta u \approx A(T)(n-1)/nm = A(T)\rho_b/\rho$.

The total system potential energy has both intra- and inter-molecular contributions which can be related to the appropriate site-site pair correlation functions through statistical mechanics. Thus, the small changes in per-particle potential energy (Figure 5.1b) must be accompanied by small changes in the fluid structure. Indeed, the site-site correlation functions can be used to numerically obtain energy differences in agreement with those of Figure 5.1b (not shown). However, the actual correlation functions themselves are indistinguishable to the eye, which is unsurprising given the smallness of the energy differences. Moreover, these correlation functions agree quantitatively with those of linear polymers of high-MW,

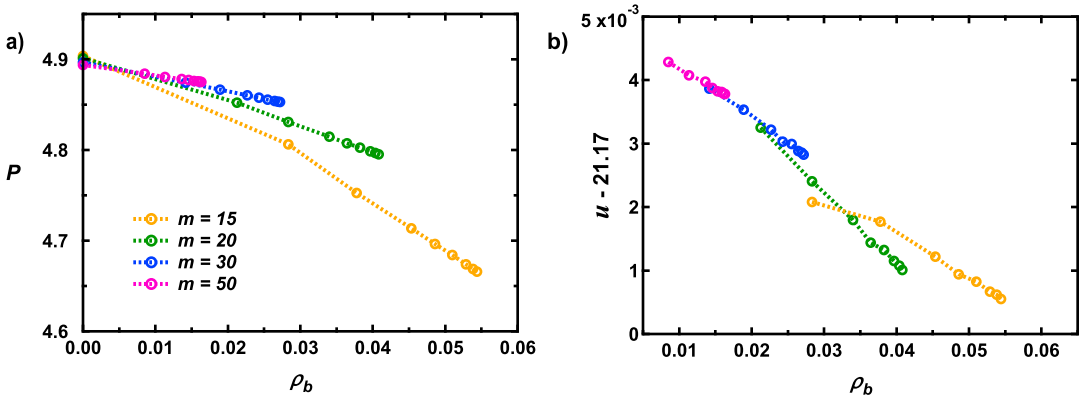

Figure 5.1: a) Pressure, and b) potential energy per particle as a function of the density of mechanical bonds (Eq. 5.1) for poly[n]catenanes with various m. The statistical errors are approximately equal to the size of the data points. Note that in part b) a common factor has been subtracted from the values to more clearly visualize the trend; also the spacing between tick marks on the vertical axis is only $10^{-3}\epsilon$, so the differences in energy are quite small.

where chain ends effects become negligible. For very small ring sizes (not discussed here), the fluid structure can indeed be significantly affected by chain length, n, which introduces a number of unusual static and dynamic properties. Such systems will be discussed in a separate work.

The results presented in this section represent some of the largest topological effects yet observed in bulk thermodynamic properties of polymer systems. In particular, the system pressure shows a strong dependence on the ring size, m, suggesting that topological effects in poly[n]catenanes will be most prevalent for smaller ring sizes. In other words, the concatenation between rings may restrict the available ring conformations more severely for smaller rings. There is also a strong dependence on the number of rings in each catenane, n, which modifies the number of mechanical bonds (i.e. concatenation constraints). To more fully understand poly[n]catenane systems, it is therefore necessary to study the conformational properties of the polymers both in terms of individual rings and at the level of the overall chain. These properties are the subject of the next two sections.

5.4 Ring Conformation

When studying the conformations of individual macrocycles within poly[n]catenanes, chain centers and chain ends must be handled separately since the former are threaded by two rings while the latter are threaded by only one; these rings should also be compared with free ring polymers ($n = 1$) which are not (permanently) threaded by any other rings. It was found that the ring conformations do not depend on n for catenanes of $n \geq 5$ and all quantities are therefore calculated from chains of length $n = 7$ for simplicity. Table 5.1 displays some structural properties of the rings. As expected, mechanical bonds increase the single macrocycle size relative to that of free rings for all values of m, as measured by both the mean squared radius of gyration, $R^2_{g,r}$ (the second subscript "r" indicating that this quantity applies to individual rings), and the mean squared diameter vector, R^2_d. The ratio $R^2_{g,r}/R^2_d$ should equal 1/3 for ideal Gaussian ring polymers and 1/4 for perfectly rigid circles. The observed ratios are indeed close to the Gaussian value for free ring polymers, with larger rings having more ideal conformations and smaller ones deviating slightly. Chain ends and chain centers deviate more strongly from ideal behavior with ratios as small as 0.27 observed for the smallest rings, suggesting that the mechanical bond leads to effectively stiffer polymer segments and more circular conformations.

Ideal (phantom) ring polymers without topological restrictions have a Gaussian-distributed diameter vector [174, 226], and real ring polymers in the melt generally obey such a distribution, even when topological interactions cause non-ideal scaling of the ring size [59]. However, this distribution may be affected by the mechanical bonds in poly[n]catenanes for the small ring sizes studied here. This effect can be quantified by a non-Gaussian parameter:

$$\alpha \equiv \frac{3\langle R^4_d \rangle}{5\langle R^2_d \rangle^2} - 1 \tag{5.3}$$

which takes on a value of zero if the diameter vector is Gaussian-distributed and -0.4 if it

Table 5.1: Data taken from poly[n]catenanes ($n = 7$) and free rings ($n = 1$). Mean square radius of gyration ($R^2_{g,r}$), apparent scaling exponent (calculated from the radius of gyration via finite difference, $\nu_{g,r}(m)$), mean square diameter vector (R^2_d), apparent scaling exponent (calculated from the diameter vector via finite difference, $\nu_d(m)$), non-Gaussian parameter of the diameter vector distribution (α), and ratio of average gyration tensor eigenvalues ($\langle\lambda_1\rangle : \langle\lambda_2\rangle : \langle\lambda_3\rangle$). Statistical uncertainties occur in the decimal places after those reported.

Topology	m	$R^2_{g,r}$	$\nu_{g,r}(m)$	R^2_d	$\nu_d(m)$	α	$\langle\lambda_1\rangle : \langle\lambda_2\rangle : \langle\lambda_3\rangle$
Free Rings	15	2.06		6.93		-0.18	1.0:2.7:6.5
	20	2.77	0.51	9.15	0.48	-0.15	1.0:2.5:6.3
	30	4.14	0.50	13.26	0.46	-0.11	1.0:2.4:6.2
	50	6.75	0.48	21.0	0.45	-0.08	1.0:2.3:6.1
Chain Ends	15	2.54		9.06		-0.28	1.0:4.4:8.5
	20	3.31	0.46	11.6	0.42	-0.24	1.0:3.5:7.5
	30	4.77	0.45	15.9	0.40	-0.18	1.0:2.8:6.8
	50	7.49	0.44	23.8	0.40	-0.12	1.0:2.5:6.3
Chain Centers	15	3.01		11.14		-0.32	1.0:6.4:11.5
	20	3.89	0.45	14.1	0.42	-0.28	1.0:4.7:9.3
	30	5.53	0.43	19.1	0.38	-0.22	1.0:3.5:7.7
	50	8.50	0.42	27.9	0.37	-0.15	1.0:2.8:6.8

is delta-function distributed. All systems exhibit negative parameters but the values tend towards zero with increasing ring size m, achieving nearly ideal statistics for the largest free rings ($m = 50$, Table 5.1). At small m, the negative values of α suggest that the conformational freedom of the rings is limited by the topological restriction that the loop be closed. In general, the mechanical bonds further reduce the non-Gaussian parameters, again indicating stiffer polymers, which is consistent with the larger ring sizes discussed above.

The mechanical bonds also affect the shape of the rings which can be determined by the ratio of the eigenvalues of the gyration tensor, also shown in Table 5.1. As expected, unthreaded rings show very similar shape for all m since they are nearly ideal ring polymers.

Threaded rings, however, are highly distorted by the mechanical bonds, particularly at small m, where they adopt nearly two-dimensional shapes as indicated by the large increases in the eigenvalue ratios. These shape changes are also observed in the ring density profiles as a function of the distance from the center-of-mass, shown in Figure 5.2. While the unthreaded rings show (nearly) monotonically decreasing density profiles for all ring sizes, the threaded rings exhibit large depletions near the center of mass and form toroidal shapes. As expected, the magnitude of this effect decreases as the ring size m is increased.

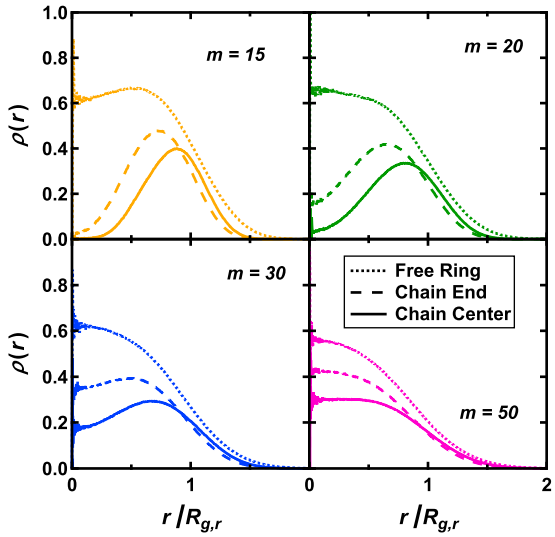

Figure 5.2: Ring density profile as a function of distance from macrocycle center-of-mass for poly[n]catenanes and ring polymers. Note that the legend in the lower right pane applies to all graphs.

As discussed in the Introduction, the size of ring polymers scales more slowly with molecular weight in the melt compared to linear polymers or ideal Gaussian rings. Since this unusual scaling is driven by topological interactions, the mechanical bonds are expected to alter the scaling of ring size within the poly[n]catenanes. Of course, the rings considered here are rather small, with ring size, m, being considerably less than the typical (linear) entanglement molecular weight for the KG model, so the quantities reported here are only apparent or crossover scaling exponents. Nevertheless, the exponent values and trends will

prove insightful in understanding the effect of the mechanical bond on ring conformations. The m-dependent apparent scaling exponents, $\nu_{g,r}(m)$ and $\nu_d(m)$, are calculated from $R^2_{g,r}$ and R^2_d, respectively, by finite difference, and are presented in Table 5.1 for various ring topologies. Free rings scale nearly ideally at small m, with exponents decreasing modestly as m increases, consistent with other simulations of ring polymer melts [56, 59, 61–63, 227]. For the threaded rings, the scaling exponents also decrease as m is increased, but the values are much smaller overall, as low as 0.37 for the largest ring sizes. These results lead to an apparent "paradox": such small scaling exponents typically indicate topological compression of rings, leading to smaller polymers, but the mechanical bonds actually expand the rings (Table 5.1). Perhaps the unusually small scaling exponents arise because the dimensions of the threaded rings are converging towards those of the unthreaded ones as m increases; this convergence would naturally lead to smaller apparent scaling exponents. Indeed, the results shown in Table 5.1 indicate that rings tend to become more ideal as m is increased for all topologies (i.e. number of threadings). This picture is also supported by the density profiles in Figure 5.2: the qualitative differences between the profiles of chain centers and free rings are considerably reduced at large ring sizes. However, this does not appear to be the case in dilute solution conditions as revealed by recent Monte Carlo simulations of linked and unlinked rings, which do not exhibit the "paradox" mentioned above. Indeed, linked rings are still considerably larger than unlinked ones in dilute solution conditions, even for very large polymers [228], and show nearly identical scaling behavior [225, 228, 229]. The primary difference between these two scenarios is the presence of intermolecular (inter-chain) interactions. These observations suggest an interplay of two effects in poly[n]catenane melts: the mechanical bonds increase the ring size and change the ring shape (Table 5.1), thus altering the intermolecular interactions with other rings in the melt, affecting the scaling of the ring size with increasing m. In summary, ring dimensions in poly[n]catenanes appear to be significantly affected by both the mechanical bonds and the intermolecular interactions.

Thus far, only the overall size and shape of the rings have been considered; now the specific conformations of the macrocycles are studied. These conformations may be quantitatively analyzed in terms of the Rouse modes, which are essentially Fourier modes of the chain [169]. For ring polymers [174], these modes and their eigenvalues are given by Eqs. 3.4 and 3.5, respectively. The mean-squared mode amplitudes $\langle X_q^2 \rangle$ contain information about the conformation of the polymer at length scales of m/q along the chain contour and their sum is proportional to $R_{g,r}^2$. When scaled by the eigenvalues, the amplitudes represent effective bond lengths (squared) at the corresponding length scale. For ideal Gaussian chains, these bond lengths are constant for all length scales; in reality, the bond lengths typically increase towards a plateau at large length scales (m/q) because of local chain stiffness effects. These effective bond lengths are plotted as a function of length scale in Figure 5.3 for all ring sizes and topologies (sets of curves for different m have been shifted vertically for clarity). At the longest length scales, the rings are expanded by the mechanical bonds, in agreement with the previously-discussed results on ring dimensions. However, at all shorter length scales, the mode amplitudes for the threaded macrocycles are smaller than those of the free rings, indicating that the mechanical bond effectively compresses the segments locally compared to free rings, with doubly-threaded rings being the most affected. As is the case for other structural properties, the size of these effects is diminished as m increases. Since these two effects were also observed in dilute solution conditions (see previous chapter and [222]), they are likely related to the mechanical bonds alone, rather than inter-molecular interactions.

The single-ring structure factor also shows some signatures of the mechanical bond. For isotropic systems, this function is defined:

$$S(k) = \frac{1}{m} \left\langle \sum_{i,j=1}^{m} \frac{\sin\left(kr_{ij}\right)}{\left(kr_{ij}\right)} \right\rangle \tag{5.4}$$

where r_{ij} is the distance between beads i and j within the same ring and the angled brackets denote an ensemble average over all rings of the same topology – i.e. all chain center or

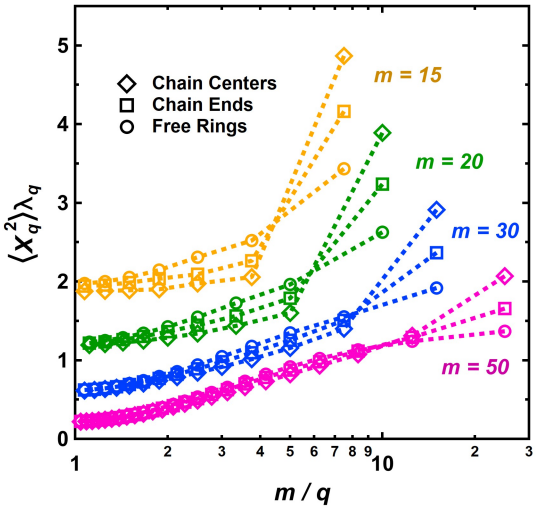

Figure 5.3: Mean squared amplitudes of the Rouse modes for rings (Eq. 3.4) within poly[n]catenanes. Sets of curves for each m have been shifted vertically for clarity.

chain end macrocycles in poly[n]catenanes, or all rings in ring polymer melts. This function provides information on polymer conformation and statistics in reciprocal space and can be obtained experimentally via neutron scattering. As expected, all systems show a Guinier regime at low-k and peaks at high-k, the latter being caused by the covalent connectivity between beads. However, for threaded rings, the structure factor also exhibits a pronounced shoulder at $kR_{g,r} \approx 4$, as shown in Figure 5.4a. This feature appears at the same value of $kR_{g,r}$ for all ring sizes, indicating that it is not caused by bead connectivity, but is instead related to the structure of rings at the segmental level. This shoulder is absent for free rings, as shown in Figure 5.4b, indicating that it is a feature unique to the mechanical bond. As with other features, the size of the effect is reduced as m is increased. This distinctive feature may be related to the peaked density profiles seen in Figure 5.2. However, the connection between the two observations is not entirely clear. For instance, free rings also show a maximum in the density profile for $m = 15$, but this system does not show any additional shoulder in the structure factor. Furthermore, the position of the peak in the density shifts to lower values of $r/R_{g,r}$ as m is increased, while the position of the peak/shoulder in the

structure factor is virtually constant for all m. Ultimately, these two quantities probe the structure in different ways, so no immediate connection between them is available.

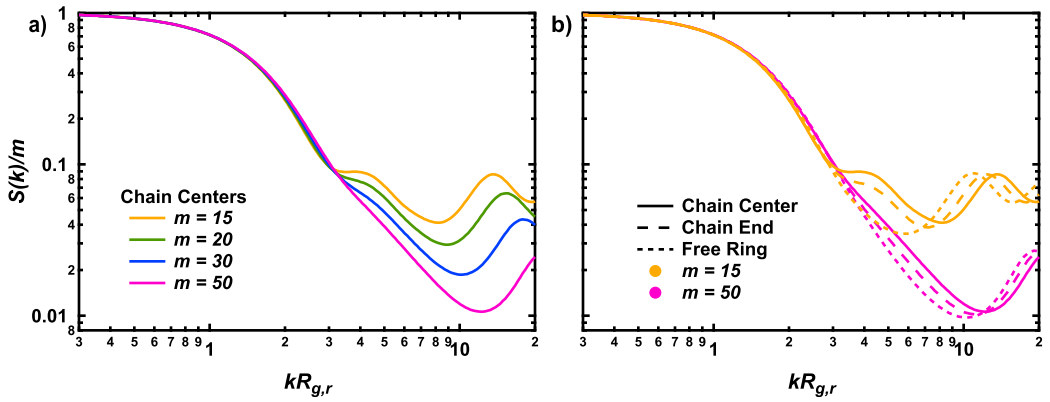

Figure 5.4: a) Chain center single-ring structure factor for various m, b) Structure factor for all ring topologies for smallest and largest m values. Note that the k-values have been scaled by the radius of gyration of each ring. These data were taken from systems with $n = 7$ but are in quantitative agreement with other values of n.

5.5 Chain Conformation

As poly[n]catenanes have an overall linear structure, their properties can be conveniently studied by coarse-graining them into simple linear polymers. Following previous work [222], each ring is defined as an effective monomer with its position given by the ring center-of-mass; the conformations of the chains are examined in terms of these effective monomers. First, structural properties that do not depend on chain length, n, are considered; among these are the mechanical bond lengths at the chain end, b_e, and chain center, b_c, defined as the separation distance between ring centers-of-mass at these points in the chain. These quantities are shown in Table 5.2; since they have essentially no dependence on n (see Appendix, Figure A.1b), they are calculated from the systems with $n = 25$ for simplicity. The bond lengths are somewhat smaller at the chain ends compared to chain centers, consistent with the previous observation that the rings are smaller at the chain ends (Table 5.1). One

would expect that these bond lengths scale with m in a manner similar to the ring size ($R_{g,r}$ or R_d). Although these apparent scaling exponents, ν_b, are indeed in the range 0.4 - 0.5 for the chain center bonds (Table 5.2), the exponents actually increase with m, in contrast to the ring size scaling exponents, which decrease with m (Table 5.1). The reason for this discrepancy is unclear but may be related to the interplay of the mechanical bonds and intermolecular interactions mentioned in the previous section; further study is required to clarify the situation.

Table 5.2: Intrinsic structural properties of poly[n]catenanes: chain center bond length (b_c), apparent scaling of b_c with m (ν_b, calculated by finite difference), chain end bond length (b_e), effective bond length (b_{eff}), apparent scaling of b_{eff} with m ($\nu_{b,\text{eff}}$, calculated by finite difference) and normalized effective bond length (b_{eff}/b_c), persistence length from radius of gyration (l_p^g), persistence length from bond vector correlations (l_p^e), estimated entanglement length (n_e, see Section 6 for details and discussion). See main text for additional details.

m	b_c	ν_b	b_e	b_{eff}	$\nu_{b,\text{eff}}$	b_{eff}/b_c	l_p^g	l_p^e	n_e
15	1.98	-	1.75	3.24	-	1.64	1.48	1.12	43
20	2.23	0.41	2.01	3.52	0.29	1.58	1.38	1.01	45
30	2.69	0.46	2.47	4.02	0.33	1.49	1.23	0.84	45
50	3.46	0.49	3.23	4.79	0.34	1.38	1.07	0.66	42

The effective bond length, b_{eff}, measures the polymer stiffness and is defined in terms of the end-to-end distance as $R_e^2 = (n-1)b_{\text{eff}}^2$; note that R_e^2 is the mean-squared distance between the centers-of-mass of the chain-end macrocycles and will be discussed later. Consistent with the results of Wittmer *et al.* [230, 231], the quantity $R_e^2/(n-1)$ depends linearly on $1/\sqrt{n}$, so a simple linear regression can be used to estimate b_{eff}^2 in the asymptotic limit ($n \to \infty$); these data and their apparent scaling exponents with m, denoted $\nu_{b,\text{eff}}$, are shown in Table 5.2. As expected, the effective bond lengths increase with m, reflecting the larger size of the elementary macrocycles. Similar to the mean bond lengths discussed above, the apparent scaling exponents of effective bond lengths increase with m. However, the actual values of the exponents are considerably smaller: in the range of 0.29-0.34. Essentially, the

effective bond lengths increase with m more slowly that the true bond lengths. The ratio of these two values, b_{eff}/b_c is simply the square root of the characteristic ratio, and therefore measures the effective stiffness of the polymer; this value (also shown in Table 5.2) decreases with m, indicating that poly[n]catenanes with larger rings are more flexible, in a relative sense. This result agrees with our previous work on isolated chains [222]. Finally, the persistence length is calculated in two ways: (i) direct calculation using the polymer radius of gyration [232] and subsequent normalization by b_c , and (ii) by fitting the bond vector orientational correlation function to an exponential decay. The first method includes information about all beads within the polymer since R_g is calculated using every bead; the second method only accounts for interactions at the macrocycle center-of-mass level. On account of this, the numerical values are quite different. In general, these two measures of persistence length do not agree with each other for "thick" macromolecules [233–235], so the result is not surprising. Nevertheless, both measures of persistence length follow the same trend as the normalized effective bond lengths: larger rings lead to more flexible poly[n]catenanes.

The observations above can be explained qualitatively with a simple excluded volume argument. Because the melt has finite compressibility, segments (i.e. rings) within the same polymer chain repel each other at short distances due to unscreened excluded volume. In turn, this excluded volume should be related to the local bead density within the segments. For poly[n]catenane macrocycles, this bead density decreases with increasing m; this is true for any molecule that is not completely globular, i.e. $R \sim N^{1/3}$. Therefore, poly[n]catenanes with larger rings experience less intra-chain repulsion between macrocycles, which makes the chains more flexible compared to those with smaller rings. Of course, the rings will also exhibit some topological excluded volume [71] which is expected to grow with m [221] but such effects should be negligible compared to the molecular (bead) excluded volume for the small rings considered here.

The apparent scaling of poly[n]catenane size with n depends strongly on the particular

measure: end-to-end distance, R_e, or radius of gyration, R_g. The former is calculated as the distance between the centers-of-mass of the chain-end macrocycles while the latter includes contributions from all beads in the system. In Appendix A.3, it is shown that the two quantities may be estimated in terms of the radius of gyration of the rings, $R_{g,r}$, and the effective bond length, b_{eff}, by the relations:

$$R_e^2 = (n-1)b_{\text{eff}}^2 \approx nb_{\text{eff}}^2 \tag{5.5}$$

$$R_g^2 \approx \frac{nb_{\text{eff}}^2}{6} + R_{g,r}^2 + \frac{b_{\text{eff}}^2}{6n} \tag{5.6}$$

Note that quantitative agreement with Eqs. 5.5 and 5.6 is not expected as a variety of approximations have been employed. Nevertheless, the same qualitative trends should be apparent in simulation data. For large values of n, Eqs. 5.5 and 5.6 indicate that both R_e and R_g, approach ideal scaling, $R_e \sim R_g \sim n^{1/2}$; this result is confirmed in Figure 5.5 for all poly[n]catenane systems. Furthermore, the distribution of end-to-end vectors becomes more Gaussian (ideal) for large n as determined by a non-Gaussian parameter similar to Eq. 5.3 (Figure 5.5 inset). These results demonstrate that poly[n]catenanes are similar to linear polymers at long length scales. The fact that the ratio R_e^2/R_g^2 is nearly equal to the ideal chain value of six at large n further supports this conclusion. However, the apparent exponents of R_e and R_g in the low-n crossover regime approach the ideal limit from different directions, as shown in Figure 5.6 (calculated by finite difference). The apparent scaling exponents of R_e are much larger than $1/2$ at small n and slowly decrease towards the ideal value while the apparent scaling exponents of R_g are considerably lower than $1/2$ at small n, with values as small as 0.2 observed for the largest ring sizes. The rapid apparent scaling of R_e is typical for linear polymers and is caused by local stiffness of the chain and unscreened excluded volume effects. On the other hand, the apparent scaling of R_g is quite unusual: such exceptionally small exponents indicate highly compact conformations which slowly relax to

ideal coils at large n. This result can be understood in terms of Eq. 5.6, which contains three terms: an ideal chain contribution (first term), an additive correction that is independent of n (second term), and a higher order correction that decays quickly with n (third term) which can be neglected in the present analysis. The second term arises from the detailed local structure of the polymer, i.e. the macrocycles, and causes reductions in the apparent scaling with n. In fact, from Eq. 5.6, the apparent scaling exponent can be approximated as $\nu \approx 1/2 - 3R_{g,r}^2/R_e^2$ (see Appendix A.3), so that corrections to the ideal chain value are related to the relative size of the macrocycles and the overall polymer. For larger rings and/or shorter chains, these corrections lead to smaller effective scaling exponents; both of these trends can be clearly seen in Figure 5.6. At large length scales, the details of the underlying ring structure become less important and the poly[n]catenanes are dominated by their overall linear architecture, at which point the ideal scaling exponent of $1/2$ is recovered.

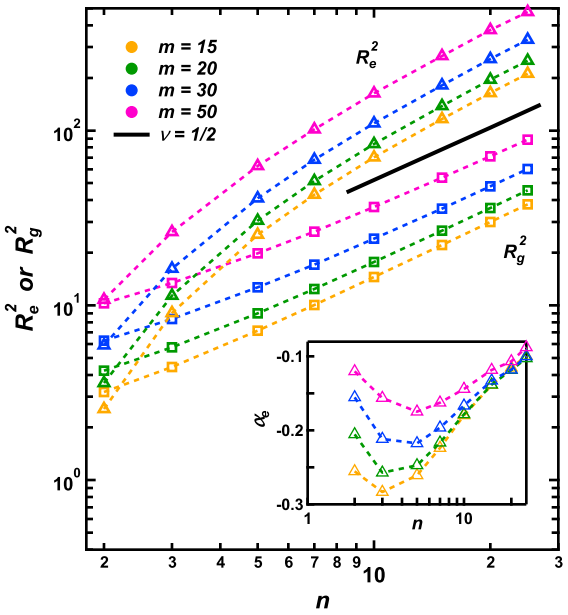

Figure 5.5: Mean-squared end-to-end distance and radius of gyration for poly[n]catenanes as a function of the number of rings per chain. Inset: non-Gaussian parameter for the distribution of end-to-end distances.

The m-dependence of R_e and R_g can also be understood in terms of Eqs. 5.5 and 5.6.

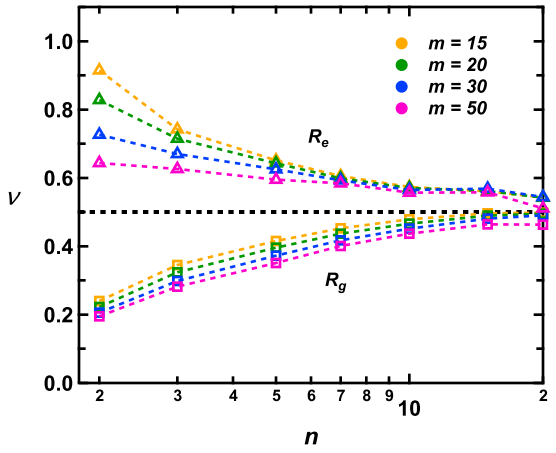

Figure 5.6: n-dependent apparent scaling exponents, ν, for end-to-end distance, R_e, and radius of gyration, R_g, of poly[n]catenanes calculated by finite difference. The dashed black line indicates the ideal (Gaussian) limit.

In particular, Eq. 5.5 indicates that R_e should depend on m only through the effective bond length, b_{eff} (neglecting chain end effects). The behavior in Eq. 5.6 is richer, as two m-dependent quantities are found: the effective bond length, b_{eff}, and the ring radius of gyration, $R_{g,r}$. As a result, no power-law behavior is expected except when the second and third terms of Eq. 5.6 can be ignored (i.e. for large n) or when both b_{eff} and $R_{g,r}$ have the same power-law dependence on m. However, the latter scenario is not observed in the simulation data as discussed above (cf. Tables 5.1 and 5.2): even for chain centers, $R_{g,r}$ increases considerably faster with m than does b_{eff}. As a result, the apparent scaling exponents of R_g with m systematically decrease with n from the free ring polymer values (roughly 1/2, see Table 5.1) at small n to the effective bond length values (roughly 1/3, see Table 5.2) at large n. In light of these observations, it is only useful to consider scaling behavior in the asymptotic limit of large n, where only the first term in Eq. 5.6 is important. In this scenario, R_e and R_g will have the same m-dependence which, as mentioned above, enters through b_{eff}; this dependence was discussed above near the beginning of this section. To restate the main points, b_{eff} (and therefore R_e and R_g) grows very slowly with m owing to a reduction in effective chain stiffness. However, the rings studied here are not large enough

to reach any asymptotic limit.

The shape of poly[n]catenanes can be characterized in more detail by the ratios of the gyration tensor eigenvalues, shown in Figure 5.7. For $n = 2$, these ratios are smallest, indicating a more spherical shape. At larger n, the ratios increase to values comparable to those of ordinary linear polymers ($\lambda_2/\lambda_1 \approx 2.6$, $\lambda_3/\lambda_1 \approx 10.7$) [23], suggesting a transition from globular to ideal coil conformations. Note that for linear polymers, the eigenvalue ratios are larger for smaller N on account of local chain stiffness. In a similar manner, the ratios for $n = 1$ (i.e. ring polymers) are greater than those for $n = 2$.

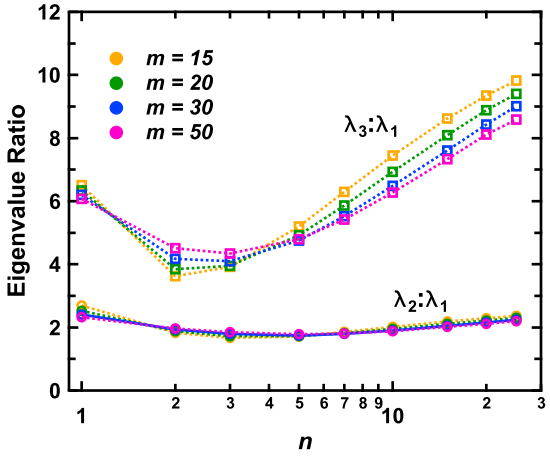

Figure 5.7: Ratio between average gyration tensor eigenvalues for poly[n]catenanes. The values for large n are close to the limiting values for linear polymers. However, the ratios for linear polymers approach this limit from above, rather than below.

Even at the largest values of n, poly[n]catenanes appear highly globular in the melt compared to dilute solution. A visualization of the molecule in the two contrasting conditions is shown in Figure 5.8. In good solvent conditions, the rings are expanded, along with chain as a whole. However, once intermolecular effects are introduced in the melt, the polymer-polymer interactions compress the macromolecules drastically, transforming them into dense globule-like structures with just a few small protruding segments. These configurations are somewhat similar to those found in ring polymer melts, which is indeed expected since the lack of (covalent) chain ends in both systems requires that any interpenetrating segments

must be loops [57, 59, 63]. Similar conformations involving segregated territories are also observed in cellular chromatin and imply considerable density inhomogeneities within single chains [229, 236]. When the polymer is examined in terms of the ring centers-of-mass, the details of the globular structure are lost and the resulting linear polymer appears quite ordinary. Because of these observations, complex features are expected in the single-chain structure factor.

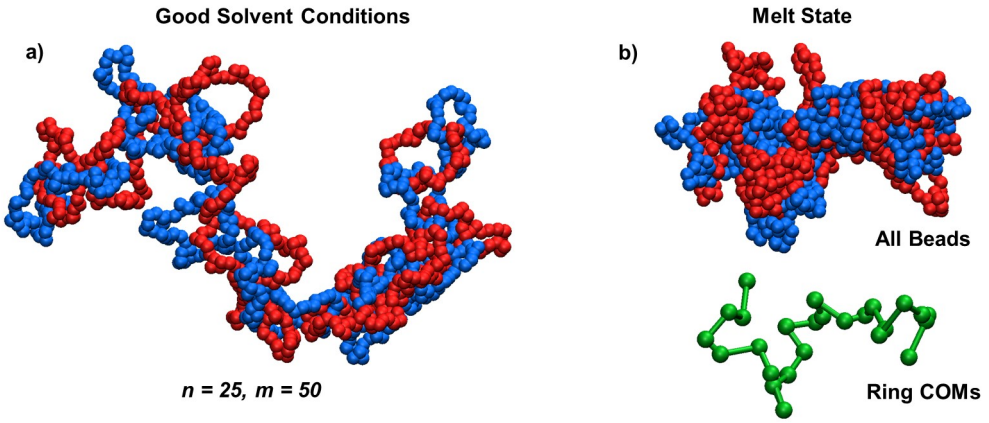

Figure 5.8: Visualizations of poly[n]catenanes with $n = 25$ and $m = 50$ in a) good solvent conditions, and b) the melt state. Alternating rings are colored differently for visual clarity. Also shown in b) are the ring centers-of-mass of the configuration (green) with the mechanical bonds represented by connections between the beads. The structure in the melt state shows several segregated territories, similar to those seen in non-concatenated ring polymers and cellular chromatin.

The single chain structure factor is calculated according to Eq. 5.4, except all pairs of beads on the same catenane (or linear chain) are included in the sum, and the average is taken over all chains in the system. For traditional linear polymers, the structure factors exhibit a large intermediate region where $S(k) \sim k^{-2}$ since polymers are statistically fractal objects, specifically ideal random walks in the melt [87, 159]. At larger k, the structure factor oscillates because of local connectivity constraints at the bead level [44]. Meanwhile, for ring polymers, an additional region of $S(k) \sim k^{-3}$ has been observed at low-k for high-MW melts corresponding to a collapsed globule structure at large length scales [59, 237].

For poly[n]catenanes, several distinct regions are observed, although they are narrow in wavevector range and therefore not well-developed, as shown in Figure 5.9. At low-k, the polymers exhibit a Guinier regime, as expected. At higher-k, a regime of ideal statistics with $S(k) \sim k^{-2}$ is expected for large n since the polymers are linear-like at large length scales, as previously discussed. However, no such regime is easily distinguished in the structure factor. To more closely examine the behavior, it is helpful to study the differential apparent fractal dimension, defined as:

$$d_f = -\frac{d \log S(k)}{d \log k} \tag{5.7}$$

These functions are shown in Figure 5.10 for various systems. In the low-k range ($\sim$ 0.1 - 0.5), the fractal dimensions exhibit a small shoulder in the neighborhood of $d_f = 2$, which slowly grows towards a quasi-plateau as n is increased. Its value is consistent with Gaussian chain statistics, and the smallness of the regime suggests that the largest poly[n]catenanes are only just beginning to display ideal chain behavior.

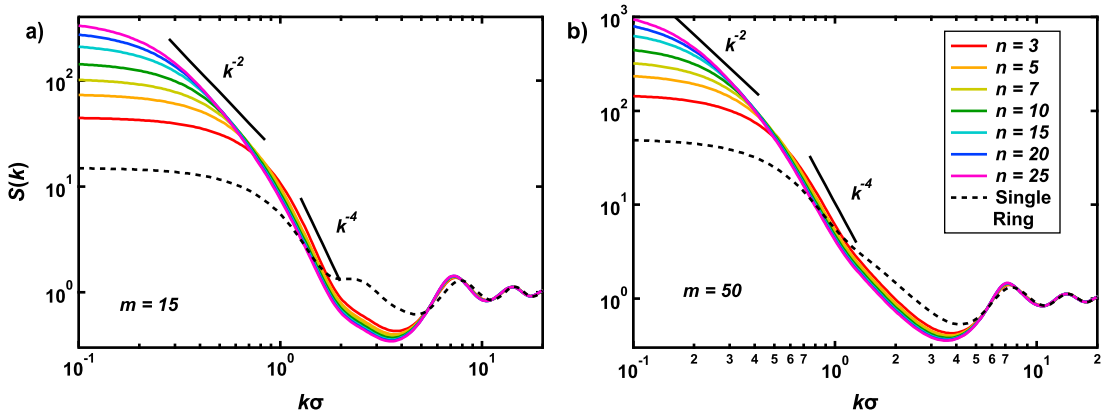

Figure 5.9: Single-chain structure factor for poly[n]catenanes of various n and a) $m = 15$, or b) $m = 50$. The dashed black curves show the single-ring structure factor for poly[n]catenane chain centers (cf. Figure 5.4a). The legend in b) applies to both graphs.

Next a small apparent regime of $S(k) \sim k^{-4}$ is observed at intermediate k-values. This Porod-like behavior is typically associated with scattering from interfaces and other systems with density inhomogeneities. As we have pointed out above, poly[n]catenanes form segre-

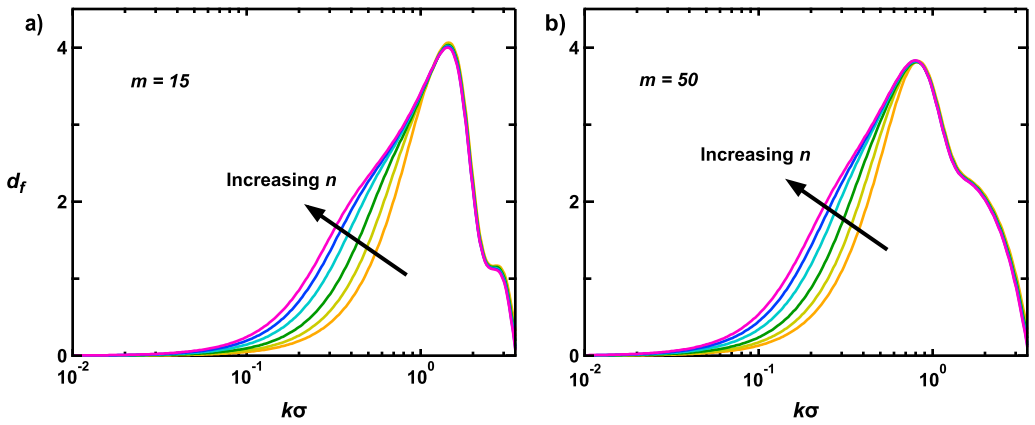

Figure 5.10: Differential fractal dimension for poly[n]catenanes of various n and a) $m = 15$, or b) $m = 50$. At low k-values $(0.1 - 0.5)$, a small plateau develops in the neighborhood of $d_f = 2$, suggesting a slow approach towards ideal chain statistics.

gated territories in the melt (Figure 5.8b) and the scattering from these regions (and their boundaries) may explain this regime. This will be discussed further below.

At even higher k-values a third regime is observed with a power-law slope that depends on m, with smaller rings showing "flatter" curves in this region. This feature appears as a small shoulder in the differential fractal dimension, with the value of d_f depending strongly on m. For $m = 15$, this "shoulder" is actually a small peak. These features are strikingly similar to the signatures of the mechanical bond in the single-ring structure factor discussed in Section 4. In fact, both these features appear at the same k-values (see Figure 5.9), suggesting that they are the same phenomenon manifested in two different scattering functions. After this regime, the structure factor is dominated by local bead connectivity constraints.

To separate out the chain and ring structural contributions, the single polymer total intramolecular structure factor is computed at the coarse-grained level, considering only the macrocycle centers-of-mass as the scattering bodies. This function is compared to the full chain structure factor in Figure 5.11. At the coarsened resolution, the polymers are nearly ideal, and the structure factors agree quantitatively with the full structure factor at large length scales (low-k). However, most of the features in the higher-k regions are absent,

indicating that all of these more unusual phenomena are intimately related to the underling structure of the rings. At high-k, the structure factor does oscillate very slightly (owing to the macrocycle connectivity), but this effect is very small and decays quickly.

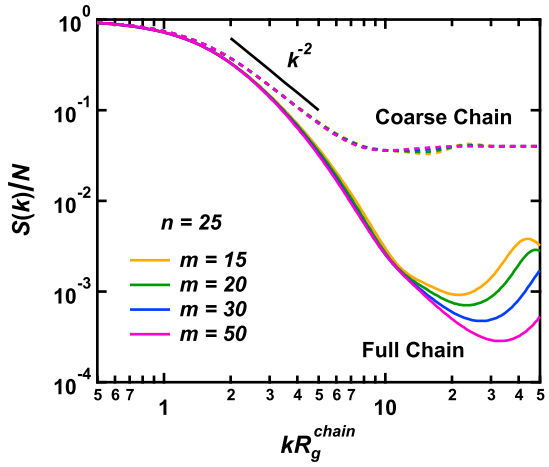

Figure 5.11: Single chain structure factor for poly[n]catenanes of various m at the coarse level compared with the fully detailed level.

Although the high-k regime can be easily interpreted as single-ring structure, the intermediate $S(k) \sim k^{-4}$ regime is quite unusual. Such scaling exponents are more typical of phase-separated systems in which the interface contributes strongly to the scattering [238–240]. However, the poly[n]catenanes considered here are neutral homopolymers, so there can be no phase separation in the ordinary sense. Nevertheless, such scaling implies density inhomogeneities along the chain, which are clearly visible in Figure 5.8b in the form of ring segments protruding from a globular-like core. To quantity these inhomogeneities, the average single-chain bead density is calculated as a function of the contour position using the following procedure. The ring center-of-mass positions of a given polymer are interpolated by a cubic spline function and twenty equidistant points are placed between each center-of-mass. The local density of a single chain at a given point is then determined by the number of beads (in the same catenane) within a given distance of the point. Because each polymer is considered individually and only the single-chain densities are calculated, the resulting

values may differ from the overall system density. To resolve differences in density at the appropriate length scales, the cutoff distance is taken to be one-half the radius-of-gyration of the chain-center macrocycles ($R_{g,r}$); other choices are also possible but give qualitatively similar results so long as the cutoff is not too large. These data are averaged over all polymers in the melt and multiple configurations for improved statistics. The resulting density profiles (denoted ρ_c) are shown as a function of contour position (denoted s) in Figure 5.12 for poly[n]catenanes with $n = 10$ and various m. For all m, these profiles show small but clear oscillations with a period of one mechanical bond in the chain contour space, indicating a "beads-on-a-string" structure. Interestingly, the maxima of the density occur at half-integer values of s, indicating that the highest densities are found at the "linked portion" of the macrocycles [54]. For the smallest rings, there is a smaller maximum found at whole integer values of s, which is likely caused by the threading segments being forced close to the ring center-of-mass by the small ring size; for larger m, this feature disappears. Different values of n yield quantitatively similar results. The length scale of the density oscillations in real space will be dominated by the separation of nearest-neighbor high-density regions. Since this separation is one mechanical bond in chain contour space, the separation in real space should be related to the mechanical bond length, b_c, and should therefore vary with m. If these oscillations cause the k^{-4} scaling in the structure factor, then the length scale of interest is determined by the position of the maximum in the differential fractal dimension: $d = 2\pi/k_{\max}$. As expected, these length scales do in fact increase with m, and although they are considerably larger than the bond lengths, b_c, the ratio $d/b_c \approx 2.28$ is fairly constant for all ring sizes. These observations suggest that the unusually fast decay in the single-chain structure factor is related to the density variations associated with the linked portions of the macrocycles. Nevertheless, the quantitative differences in bond length and Porod-like length scales demand further study to better understand the territorial segregation observed in these polymers. In particular, it is not clear why the length scale d is so large - even larger

than b_{eff} - so it is possible that there are multiple length scales associated with the density fluctuations in the polymers.

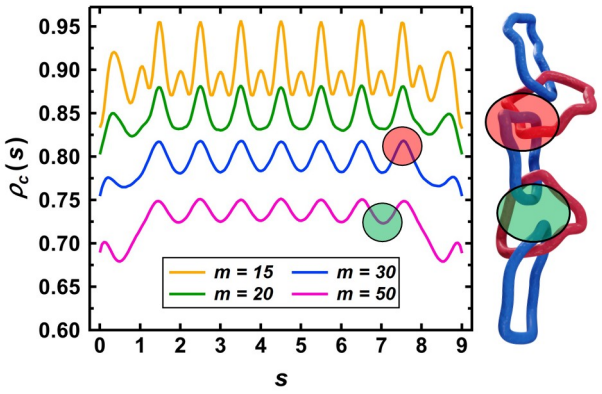

Figure 5.12: Single-chain density as a function of chain contour position for poly[n]catenanes of $n = 10$ and various m and companion illustration. See main text for details of the calculation. The maxima occur at approximately half-integer values of s, which correspond to the linked portions of the rings (red shaded areas), while the minima correspond to the chain centers (green shaded areas). For $m = 15$, the smaller maxima are caused by the close interaction of linked segments of next-nearest neighbor rings.

5.6 Intermolecular Structure

In the melt, high-MW linear and ring polymers interact strongly with neighboring chains, and these interactions can greatly affect both structure and dynamics. In particular, the inter-polymer packing correlations are a functional of polymer conformation via the intra-molecular structure factor examined in the previous section and the two functions are self-consistently coupled. Given the unusual intra-molecular correlations studied earlier, it is expected that inter-molecular structure may also show signatures of the complex poly[n]catenane architecture. A key quantity is the intermolecular site-site correlation function, $g(r)$. Results are shown in Figure 5.13 for catenanes of $n = 25$ and various ring sizes. Like linear polymers, a pronounced correlation hole effect [159] is observed which is nearly independent of ring size. For large n, the correlated part of $g(r)$ (defined as $h(r) = g(r) - 1$)) exhibits an

exponential decay beyond very local length scales (Figure 5.13 inset), with a decay length of order the chain R_g. This feature is qualitatively the same as for melts of random coil chains, however the form of the correlation is for those systems is Yukawa, $h(r) \sim (1/r)\exp(-r/R_g)$. For a fixed value of m, the depth/width of the correlation hole increases with n as expected, as shown in Figure 5.14. However, when normalized by R_g, the width of the correlation hole actually decreases with n (Figure 5.14b inset), indicating that larger poly[n]catenanes exclude each other less strongly, similar to linear polymers (Figure 5.14a).

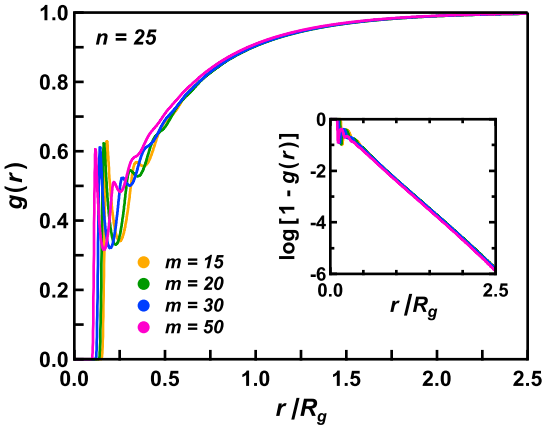

Figure 5.13: Intermolecular bead-bead correlation function for poly[n]catenanes of various m. Normalizing the distances by the polymer R_g results in collapse to a master curve for a given n. Inset: the logarithm of the non-random part of the correlation function. The linear dependence indicates exponential decay.

The dynamics of a tagged polymer in a dense liquid are often intimately related to the number of neighboring polymers it interacts with; this is true for linear chains, and ring polymers [59], and is likely important for other complex architectures. Here, the number of neighbors, n_p, is calculated using both a direct and indirect method, which reveal different aspects of the interpenetrating melt structure. In the direct method, the intermolecular pair correlation function of the poly[n]catenane centers-of-mass is calculated and then integrated to a separation of R_g [59]. In the indirect method, the intermolecular site-site correlation function, $g(r)$, is integrated to R_g and then divided by N [237]. The direct method focuses

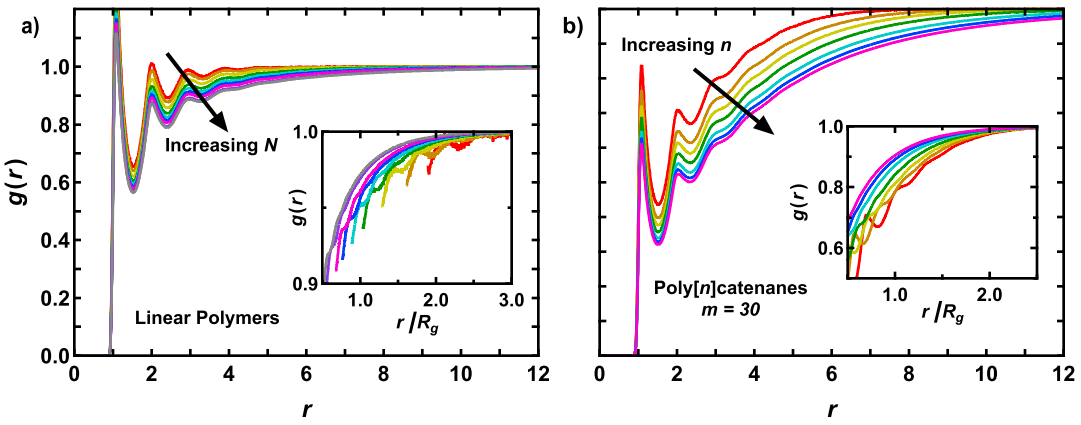

Figure 5.14: Intermolecular bead-bead correlation function for a) linear polymers of variable N, and b) poly[n]catenanes of $m = 30$ and variable n. The depth and width of the correlation hole effect increases with n and N, although the size of the effect is much larger for poly[n]catenanes. Inset: the same data with distance normalized by polymer R_g. For clarity, only the data beyond the third solvation shell is displayed in the inset of a). The two systems are qualitatively similar, suggesting that poly[n]catenanes are comparable to linear polymers at long length scales.

on a coordination number at a coarse grained center-of-mass level in the spirit of polymers as soft particles, while the indirect method is the more local bead level analog. The results are shown in Figure 5.15. For linear polymers, the two methods give similar numerical values (Figure 5.15a) which scale nearly ideally with degree of polymerization, $n_p \sim N^{1/2}$. On the other hand, unlinked ring polymers have far fewer neighbors than linear chains and the two methods disagree significantly, with the direct method giving values more than an order of magnitude smaller than the indirect one for small N. The small values of the direct method indicate that ring centers-of-mass cannot easily approach each other, while the larger values based on the indirect method reflect bead-bead contacts in the surface region of two partially overlapping macromolecules. This interpretation is supported by previous simulation results [59, 237]. For poly[n]catenanes (Figure 5.15b), the indirect method yields $n_p \sim n^{1/2}$, as expected for ideal polymers. The quantitative values increase with increasing m, suggesting that larger rings allow for more interpenetration and more neighbors. However, for small n, the direct method gives values that are several orders of magnitude smaller, indicating

that poly[n]catenane centers-of-mass cannot easily approach each other. The values do increase for larger m, but are still far smaller than those of the indirect method. These results are qualitatively similar to those of unlinked ring polymers, indicating that short poly[n]catenanes primarily interact with their neighbors at the surface of the polymers and interpenetrate each other only weakly, consistent with the globular conformations at small n. At larger values of n, the results of the two methods approach each other, indicating a transition to more ideal chain behavior. For the KG model considered here, the entanglement length for linear chains is approximately $N_e \approx 85$ [47], at which point $n_p \approx 4$; this value is considerably larger than that of the longest poly[n]catenanes studied here, which have $n_p < 2$. As a result, it is unlikely that poly[n]catenanes of this length will be able to entangle in a meaningful way. Of course, the specific values reported in Figure 5.15 could be altered by adjusting the integration cut off for the two methods, but the same general trends are observed.

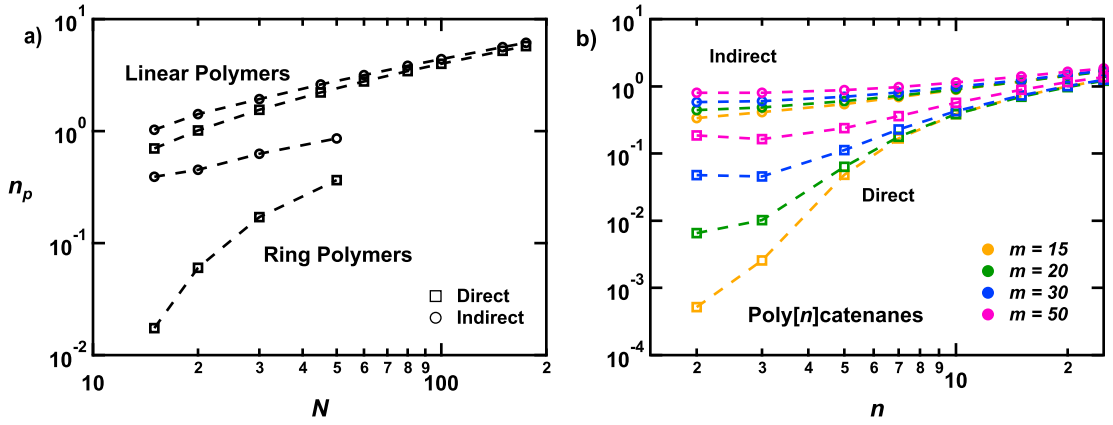

Figure 5.15: Average number of neighboring chains as calculated by the direct and indirect methods (see main text) for a) linear and ring polymers as a function of N, and b) poly[n]catenanes of various m as a function of n. Note that the scale bars for the two graphs are different – the poly[n]catenane values vary over a much larger range and are generally smaller than those of linear polymers.

The density profiles of individual rings as a function of their distance from the overall polymer center of mass, also known as the self-density, also provides information on polymer

structure and interpenetration. The results for the smallest and largest poly[n]catenanes are shown in Figure 5.16 along with data for linear and ring polymers for comparison. For poly[n]catenanes with small rings, the profile shows distinct peaks/humps, which likely arise because of conformational restrictions imposed by the fluid structure, i.e. the molecules are small enough that the solvation shells still influence the structure significantly; these features disappear as the molecular weights (and therefore polymer sizes) increase. For all ring sizes, as n increases, the density profiles become broader and the density at $r = 0$ decreases, indicating improved chain interpenetration. In general, the self-densities near $r = 0$ tend to be larger for poly[n]catenanes and ring polymers compared to linear chains. For ideal linear polymers, the self-density in this limit scales as $N^{-1/2}$, per the correlation hole effect. Figure 5.17a shows these data as a function of N for linear and ring polymers. The linear polymers obey ideal scaling while the self-density of ring polymers is nearly independent of N, in agreement with previous simulations [59]. The same data for poly[n]catenanes are displayed in Figure 5.17b, which shows two distinct regimes. At small n, the self-density at the origin is nearly constant and quite large (note the total density is 0.85), similar to the behavior of ring polymers. In this region, the polymers strongly exclude their neighbors due to their globular shape and interpenetration is limited. As n increases, the self-density then begins to decay according to the ideal scaling law $\sim n^{1/2}$, similar to linear polymers. The two regimes are quite sharply separated at $n = 10$, suggesting that there is a critical threshold above which poly[n]catenanes cross over from a globule-like conformation to an ideal chain conformation, although no such sharp transition is observed in the single-chain conformational properties (Section 5).

Finally, we consider the question of interchain entanglement of the polymers, which has important implications for the dynamics of these systems. For linear polymers, entanglements may be defined, identified, and quantified in many ways [45–54]. However, these methods cannot be directly applied to poly[n]catenanes since these polymers do not have

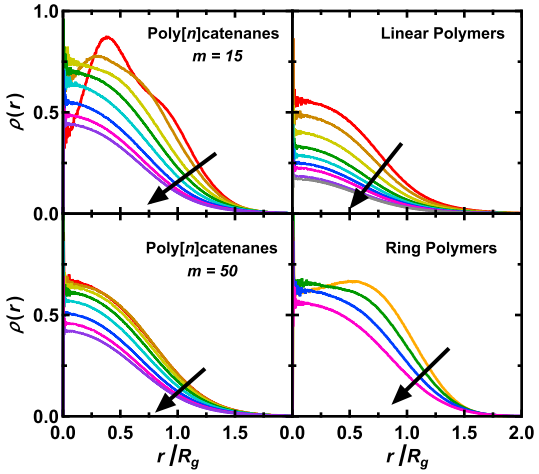

Figure 5.16: Single-chain bead density profiles as a function of distance from polymer center of mass for poly[n]catenanes with various m and $n = 2 - 25$ (left), compared with profiles for linear polymers of $N = 15 - 175$ and ring polymers of $N = 15 - 50$ (right). The arrows indicate increasing molecular weight (n or N).

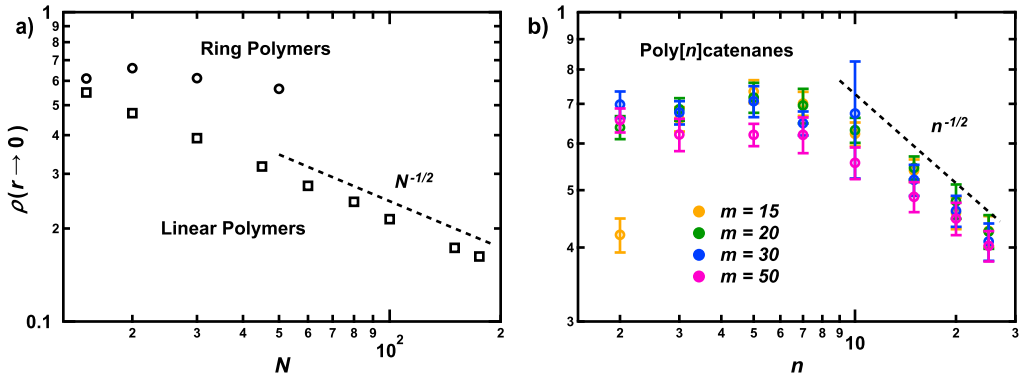

Figure 5.17: The single chain bead density at the polymer center of mass (also known as the self-density) for a) linear and ring polymers as a function of N and b) poly[n]catenanes of various m as a function of n. The dashed lines indicate the ideal linear polymer scaling laws. The error bars for the linear and ring polymer data are approximately the size of the data points and are therefore omitted for clarity. The wayward data point at $n = 2$ for $m = 15$ in b) is caused by local bead packing effects.

continuous (covalent) contours. Furthermore, any attempt to generate an equivalent linear polymer from a poly[n]catenane would necessarily lose information concerning local ring conformations. To keep the analysis simple, an estimate for the number of rings between

entanglements, n_e, is calculated using the overlap parameter:

$$O = \frac{\rho R_e^3}{N} = \frac{\rho (n b_{\text{eff}}^2)^{3/2}}{nm} = \frac{\rho n^{1/2} b_{\text{eff}}^3}{m} \tag{5.8}$$

Linear polymers typically become entangled when $O \approx 10 - 20$; for instance, the linear polymers systems studied here have $N_e \approx 85$, which corresponds to $O \approx 18$. Therefore, n_e is estimated conservatively by setting $O = 10$ in Eq. 5.8 and solving for n. Of course, this analysis is highly simplified, as Eq. 5.8 is empirical and generally not applicable for cyclic or topologically complex polymers. Nevertheless, it provides a useful starting point for studying the entanglement properties of these polymers as their overall architecture is linear at long length scales and inter-chain entanglement is fundamentally a large-length scale phenomenon. The results of the calculation are shown in Table 5.2. The values are all roughly $n_e \approx 45$, independent of m, and much larger than the longest chains studied ($n = 25$). The large estimates of n_e agree well with the earlier observation that these polymers and their rings do not interpenetrate each other strongly. The lack of dependence on m is somewhat unexpected since an idealized poly[n]catenane would have an effective bond length proportional to ring size $b_{\text{eff}} \sim m^{1/2}$ and therefore $n_e \sim m^{-1}$ by Eq. 5.8. However, as discussed previously, the effective bond lengths grow slowly with m, leading to greater relative flexibility and therefore modifying the scaling of n_e with ring size. Based on these results, interchain entanglement should not affect the dynamics of the poly[n]catenanes studied here, which will be discussed in the next chapter.

5.7 Conclusions

In this chapter, the static properties of poly[n]catenane melts have been systematically studied by molecular dynamics simulations and the key features that distinguish these unusual polymers from their linear (and cyclic) counterparts identified. The mechanical bonds signif-

icantly perturb the thermodynamics of the system, with large deviations in pressure observed as a consequence of the topological attraction between linked rings. These same mechanical bonds alter the conformations of the rings within catenanes and lead to nontrivial scaling with ring size. The polymers possess complicated intramolecular scattering functions which exhibit many more features than linear polymers, including unusual scaling relationships which can be attributed to density inhomogeneities along the poly[n]catenane chain contour arising from the mechanical bonds and intermolecular topological effects. For relatively small degrees of polymerization, the poly[n]catenanes are highly globular and interact with their neighbors only at the surface of the polymer. As the number of rings is increased, the conformations of poly[n]catenanes begin to resemble those of ideal chains with the number of neighboring chains following the expected scaling.

For the current synthetically-accessible chain lengths studied here ($n < 25$), there is no indication that inter-chain entanglement plays a significant role. In fact, the large n_e values of poly[n]catenanes may explain some of the properties observed experimentally [19]. In particular, these polymers form powders, while chemically similar linear polymers of comparable molecular weight can be processed into stable films. This difference may be caused by the intermolecular interactions: these molecules contain many rigid aromatic groups (necessary for the metal-templating synthesis), which can result in pervasive $\pi - \pi$ stacking interactions between the polymers. Such interactions are probably somewhat inhibited by the interlocking structure, reducing the cohesive energy density. However, based on the results presented here, interchain entanglement is likely also a factor. Since linear polymers entangle at much lower molecular weights than poly[n]catenanes, the stable films obtained experimentally from linear polymers of similar chemistries are likely entangled, improving stability below the glass transition temperature. Experimental linear poly[n]catenanes prepared to date have average degrees of polymerization (n) of 10-15, far too small to entangle according to our simulations, which suggest that at least an n of 45 is required in order to access poly[n]catenane materi-

als suitable for rheological testing. Note, however, that the model poly[n]catenanes studied here are composed of fully flexible segments with no complex chemical motifs present, so the results here may not be immediately applicable to synthetically-realizable systems. More generally, the results presented here suggest that macrocycle size is a key design parameter for poly[n]catenane systems. The ring size not only influences the polymer contour length, but also alters its flexibility and may enhance or inhibit interchain entanglement at large n. More interestingly, catenanes are typically stimuli-responsive moieties, with dynamical motions that may be switched on or off by the appropriate stimulus [14], and poly[n]catenanes are no exception [19]. The ring size will control the length scale associated with such switching behavior and how its effects are propagated along the chain.

CHAPTER 6

DYNAMICS OF POLY[*N*]CATENANE MELTS

6.1 Introduction

As discussed in the Introduction, the dynamics of mechanically interlocking polymers such as poly[n]catenanes have been only sparingly studied. In Chapter 3 [222], we sought to address this gap using molecular simulations of isolated poly[n]catenanes, quantifying and analyzing the dynamics in terms of the Rouse modes [169]. It was found that at length scales comparable to the size of the mechanical bond, the dynamics are significantly slowed and the distributions of relaxation times are broadened; these same effects have been observed in entangled linear polymers but at long length scales [170], suggesting an analogy with respect to kinetic/topological constraints. Although intriguing, this initial investigation was conducted on isolated molecules with no solvent effects or intermolecular interactions. Just as the dynamics of linear polymers are much different in the melt compared to dilute solution, poly[n]catenane dynamics are also expected to be significantly influenced by the presence of neighboring molecules in the melt.

In this chapter, we expand our study of poly[n]catenane dynamics into the melt state. To begin, a minimal Rouse-like model of poly[n]catenane dynamics is presented along with the key insights found from its analytical solution; this simple model defines "ideal" poly[n]-catenane dynamics to which simulation results can be compared. The diffusive properties of poly[n]catenanes and their segments/monomers are examined along with the relaxation times of both the constituent rings and the overall chain at various length scales; linear and ring polymer melts are also examined for comparison. While the simplified Rouse model does produce some qualitative agreement with simulation results, there are a number of important failures, which can most likely be attributed to topological and/or intermolecular effects. These effects also become important in the stress relaxation behavior, which shows

unusual trends as the ring size changes. Directions for future research and implications for materials synthesis and design are offered in the concluding remarks. The systems studied are exactly those of Chapter 5; simulation details can be found in Sections 5.2 and A.2.

6.2 Double-Rouse Model for Poly[n]catenanes

In search for an "ideal" model for poly[n]catenane melts, the Rouse model [169] serves as a natural starting point. Any such model makes several simplifications: (i) the conformational statistics of the molecules are assumed to be ideal/Gaussian, (ii) it is assumed that the intermolecular forces on different beads on the same polymer are spatially uncorrelated, which corresponds to the elementary friction constant being the same on all length scales or for all Rouse modes, (iii) there is no viscoelastic memory associated with intermolecular forces corresponding to delta-function in time correlations of intermolecular forces and white noise fluctuating forces, (iv) the motion of the polymer CM is independent of the internal polymer relaxations, (v) excluded volume and topological contributions are absent along with all non-bonded contributions to the stress, (vi) the motions of different chains within the melt are independent, so the single-chain results can be directly translated to the melt by summing up the contributions of each polymer independently. Despite these simplifications, the Rouse model succeeds fairly well in describing the dynamics of unentangled linear and ring polymer melts [13, 174], and therefore remains a common lens through which polymer systems are examined. Additionally, the model can be easily extended to arbitrary polymer architectures, making it a useful starting point for studying poly[n]catenane dynamics, especially since the polymers simulated here are not long enough to exhibit interchain entanglement [224] and therefore should not obey reptation-type dynamics. Mathematical details of the Rouse model for general polymer architectures are reviewed in Appendix A.4 and were also discussed at a high level in Section 3.3.

A Rouse-like model for poly[n]catenanes must consider two levels of polymer structure:

the cyclic structure of the macrocycles and the linear structure of the overall chain. To do so, each macrocycle is modeled as a Rouse ring polymer of m beads [174, 217, 241]. To introduce mechanical bonds in as simple a manner as possible, the centers-of-mass of n such rings are connected in series by additional harmonic bonds of mean-squared length b^2, maintaining an overall linear architecture. Conceptually, the model couples two different versions of the Rouse theory and is therefore termed the "double-Rouse" model; the model is illustrated schematically in Figure 6.1 along with a visualization of a poly[n]catenane from a simulation trajectory. The three parameters n, m, and b^2 control dynamics; other parameters such as temperature and friction constant only shift the time scale of the dynamics in a Rouse mode-independent manner. In reality, the parameters m and b^2 are not truly independent, since the mechanical bond length will depend on the ring size; intuitively, the bond length should be on the order of the macrocycle dimensions and therefore scales with m in a manner similar to the radius of gyration of the ring: $b \sim R_{g,r} \sim m^{\nu}$, where ν is the scaling exponent of the ring. The real situation is more subtle [224], but this approximation will suffice for determining scaling relationships in poly[n]catenane systems.

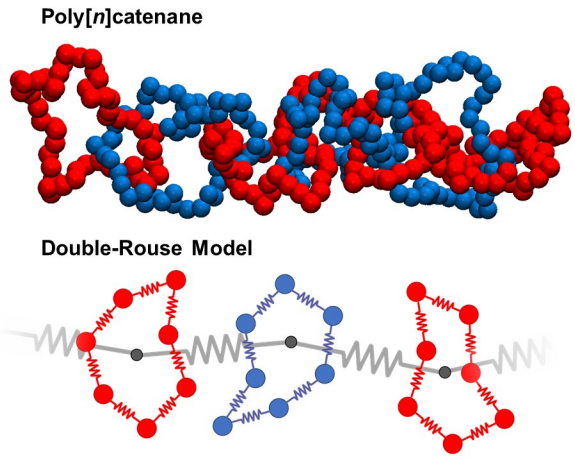

Figure 6.1: Visualization of a poly[n]catenane with $n = 7$ rings of $m = 50$ beads each and a cartoon illustration of the double-Rouse model ($n \geq 3$, $m = 7$). Alternating macrocycles are colored differently to more easily observe the interlocking structure.

The double-Rouse model is formulated in more detail and solved exactly in the Sec-

tion A.5. However, the qualitative features of the model may be understood intuitively: the solution is a direct superposition of the ring and linear Rouse models. More specifically, there are two distinct sets of normal modes: ring-like and linear-like. The ring-like modes, denoted $\boldsymbol{X}_q$, are identical in form to those of ordinary ring polymers and an independent set of these modes exists for each of the n macrocycles. The linear-like modes, denoted $\boldsymbol{X}_p$, are identical to the normal modes for traditional linear polymers, but with the macrocycle centers-of-mass taken as "effective" monomers. For the systems simulated here, both sets of modes are orthogonal to a good approximation (see Section A.6). Throughout the remainder of the chapter, ring-like modes and dynamical quantities will appear with a subscript q, while linear-like ones will appear with a subscript p. This same decomposition into "ring-like" and "chain-like" modes was introduced in an ad hoc manner in Chapter 3. As a result of this superposition, the double-Rouse model predicts that the melt dynamics will be separable into ring-like and chain-like contributions. Furthermore, the diffusion coefficient is expected to scale as $D \sim 1/(nm)$, i.e. inversely proportional to the total number of beads. However, this model neglects the complex topological character of the mechanical bonds and these complexities affect both structure and dynamics at intermediate length/time scales,as demonstrated in Chapters 3 and 5, so significant deviations from the double-Rouse model are expected in the simulation data in these regimes. Indeed, physical insight can be gained by examining the manner in which the simulated dynamics differ from the predicted ones in poly[n]catenane systems.

6.3 Monomer and Polymer Motion

The dynamics of polymer melts can be quantified by the mean-squared displacements (MSDs) of monomers and polymer centers-of-mass (CM). For linear [23, 44] and ring [61, 64, 76, 176]

polymers, three distinct measures are typically used:

$$g_1(t) = \left\langle [\boldsymbol{R}_i(t) - \boldsymbol{R}_i(0)]^2 \right\rangle \tag{6.1}$$

$$g_2(t) = \left\langle [(\boldsymbol{R}_i(t) - \boldsymbol{R}_{\rm cm}(t)) - (\boldsymbol{R}_i(0) - \boldsymbol{R}_{\rm cm}(0))]^2 \right\rangle \tag{6.2}$$

$$g_3(t) = \left\langle [\boldsymbol{R}_{\rm cm}(t) - \boldsymbol{R}_{\rm cm}(0)]^2 \right\rangle \tag{6.3}$$

where $\boldsymbol{R}_i$ is the position of monomer i in the polymer, $\boldsymbol{R}_{\rm cm}$ is the position of the polymer CM, and the angled brackets indicate an average over all initial conditions (i.e. an ensemble average). For linear polymers (and poly[n]catenanes), the average is also evaluated over all chains in the system and over a small number of beads near the chain center to improve statistics and reduce chain end effects. For ring polymers, the average may be taken over all beads in the system as there are no chain ends and all beads are physically equivalent. These three quantities represent the MSD of the monomers (Eq. 6.1), the polymer CM (Eq. 6.3), and the monomers relative to the polymer CM (Eq. 6.2). In all cases, the displacement of the system CM is subtracted out.

In general, the polymer CM can undergo sub-diffusion in many macromolecular systems, depending on architecture and molecular weight. For unentangled linear melts, the Rouse model predicts ordinary diffusive behavior $g_3(t) \sim t^1$ at all time scales with a diffusion coefficient, D, that is inversely proportional to N, as mentioned in the previous section. However, the correlation hole effect [159] leads to an early-time regime of $g_3(t) \sim t^{0.75-0.8}$ before ordinary diffusive motion sets in [242–245]. For entangled linear chains, stronger sub-diffusion is observed, with a scaling of $g_3(t) \sim t^{1/2}$ at intermediate timescales before Fickian diffusion is recovered at long times [13, 25]. In this case, the long-time diffusion constant scales as $D \sim N^{-2.3}$ [246]. High-MW ring polymer melts appear to exhibit similar correlation hole effects [61, 64, 77, 247, 248] and scaling of the diffusion constant [61, 62, 64, 249, 250], but limited data are available due to the computational cost of simulating such

systems, so the situation is not yet entirely clear.

The center-of-mass diffusion of poly[n]catenanes resembles closely that of unentangled linear polymers. Figure 6.2a shows the quantity $n \times g_3(t)$ for poly[n]catenanes of $m = 30$ and various n. At long times, these curves should converge if Rouse-like dynamics are obeyed, which is indeed the case, with only small differences associated with different chain lengths. At short to intermediate time scales, there is a regime of $g_3(t) \sim t^{0.7-0.8}$, observed for all catenanes, which agrees well with the correlation hole effect discussed above. In the previous chapter on static properties, it was found that poly[n]catenanes are highly globular polymers at small n and strongly repel their neighbors [224], so significant correlation hole effects are indeed expected in the dynamics. For all systems (linear, ring, and poly[n]catenanes), free diffusion ($g_3(t) \sim t^1$) sets in at displacements considerably smaller than the polymer size: $g_3(t) \approx R_g^2/2$.

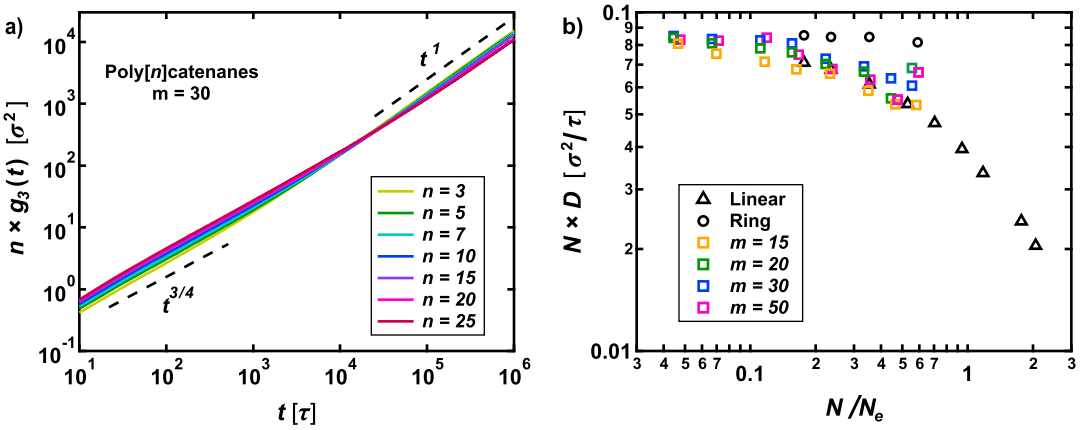

Figure 6.2: a) The center-of-mass mean-squared displacement, $g_3(t)$, multiplied by the number of rings, n, for poly[n]catenanes of $m = 30$ as a function of time, t. Terms in brackets are the units of measurement. b) Diffusion constants, D, multiplied by total molecular weight, N, for ring polymers (circles), linear polymers (triangles) and poly[n]catenanes (squares) of various m as a function of total molecular weight scaled by estimated entanglement molecular weight, N_e ($\approx 45m$ for poly[n]catenanes, ≈ 85 for linear and ring polymers [47]). 95% confidence intervals are at most twice the size of the data points.

Interestingly, at intermediate times, the curves in Figure 6.2a cross over one another, with larger polymers showing larger values of $ng_3(t)$ at short times, but smaller ones at long

times. Halverson *et al.*[64] observed this same feature in ring polymer melts, and described it as a distinctive feature of those systems. However, the linear polymer melts studied here also exhibit this phenomenon (data not shown), albeit at significantly shorter times than in the ring and catenane systems. Since Halverson *et al.* only studied diffusive motion on timescales longer than $10^3\tau$, it is possible that this crossover simply occurred at an earlier time. Based on the data gathered here, it seems that this crossover may be found in many polymer systems, although the associated timescale appears to be architecture specific.

The long-time diffusion constants, scaled by molecular weight, $N \times D$, are shown in Figure 6.2b for all systems studied, including ring and linear polymers. To compare the data on equal footing, the total molecular weight is normalized by the estimated entanglement molecular weight. For ring/linear polymers, the literature value $N_e = 85$ is used [47]. For poly[n]catenanes, it is assumed that all entanglement occurs at the interchain level, so that $N_e = m \times n_e$ and the estimates for n_e are taken from the prior work on their static properties (see previous chapter), which found that $n_e \approx 45$ for all m [224]. While the quantity ND is relatively constant for ring polymers (for the range of ring sizes considered here), it has a clear dependence on N/N_e for poly[n]catenanes and linear polymers, with larger polymers exhibiting relatively slower diffusion, i.e. larger center-of-mass friction. These changes in friction represent deviations from the double-Rouse model, and since all linear and poly[n]catenane data collapse onto a single curve, it seems likely that these effects have the same physical origin in both systems: interchain interactions. Although these deviations are quite large for the longest linear chains studied, for which $N > 2N_e$, the poly[n]catenane systems are clearly far less affected by entanglements, with ND decreasing by only about $\sim 30\%$ at most, and $N < 0.6N_e$. This conclusion was also demonstrated by an analysis of the chain overlap parameter in the prior work on structural properties [224].

The MSDs of individual monomers describe the internal dynamics of polymers at short time and length scales. For instance, the monomer displacement, $g_1(t)$, exhibits sub-diffusive

behavior at intermediate timescales for both linear and ring polymers with the Rouse model predicting $g_1(t) \sim t^{1/2}$ at times between the segmental and terminal relaxation times for unentangled systems. The reptation model predicts multiple sub-diffusive regimes for entangled linear polymers, most notably $g_1(t) \sim t^{1/4}$ at time scales beyond the entanglement time, prior to which Rouse-like dynamics are observed [25]. A similar scaling regime has also been observed in high-MW ring polymer melts [64, 249]. For both linear and ring systems, $g_2(t)$ typically follows the same scaling as g_1 at short times, although for entangled linear chains it disagrees at longer time scales [23, 25]. However, for all systems, $g_2(t)$ eventually becomes constant at a value proportional to the mean squared radius of gyration of the polymer.

Since poly[n]catenanes have a complex internal structure, additional measures of monomer motion beyond Eqs. 6.1 and 6.2 are needed to study the dynamics fully and more appropriately compare the results with linear/ring polymer systems. The following quantities are defined for this purpose:

$$g_4(t) = \left\langle [(\boldsymbol{R}_i(t) - \boldsymbol{R}^r_{\rm cm}(t)) - (\boldsymbol{R}_i(0) - \boldsymbol{R}^r_{\rm cm}(0))]^2 \right\rangle \tag{6.4}$$

$$g_5(t) = \left\langle [\boldsymbol{R}^r_{\rm cm}(t) - \boldsymbol{R}^r_{\rm cm}(0)]^2 \right\rangle \tag{6.5}$$

$$g_6(t) = \left\langle [(\boldsymbol{R}^r_{\rm cm}(t) - \boldsymbol{R}_{\rm cm}(t)) - (\boldsymbol{R}^r_{\rm cm}(0) - \boldsymbol{R}_{\rm cm}(0))]^2 \right\rangle \tag{6.6}$$

where $\boldsymbol{R}^r_{\rm cm}$ is the CM of the individual macrocycle which contains monomer i, the average is taken over the central rings in all polymers in the system, and the system center-of-mass motion is subtracted out, as above. These new quantities represent, respectively, the monomer MSD relative to ring CM, the MSD of the ring CM itself, and the MSD of the ring CM relative to polymer CM. The first quantity measures the internal dynamics of the macrocycles while the other two measure large-scale chain-like motion of the polymer. $g_4(t)$, $g_5(t)$, and $g_6(t)$ have no direct counterparts for linear/ring polymers, but it is expected that $g_4(t)$ will be qualitatively similar to the $g_2(t)$ of low-MW ring polymers, and $g_5(t)$ and $g_6(t)$

will be similar to the $g_1(t)$ and $g_2(t)$, respectively, of unentangled linear chains.

To begin, two representative systems are considered: a linear polymer of $N = 80 \approx N_e$, and a large poly[n]catenane with $n = 25$ and $m = 30$, shown in Figures 6.3a and 6.3b, respectively. First, consider the time at which $g_2(t)$ and $g_3(t)$ cross, i.e. when the monomers are effectively moving in concert with the polymer CM; this point can be used to define the transition to free diffusion. For both linear and poly[n]catenane systems, this crossover occurs at displacements comparable to the polymer size, $g_3(t) \approx 0.9R_g^2$, in agreement with previous work [64]. For poly[n]catenanes, the ring CM displacements relative to polymer CM, $g_6(t)$, also crosses $g_3(t)$ at approximately the same position. This result is fully consistent with the observation that poly[n]catenanes and linear polymers have similar structure at large length scales and should therefore exhibit qualitatively similar dynamics [21, 222, 224].

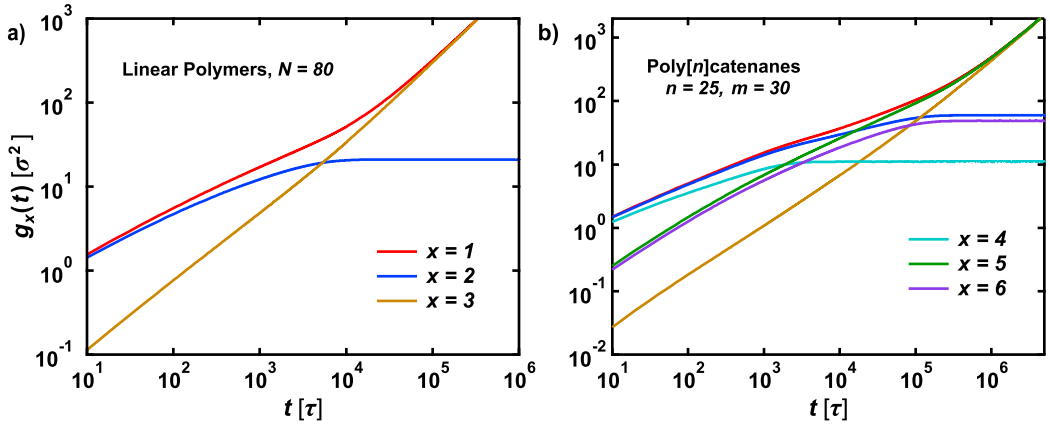

Figure 6.3: Measures of monomer and polymer mean-squared displacements, $g_x(t)$, for $1 \leq x \leq 6$, as defined by Eqs. 6.1-6.6 for (a) linear polymers of $N = 80$, and (b) poly[n]catenanes of $n = 25$, and $m = 30$. Note that the legend in part (a) also applies to part (b).

Next, consider $g_1(t)$ and $g_2(t)$ (red and blue curves in Figure 6.3, respectively) at short times. For both architectures, these displacements obey Rouse scaling at short times, but at longer times $\sim 10^3\tau$, the curves appear to "turn over" and increase more slowly before reaching the terminal diffusive/constant regimes (most easily seen in $g_2(t)$). This behavior is expected for the linear polymer system owing to interchain entanglements but is unusual

for the poly[n]catenanes. Indeed, the previous results on CM diffusion indicated that these poly[n]catenanes are not strongly affected by traditional interchain entanglement, so the sub-Rouse scaling observed in $g_1(t)$ and $g_2(t)$ must have a different physical origin. The same sub-Rouse diffusion behavior is also observed in $g_4(t)$, but is not seen in $g_5(t)$ or $g_6(t)$, which suggests that these trends are associated with the internal dynamics of the rings.

To better resolve the scaling behavior of the various MSDs, the displacements Eqs. 6.1 - 6.6 are written as apparent power laws with time-dependent (or instantaneous) scaling exponents following Nahali and Rosa [251]:

$$g_x(t) \sim t^{\gamma_x(t)} \tag{6.7}$$

for $1 \leq x \leq 6$. The exponents $\gamma_x(t)$ are simply the slopes of the curves in Figure 6.3 and attain constant values in well-defined scaling regimes. At long times, these values always converge to either zero ($x = 2, 4, 6$) or one ($x = 1, 3, 5$). Figure 6.4 shows the exponents for the two systems discussed above. As expected, $\gamma_3(t)$ is less than unity at short times for both architectures and decreases towards a minimum value near $3/4$ before recovering ordinary diffusive scaling, consistent with the earlier analysis of CM motion. For linear polymers, the scaling exponent $\gamma_1(t)$ decreases smoothly to a minimum just below $1/2$ before transitioning to ordinary diffusion, as expected. $\gamma_2(t)$ behaves similarly but the exponent decreases sharply to zero near the longest relaxation time of the chain. As discussed above, $\gamma_5(t)$ in poly[n]catenanes should be qualitatively similar to $\gamma_1(t)$ in linear systems. Indeed, ring CMs in poly[n]catenanes move in a Rouse-like manner: the exponent $\gamma_5(t)$ decreases to a plateau of around $\sim 1/2$ before recovering ordinary diffusion at long times. However, the plateau at $1/2$ is not fully developed (i.e. constant), suggesting that finite-size chain effects are still present. A somewhat similar trend is observed in $\gamma_6(t)$, but only a small shoulder is present in this region before terminal decay.

Certainly, the most remarkable results in Figure 6.4 are the apparent scaling exponents of

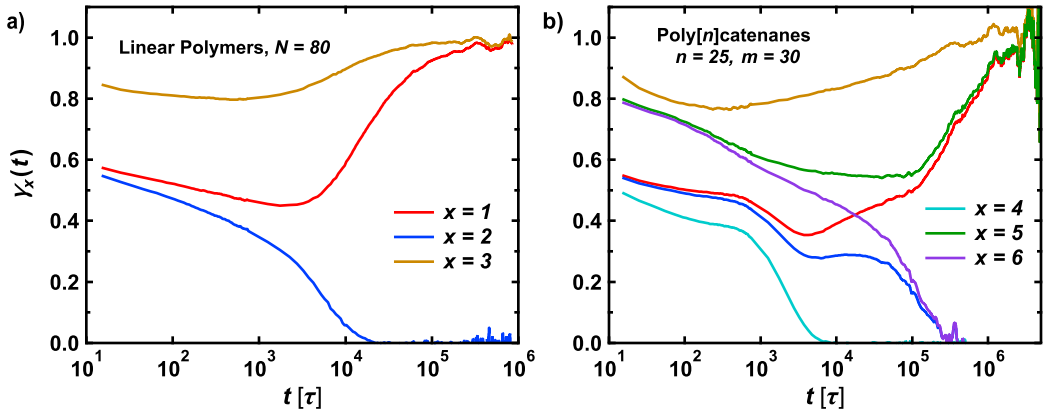

Figure 6.4: Instantaneous scaling exponents, $\gamma_x(t)$, (see Eq. 6.7) for various measures of monomer/polymer motion, $g_x(t)$, $1 \leq x \leq 6$, as defined by Eqs. 6.1-6.6, for a) linear polymer melts of $N = 80$ (unentangled) and b) a large poly[n]catenane of $n = 25$ and $m = 30$. Note that the legend in part a) also applies to part b).

the monomer MSDs ($\gamma_1(t)$ and $\gamma_2(t)$) in poly[n]catenanes: they attain values much smaller than $1/2$, and in some cases, these exponents vary non-monotonically with time. For instance, at short times, $\gamma_1 \approx 1/2$ indicating Rouse-like dynamics, consistent with unentangled ring and linear polymers. However, at around $t \sim 10^3\tau$, the exponent drops sharply, reaching a minimum of around 0.35, then increases to a second "plateau" at around $1/2$ before recovering diffusive behavior at long times. The effects are even more dramatic in $\gamma_2(t)$, which shows extended regions of exponents as small as 0.3; for smaller ring sizes, the local maximum at long times (e.g. at $\sim 2 \times 10^4\tau$ in Figure 6.4) can become quite pronounced.

The two-plateau character of $\gamma_1(t)$ brings to mind the predictions of the double-Rouse model discussed in Section 6.2: the first plateau corresponds to Rouse-like dynamics within the rings while the second corresponds to Rouse-like behavior on the scale of the entire chain (i.e. with the rings as effective monomers). To further demonstrate this, $\gamma_1(t)$ is examined as a function of n and m. Figure 6.5 shows $\gamma_1(t)$ for poly[n]catenanes of $m = 30$ for various n. All curves clearly show the initial regime of Rouse-like dynamics, consistent with the hypothesis of internal ring motion dominating the dynamics at short times. As n increases, the "dip" in the exponent at $t \sim 5 \times 10^3\tau$ becomes more pronounced and eventually

saturates at large n; notably, the position of this minimum is approximately constant for all n, suggesting that it is a relatively local property. Indeed, the scaling exponent associated with internal ring motion, γ_4, decays to its terminal value (zero) at around this time (Figure 6.4b), suggesting that any further diffusion arises from ring CM diffusion. Returning to Figure 6.5, at longer times, a second "plateau" begins to develop in $\gamma_1(t)$, but only for large n; the exact same behavior may be observed in the Rouse model for linear polymers, lending further support to the double-Rouse model. Once the monomer displacement reaches approximately $g_1(t) \approx 2R_g^2$, the polymers transition to ordinary diffusive motion.

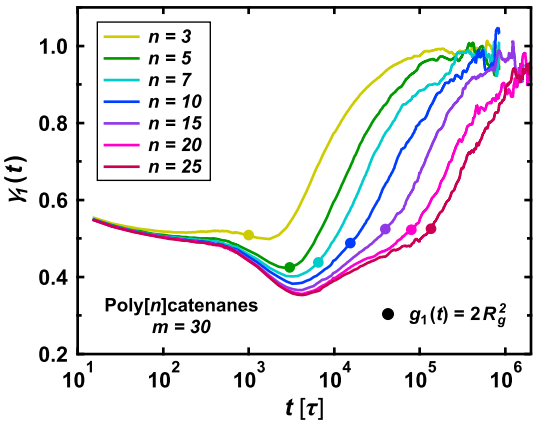

Figure 6.5: Instantaneous scaling exponent (γ_1, Eq. 6.7) for monomer mean-squared displacement, $g_1(t)$, in poly[n]catenanes with $m = 30$ and various n. The circles indicate the times at which the monomer displacement $g_1(t) = 2R_g^2$.

The exponent $\gamma_1(t)$ also depends on m, but only at short time and length scales, as shown in Figure 6.6. Here the time scale has been normalized by the longest Rouse time of the central rings of the catenane, denoted $\tau_{R,\text{ring}}$ (see next section). Although the curves show marked differences at short times, they collapse onto one another for times greater than $t \sim 3\tau_{R,\text{ring}}$. This indicates that the large length/time-scale motion of poly[n]catenanes does not depend on the underlying ring structure but is instead dominated by the overall linear architecture of the polymers. Indeed, the position of the minimum exponent ($\gamma_1 \approx 0.35$ for all systems) occurs at the same relative timescale for all m, which is considerably larger than

the longest relaxation time of the rings. Moreover, the monomer displacement at this point is many times larger than the ring size, $g_1(t) \approx 4.7R^2_{g,\mathrm{ring}}$. These results suggest that this minimum is associated with a transition between the ring-scale and chain-scale dynamics. At long times, all systems begin their transition to free diffusion at displacements $g_1(t) \approx 2R_g^2$, as expected from previous results.

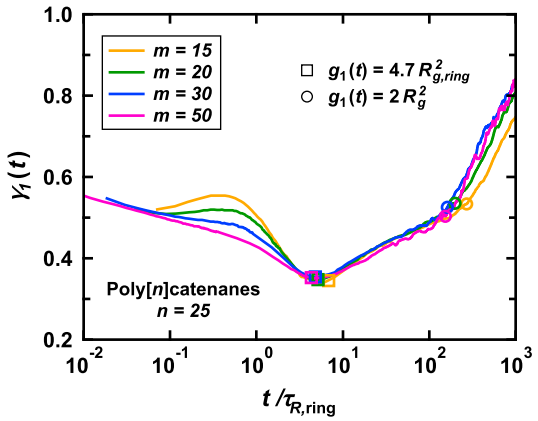

Figure 6.6: Instantaneous scaling exponent ($\gamma_1(t)$, Eq. 6.7) for monomer mean-squared displacement,$g_1(t)$, in poly[n]catenanes with $n = 25$ and variable m as a function of time, scaled by the longest Rouse time of the macrocycles. The squares and circles represent the points at which the monomer displacements $g_1(t)$ are equal to $4.7R^2_{g,\mathrm{ring}}$ and $2R_g^2$, respectively.

The non-universal behavior of $\gamma_1(t)$ at short times is unusual – the Rouse model would predict identical behavior for all m and certainly does not predict the non-monotonic behavior (i.e. the "hump") found in the curves for $m = 15$ and 20. This same behavior is observed in $\gamma_4(t)$, and is therefore attributed to intra-macrocycle relaxations. The fact that this "hump" eventually becomes merely a "shoulder" at larger m would seem to indicate that the dynamical effects of the mechanical bonds become unimportant for large m, in analogy with various structural properties, as discussed in the previous chapter [224]. However, this interpretation is *not* correct, as the dynamics of the largest rings are still significantly affected by the mechanical bonds, as will be discussed in the next section. Rather, we have found that this hump emerges when the ratio between the longest and second-longest Rouse

mode relaxation times of the rings becomes much larger than the ideal chain prediction, i.e. much greater than four (data not shown).

At this point, the double-Rouse model seems to be reasonably well supported by the simulation data, but even more evidence may be brought to bear. According to this theoretical picture, the rings can be considered "effective monomers" in a linear chain and the motion of these monomers, characterized by $g_5(t)$ and $\gamma_5(t)$, should correspond to ordinary Rouse behavior. The scaling exponent $\gamma_5(t)$ is shown in Figure 6.7a for poly[n]catenanes with $m = 30$ and various n. As n is increased in the poly[n]catenane systems, a large plateau region develops at long times with a lower bound that saturates at $\gamma_5(t) = 1/2$, in agreement with the Rouse model. In fact, if we compare this to the analogous $\gamma_1(t)$ behavior of ordinary linear polymers shown in Figure 6.7b, poly[n]catenanes appear to be more Rouse-like than linear chains of the same chemical composition. Indeed, for the flexible polymer model considered here, $\gamma_1(t)$ decreases continuously past $1/2$ over time with no true plateau observed for any N, which is attributed to interchain entanglement effects. Since poly[n]catenanes resist such entanglement, such $\gamma_5(t)$ does not show this trend. For poly[n]catenanes, the molecules transition to free diffusion at ring CM displacements of $g_5(t) \approx 2R_g^2$; analogously, linear polymers become freely diffusive when $g_1(t) \approx 2R_g^2$.

Since $\gamma_1(t)$ exhibits the most unusual features in poly[n]catenanes, the quantitative predictions of the double-Rouse model for this function are of interest. These predictions are shown in Figure 6.8 for various n and selected values of m and b; note that the time scale should not be interpreted in terms of Lennard-Jones units used elsewhere in this paper. Some qualitative agreement with the simulation data is indeed observed: there are two regimes of Rouse-like dynamics ($\gamma_1(t) \approx 1/2$) separated by a pronounced sub-diffusive region (cf. Figure 6.5). The latter of the Rouse-like regimes grows in temporal breadth increasing n, again in agreement with the simulation results (cf. Figure 6.5). Thus, these elementary features can be attributed purely to the unique connectivity of the polymers, without having

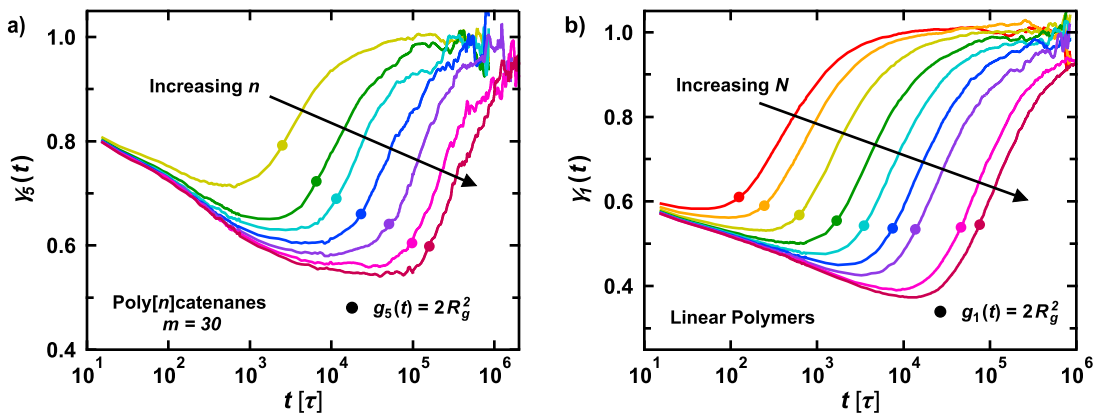

Figure 6.7: Instantaneous scaling exponent (γ_x, see Eq. 6.7) for a) macrocycle center-of-mass mean square displacement (g_5) for poly[n]catenanes of $m = 30$ and $n = 3 - 25$, and b) monomer mean squared displacement (g_1) for linear polymers of $N = 15 - 175$. The circles denote the points where a) $g_5(t) = 2R_g^2$ or b) $g_1(t) = 2R_g^2$.

to consider any complicated physics associated with mechanical bonds.

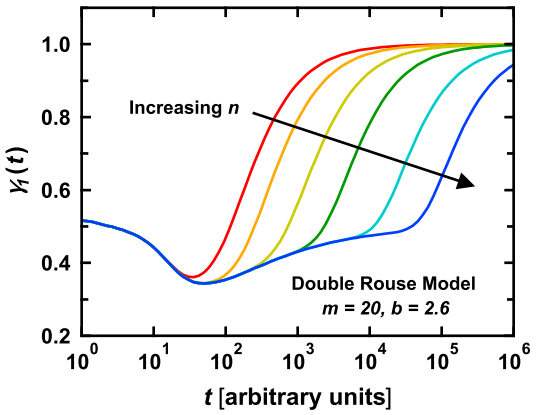

Figure 6.8: Instantaneous scaling exponent obtained from the double-Rouse model for poly[n]catenanes with $n = 3$, 7, 10, 20, 50, or 100 rings, $m = 20$ beads, and mechanical bond length $b = 2.6$ times the covalent bond length. Note that the unit of time is arbitrary and not related to the Lennard-Jones units used elsewhere in the paper.

Despite the above successes of the double-Rouse model, the simulation data cannot be quantitatively accounted for without a number of issues arising, as demonstrated in Figure 6.9. First, the model cannot capture the observed dynamics in the time period directly after the minimum in scaling exponent, even when very different fit parameter sets are used.

This regime corresponds to chain-scale dynamics, as the monomer displacements are much larger than the ring size, but still smaller than the overall chain dimensions (cf. Figures 6.5 and 6.6). Moreover, small values of n are required to simultaneously match the minima of the apparent exponent and the terminal decay (where the exponent is unity), no matter what values of m and b are used. Specifically, model values of $n = 12 - 14$ are required to match simulation data with $n = 25$. These results suggest that the various relaxation times in poly[n]catenanes do not have the same effective friction coefficient, i.e. the length-scale-invariant friction and/or no memory approximations of the Rouse model are not appropriate. Furthermore, the non-monotonic variations in the exponents $\gamma_1(t)$ and $\gamma_4(t)$ for small m cannot be explained since the mechanical bonds are modeled quite crudely. Clearly, the double-Rouse model is a good starting point for interpreting poly[n]catenane dynamics but is inadequate in many ways. The limits of validity of the model will be discussed in the subsequent sections on ring and chain dynamics.

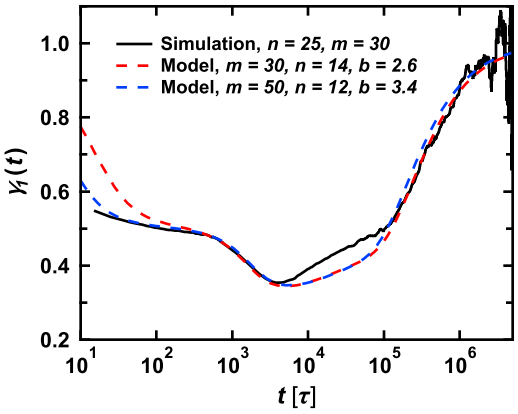

Figure 6.9: Simulation data for the scaling exponent $\gamma_1(t)$ and sample fits using the double-Rouse model.

6.4 Ring Dynamics

As described in the previous section, the double-Rouse model can reproduce some qualitative features of the monomer motion within poly[n]catenanes. To more thoroughly evaluate the system, the dynamics of the modes should be studied via their time autocorrelation functions through a Rouse-mode analysis (see Section 3.3). This section focuses on the ring-like modes, $\boldsymbol{X}_q$ which describe the internal dynamics of the macrocycles. For ordinary ring polymers, the Rouse modes are defined according to Eq. 3.4 [174, 217, 241] these same exact modes also appear in the double-Rouse model (see Eq. A.31) and are therefore useful in characterizing the macrocycle dynamics. The center-of-mass mode(s), whose motion was discussed in the previous section ($g_5(t)$, $g_6(t)$), will be ignored in this section. For simplicity, all data presented in this section were obtained from systems with $n = 7$, although the results are independent of n for $n \geq 5$.

To begin, the longest effective relaxation times ($\tau_{R,\text{ring}} = \tau_2^{\text{eff}}$) are studied as a function of m, as shown in Figure 6.10 for rings of all sizes and topologies. The predicted Rouse scaling is $\tau_{R,\text{ring}} \sim m^2$ for Gaussian ring polymers, but the observed scaling exponent is somewhat smaller, at approximately 1.85. However, in prior work [224], it was found that the sizes of macrocycles within catenanes scale considerably slower than those of ideal random walks, which also affects the dynamics. Scaling arguments (see Section A.4) predict $\tau_{R,\text{ring}} \sim m^{1+2\nu}$ for arbitrary scaling exponent ν, and the data for free ring polymers therefore suggest a scaling exponent of $\nu \approx 0.425$, in reasonable agreement with the scaling observed for ring radius of gyration ($R_{g,\text{r}}$) in the prior work on static properties [224].

For poly[n]catenane chain ends, the data appear to exhibit similar scaling, but the exponents are in fact significantly lower, $\tau_{R,\text{ring}} \sim m^{1.6}$. Importantly, 95% confidence intervals are much smaller than the data points in Figure 6.10, so the difference in scaling between the free rings and the chain ends cannot be dismissed as statistical noise. Although threaded

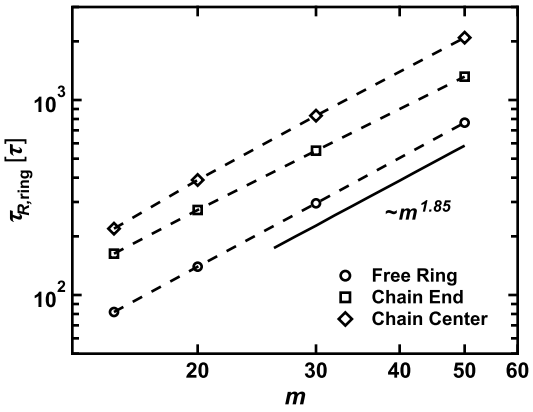

Figure 6.10: Longest ring-like Rouse relaxation times ($\tau_{R,\mathrm{ring}} = \tau_2^{\mathrm{eff}}$) of macrocycles within poly[n]catenanes compared to free ring polymers. Expected scaling is indicated by the solid line. Statistical uncertainties are much smaller than the data points.

macrocycles do exhibit slower scaling of ring size with m [224], the exponent of $\nu \approx 0.3$ implied by the dynamics data is unphysical, involving a fractal dimension larger than the spatial dimension. It is possible that as m increases, the chain ends will behave more and more like unthreaded rings as the mechanical bond affects the structure of the rings less as m increases. However, additional studies on larger rings are necessary to test this hypothesis. The chain centers further confound the situation as their longest relaxation times scale as $\tau_{R,\mathrm{ring}} \sim m^{1.9}$, faster than either the free rings or the chain ends. This result is difficult to interpret, however, because the apparent scaling exponent depends on m, so the behavior is clearly not asymptotic. In general, asymptotic dynamical scaling regimes are not always easy to identify in polymer systems [13] and the chain lengths considered here are certainly too short to achieve limiting behavior given that $m < N_e$ for all systems. Of course, as m is increased, the rings will become topologically compressed by their neighbors, which introduces another set of unusual dynamical consequences [1, 65]. Clearly, the mechanical bonds affect ring dynamics in a non-trivial way and do not allow for a simple self-consistent treatment based on static or dynamic scaling arguments. Any further conclusions cannot be supported by the simulation data collected here, so further study is required.

As discussed in the previous section, a key issue in the double-Rouse model is the assumption of unique friction coefficient on all length scales. To more closely investigate this point, the effective friction constant is calculated as a function of the length scale using the Rouse modes. The former is given by m/q according to the definition of the modes (Eq. 3.4) while the latter is defined as $\xi_q^{\text{eff}} = 3k_BT\tau_q^{\text{eff}}/\langle X_q^2\rangle$ (see Section A.4, Eq. A.22). Larger values of ξ_q^{eff} indicate slower dynamics at the associated length scale. For ideal Rouse dynamics, the effective friction is simply a constant, but topological interactions, such as entanglement in linear polymers, can cause deviations in this behavior [170, 171, 252]. For example, in isolated poly[n]catenanes, the dynamics of the lowest modes (longest length scales) of the macrocycles are reduced by up to an order of magnitude compared to free rings, while dynamics at short length scales are largely unaffected [222]. Moreover, the stretching exponents, β_q, are considerably reduced for rings with more threadings, indicating broader distributions of relaxation times. Both of these effects have been observed previously in entangled linear polymers [170], suggesting a common origin in topological constraints on polymer dynamics. In the poly[n]catenane melts studied here, a similar trend is observed, but somewhat smaller in magnitude compared to dilute solution, as shown in Figure 6.11, with effective friction about twice as large for chain centers as compared to free ring polymers. As was the case in isolated polymers, the mechanical bonds reduce the stretching exponents for the longest modes, decreasing from values of around 0.9 for free ring polymers to values as low as 0.76 for chain center rings. Interestingly, for the longest wavelength mode, $q = 2$, the effective friction and stretching exponent is constant for all m in free ring polymer melts, but for chain centers, the friction *increases* and the stretching exponent *decreases* with increasing m, indicating that the dynamical effects of the mechanical bond actually *grow* as m is increased. This directly contrasts with the results of the previous chapter on statics: structural signatures of the mechanical bonds typically decrease as m increases. This counter-intuitive result demonstrates that macrocycle dynamics cannot be understood on a single-ring level,

even in an effective sense. Instead, the topological linking and intermolecular effects should be considered more directly, which presents a formidable theoretical challenge. Clearly, the mechanical bond limits the ways in which the rings can move or relax, and this restriction apparently becomes increasingly important as the rings become larger. Interestingly, such new physics is apparent even for the relatively short rings studied here, which are far too small to exhibit the unusual dynamical properties observed in ordinary, unthreaded ring polymers.

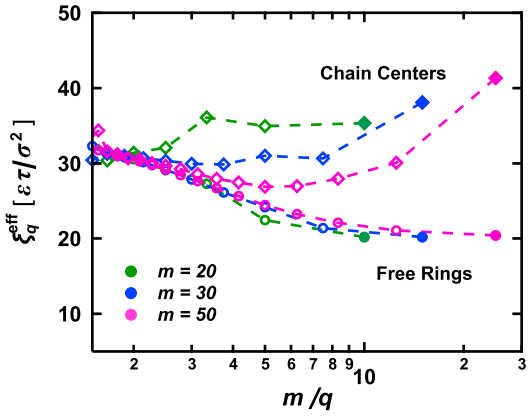

Figure 6.11: Effective friction coefficients for the ring Rouse modes as a function of corresponding length scale for free ring polymers (circles) and chain center macrocycles (diamonds) of various m. The data for $m = 15$ are omitted for visual clarity but follow similar trends. Statistical uncertainties are smaller than the data points.

6.5 Chain Dynamics

As discussed earlier, at long time and length scales, the dynamics of poly[n]catenanes are dominated by the overall linear structure of the polymers. Accordingly, this section focuses on the linear-like modes of the double-Rouse model to more closely study the dynamics on these larger scales. These modes are given in terms of the ring centers-of-mass according to Eq. 3.7 and, apart from the multiplicative pre-factor, are identical to the modes for ordinary linear polymers with the macrocycle centers-of-mass (CM) taken as "effective" monomers [169,

170, 222, 253]. As in the previous section, we perform a mode analysis where autocorrelation functions are calculated from simulation trajectories and fit to stretched exponential (KWW) functions to extract effective relaxation times, τ_p^{eff}, and stretching exponents, β_p. For the modes studied here, the p^{th} mode corresponds to a segment length scale of n/p effective monomers, i.e. macrocycles.

The longest relaxation times ($\tau_R = \tau_1^{\text{eff}}$) are shown in Figure 6.12 as a function of chain length, n, for catenanes with various m. For unentangled, linear chains as well as poly[n]catenanes, the double-Rouse model predicts the scaling $\tau_R \sim n^2$ (see Section A.5, Eq. A.33) and this is indeed observed for large n. At small n, the scaling exponent appears to be slightly larger, which can be attributed to local stiffness effects; these effects are stronger for small m as these poly[n]catenanes have a larger relative stiffness [224].

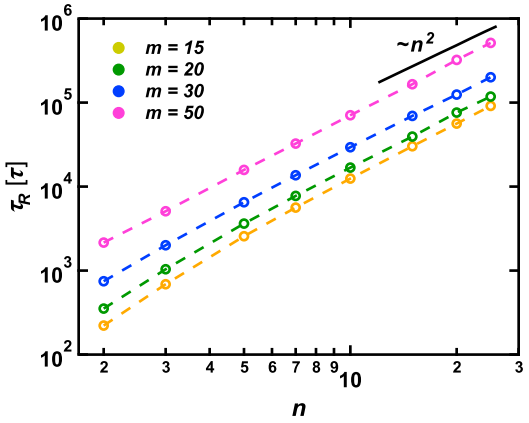

Figure 6.12: Longest Rouse relaxation times $\tau_R = \tau_1^{\text{eff}}$ for poly[n]catenanes of various m as a function of n. Ideal Rouse scaling is indicated by the black line. Statistical uncertainties are smaller than the data points.

The longest relaxation times, τ_R, also depend strongly on ring size, m. Per the double-Rouse model, these times are expected to scale as $\tau_R \sim m^{1+2\nu}$, where ν is the scaling exponent for the effective mechanical bond length, b_{eff} (see Section A.5, Eq. A.33 and discussion thereafter). Within the term $m^{1+2\nu}$, one factor of m is due to the effective friction experienced by the ring center-of-mass while a factor of $m^{2\nu}$ is related to the changes in mechanical

bond length associated with changing the ring size. Along with the longest Rouse time, the diffusion time, $\tau_D = R_g^2/6D$, is also calculated, which is the time required for the polymer to diffuse its own size. In the context of the Rouse model, τ_D may be thought of as the relaxation time of the zeroth mode (i.e. the polymer center-of-mass). This quantity should also obey the scaling $\tau_D \sim m^{1+2\nu}$ according to the double-Rouse model since $D \sim 1/nm$ and $R_g^2 \sim nb_{\text{eff}}^2 \sim nm^{2\nu}$. The exponent ν is roughly 1/3 [224], suggesting a scaling of approximately $\tau_R \sim \tau_D \sim m^{5/3}$. Note that in the previous section on ring dynamics, the scaling exponent of interest was that which governed ring dimensions rather than bond lengths; more discussion on this point can be found in Section A.5. The two relaxation times τ_R and τ_D are shown in Figure 6.13 as a function of m for the longest poly[n]catenanes studied ($n = 25$) along with power law fits with the expected scaling exponent of 5/3. The diffusion times, τ_D, show the expected m-dependence throughout the range of values investigated to within the statistical uncertainty of the data. However, the scaling of the Rouse relaxation times, τ_R, is somewhat different: at large m, the expected scaling is indeed observed, but as m is decreased, there is an "upturn" in the relaxation times, indicating slower scaling and increased friction in this regime. More quantitatively, the apparent scaling exponent obtained by considering the smallest two m-values is just 0.91, less than half the expected value. The relaxation times τ_R have considerably smaller statistical error than τ_D, so this deviation is indeed significant.

Both the diffusive and Rouse relaxation times measure polymer dynamics at long length andtime scales, so the qualitative disagreement between the two is unexpected. It is possible that the discrepancy can be explained by the underlying forces responsible for the dynamics. The polymer CM diffusion depends on intermolecular forces. Although these forces are coupled self-consistently to the polymer structure, it is possible that (to a zeroth order approximation) these intermolecular forces do not possess any significant non-local features, either spatially or temporally, and that any differences in polymer structure that result from

changing m are not significant enough to introduce any additional complications. This idea is somewhat consistent with the observation that the diffusive friction of poly[n]catenanes depends only weakly on m (cf. Figure 6.2b); such differences apparently are not enough to cause τ_D to deviate significantly from the expected scaling. In this picture, it then follows that the anomalous m-dependence of the Rouse relaxation times is related to unique intramolecular force/stress correlations. These comments are merely speculative at this stage, but also appear to be relevant to stress relaxation, as discussed in the next section.

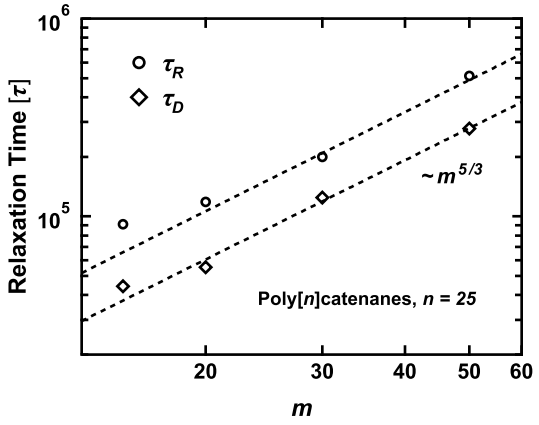

Figure 6.13: Rouse times (τ_R, circles) and diffusion times (τ_D, diamonds) for poly[n]catenanes of $n = 25$ as a function of m. Dashed lines are fits to power-law relations with the expected scaling exponent. Error bars are much smaller than the data points for τ_R and roughly the size of the data points for τ_D.

As in the previous section, the effective friction constants, denoted ξ_p^{eff} for linear-like modes, provide insight into the dynamics at various length scales within the polymer. The results are shown in Figure 6.14a for ordinary linear polymers of various molecular weights. At short length scales (small N/p) the effective friction decreases modestly with increasing length scale and the various systems agree quantitatively. At larger length scales (large N/p), the friction increases significantly as N is increased, which is attributed to the onset of entanglement. These results are consistent with previous literature on the topic [170].

Poly[n]catenanes of fixed m and variable n exhibit behavior that is qualitatively similar to that of unentangled linear polymers, with the friction at long length scales being nearly

independent of n (data not shown). However, unusual behavior is observed as m is varied, as shown in Figure 6.14b. The effective friction increases strongly – in some cases by a factor of almost five – at relatively short length scales (small n/p) as m is decreased. These observations indicate that the dynamics of small groups of chain segments are significantly slowed by the mechanical bonds. Such a trend is consistent with what was found in dilute solutions (see Chapter 3) [222]. Interestingly, the effective friction constant decreases with m at essentially all length scales; the exact opposite trend was found when examining the internal ring dynamics in the previous section, although those effects were considerably smaller (cf. Figure 6.11). The reason for this discrepancy is unclear, but it is possible that the internal dynamics of the macrocycles may become decoupled from the ring center-of-mass motion, which is associated with the chain mode relaxations. Such a decoupling has been suggested in simulations of high-MW ring polymer melts, where the orientational and diffusive relaxation times scale differently with N [62, 64, 249]. It is not obvious how mechanical bonds would affect such dynamics and further study is necessary.

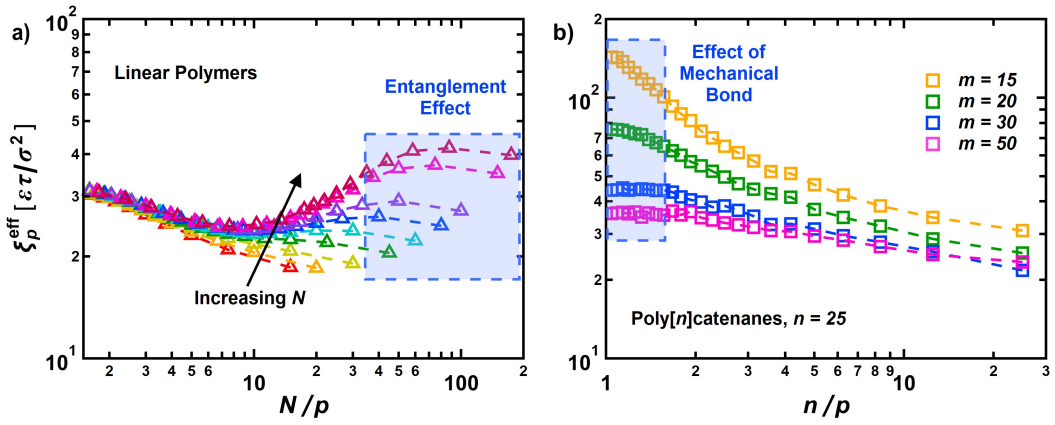

Figure 6.14: Effective friction coefficients for the Rouse mode autocorrelation functions in a) linear polymer melts with $N = 15 - 175$, and b) poly[n]catenanes with $n = 25$ and various m. At long length scales, interchain entanglement causes increases in the effective friction in linear polymers. Statistical uncertainties are roughly the size of the data points.

The stretching exponents, β_p, also differ remarkably in linear polymers and poly[n]catenanes, as shown in Figure 6.15. For linear polymers, the exponents remain in the range

0.8-1.0 at short length scales but decrease towards a minimum at longer length scales as N is increased. For very long polymers, this minimum has previously been associated with N_e, and therefore these qualitative changes in the relaxation behavior may be attributed to interchain entanglement, i.e. kinetic constraints on polymer motion [170, 171, 252, 254]. By contrast, poly[n]catenanes do not show decreases in stretching exponent at long length scales, even for the largest chains considered in this study. However, at short length scales, the exponents are dramatically lowered to values as small as 0.55, comparable with values found for well-entangled linear chain melts. This finding suggests that poly[n]catenane motion is restricted at the length scale of individual effective segments, which must be attributed to the mechanical bonds. The m-dependence of the behavior further supports this picture as more mild decreases in the stretching exponents are seen for larger rings, just as the increase in effective friction at short length scales is also mitigated by increasing the ring size (cf. Figure 6.14b).

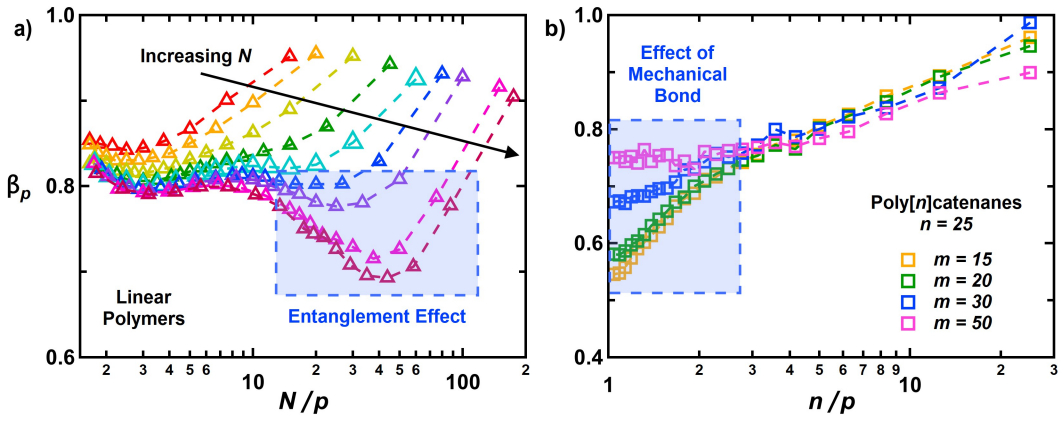

Figure 6.15: Stretching exponents for the Rouse mode autocorrelation functions in a) linear polymer melts with $N = 15 - 175$, and b) poly[n]catenanes with $n = 25$ and various m. Statistical uncertainties are roughly the size of the data points.

Such small stretching exponents in dynamical measures are also associated with "caging" effects in supercooled liquids [255]. This seems to be a more natural comparison than the entanglement analogy presented above as the anomalous dynamics appear to be most dra-

matic at short, rather than long length scales. However, the data does not support this interpretation. All systems, regardless of n or m, have essentially identical fluid structure at all length scales, both in terms of the site-site correlation function (radial distribution function) and the total structure factor, which are essentially indistinguishable [224]. Furthermore, the alpha relaxation times, which determine how easily beads can break out of their local cages, show no n or m dependence except for very small rings ($m = 10$), which are not considered here. Since a variety of ring polymer systems have been shown to exhibit glassy dynamics on the macromolecular scale under various circumstances [76–78], one may suspect that the caging effect could occur at the level of the ring center-of-mass rather than the individual beads. However, this explanation is also unsatisfactory, since previous simulations on isolated poly[n]catenanes – i.e. in the complete absence of intermolecular interactions - exhibited similar trends in the dynamics [222]. These results indicate that the retarded dynamics at small length scales are not caused by any glassy behavior, but are instead related to the topological interaction inherent in the mechanical bond.

This section and the previous ones have shown that the double-Rouse model can describe many of the qualitative features of poly[n]catenane dynamics, including the separation of ring-like and linear-like contributions to the monomer displacements and the overall scaling behavior of the relaxation times. Such success implies that these phenomena can be explained simply by the unique connectivity of the polymers. However, the model cannot describe the motion on intermediate length scales without resorting to highly mode-dependent effective friction, which may have different dependencies on m for different methods of calculation. These discrepancies are likely related to the fact that the model fails to simultaneously capture both the terminal ring and chain relaxation times in the monomer MSDs discussed at the end of Section 6.3 (Figure 6.9). The data further suggest that the topological interactions of the mechanical bonds are responsible for these non-ideal dynamics at intermediate time and length scales.

6.6 Stress Relaxation

The rheological properties of polymeric liquids have important implications in many industrial and biological processes and a great deal of effort has been invested into determining the impact of polymer architecture on stress relaxation and linear viscoelastic response. Near equilibrium, the rheological behavior of fluids at various time scales is described by the shear stress relaxation modulus, $G(t)$, which is related to the stress autocorrelation function (SACF):

$$G(t) = \frac{V}{k_B T}\langle \sigma_{\alpha\beta}(t)\sigma_{\alpha\beta}(0)\rangle \tag{6.8}$$

where the average is taken over all initial conditions, and $\sigma_{\alpha\beta}$ indicates an off-diagonal component of the stress tensor. In the context of the Rouse model, the modulus can be expressed as a sum of exponentials with decay times equal to half the mode relaxation times (Section A.4, Eq. A.28):

$$G(t) = \frac{\rho k_B T}{N}\sum_{p=1}^{N-1} e^{-2t/\tau_p} \tag{6.9}$$

Note that Eq. 6.9 holds generally for all architectures, as long as the sum extends over all modes which all contribute equally in an amplitude sense to the stress.

Eqs. 6.8 and 6.9 suggest two methods of calculating $G(t)$ in polymer systems: (i) compute the stress using the virial pressure, evaluate the SACF directly, and insert into Eq. 6.8; (ii) substitute the empirically determined mode relaxation times into Eq. 6.9. The first method calculates the true modulus but is prone to large statistical error and long simulations are required for even modest accuracy. On the other hand, despite much smaller statistical error, the Rouse-inspired method is plagued by all the usual model assumptions mentioned in Section 6.2 above. Most crucially, it neglects all non-bonded and intermolecular stresses and in the case of poly[n]catenanes, inter-macrocycle stresses, even those between neighboring (linked) rings. The hope is that some of these effects may be included implicitly if they

also impact the mode relaxation times or effective friction coefficients; indeed, several other authors have used an analysis of the Rouse modes to obtain accurate estimates of $G(t)$ for various linear polymer systems [253, 256, 257]. However, it is not clear that such an analysis will be successful for poly[n]catenanes, even if the friction is strongly mode-dependent, as shown in the previous sections. Accordingly, data obtained from both the Rouse-mode analysis and SACF methods will be presented and the similarities and differences will be used to gain physical insight into the system dynamics.

To reduce statistical noise in the data, the SACF is calculated using the pre-averaged stress described by Lee and Kremer [258], wherein the stress tensor is averaged over time periods of 10τ prior to evaluating the SACF. Despite this pre-averaging, the SACF is still very noisy at long times when calculated directly. To further reduce the scatter, the pre-averaged stress is passed through a multiple-tau correlator as described by Likhtman and coworkers [259, 260]. This is conceptually similar to smoothing the SACF at logarithmically-spaced time points. The short-time data are not perturbed, but the noise in the data at long times is significantly reduced, allowing for easier analysis of the results.

To calculate $G(t)$ from the Rouse mode relaxations, the exponentials in Eq. 6.9 are replaced by the more accurate KWW function determined from simulation and the empirically determined linear-like and ring-like relaxation times (τ_p and τ_q, respectively) and stretching exponents (β_p and β_q, respectively) are used to generate an analytic function of time for a given n and m. For simplicity, the chain center relaxation times are used for each of the $n-2$ doubly-threaded macrocycles in each poly[n]catenane. This analysis is similar to that developed by Vladkov and Barrat [253] and further utilized by Kuhnhold and Paul [256, 257] but makes the additional assumption that the different Cartesian components of the modes are fully independent, i.e. $\langle X_{p,x}^2 X_{p,y}^2 \rangle \approx \langle X_{p,x}^2 \rangle \langle X_{p,y}^2 \rangle = \langle X_{p,x}^2 \rangle^2$. For the systems studied here, this approximation is generally satisfied to within a few percent.

For ideal (unentangled) Gaussian linear and ring polymers, the mode relaxation times

scale as $\tau_p \sim (N/p)^2$, which leads to a power-law decay of the form $G(t) \sim t^{-1/2}$ at time scales $t < \tau_R$ [87]. In this intermediate regime, $G(t)$ is predicted to be independent of N, although chain end effects as well as interchain entanglement may preclude quantitative agreement. In particular, entangled linear polymer melts exhibit the well-known "rubbery plateau" where $G(t)$ is roughly constant for an extended period of time due to the topological constraints of neighboring chains [13, 87]. Figure 6.16a shows $G(t)$ for linear polymers of various N (calculated from the SACF), in which the trends mentioned above are clearly visible. At small N, the modulus increases monotonically with N at all times as finite-size and chain-end effects are reduced. For sufficiently high N, $G(t)$ does indeed saturate at short times, achieving behavior consistent with the Rouse model. However, for the largest molecular weights, $G(t)$ shows small deviations from Rouse scaling and the stress decays slower than $\sim t^{-1/2}$, consistent with the emergence of entangled dynamics.

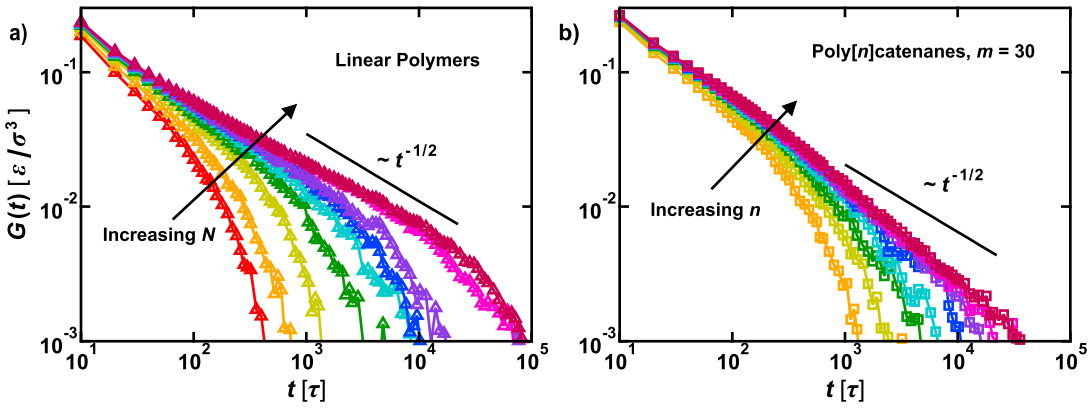

Figure 6.16: Stress relaxation modulus calculated from the stress autocorrelation function for a) linear polymers with $N = 15$ (red), 20 (orange), 30 (yellow), 45 (green), 60 (cyan), 80 (blue), 100 (violet), 150 (pink), and 175 (magenta), and b) poly[n]catenanes of $m = 30$ and $n = 2$ (orange), 3 (yellow), 5 (green), 7 (cyan), 10 (blue), 15 (violet), 20 (pink), and 25 (magenta). The solid lines indicate the expected scaling for Rouse (ideal) dynamics.

For poly[n]catenanes, the double-Rouse model predicts a decomposition into ring-like and linear-like stress relaxation contributions, as was also observed in the monomer diffusion studied previously in Section 6.3. Specifically, the modulus can be written (see Appendix,

Section A.5, Eq. A.35):

$$G(t) = G_{\text{ring}}(t; m) + \frac{1}{m} G_{\text{lin}}(t; n, m) \tag{6.10}$$

where $G_{\text{ring}}(t; m)$ and $G_{\text{lin}}(t; n, m)$ are the moduli of a melt of pure rings of size m and a melt of pure linear polymers of size n, respectively, at the specified temperature and density; their dependencies on the parameters n and m are emphasized. In general, Eq. 6.10 predicts two separate regimes of Rouse-like decay ($G(t) \sim t^{-1/2}$) corresponding to ring-like and linear-like relaxations. These regimes should be separated by a transition region with rapid, exponential decay owing to the terminal relaxation of the ring contributions. Such a decomposition is indeed suggested by the simulation data for poly[n]catenanes, as shown in Figure 6.16b for $m = 30$ and various n (calculated from the SACF). The stress relaxation appears to be approximately Rouse-like at short time scales, but at times beyond $\sim 10^3\tau$, it decays considerably faster. For other values of m, the results appear qualitatively similar, although there are differences which will be discussed later on.

The general form of Eq. 6.10 also implies a specific n-dependence of $G(t)$. The first term in Eq. 6.10 has no dependence on n, so the stress relaxation is identical for all systems at times shorter than the ring relaxation time, $t < \tau_{R,\text{ring}}$. At longer times, the linear contribution to the stress relaxation will also have no dependence on n, if the system has not reached terminal decay, i.e. $t < \tau_R$. As a result, as n is increased, the exact same stress relaxation behavior is expected for all systems up to the terminal relaxation time. Of course, for non-ideal poly[n]catenanes, the differences in dynamics between chain end and chain center macrocycles (Section 6.4) will lead to considerable chain end effects, which are clearly observed for small n in Figure 6.16b. Nevertheless, for $n > 10$, all relaxation curves agree with one another quantitatively until terminal decay, in qualitative agreement with the double-Rouse theory.

Following Lihktman and coworkers [259], the stress relaxation can be more easily analyzed by dividing the modulus by the expected Rouse scaling, $t^{-1/2}$; these data are shown in

Figure 6.17 (calculated from the SACF). In this view, ideal dynamics correspond to a flat line, $G(t)t^{1/2} = \text{const.}$, as seen for early times in linear polymers (Figure 6.17a). For such systems, entanglements cause increases in $G(t)t^{1/2}$ over time, which can be clearly seen for linear polymers with $N > 100$. For poly[n]catenanes, three distinct regimes can be clearly identified, as shown in Figure 6.17b. First, there is a roughly flat regime, suggesting Rouse-like dynamics at early times associated with the ring-like modes. After about 400τ, the plateau gives way to a second regime characterized by rapid stress relaxation. The start of the transition between these regions coincides with the longest relaxation time of the chain center macrocycles of these polymers ($\sim 800\tau$; note that the stress relaxation times in the Rouse model are a factor of two smaller than the mode relaxation times, see Eq. 6.9). At long times, there is a third regime of stress relaxation which undergoes terminal decay at long times that increase with n, indicating that this behavior is related to overall chain relaxation i.e. the linear-like modes. In summary, the observed stress relaxation processes in poly[n]catenanes are qualitatively consistent with the double-Rouse model. Therefore, although the scaled modulus never attains a true plateau for the chain lengths studied here, it is expected that larger values of n will indeed lead to such Rouse-like scaling at long times, assuming interchain entanglements are still unimportant.

Thus far, only the modulus from the SACF has been discussed, however it is helpful to examine the modulus as computed from the Rouse mode relaxations, Eq. 6.9. These data for poly[n]catenanes are shown in the inset of Figure 6.17b. At very early times, there are pronounced deviations from the "true" SACF-based modulus, but this is not surprising as the Rouse model does not account for any dynamics associated with local fluid structure i.e. the "glassy" or "colloidal" relaxations of the liquid [259]. Despite these short-time disagreements, the same chain-end effects and three-regime stress relaxation can be seen (in an exaggerated form) in this data as in the SACF-based modulus. Despite this qualitative agreement, the transition between the ring-like and linear-like regimes is quite sharp in the Rouse mode

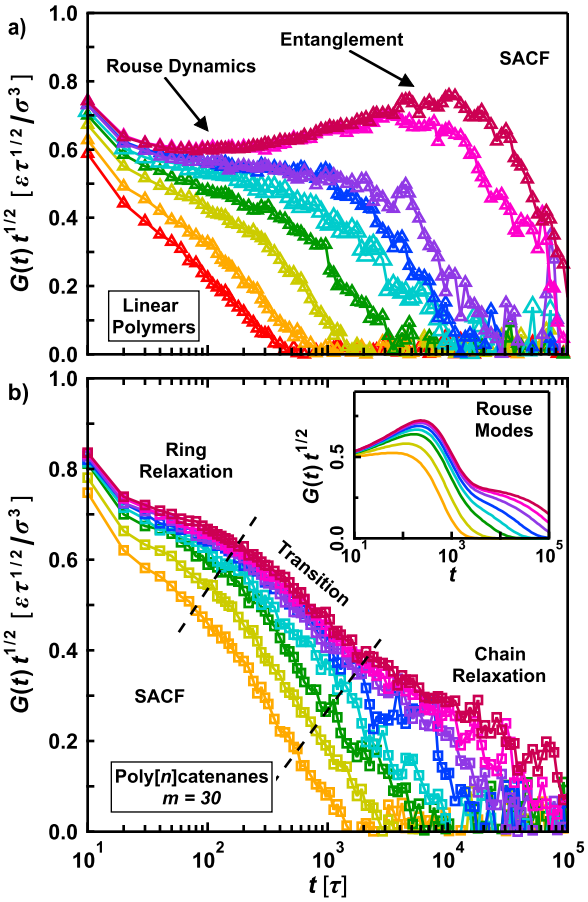

Figure 6.17: Scaled stress relaxation modulus calculated from the stress autocorrelation function (SACF) for a) linear polymers with N = 15, 20, 30, 45, 60, 80, 100, 150, and 175, and b) poly[n]catenanes of m = 30 and n = 2, 3, 5, 7, 10, 15, 20, and 25. The various curves correspond to different molecular weights, which increase from left to right (bottom to top) as in Figure 16. The dashed lines are included to guide the eye. Part b) inset: Scaled modulus for the poly[n]catenane systems as determined from the Rouse mode relaxation times.

analysis ($\sim 10^3\tau$) but is blurred in the true modulus. This suggests that the Rouse mode relaxation times – even the empirically determined ones – fail to capture the dynamics at these time/length scales. It is certainly no coincidence that this is the length scale of the topological interactions within the chains, i.e. the mechanical bonds and short segments of catenated rings; these results are fully consistent with those of Sections 6.4 and 6.5.

Even more interesting behavior is observed when comparing the stress relaxation of

poly[n]catenanes with varying ring sizes at constant n, owing to the $1/m$ prefactor in Eq. 6.10. For instance, at times shorter than the longest ring-like relaxation time, $t < \tau_{R,\text{ring}}$, the ring stress $G_{\text{ring}}(t)$ is expected to relax at the same rate for all ring sizes, m, while the linear-like modulus $G_{\text{lin}}(t)$ should be fairly constant at its initial value, as the linear-like relaxation times are much longer than the ring-like ones. As a result, at these time scales, systems with larger m will have lower stress - or will effectively relax stress faster - than those with smaller m. This result stands in strong contrast to linear polymers, which relax more slowly when molecular weight N is increased, even at short times (Figure 6.17a). However, since $\tau_{R,\text{ring}}$ increases with m, the curves for various m will cross in the transition region (cf. Figure 6.17b) as the smaller rings relax completely while the bigger ones still retain their large-length scale correlations. Conceptually, the cause of this short-time behavior is similar to the dilution effect in bottlebrushes, in which increasing side chain length or grafting density reduces the overall density of polymers in the system [10, 261, 262]; it is possible that such a result may be found more generally in any polymer system with multiple distinct mechanisms of stress relaxation.

To test these predictions, Figure 6.18 shows the scaled modulus for poly[n]catenanes of $n = 25$ and various m (computed from the SACF). At short times $t < 300\tau$, the stress relaxation is clearly accelerated for the larger rings, as the early-time plateau values are considerably smaller, consistent with the separation of ring-like and linear-like stress relaxation described above (note that the initial values $G(0)$ are identical for all systems). Similar trends are also crudely observed in the modulus as calculated from the Rouse mode relaxations (Figure 6.18 inset). Such accelerated stress relaxation for larger polymers is not seen in linear polymer systems (Figure 6.17a) nor in the ring polymer melts considered here (data not shown); rather, it follows from the complex poly[n]catenane architecture.

As mentioned above, at intermediate times on the order of $\tau_{R,\text{ring}}$, the double-Rouse model predicts that the $G(t)$ curves (or equivalently, $G(t)t^{1/2}$) will cross. Such behavior is

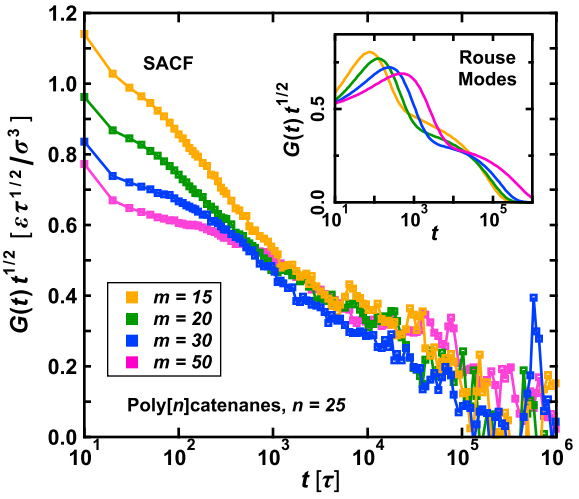

Figure 6.18: Stress relaxation modulus normalized by Rouse scaling for poly[n]catenanes of $n = 25$ and various m, calculated from the stress autocorrelation function (SACF). Inset: the same data calculated from the Rouse modes.

indeed observed in the moduli calculated from the Rouse modes (Figure 6.18 inset) but is not consistently seen in the SACF data. For instance, in the SACF data the curves for $m = 15$ (orange) and $m = 50$ (pink) cross at $t \approx 2 \times 10^3 \tau$, but the $m = 15$ and $m = 30$ (blue) curves *never* cross, even at very long times. This behavior is extremely unusual. After all, at long times, the first term in Eq. 6.10 vanishes, and all stress relaxation should be occurring at the chain segment level via the linear-like modes, i.e. the second term in Eq 6.10. As the linear-like mode relaxation times increase with m, the stress relaxation should be slower and last longer for catenanes with larger m, so $G(t)$ at long times will increase with increasing m. As with the short-time crossover, this trend is clearly seen in the moduli obtained from the Rouse modes but is not in the SACF data.

The reasons for these observations are unclear; certainly, they are not related to any changes in the fluid relaxation times or any "caging" effects at the ring CM level, as discussed in Section 6.5. However, the fact that the Rouse modes indicate qualitatively different stress relaxation behavior compared to the SACF suggests some possible explanations. The modulus determined from the Rouse mode relaxations, Eq. 6.9, neglects potential

cross-correlations and stresses which may exist between modes. However, as shown in the Appendix (Section A.6), the modes are indeed orthogonal to good approximation. The discrepancy between the Rouse-mode and SACF moduli may therefore be related to either the intermolecular stresses at the ring level (since interchain entanglement is not prevalent, see Section 6.3) or to inter-ring, intra-chain stresses. In reality, these two effects are coupled, as discussed in the previous chapter on static properties [224]. Frustratingly, any correlations between different rings cannot be understood in terms of Rouse mode cross-correlations, as these vanish identically because of the symmetries inherent in ring polymers (see Section A.6). In any case, this line of thinking is merely speculative at this time and further studies are needed to understand how the dynamics of linked ring polymers couple to one another. Nevertheless, the data presented here demonstrate that the stress relaxation behavior of poly[n]catenanes cannot be understood in terms of single-chain and single-ring dynamics, even empirically measured ones

The zero shear-rate viscosity, η, can be determined from the equilibrium dynamics via the integral of the shear stress relaxation modulus:

$$\eta = \int_0^\infty G(t)dt \tag{6.11}$$

In the context of the Rouse model, Eqs. 6.9 and 6.11 indicate that the viscosity is proportional to the sum of the (effective) mode relaxation times:

$$\eta = \frac{\rho k_B T}{N} \sum_{p=1}^{N-1} \tau_p^{\text{eff}} \tag{6.12}$$

which, like Eq. 6.9, holds for arbitrary polymer architectures. As in the case of $G(t)$, two methods will be used to calculate and study the viscosities: (i) directly integrate the SACF (Eq. 6.11, see Section A.7 for details), and (ii) sum the effective mode relaxation times found in Sections 6.4 and 6.5 (Eq. 6.12).

The viscosities are shown in Figure 6.19 for all systems studied, calculated according to the SACF. Linear and ring polymers (Figure 6.19a) show the expected dependence of viscosity on N [13, 66, 79, 174, 249] and the results are in quantitative agreement with previous literature values for this model [259, 263]. At low N, the linear polymer melt viscosity scales roughly linearly with N and curves upward towards more rapid scaling as interchain entanglement becomes prevalent. The ring polymer viscosities show moderate sub-linear scaling, consistent with the smaller scaling exponents observed for measures of ring size.

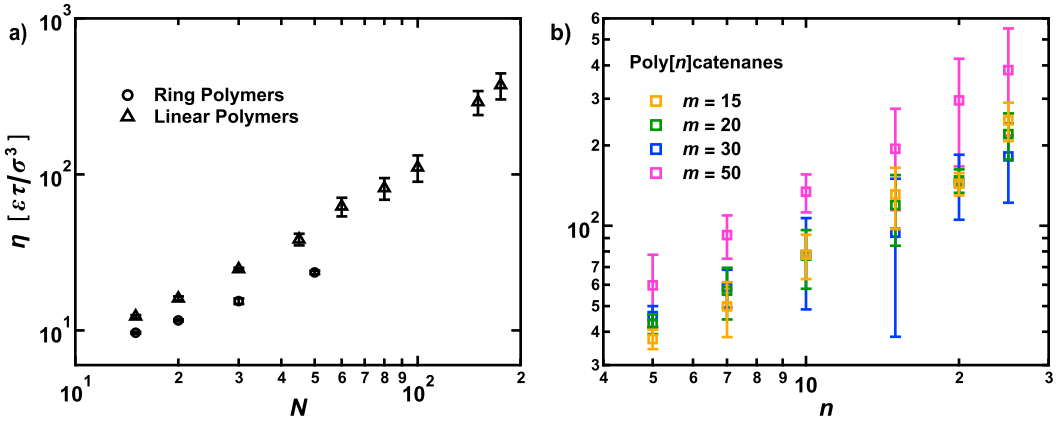

Figure 6.19: Zero shear-rate viscosities as computed from the stress autocorrelation function for a) linear and ring polymers as a function of N, and b) poly[n]catenanes of various m as a function of n. Error bars indicate 95% confidence intervals.

For poly[n]catenanes, the double-Rouse model predicts a linear form for the viscosity following directly from Eq. 6.10 (see Appendix, Eq. A.36):

$$\eta \sim (2nb^2 + m) \tag{6.13}$$

where the first term represents the linear-like contributions and the second represents the ring-like contributions. On account of the additional ring term, the *apparent* scaling of viscosity with n will be sub-linear at low n, which is consistent with the simulation data in Figure 6.19b. However, the observed m-dependence of the viscosity differs greatly from

the predictions of the double-Rouse model. In particular, scaling arguments can be used to show that poly[n]catenane viscosity should scale as $\eta \sim m^{2/3}$ for n not too small (see Section A.5). This trend is obeyed at low n (e.g. $n = 5$) in the simulation data, but at larger n, the viscosity first *decreases* as m increases up to $m = 30$, and then increases greatly for $m = 50$ (e.g. $n = 25$). Despite the sizable statistical error, the difference between the viscosities of poly[n]catenanes with $n = 25$ and $m = 15$ vs. $m = 30$ seems statistically significant (p-value ≈ 0.06). Such a result is also visually apparent from the data in Figure 6.18 as $G(t)$ is greater for $m = 15$ than for $m = 30$ at all times. However, even if this difference at large n is rejected as insignificant and the two samples are deemed statistically indistinguishable, this would still be an unusual result. After all, the double Rouse model predicts a viscosity scaling of $\eta \sim m^{2/3}$; thus, a doubling of the ring size, say from $m = 15$ to $m = 30$, should increase the viscosity by a factor of at least 1.6. Using this ratio, the viscosity for the $= 30$ system is predicted to be far larger than the observed value; in fact, it is even larger than the viscosity calculated for the largest ring size of $m = 50$. Clearly, the dependence of the viscosity on ring size represents a clear qualitative failure of the double-Rouse model at large length scales.

The n-dependence of the poly[n]catenane viscosities also deviates qualitatively from the double-Rouse model. Figure 6.20 shows the viscosity as a function of n on a linear-linear scale along with fits to the functional form Eq. 6.13 (i.e. linear regressions) for each m-value. Although each data set can be fit by this simple form, the resulting slopes show a non-monotonic dependence on m, with the slopes decreasing with m up to $m = 30$ followed by an increase for $m = 50$, the same trend observed in the viscosities for large n, as mentioned above. Visually, the curves for $m = 15 - 30$ cross at $n \approx 10$ because of the decreasing slopes in this range of m-values. In the double-Rouse model, these slopes are related to the product of the mean-square mechanical bond length, b^2, and the effective friction. Since the bond lengths must (and do) increase with m [224], the reduction in the slope may be interpreted

as a strong decrease in the friction for increasing m, which agrees qualitatively with the results of the previous section on chain dynamics (Figure 6.14b), although those changes are mild by comparison. However, this trend is not obeyed by the largest ring size, $m = 50$, where the slope is larger than all other m-values, consistent with increased bond length and constant friction.

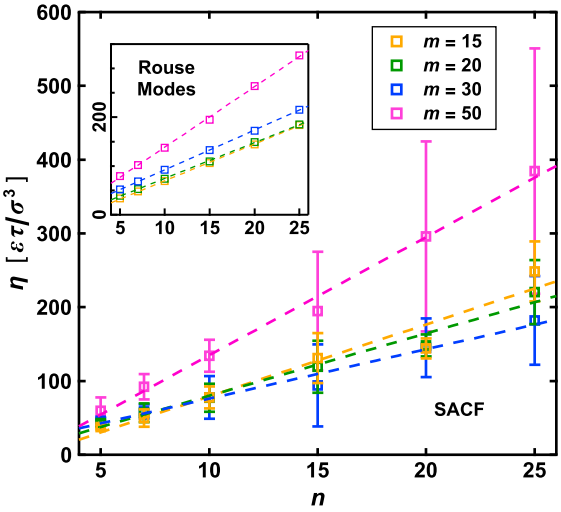

Figure 6.20: Poly[n]catenane viscosity as a function of n for various m on a linear-linear scale as determined by the stress autocorrelation function (main figure) and the Rouse mode relaxation times (inset). The dashed lines are linear fits to the data. The error bars indicate 95% confidence intervals and are smaller than the data points in the inset. The axis labels apply to both the main figure and the inset.

Since the empirically determined from simulation Rouse relaxation times and the SACF-determined viscosities both imply decreasing friction with increasing m (at least for $m < 50$), perhaps the former may predict the latter. The viscosities of poly[n]catenanes obtained from the Rouse mode relaxation times according to Eq. 6.12 are shown in the inset of Figure 6.20, along with linear fits of the data. As was the case for the SACF data, the Rouse mode data predicts slopes that do not simply increase with m. However, the results show only a small decrease in slope as m is increased from 15 to 20 followed by increases for $m = 30$, which is not consistent with the SACF results. On the other hand, although the simulation-deduced

Rouse relaxation times when combined with Eq. 6.12 do not predict a decrease in viscosity with increasing m, they do predict viscosities that increase only very slightly, and much less than that predicted by the naïve (literal) double-Rouse model ($\eta \sim m^{2/3}$). For instance, the predicted viscosity for $n = 25$ is the same for $m = 15$ and $m = 20$, whereas a $\sim$20% increase is expected in the double-Rouse picture.

The qualitative changes in viscosity scaling can be more clearly observed by plotting the data as a function of m for various n, with the values of each series normalized by those of $m = 15$: $\eta(n, m)/\eta(n, 15)$. This ratio should increase as $\sim (m/15)^{2/3}$ for the double Rouse model, so we expect a function which increases substantially, although sub-linearly. The results are shown in Figure 6.21 for $n = 1$, 5, and 25 for both the SACF and Rouse-mode viscosities. For simple ring polymers ($n = 1$), the viscosities do indeed increase linearly, as expected. As n increases, the data points in the central region ($m = 20, 30$) are systematically reduced; in the SACF data, these values actually become smaller than the initial value, indicating decreases in viscosity with increasing m, as pointed out above. The same general trend is also observed in the Rouse-mode based data, but in a milder form, with no values falling below unity. Thus, although the Rouse relaxation times plus Eq. 6.12 are not quantitatively consistent with the SACF results, they do at least suggest some of the same unusual trends. Therefore, it seems likely that the same physics is responsible for the mode-dependent variations in friction (cf. Sections 6.4 and 6.5) and the unusual m-dependence of the viscosity, even if the two effects do not lead to the same quantitative predictions.

As discussed above in the context of $G(t)$, it is possible that unusual m-dependence at large n can be explained by inter-ring stresses (see Figure 6.18 and related discussion). For instance, if such stresses/correlations exist, they should become smaller in magnitude as m is increased; moreover, these stresses should relax more quickly for larger rings as the macrocycles would be able to move more easily. However, above a certain ring size, these

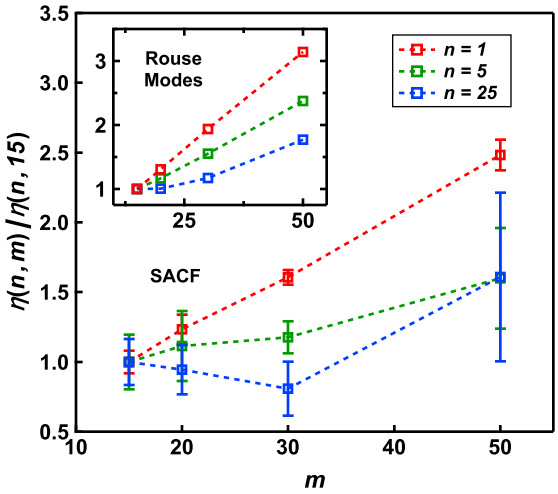

Figure 6.21: Viscosity for poly[n]catenanes of various n as a function of m normalized by the viscosity for $m = 15$. Data in the main figure is calculated from the stress autocorrelation function (SACF) and data in the inset is calculated by summing the Rouse mode relaxation times per Eq. 6.12 (the main figure axis labels apply to the inset as well).

stresses would be so small and relax so quickly that they ought to be inconsequential; for such ring sizes, we should recover the expected Rouse-like scaling, where viscosity increases with m. In the systems studied here, it would seem that such correlations are no longer important for $m > 30$, hence the ideal-like scaling for $m = 50$. The hypothesis of inter-ring stresses is also consistent with the data presented in Figure 6.21: clearly, such stresses would be more prominent in doubly threaded rings compared to the singly threaded chain ends. Since the relative number of chain ends decreases for larger n, we expect that any anomalous scaling would be more pronounced for larger n. While this is an intuitively appealing explanation, it requires that the inter-ring stresses are much more long-lived than the intra-ring ones or even the stresses associated with short segmental modes, which would be quite unusual. Moreover, it is not clear how one would measure or analyze such stresses (if they do indeed exist) owing to the symmetries of the rings, which complicate such efforts (see Section A.6). Further study on single-molecule and/or small-n systems may prove useful in these endeavors.

There are other polymer systems for which the viscosity is known to decrease with in-

creasing molecular weight. For instance, adding or lengthening side chains in comb or bottlebrush polymers is known to reduce melt viscosity by reducing the number of interchain entanglements, depending on the architectural parameters of the brush [10, 264]. This disentanglement results from the increased tube diameter of the brush backbone while the effective Kuhn length and therefore primitive path length may be only slightly modified [261, 262]. However, this is not the mechanism operating in poly[n]catenanes as increases in m will not simply expand the tube (even if this concept is relevant), but will also increase the contour length, so that changes in the entanglement properties are ameliorated. Indeed, as discussed in the previous chapter on the structural parameters of poly[n]catenanes, the conservatively estimated entanglement chain length, n_e, is fairly constant for all ring sizes and is considerably larger than even the longest chains considered here ($n/n_e \approx 0.6$). Furthermore, such disentanglement should reduce the chain reorientation/relaxation times or at least change their qualitative scaling with n, but these times increase monotonically with m for all chain lengths and the scaling obeys the Rouse model prediction quite faithfully (Figure 6.12). Moreover, the fact that the viscosity does indeed increase with m for $m > 30$ suggests that at larger ring sizes more intuitive behavior is obtained, which further highlights the unusual nature of the viscosity at small macrocycle sizes and suggests the presence of other contributions to the stress relaxation.

6.7 Conclusions

In this chapter, the dynamics of unentangled model poly[n]catenanes have been studied by extensive molecular dynamics simulations. To establish a theoretical baseline, a "double-Rouse" model has been formulated and solved exactly. This "ideal" poly[n]catenane model decomposes the dynamics into ring-like and linear-like contributions at short and long times, respectively. This separation introduces a number of intriguing dynamical signatures which are indeed observed in simulations. For instance, the monomer motion exhibits numerous

sub-diffusive regimes with apparent power-law exponents as low as 0.3, despite the lack of inter-chain entanglement. This behavior can be explained qualitatively by Rouse-like motion of the rings at short times and Rouse-like motion of the overall chain at long times, with a transition period in between, all of which are predicted by the double-Rouse model. The stress relaxation of the systems also shows clear ring-like and chain-like contributions, separated by a regime of very fast stress relaxation, again consistent with the double-Rouse picture. The model also predicts the correct scaling behavior of the ring and chain relaxation times.

Although the double-Rouse model is qualitatively consistent with the dynamical properties mentioned above, it is unable to capture the topological effects of the mechanical bonds, which lead to qualitatively different dynamics at intermediate length and time scales in the simulated systems. For instance, the dynamics at long length scales within the macrocycles or at short length scales within the overall chain lead to inconsistent (i.e. mode-dependent) measures of effective friction. Moreover, the dynamics do not always obey the anticipated dependence on ring size. However, the most puzzling observation is that the viscosity has a non-monotonic dependence on macrocycle size for large chain lengths, with intermediate ring sizes leading to smaller values. This behavior is inconsistent with both the observed conformational relaxation times and the entanglement properties of the systems and cannot be explained by the double-Rouse model, even when the empirically determined relaxation times are used for the analysis. Since the double-Rouse model neglects all inter-ring correlations, it is possible that related stresses may be responsible for these observations, but further study is required.

For many decades, chemists have eagerly pursued poly[n]catenanes as the ideal interlocking polymer architecture. The large number of mechanical bonds within the polymers led some to speculate that the molecules would have excellent energy damping properties and rapid stress relaxation [17, 19, 20]. It was supposed that the low activation energy for

ring "rotation" (and therefore chain motion) would be the primary driver for these dynamics. But even the crude double-Rouse model presented here - in which relative motion of the rings is completely uninhibited - does not lead to any particularly unusual consequences and can indeed offer some qualitative agreement with the simulation data. Furthermore, the mechanical bond actually slows down the dynamics of the polymers considerably, which ought to lead to slower, not faster, stress relaxation. Nevertheless, the stress relaxation is indeed surprising: no straightforward arguments can explain the non-monotonic dependence of the viscosity on ring size for large n. The precise origin of these rheological properties is unclear, but the evidence presented in this work serves to eliminate a number of possible explanations and offer a plausible hypothesis: the mechanical bonds may introduce long-lived inter-ring correlations which contribute to the system stress. As the macrocycles become larger, these stresses are reduced, and the system may return to dynamics consistent with the double-Rouse model.

CHAPTER 7

CONCLUSIONS AND OUTLOOK

In this dissertation, we have presented the results of molecular simulations of poly[n]catenanes in solution and in the melt and established foundational knowledge regarding the physics of these systems. Our results, particularly with regards to dynamics, demonstrate that poly[n]catenanes are not merely a chemical curiosity but rather a novel polymer architecture with unique and unexpected dynamical properties. The large number of topological interactions in the system leads to abnormal segmental dynamics at intermediate length scales and to non-intuitive and fascinating viscoelastic properties, making them excellent candidates for further synthesis and research.

From a theoretical perspective, we have demonstrated that poly[n]catenanes (and catenated polymers in general) possess high degrees of symmetry which can considerably simplify otherwise intractable mathematics. Having used these symmetries to develop new Brownian dynamics simulation algorithms, we can now study a wide variety of interlocking polymer systems in myriad conditions, both equilibrium and non-equilibrium. In particular, DNA-based kinetoplasts and Olympic gels represent experimentally relevant systems whose dynamics can now be studied. The behavior of catenated polymers in shear and extensional flows is also a promising avenue of research. Many authors have demonstrated a complex coupling between topology and hydrodynamics in unlinked ring polymers but the topic remains unexplored in catenanes.

In the melt state, it is clear that macrocycle size will be a key design parameter for poly[n]catenane materials which may be exploited by chemists and materials engineers to control the dynamical properties of these polymers. However, the reasons for the unusual stress relaxation in poly[n]catenane melts is not yet clear. Additional studies of polymeric [2]catenanes or more direct quantification of inter-ring stresses may prove useful in this regard.

Although many of the systems studied in this work were idealized model polymers, this restriction must be lifted in the future. As demonstrated in the Chapters 2 and 3, the behaviors of poly[n]catenanes will be strongly impacted by chemically specific properties such as ring stiffness and anisotropic segment interactions. It is imperative that these interactions be included in coarse-grained models in order for meaningful comparison with future experiments. Although the physics of poly[n]catenanes is a very new field, it has already revealed to us a rich set of phenomena and raised many deep physical questions regarding topology and dynamics, suggesting many exciting directions for future research.

APPENDIX A

SUPPORTING INFORMATION

A.1 Brownian Forces in Linked Ring Polymers

To integrate Eqs. 4.8, we must first find a matrix $\widehat{\boldsymbol{B}}$ that satisfies $\widehat{\boldsymbol{B}}\widehat{\boldsymbol{B}}^T = \widehat{\boldsymbol{H}}$ and that also has the form of Eq. 4.7. Starting from Eq. 4.7, we first split the transformed mobility matrix into inter-ring and intra-ring contributions, $\widehat{\boldsymbol{H}} = \widehat{\boldsymbol{H}}_{\text{inter}} + \widehat{\boldsymbol{H}}_{\text{intra}}$, as follows:

$$\widehat{\boldsymbol{H}}_{\text{inter}} = \boldsymbol{C} \begin{bmatrix} \boldsymbol{h}_0^{11} & \boldsymbol{h}_0^{12} & \dots & \\ \boldsymbol{h}_0^{12} & \boldsymbol{h}_0^{22} & & \\ \vdots & & \ddots & \\ & & & \boldsymbol{h}_0^{nn} \end{bmatrix} \equiv \boldsymbol{C} \otimes \widehat{\boldsymbol{H}}'_{\text{inter}} \tag{A.1}$$

$$\widehat{\boldsymbol{H}}_{\text{intra}} = \begin{bmatrix} \widehat{\boldsymbol{G}}^{11} & \boldsymbol{0} & \dots & \\ \boldsymbol{0} & \widehat{\boldsymbol{G}}^{22} & & \\ \vdots & & \ddots & \\ & & & \widehat{\boldsymbol{G}}^{nn} \end{bmatrix} \tag{A.2}$$

where we have defined the $n \times n$ matrix $\widehat{\boldsymbol{H}}'_{\text{inter}}$ in Eq. A.1 and $\widehat{\boldsymbol{G}}^{\alpha\alpha} = \widehat{\boldsymbol{H}}^{\alpha\alpha} - \boldsymbol{h}_0^{\alpha\alpha}\boldsymbol{C}$ in Eq. A.2.

We now notice that square roots can be found quite easily for both $\widehat{\boldsymbol{H}}_{\text{inter}}$ and $\widehat{\boldsymbol{H}}_{\text{intra}}$. In particular, since $\boldsymbol{C}^T = \boldsymbol{C}$ and $\boldsymbol{C}^T\boldsymbol{C} = \boldsymbol{C}$, finding the square root (or other decomposition) of $\widehat{\boldsymbol{H}}_{\text{inter}}$ is equivalent to finding the square root (or other decomposition) of the much smaller matrix $\widehat{\boldsymbol{H}}'_{\text{inter}}$. In the context of a BD simulation, a Cholesky decomposition is typically used for such an operation so that this simplification reduces the computational complexity

from $\mathcal{O}(n^3m^3)$ to $\mathcal{O}(n^3)$. Since m is on the order of tens to hundreds, the computational speed up is tremendous. This computation yields a matrix $\widehat{\boldsymbol{B}}_{\text{inter}} = \boldsymbol{C} \otimes \widehat{\boldsymbol{B}}'_{\text{inter}}$ where $\widehat{\boldsymbol{B}}'_{\text{inter}}\widehat{\boldsymbol{B}}'^{T}_{\text{inter}} = \widehat{\boldsymbol{H}}'_{\text{inter}}$. The matrix $\widehat{\boldsymbol{H}}_{\text{intra}}$ is also easy to handle as it is fully diagonal, so a square root is immediately found by taking the square root of each of its elements. Computationally, this is an $\mathcal{O}(nm)$ operation. The result is a new diagonal matrix $\widehat{\boldsymbol{B}}_{\text{intra}}$ with elements $\widehat{\boldsymbol{B}}^{\alpha\alpha}$ of the same form as Eq. A.2 above.

Crucially, the matrices $\widehat{\boldsymbol{G}}^{\alpha\alpha}$, and therefore $\widehat{\boldsymbol{B}}^{\alpha\alpha}$, are diagonal with zeros in their upper left corners. As a result, we have $\widehat{\boldsymbol{B}}^{\alpha\alpha}\boldsymbol{C} = \boldsymbol{C}\widehat{\boldsymbol{B}}^{\alpha\alpha} = 0$, which further implies that $\widehat{\boldsymbol{B}}_{\text{intra}}\widehat{\boldsymbol{B}}^{T}_{\text{inter}} = \widehat{\boldsymbol{B}}_{\text{inter}}\widehat{\boldsymbol{B}}^{T}_{\text{intra}} = 0$. This result indicates that $\widehat{\boldsymbol{B}}$ can be calculated by simply summing $\widehat{\boldsymbol{B}}_{\text{inter}}$ and $\widehat{\boldsymbol{B}}_{\text{intra}}$:

$$\widehat{\boldsymbol{B}}\widehat{\boldsymbol{B}}^{T} = \left(\widehat{\boldsymbol{B}}_{\text{inter}} + \widehat{\boldsymbol{B}}_{\text{intra}}\right)\left(\widehat{\boldsymbol{B}}_{\text{inter}} + \widehat{\boldsymbol{B}}_{\text{intra}}\right)^{T} = \widehat{\boldsymbol{B}}_{\text{inter}}\widehat{\boldsymbol{B}}^{T}_{\text{inter}} + \widehat{\boldsymbol{B}}_{\text{intra}}\widehat{\boldsymbol{B}}^{T}_{\text{intra}} = \tag{A.3}$$

$$\widehat{\boldsymbol{H}}_{\text{inter}} + \widehat{\boldsymbol{H}}_{\text{intra}} = \widehat{\boldsymbol{H}} \tag{A.4}$$

Since $\widehat{\boldsymbol{B}}_{\text{inter}}$ and $\widehat{\boldsymbol{B}}_{\text{intra}}$ have the same form as $\widehat{\boldsymbol{H}}_{\text{inter}}$ and $\widehat{\boldsymbol{H}}_{\text{intra}}$, i.e. Eqs. A.1 and A.2 respectively, the sum $\widehat{\boldsymbol{B}}$ will have the same form as $\widehat{\boldsymbol{H}}$, i.e. Eq. 4.7. Furthermore, if we denote the elements of $\widehat{\boldsymbol{B}}'_{\text{inter}}$ by $\boldsymbol{b}_0^{\alpha\beta}$ and the (diagonal) elements of $\widehat{\boldsymbol{B}}_{\text{intra}}$ by $\boldsymbol{b}_q^{\alpha\alpha}$ $(1 \leq q \leq m)$, we arrive at the Eqs. 4.8. In summary, the decomposition of $\widehat{\boldsymbol{H}}$ may be achieved by two fast operations ($\mathcal{O}(n^3)$+$\mathcal{O}(nm)$) rather than one slow one, as in ordinary Cholesky decomposition during BD simulations ($\mathcal{O}(n^3m^3)$).

A.2 System Preparation for Poly[n]catenane Melts

Due to very long relaxation times, simulations of high-MW linear polymers require sophisticated techniques for efficient and proper equilibration [265–268]. Unfortunately, many of these methods allow for chain crossings or otherwise alter the molecular topology and therefore cannot be applied to poly[n]catenanes; brute force equilibration must therefore be used.

The systems studied here were prepared by a multi-step process:

1. A single, isolated poly[n]catenane was constructed and simulated for $5\times10^5\tau$ to achieve an equilibrium conformation. Note that this time period is many times the longest relaxation time of the isolated molecule (even for the largest n and m values).

2. The molecule was duplicated and placed with random orientation at the vertices of a large cubic lattice while ensuring that no two molecules were overlapping.

3. The system was evolved according to the production parameters given in the main text under the additional influence of a Berendsen barostat [269] with a time constant of 2τ and a pressure of $5\epsilon/\sigma^3$ to compress it while recording particle coordinates periodically.

4. A configuration with density close to the target value ($\rho = 0.85\sigma^{-3}$) was selected and box dimensions were adjusted to precisely match the desired density.

5. The system was equilibrated for $10^6 - 10^7\tau$, depending on its size (see Table A.1 for details, "Equil. #1").

6. To generate independent realizations for statistical analysis, the final configuration from Step 5 was given new particle velocities (drawn from a Boltzmann distribution) and evolved for an additional $10^6 - 5\times10^6\tau$, depending on the system size (Table A.1, "Equil. #2"). The process was repeated to generate five independent realizations of the system. The resulting configurations were used as the starting points for production simulations.

After this procedure, the systems are well-equilibrated by several common measures. During Step 5 above, it is observed that the poly[n]catenane center-of-mass mean-squared-displacement reaches values several times larger than the polymer size and that the average end-to-end vector autocorrelation function completely decays well before the end of the equilibration period (note that the end-to-end vector is defined by the centers-of-mass of

the chain end macrocycles as discussed in the main text). Furthermore, both equilibration periods are much longer than the longest relaxation times of the polymers (see Figure 6.12).

Table A.1: Summary of poly[n]catenane systems studied and the equilibration/production simulation times.

$\mathcal{N}$	n	m	Equil. #1 (τ)	Equil. #2 (τ)	Prod. (τ)
500	1	15 - 50	10^6	10^6	10^6
250	2	15 - 50	10^6	10^6	10^6
250	3	15 - 50	10^6	10^6	10^6
200	5	15 - 50	10^6	10^6	10^6
200	7	15 - 50	10^6	10^6	10^6
200	10	15 - 30	10^6	10^6	10^6
200	10	50	5×10^6	10^6	5×10^6
150	15	15 - 30	5×10^6	10^6	2×10^6
150	15	50	5×10^6	10^6	5×10^6
100	20	15 - 30	5×10^6	10^6	3.5×10^6
100	20	50	5×10^6	2.5×10^6	5×10^6
100	25	15 - 30	5×10^6	10^6	5×10^6
100	25	50	10^7	2.5×10^6	$\times 10^7$

Equilibration was also confirmed by examining polymer conformations directly. For linear polymer melts, the reduced mean squared internal distances (Eq. 3.12) are often used as an "objective function" to assess equilibration [266]. These values can be obtained directly from simulation trajectories and then used to assess system equilibration for any N. As the conformations of poly[n]catenanes are qualitatively similar to those of linear polymers at large length scales [21, 22, 222], a similar measure may be employed for these systems. In analogy with linear polymers, this objective function should be independent of n and l for large l. Systems of long poly[n]catenanes are evaluated by comparing the mean squared internal distances to those of a slightly shorter polymers; n is built up gradually from $n = 1$ to 25, ensuring proper equilibration along the way. The reduced mean squared internal distances are shown in Figure A.1a for poly[n]catenane systems with $n > 3$. The data are averaged over the final 10-50% of the first equilibration period (Step 5, above). For

each value of m, the data for all n and l are in excellent quantitative agreement, indicating well-equilibrated chain structures. At large l, the values decrease slightly, diverging from the apparent master curves. These deviations are caused by shortened mechanical bond lengths at the chain ends (Figure A.1b). The chain ends contribute more strongly to the mean internal distances at larger l, thus lowering the values. In Figures A.1a and A.1b, the data sets achieve plateau values at large distances. These plateau values are related to the squared effective bond length, b_{eff}^2, and the central bond length, b_c, of the polymers (Table 5.2), respectively, and are discussed in Section 5.5.

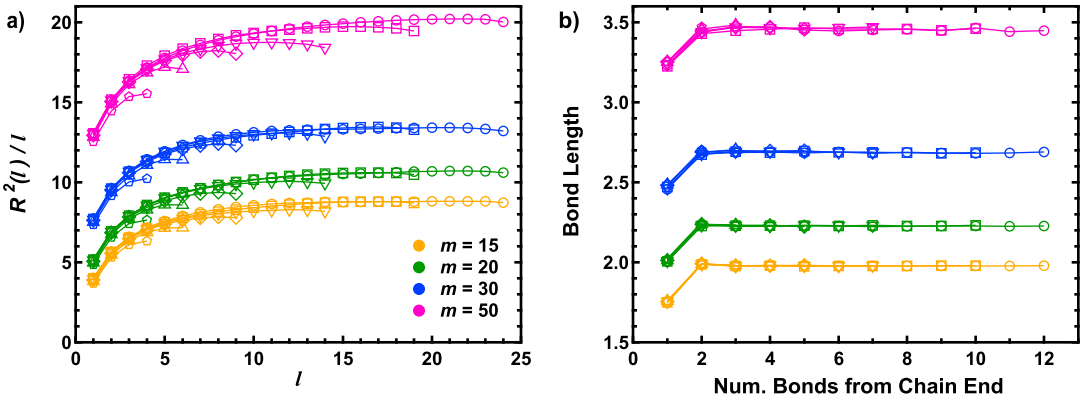

Figure A.1: a) Reduced mean-squared internal distances for poly[n]catenanes of various ring sizes, m (Eq. 3.12). b) Mechanical bond length as a function of the number of bonds away from the catenane chain end. The different symbols indicate different values of n: 5 (pentagons), 7 (triangles), 10 (diamonds), 15 (downward triangles), 20 (squares), and 25 (circles).

Linear polymer systems were equilibrated by the DPD push off method [267], followed by an additional equilibration period of $10^6\tau$. To generate independent samples for statistical analysis, the particles were given new velocities and equilibrated for a further $10^6\tau$ to generate five independent realizations of each system to use as starting points for production simulations. See Table A.2 for details of the linear systems studied in this work. As with the poly[n]catenanes, the mean squared internal distances were used to validate the systems and the results (not shown) agree quantitatively with the existing literature [266].

Table A.2: Summary of linear polymer systems studies and the production simulation times.

$\mathcal{N}$	N	Prod. (τ)
500	15	10^6
500	20	10^6
500	30	10^6
500	45	10^6
500	60	10^6
500	80	10^6
500	100	10^6
500	150	3×10^6
500	175	5×10^6

A.3 Poly[n]catenane Dimensions

The mean-squared radius of gyration of a poly[n]catenane can be calculated from the average distance between all pairs of beads in the polymer according to the formula:

$$R_g^2 = \frac{1}{2N^2} \sum_{i,j=1}^{N} \langle x_{ij}^2 \rangle \tag{A.5}$$

where $N = nm$ and $\langle x_{ij}^2 \rangle$ is the mean-squared distance between beads i and j. R_g^2 is therefore calculated by evaluating each of the terms in the symmetric $N \times N$ matrix $\langle x_{ij}^2 \rangle$. It is convenient to break up this matrix into blocks of size $m \times m$, such that the diagonal blocks represent the distances between beads on the same ring and off-diagonal ones represent the distances between beads on different rings. Making the approximation that all n rings are statistically identical and ignoring chain end effects, Eq. A.5 can be rewritten as:

$$R_g^2 \approx \frac{1}{2N^2} \left[n \sum_{i,j=1}^{m} \langle x_{\alpha i,\alpha j}^2 \rangle + \sum_{k=1}^{n-1} 2(n-k) \sum_{i,j=1}^{m} \langle x_{\alpha i,(\alpha+k) j}^2 \rangle \right] \tag{A.6}$$

where $\langle x^2_{\alpha i,\beta j}\rangle$ represents the mean-squared distance between bead i on ring α and bead j on ring β. The first term in brackets represents the diagonal blocks of the matrix $\langle x^2_{ij}\rangle$ while the second term represents the off-diagonal ones. The diagonal blocks are evaluated directly using Eq. A.5 applied to individual macrocycles:

$$R^2_{g,r} = \frac{1}{2m^2}\sum_{i,j=1}^{m}\langle x^2_{\alpha i,\alpha j}\rangle \tag{A.7}$$

Rearranging Eq. A.7 and substituting into the first term in brackets in Eq. A.6, one finds:

$$R^2_g \approx \frac{1}{2N^2}\left[2nm^2R^2_{g,r} + \sum_{k=1}^{n-1}2(n-k)\sum_{i,j=1}^{m}\langle x^2_{\alpha i,(\alpha+k)j}\rangle\right] \tag{A.8}$$

The off-diagonal components (second term in brackets in Eq. A.8) can also be computed under certain approximations. To do so, $\langle x^2_{\alpha i,\beta j}\rangle$ is expressed as the sum of a series of vectors:

$$\langle x^2_{\alpha i,\beta j}\rangle = \langle[(\boldsymbol{R}_{\alpha i} - \boldsymbol{R}_{\alpha,\mathrm{cm}}) + (\boldsymbol{R}_{\alpha,\mathrm{cm}} - \boldsymbol{R}_{\beta,\mathrm{cm}}) - (\boldsymbol{R}_{\beta j} - \boldsymbol{R}_{\beta,\mathrm{cm}})]^2\rangle \tag{A.9}$$

where $\boldsymbol{R}_{\alpha i}$ is the position of bead i on ring α and $\boldsymbol{R}_{\alpha,\mathrm{cm}}$ is the position of the center-of-mass of ring α. The three vectors in Eq. A.9 are approximated as statistically independent, which is not the case for neighboring (i.e. linked) rings especially at small m, but should be fairly accurate for separations greater than the Kuhn length and therefore suffices for a first approximation. Expanding the square and evaluating the average, all cross terms disappear:

$$\langle x^2_{\alpha i,\beta j}\rangle \approx \langle(\boldsymbol{R}_{\alpha i} - \boldsymbol{R}_{\alpha,\mathrm{cm}})^2 + (\boldsymbol{R}_{\alpha,\mathrm{cm}} - \boldsymbol{R}_{\beta,\mathrm{cm}})^2 - (\boldsymbol{R}_{\beta j} - \boldsymbol{R}_{\beta,\mathrm{cm}})^2\rangle \tag{A.10}$$

It is now helpful to recall that the radius of gyration of a polymer of N segments can also be expressed as the average mean squared distance between each particle and the polymer

center-of-mass, denoted $\boldsymbol{R}_{\rm cm}$:

$$R_g^2 = \frac{1}{N}\sum_{i=1}^{N}\langle(\boldsymbol{R}_i - \boldsymbol{R}_{\rm cm})^2\rangle \tag{A.11}$$

Summing Eq. A.10 over all i and j, substituting Eq. A.11 and assuming Gaussian statistics for the ring center of mass separations, we find:

$$\sum_{i,j=1}^{m}\langle x_{\alpha i,\beta j}^2\rangle \approx 2m^2R_{g,r}^2 + m^2|\beta-\alpha|b_{\rm eff}^2 \tag{A.12}$$

This expression is substituted into Eq. A.8 to obtain:

$$R_g^2 \approx \frac{1}{2N^2}\left[2nm^2R_{g,r}^2 + \sum_{k=1}^{n-1}2(n-k)(2m^2R_{g,r}^2 + km^2b_{\rm eff}^2)\right] \tag{A.13}$$

The sum can now be evaluated directly and the pre-factor distributed among each of the terms. Making the substitution $N = nm$, the result reads:

$$R_g^2 \approx \frac{nb_{\rm eff}^2}{6} + R_{g,r}^2 + \frac{b_{\rm eff}^2}{6n} \tag{A.14}$$

To estimate the effective scaling of Eq. A.14 with n, the logarithmic derivative is calculated:

$$\nu = \frac{1}{2}\frac{d\log R_g^2}{d\log n} = \frac{n}{2R_g^2}\frac{dR_g^2}{dn} \tag{A.15}$$

Evaluating Eq. A.15 up to order n^{-1}, the result after some manipulation is:

$$\nu \approx \frac{1}{2} - \frac{3R_{g,r}^2}{R_e^2} \tag{A.16}$$

where $R_e^2 = (n-1)b_{\rm eff}^2$ is the end-to-end distance squared, defined as the mean squared distance between the centers-of-mass of chain end macrocycles. The latter follows from the

assumption of Gaussian statistics for the ring center-of-mass separations invoked prior to Eq. A.12.

A.4 Rouse Model for General Polymer Architectures

Here the Rouse model [169] is reviewed for macromolecules of arbitrary architecture and a number of useful relationships are derived for use in the main text. The specific application to poly[n]catenanes is discussed in Section A.5 of this document. The macromolecule is represented as an assembly of N beads connected by harmonic springs, undergoing overdamped Brownian motion. Since the bonds are harmonic, the forces are given by linear combinations of the bead positions, so the equation of motion for all N beads can be written in the succinct form:

$$\xi \frac{d\boldsymbol{R}}{dt} = -\boldsymbol{\Pi} \cdot \boldsymbol{R} + \boldsymbol{f}(t) \tag{A.17}$$

where ξ is the segment or monomer friction constant, $\boldsymbol{R} \equiv (\boldsymbol{R}_1, \boldsymbol{R}_1, ..., \boldsymbol{R}_N)$ is a vector of bead positions, $\boldsymbol{\Pi}$ is a matrix describing the bead connectivity, and $\boldsymbol{f}(t)$ is a vector of Gaussian random variables that satisfy the fluctuation dissipation theorem:

$$\langle f_i^{\alpha}(t) \rangle = 0 \tag{A.18}$$

$$\langle f_i^{\alpha}(t) f_j^{\beta}(t') \rangle = 2k_B T \xi \delta_{ij} \delta_{\alpha\beta} \delta(t - t') \tag{A.19}$$

where i, j indicate bead numbers/indices and α, β indicate spatial dimensions.

As long as the forces act between beads (or linear combinations thereof), the matrix $\boldsymbol{\Pi}$ will be real and symmetric, and each of its rows will sum to zero, regardless of the precise architecture. Any information about the strength of the bonds (i.e. spring constants) has been subsumed into $\boldsymbol{\Pi}$ such that its entries have units of energy per length-squared. Because of the aforementioned properties, $\boldsymbol{\Pi}$ can be diagonalized by an orthogonal matrix, $\boldsymbol{U}$; one of

the associated eigenvalues will be zero and the others will be positive. The zero eigenvalue is related to the polymer center-of-mass and does not contribute to stress or orientational relaxations. Using the orthonormal basis set to transform Eq. A.17, the resulting equation of motion is:

$$\xi \frac{d\boldsymbol{X}}{dt} = -\boldsymbol{\lambda} \cdot \boldsymbol{X} + \boldsymbol{g}(t) \tag{A.20}$$

where $\boldsymbol{X} = \boldsymbol{U}^T \cdot \boldsymbol{R}$ and $\boldsymbol{g}(t) = \boldsymbol{U}^T \cdot \boldsymbol{f}(t)$, and $\boldsymbol{\lambda}$ is a diagonal matrix with each entry given by an eigenvalue of $\boldsymbol{\Pi}$. Note that because $\boldsymbol{U}$ is orthogonal, the statistical properties of $\boldsymbol{g}(t)$ are the same as those of $\boldsymbol{f}(t)$ (cf. Eqs. A.18 A.19). The elements of $\boldsymbol{X}$ are the normal modes for the polymer and their motions are decoupled due to the diagonal character of $\boldsymbol{\lambda}$, which has elements denoted as λ_p. Thus, a separate, independent equation of motion can be written for each mode. For all modes $p > 0$, taking the dot product of each of these equation with the initial value of the corresponding mode, $\boldsymbol{X}_p(0)$, and performing an ensemble average results in a differential equation for the autocorrelation functions of the modes. The solution is:

$$\langle \boldsymbol{X}_p(0) \cdot \boldsymbol{X}_p(t) \rangle = \langle X_p^2 \rangle \exp\left(-\frac{t}{\tau_p}\right) \tag{A.21}$$

where the characteristic times are defined as $\tau_p = \xi/\lambda_p$ and the mean-square amplitudes are given by $\langle X_p^2 \rangle = 3k_B T/\lambda_p$ according to the equipartition theorem. For the center-of-mass mode ($p = 0, \lambda_p = 0$), the equation of motion results in ordinary random walk behavior with a diffusion coefficient $D = k_B T/N\xi$ [13]. The dynamics of the polymer (and its monomers) can be described entirely in terms of the center-of-mass diffusion and the autocorrelation functions.

The above results rely on the harmonic nature of the bonds and the absence of excluded volume or other non-covalent interactions. Any anharmonicity in the Hamiltonian will invalidate the simple equation of motion, and the resulting modes will no longer be orthogonal so that cross-correlations are also needed to describe the dynamics. Such interactions and

correlations are most pronounced at short length scales along the polymer backbone, which is why the Rouse model is most successful at larger scales, provided the molecules are not subject to topological constraints.

All information about monomer/bead connectivity is contained in the matrix $\mathbf{\Pi}$. Therefore, the results above are applicable to any polymer architecture as we only made use of properties of $\mathbf{\Pi}$ that are generically true for any topology. For certain simple architectures (e.g. linear and cyclic polymers), analytical solutions for the eigenvalues and eigenvectors can be obtained. In these cases, the structure of the eigenvectors/values can be used to gain physical insight into the dynamics of the system. However, for more complicated architectures, this may not be possible. Nevertheless, exact solutions for the dynamics can always be obtained numerically as done in practice to generate the data in Figures 6.8 and 6.9 of the main text.

Some results are now presented which are used to analyze the dynamics of poly[n]catenanes in the main text. In simulations, the mean-square amplitudes of the modes as well as effective relaxation times, τ_p^{eff}, can be directly measured. Using these two quantities and the relationships above, the effective friction coefficient may be defined:

$$\xi_p^{\text{eff}} = \frac{3k_BT\tau_p^{\text{eff}}}{\langle X_p^2 \rangle} \tag{A.22}$$

For ideal Rouse-type dynamics, this value will not depend on the mode number, p. However, deviations from a constant value can be interpreted as non-ideal behavior at certain length/time scales, although the physical interpretation may not be so simple depending on the architecture as this information is encoded in the eigenvectors. A similar effective friction can also be defined in terms of the empirically measured diffusion constant, D:

$$\xi_D^{\text{eff}} = \frac{k_BT}{ND} \tag{A.23}$$

The monomer mean-squared-displacements considered in Section 4 can also be expressed in terms of the mode amplitudes and relaxation times. Without loss of generality, the equations are non-dimensionalized by dividing by the mean squared bond length and incorporating the friction constant ξ and thermal energy k_BT into the unit of time. To start, consider $g_1(t)$ (Eq. 6.1) for a specific monomer, labeled i. Applying the inverse transformation $\boldsymbol{R} = \boldsymbol{U} \cdot \boldsymbol{X}$:

$$g_1^i(t) = \langle [\boldsymbol{R}_i(t) - \boldsymbol{R}_i(0)]^2 \rangle = \sum_{p,q} U_{ip} U iq \langle [\boldsymbol{X}_p(t) - \boldsymbol{X}_p(0)] \cdot [\boldsymbol{X}_q(t) - \boldsymbol{X}_q(0)] \rangle \tag{A.24}$$

where the sums over p and q run from zero to $N-1$. Since the modes are orthogonal, the ensemble average will eliminate all cross terms in the sum. The resulting expression is:

$$g_1^i(t) = \sum_p U_{ip}^2 \langle [\boldsymbol{X}_p(t) - \boldsymbol{X}_p(0)]^2 \rangle \tag{A.25}$$

The first term in the sum ($p = 0$) corresponds to the mean-squared displacement of the center-of-mass and the associated eigenvector always has elements equal to $U_{i0} = N^{-1/2}$, regardless of architecture, since the rows of $\boldsymbol{\Pi}$ all sum to zero. As a result, the contribution from this term is proportional to t/N as the polymer center-of-mass undergoes ordinary diffusion. The rest of the terms in the sum can be found by expanding the dot product and evaluating the ensemble averages, which can be expressed in terms of the mean-square mode amplitudes and the autocorrelation functions. The result is:

$$g_1^i(t) = \frac{6t}{N} + \sum_{p=1}^{N-1} 2U_{ip}^2 \langle X_p^2 \rangle \left[1 - \exp\left(-\frac{t}{\tau_p} \right) \right] \tag{A.26}$$

For certain cases where symmetries exist (for example, ring polymers), it may be useful to

average this function over all monomers. The function then takes the form:

$$g_1(t) = \frac{6t}{N} + \frac{2}{N}\sum_{p=1}^{N-1}\langle X_p^2\rangle\left[1 - \exp\left(-\frac{t}{\tau_p}\right)\right] \tag{A.27}$$

For orthogonal, Gaussian modes, the stress relaxation modulus can be written as a sum of exponentials [13]:

$$G(t) = \frac{\rho k_B T}{N} + \sum_{p=1}^{N-1}\exp\left(-2t/\tau_p\right) \tag{A.28}$$

where ρ is the monomer number density. The zero shear-rate viscosity follows by integration:

$$\eta = \frac{\rho k_B T}{2N}\sum_{p=1}^{N-1}\tau_p \tag{A.29}$$

Some qualitative results for Rouse-like dynamics can also be obtained by dimensional analysis and dynamical scaling arguments for arbitrary polymer architectures [13]. For instance, if macromolecule size scales as $R \sim N^{\nu}$, then the diffusion constant still scales as $D \sim 1/N$, but the longest polymer relaxation time, τ_R, scales as $\tau_R \sim N^{1+2\nu}$. In analogy to Eq. A.29, the viscosity can be approximated at the scaling level as $\eta \sim \tau_R/N \sim N^{2\nu}$.

A.5 Double-Rouse Model for Poly[n]catenanes

Having reviewed the Rouse model for general polymer architectures, it is now applied to poly[n]catenanes and the results are examined. Consider n independent ring polymers of m beads, each of which is described by the Rouse model. The energy is augmented with additional harmonic bonds that act on the centers-of-mass of the rings maintaining an overall linear architecture. Since the forces are all harmonic and act only between the beads (or between positions given by linear combinations of beads), the interaction matrix $\mathbf{\Pi}$ will have all the properties necessary for the relationships in Section A.4 above to hold true. Denoting

the position of the j^{th} bead in the i^{th} ring as $\boldsymbol{R}_{i,j}$, the effective energy function is:

$$U(\boldsymbol{R}) = \sum_{i=1}^{n}\sum_{j=1}^{m}\frac{k_r}{2}\left(\boldsymbol{R}_{i,j} - \boldsymbol{R}_{i,(j\%m)+1}\right)^2 + \sum_{i=1}^{n-1}\frac{k_c}{2}\left[\left(\frac{1}{m}\sum_{j=1}^{m}\boldsymbol{R}_{i,j}\right) - \left(\frac{1}{m}\sum_{j=1}^{m}\boldsymbol{R}_{i+1,j}\right)\right]^2 \quad \text{(A.30)}$$

where the spring constants k_r and k_c represent the strength of bonds between beads within rings and between ring centers-of-mass, respectively; in general, these are different. Note that the modulo operator is required to ensure proper boundary conditions for the ring polymers. In this model, the mechanical bonds are introduced explicitly in the effective energy function; in real interlocking polymers, these bonds are more accurately described by restrictions on the phase space integral [69, 70]. Nevertheless, in the search for an analytically tractable model, the explicit bonds between ring centers-of-mass serve the required purpose of ensuring chain connectivity in a simple manner.

To obtain analytic expressions for the dynamics, the gradient of $U(\boldsymbol{R})$ is used to generate an interaction matrix, which is then diagonalized. However, it is helpful to first deduce the basic form of the result based on intuitive arguments. Since the center-of-mass position evolves independently in the Rouse model, forces acting on it will not affect any of the other normal modes. Thus, one may anticipate that the solution of the double-Rouse model will be a superposition of the linear and ring Rouse model results. This is in fact the case, and

the full interaction matrix can be diagonalized by the following set of normal modes:

$$\boldsymbol{X}_{p,q} = \begin{cases} \left(\frac{1}{nm}\right)^{1/2} \sum_{i=1}^{n}\sum_{j=1}^{m} \boldsymbol{R}_{i,j} & \text{for } p = q = 0 \\ \left(\frac{2}{nm}\right)^{1/2} \sum_{i=1}^{n}\sum_{j=1}^{m} \boldsymbol{R}_{i,j} \cos\left[\frac{p\pi}{n}\left(i - \frac{1}{2}\right)\right] & \text{for } 0 \leq p \leq n-1, q = 0 \\ \left(\frac{2}{nm}\right)^{1/2} \sum_{j=1}^{m} \boldsymbol{R}_{p+1,j} \cos\left(\frac{2\pi jq}{m}\right) & \text{for } 1 \leq q < m/2 \\ \left(\frac{2}{nm}\right)^{1/2} \sum_{j=1}^{m} \boldsymbol{R}_{p+1,j} (-1)^j & \text{for } q = m/2 \\ \left(\frac{2}{nm}\right)^{1/2} \sum_{j=1}^{m} \boldsymbol{R}_{p+1,j} \sin\left(\frac{2\pi jq}{m}\right) & \text{for } m/2 < q \leq m-1 \end{cases} \tag{A.31}$$

Note that the normal modes are most conveniently denoted by two indices, p and q, just as the bead positions were denoted by the two indices i and j; the ranges of allowable values for p (0 to $n-1$) and q (0 to $m-1$), are different from those of i and j. The modes $q = 0$ (first two lines in Eq. A.31) correspond to the overall linear structure of the molecule as they have the same form as the linear Rouse modes but taken with respect to the zeroth Rouse modes of the individual rings [170, 186, 253, 254]. The modes $q > 0$ (last three lines in Eq. A.31) are simply the ordinary ring polymer Rouse modes for the $(p+1)^{\text{th}}$ ring in the catenane [174, 217, 241]. Note that when m is odd, the fourth line is not applicable. These definitions are equivalent to those given in the main text (cf. main text, Eqs. 3.4, 3.7), although with slightly different notation. A formal (and very tedious) calculation is also possible and yields the same results. In practice, only line 3 or 5 in Eq. A.31 needs be considered as the two are identical but for a shift in indices. Thus, in what follows, we consider only modes $1 \leq q \leq m/2$. The corresponding eigenvalues for the modes above are:

$$\lambda_{p,q} = \begin{cases} \frac{4k_c}{m} \sin^2\left(\frac{p\pi}{2n}\right) & \text{for } p > 0, q = 0 \\ 4k_r \sin^2\left(\frac{q\pi}{m}\right) & \text{for } q \neq 0 \end{cases} \tag{A.32}$$

which have the same form as those for linear and ring polymers. Because of the periodic nature of the sine function, each ring eigenvalue (second line in Eq. A.32) appears twice, thus having a degeneracy of two within each ring and a total degeneracy of $2n$ within the whole polymer [174]. With these eigenvalues, one can now make predictions for the relaxation times, monomer motion, and viscoelastic behavior using the results discussed previously for the general Rouse model.

Before continuing, it is helpful to make certain substitutions for the spring constants appearing in the eigenvalues. For harmonic bonds, the spring constant can be related to a length scale by $k = 3k_BT/l^2$ where l is a root-mean-squared bond length. The constant k_r is therefore connected with the covalent bond length, which in turn is taken as the generic unit of length. k_c is expressed in terms of the mean-squared mechanical bond length, b^2, which is now an adjustable parameter in the model and given in units of the covalent bond length defined through k_r. As a result, this model has three parameters: n, m, and b^2. The latter two are not in fact independent since the mechanical bond length will be on the order of the ring dimensions, which depends on m. As a result, the number of independent parameters is reduced to just n and m for practical purposes. Variations in the other parameters such as the friction constant and temperature simply shift the characteristic time scale of the dynamics and do not qualitatively change the results. In what follows, all quantities are non-dimensionalized and the friction constant and k_BT are subsumed into the unit of time.

To obtain scaling relations, it is convenient to adopt a continuum (not discrete bead) perspective [13]. The eigenvalues are expanded up to quadratic order in p/n or q/m and the spectrum of relaxation times is determined to be:

$$\tau_{p,q} = \begin{cases} \dfrac{mn^2b^2}{3\pi^2p^2} & \text{for } p > 0, q = 0 \\ \dfrac{m^2}{12\pi^2q^2} & \text{for } q \neq 0 \end{cases} \tag{A.33}$$

The longest ring relaxation time (second line in Eq. A.33, $q = 1$) therefore scales as $\tau_{R,\text{ring}} \sim$

m^2. However, as discussed in Chapter 5, the ring size does not obey typical Gaussian statistics, so in practice, a scaling of the form $\tau_{R,\text{ring}} \sim m^{1+2\nu}$ is expected (see Section A.4 above) with $\nu \approx 0.4-0.45$ the scaling exponent associated with ring dimensions (e.g. radius-of-gyration) [224], leading to a dependence $\tau_{R,\text{ring}} \sim m^{1.8-1.9}$. For the overall chain, the longest relaxation time (first line in Eq. A.33, $p = 1$) should scale as $\tau_R \sim n^2$ in agreement with the standard Rouse model for linear polymers. This quantity also has an m-dependence, which is found both directly (by a multiplicative factor) and through the mean-squared bond length, b^2. Since the long-length scale behavior is of interest, the effective bond length, b_{eff}, which accounts for chain stiffness effects, should be used in this relation. As described in Chapter 5 [224], this quantity scales approximately as $b_{\text{eff}} \sim m^{1/3}$, leading to an expected scaling of $\tau_R \sim m^{5/3}$ according to Eq. A.33.

The shear stress relaxation modulus for poly[n]catenanes can be found by employing the mode relaxation times of Eq. A.33 and Eq. A.28. However, simply by leveraging the separation of the dynamics into ring-like and linear-like modes, some useful insight can be obtained. In particular, the modulus can be expressed (in non-dimensionalized units, as discussed above) as:

$$G(t) = \frac{\rho}{nm}\sum_{p,q} e^{-2t/\tau_{p,q}} = \frac{\rho}{nm}\left[\sum_{p=0}^{n-1}\sum_{q=1}^{m-1} e^{-2t/\tau_{p,q}} + \sum_{p=1}^{n-1} e^{-2t/\tau_{p,0}}\right] \tag{A.34}$$

where the center-of-mass mode ($p = q = 0$) is to be excluded from the summation. On the right-hand side of Eq. A.34 the first sum inside the brackets represents the ring-like dynamics while the second term represents the chain-like ones. Distributing the pre-factors and using the fact that all n rings have identical relaxation times, the modulus is then given by:

$$G(t) = \frac{\rho}{m}\sum_{q=1}^{m-1}\exp(-2t/\tau_{0,q}) + \frac{\rho}{nm}\sum_{p=1}^{n-1}\exp(-2t/\tau_{p,0}) = G_{\text{ring}}(t;m) + \frac{1}{m}G_{\text{lin}}(t;n,m) \tag{A.35}$$

where $G_{\text{ring}}(t;m)$ and $G_{\text{lin}}(t;n,m)$ are the moduli of a melt of pure rings of size m and a melt of pure linear polymers of size n, respectively, at the specified temperature and density; their dependence on the parameters n and m are emphasized in Eq. A.35.

The viscosity is found by integrating $G(t)$, which is equivalent to summing the relaxation times with the upper limit on the sum now being infinity for both p and q as in the continuum description. Accounting for the degeneracy discussed earlier, the viscosity is:

$$\eta = \frac{\rho}{2nm}\left(\sum_{p=1}^{n-1}\tau_{p,0} + n\sum_{q=1}^{m-1}\tau_{0,q}\right) = \frac{\rho}{72}(2nb^2+m) \tag{A.36}$$

The viscosity has two contributions: one proportional to n (corresponding to the overall chain relaxation) and another proportional to m (which results from the relaxation of the rings). For large n, the first term dominates and the viscosity recovers ordinary Rouse scaling of $\eta \sim n^1$. For relatively small n, the two contributions to the viscosity prevent simple power law scaling as the ring contribution does not depend on n and is effectively an additive constant. As a result, the apparent scaling exponent will be less than unity for small n. Each term in the viscosity also has an m-dependence either directly or indirectly through the bond length, b, which as above is replaced with b_{eff}. In general, the ring radius-of-gyration and the effective bond lengths scale differently [224]. However, for large n, Eq. A.36 indicates that the former will dominate the scaling behavior. Using the approximate relationship $b_{\text{eff}} \sim m^{1/3)}$ we predict a scaling of $\eta \sim m^{2/3}$ for not-too-small n. We further note that the ring dimensions scale faster than the effective bond length, with exponents on the order of 0.4 - 0.45, so that the second term in Eq. A.36 would suggest $\eta \sim m^{2\nu} \sim m^{0.8-0.9}$. Thus, the 2/3 exponent should be considered a lower limit and for small n, larger exponents are expected.

A.6 Cross-Correlations in the Double-Rouse Model

Many of the results presented in the previous two sections rely on the fact that the Rouse modes are orthogonal, i.e. statistically independent. For non-ideal polymers this is not necessarily the case. In this section, cross-correlations in the double-Rouse model are analyzed mathematically and, where applicable, calculated from simulation data.

To begin, consider the coupling between ring-like modes within the same ring, denoted $\boldsymbol{X}_q$ as in the main text (Eq. 3.4), keeping in mind that these modes are equivalent to those of ordinary ring polymers. Cross correlations between different modes, $\phi_{qq'}$ are then evaluated according to:

$$\phi_{qq'} \equiv \langle \boldsymbol{X}_q \cdot \boldsymbol{X}_{q'} \rangle = \left\langle \left(\sum_{i=1}^{m} U_{qi}^T \boldsymbol{R}_i \right) \cdot \left(\sum_{j=1}^{m} U_{q'j}^T \boldsymbol{R}_j \right) \right\rangle \tag{A.37}$$

where $\boldsymbol{R}_i$ is the position of bead i in the ring and $\boldsymbol{U}$ is the Rouse transformation matrix for ring polymers. We ignore the modes $q = 0$ as these correspond to linear-like modes in the double-Rouse model (see Eq. A.31). The translational invariance of the system requires that the modes $q > 0$ do not depend on the ring center-of-mass position, $\boldsymbol{R}_{\mathrm{cm}}$, so this quantity can be subtracted from the bead positions in Eq. A.37 to achieve a more physically intuitive form. Making this substitution and expanding the product, the result is:

$$\phi_{qq'} = \sum_{i,j=1}^{m} U_{qi}^T \langle (\boldsymbol{R}_i - \boldsymbol{R}_{\mathrm{cm}}) \cdot \big(\boldsymbol{R}_j - \boldsymbol{R}_{\mathrm{cm}}\big) \rangle U_{jq'} = \sum_{i,j=1}^{m} U_{qi}^T \mathcal{R}_{ij} U_{jq'} \tag{A.38}$$

where we have defined the matrix $\boldsymbol{\mathcal{R}}$ with elements $\mathcal{R}_{ij} = \langle (\boldsymbol{R}_i - \boldsymbol{R}_{\mathrm{cm}}) \cdot (\boldsymbol{R}_j - \boldsymbol{R}_{\mathrm{cm}}) \rangle$. Eq. A.38 can be rewritten as a compact matrix equation:

$$\boldsymbol{\phi} = \boldsymbol{U}^T \boldsymbol{\mathcal{R}} \boldsymbol{U} \tag{A.39}$$

Since all beads in a ring polymer are statistically identical, each row/column of $\boldsymbol{\mathcal{R}}$ is identical

but for a shift of indices; in other words, the matrix is circulant. Circulant matrices have the convenient property that they all share a known set of eigenvectors. Therefore, since the interaction matrix, $\mathbf{\Pi}$, for ring polymers is also circulant [174, 217, 241], $\mathbf{\Pi}$ and $\boldsymbol{\mathcal{R}}$ share an eigenbasis. Since $\boldsymbol{U}$ diagonalizes $\mathbf{\Pi}$ by definition (see Section A.4 above), the matrix $\boldsymbol{\phi}$ in Eq. A.39 must also be diagonal, so that all cross-correlations between ring-like modes within the same ring vanish identically. This result does not require that the ring polymers be ideal or Gaussian, it only requires that they be closed loops possessing continuous symmetry. Therefore, this finding holds even for non-ideal rings such as those in poly[n]catenanes.

Next, consider the average cross-correlation, $\phi_{qq'}^{\alpha\beta}$, between two Rouse modes with mode numbers q and q' of different rings, α and β. As before, we ignore the center of mass modes ($q = 0, q' = 0$). $\phi_{qq'}^{\alpha\beta}$ can be expressed in a manner similar to Eq. A.38:

$$\phi_{qq'}^{\alpha\beta} = \sum_{i,j=1}^{m} U_{qi}^{T} \left\langle (\boldsymbol{R}_i^{\alpha} - \boldsymbol{R}_{\mathrm{cm}}^{\alpha}) \cdot \left(\boldsymbol{R}_j^{\beta} - \boldsymbol{R}_{\mathrm{cm}}^{\beta} \right) \right\rangle U_{jq'} \tag{A.40}$$

where $\boldsymbol{R}_i^{\alpha}$ is the position of bead i on ring α, $\boldsymbol{R}_{\mathrm{cm}}^{\alpha}$ is the center-of-mass of ring α, and we have defined the matrix $\boldsymbol{\mathcal{R}}^{\alpha\beta}$ with elements $\mathcal{R}_{ij}^{\alpha\beta} = \left\langle (\boldsymbol{R}_i^{\alpha} - \boldsymbol{R}_{\mathrm{cm}}^{\alpha}) \cdot \left(\boldsymbol{R}_j^{\beta} - \boldsymbol{R}_{\mathrm{cm}}^{\beta} \right) \right\rangle$. The elements of the matrix $\boldsymbol{\mathcal{R}}^{\alpha\beta}$ cannot depend on i or j, since, as mentioned above, all beads within ring polymers are statistically identical. The elements $\mathcal{R}_{ij}^{\alpha\beta}$ are therefore all equal and depend only on α and β even for non-ideal (real) catenanes, as they must also possess this symmetry. Setting $\mathcal{R}_{ij}^{\alpha\beta} = \mathcal{R}(\alpha, \beta)$, the double-sum in Eq. A.40 then factorizes into a product of two sums:

$$\phi_{qq'}^{\alpha\beta} = \mathcal{R}(\alpha, \beta) \left(\sum_{i=1}^{m} U_{iq} \right) \left(\sum_{j=1}^{m} U_{jq'} \right) \tag{A.41}$$

The second equality holds since the elements of the eigenvectors $\boldsymbol{U}_q$ sum to zero for $q \neq 0$. As with the previous analysis, this result does not require that the rings be ideal or Gaussian. The vanishing of these correlations makes it difficult to quantify inter-ring correlations or stresses in a meaningful way. The symmetries of the rings also prohibit any cross-correlations

between ring-like and linear-like modes by similar arguments. This analysis does not mean that the motions of different rings are not coupled to one another or that they are not coupled to the dynamics of the overall chain; indeed they must be to some degree. Rather, these calculations show that that the inherent symmetry of ring polymers makes such correlations invisible in the Fourier mode space.

Since all cross-correlations involving ring-like modes vanish identically, the only possible couplings are between linear-like modes. Linear polymers lack the high symmetries of rings, so these couplings can indeed be non-zero for real chains. To quantify inter-mode coupling, we compute the normalized absolute cross-correlations $\chi_{pp'}$ previously used for isolated polymers in Chapter 3 (Eq. 3.9). By translational symmetry, cross-correlations with the center-of-mass mode vanish, so only modes $p > 0$ are considered. For ideal polymers, $\chi_{pp'} = \delta_{pp'}$. Since the most unusual physical results are observed for long catenanes with small rings, the largest cross-correlations are expected for the poly[n]catenanes with $n = 25$ and $m = 15$. Even for this system, the largest cross-coupling is just 0.0170 and the mean cross-correlation just 0.0043, nearly three orders of magnitude smaller than the self-correlation. The full range of cross-correlations for this system is displayed as a heat map in Figure A.2. For systems with bigger rings, the maximum and mean cross-couplings are reduced, while systems with smaller chain lengths typically show increased cross-couplings. However, even the largest cross-correlations observed for any system are still quite small (maximum of 0.070, mean of 0.023 for $n = 5$, $m = 15$). These results demonstrate that the modes provided by the double-Rouse model are indeed orthogonal to a good approximation and that mode cross-couplings cannot be responsible for the unusual dynamics observed.

A.7 Numerical Calculation of Viscosity

The zero shear-rate viscosity is given by the integral of the stress relaxation modulus $G(t)$ (main text, Eq. 13). In practice, the integral can be difficult to compute as the long-time

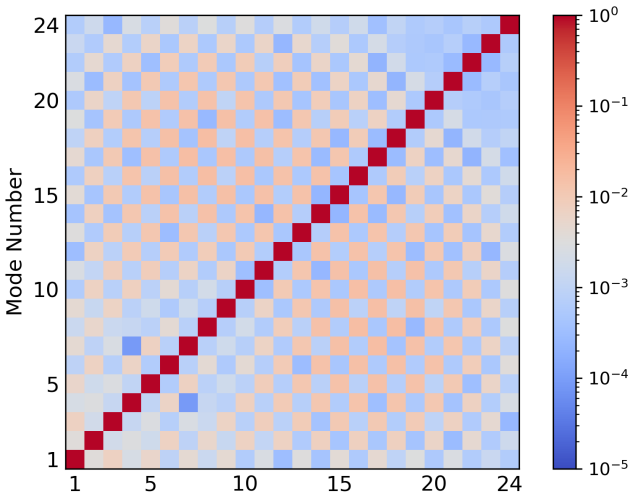

Figure A.2: Normalized absolute cross-correlations (Eq. 3.9) in poly[n]catenanes with $n = 25$ and $m = 15$.

behavior of the modulus is dominated by large statistical noise and must therefore be cutoff at some upper time limit. Fortunately, including data from such long times is actually unnecessary as the stress typically decays exponentially after the terminal time, such that the time-dependent running integral reaches a plateau. According to the Rouse model, this terminal time is one half the longest Rouse mode relaxation time (Eq. A.28); this result suggests that if one knows the longest relaxation time of an individual polymer (regardless of architecture), it can be used to determine a suitable integration limit. Here, an upper-time limit of $2\tau_R$ is used, and at this time the slowest stress relaxation mode should have decayed to about 2% of its initial value. This represents an estimate of the systematic error in the calculation; it is generally much smaller than the statistical error, so the resulting data can be regarded as "true" viscosities for practical purposes. To illustrate, in Figure A.3 the running integral of the viscosities is shown for linear polymers of various N:

$$\eta(t) = \int_0^t G(s)ds \tag{A.42}$$

with the integration limits clearly marked. By a time of $2\tau_R$, the integral has reached a terminal plateau region and the resulting viscosities are in very good quantitative agreement with previous literature [259, 263]. The same approach is used for poly[n]catenane and ring polymer melts as well. Note that the integration is performed on the raw autocorrelation functions i.e. before passing them through the multiple-tau correlation (see main text). However, there is essentially no difference in either the mean values or the statistical errors when performing the integration on the processed data.

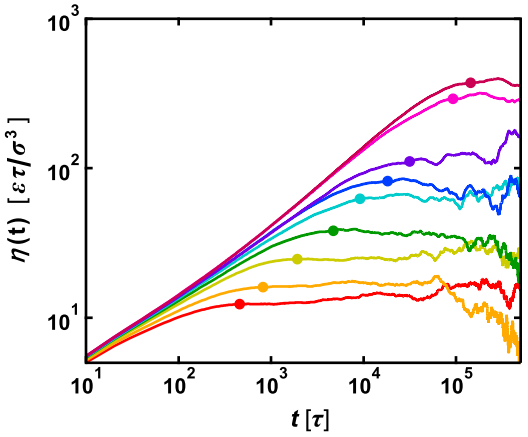

Figure A.3: Running integrals of the stress relaxation modulus (Eq. A.42) for linear polymers of various N (15, 20, 30, 45, 60, 80, 100, 150, and 175, from bottom to top). The cutoff of the integrations ($=2\tau_R$) for calculating viscosities are marked as points on the curves. At times beyond these points, the values of the integrals do not change significantly, but statistical noise increases.

REFERENCES

1. Richter, D., Gooßen, S. & Wischnewski, A. Celebrating Soft Matter's 10th Anniversary: Topology matters: structure and dynamics of ring polymers. *Soft Matter* **11,** 8535–8549 (2015).
2. Haque, F. M. & Grayson, S. M. The synthesis, properties and potential applications of cyclic polymers. *Nature Chemistry,* 1–12 (2020).
3. Kricheldorf, H. R. Cyclic polymers: Synthetic strategies and physical properties. *Journal of Polymer Science, Part A: Polymer Chemistry* **48,** 251–284 (2010).
4. Wang, Z. G. 50th Anniversary Perspective: Polymer Conformation - A Pedagogical Review. *Macromolecules* **50,** 9073–9114 (2017).
5. Polymeropoulos, G. *et al.* 50th Anniversary Perspective: Polymers with Complex Architectures. *Macromolecules* **50,** 1253–1290 (2017).
6. Zeng, F. & Zimmerman, S. C. Dendrimers in supramolecular chemistry: From molecular recognition to self-assembly. *Chemical Reviews* **97,** 1681–1712 (1997).
7. Mintzer, M. A. & Grinstaff, M. W. Biomedical applications of dendrimers: A tutorial. *Chemical Society Reviews* **40,** 173–190 (2011).
8. Ren, J. M. *et al.* Star Polymers. *Chemical Reviews* **116,** 6743–6836 (2016).
9. Khanna, K., Varshney, S. & Kakkar, A. Miktoarm star polymers: Advances in synthesis, self-assembly, and applications. *Polymer Chemistry* **1,** 1171–1185 (2010).
10. Abbasi, M., Faust, L. & Wilhelm, M. Comb and Bottlebrush Polymers with Superior Rheological and Mechanical Properties. *Advanced Materials* **31,** 1806484 (2019).
11. Verduzco, R., Li, X., Pesek, S. L. & Stein, G. E. Structure, function, self-assembly, and applications of bottlebrush copolymers. *Chemical Society Reviews* **44,** 2405–2420 (2015).
12. Paturej, J., Sheiko, S. S., Panyukov, S. & Rubinstein, M. Molecular structure of Bottlebrush polymers in melts. *Science Advances* **2,** e1601478 (2016).
13. Doi, M. & Edwards, S. *The Theory of Polymer Dynamics* (Oxford University Press, New York, 1986).
14. Bruns, C. J. & Stoddart, J. F. *The Nature of the Mechanical Bond: From Molecules to Machines* (John Wiley & Sons, Inc., Hoboken, NJ, USA, 2016).
15. Arunachalam, M. & Gibson, H. W. Recent developments in polypseudorotaxanes and polyrotaxanes. *Progress in Polymer Science* **39,** 1043–1073 (2014).
16. Noda, Y., Hayashi, Y. & Ito, K. From topological gels to slide-ring materials. *Journal of Applied Polymer Science* **131,** 40509 (2014).
17. Mena-Hernando, S. & Pérez, E. M. Mechanically interlocked materials. Rotaxanes and catenanes beyond the small molecule. *Chemical Society Reviews* **48,** 5016–5032 (2019).

18. Niu, Z. & Gibson, H. W. Polycatenanes. *Chemical Reviews* **109,** 6024–6046 (2009).

19. Wu, Q. *et al.* Poly[n]catenanes: Synthesis of molecular interlocked chains. *Science* **358,** 1434–1439 (2017).

20. Weidmann, J.-L. *et al.* Poly[2]catenanes and Cyclic Oligo[2]catenanes Containing Alternating Topological and Covalent Bonds: Synthesis and Characterization. *Chemistry - A European Journal* **5,** 1841–1851 (1999).

21. Brereton, M. G. The statistical mechanics of a concatenated polymer chain. *Journal of Physics A: Mathematical and General* **34,** 5131 (2001).

22. Pakula, T. & Jeszka, K. Simulation of Single Complex Macromolecules. 1. Structure and Dynamics of Catenanes. *Macromolecules* **32,** 6821–6830 (1999).

23. Kremer, K. & Grest, G. S. Dynamics of entangled linear polymer melts: A molecular-dynamics simulation. *The Journal of Chemical Physics* **92,** 5057–5086 (1990).

24. Edwards, S. F. The statistical mechanics of polymerized material. *Proceedings of the Physical Society* **92,** 9–16 (1967).

25. De Gennes, P.-G. Reptation of a Polymer Chain in the Presence of Fixed Obstacles. *The Journal of Chemical Physics* **55,** 572–579 (1971).

26. Doi, M. & Edwards, S. F. Dynamics of concentrated polymer systems. Part 1.—Brownian motion in the equilibrium state. *J. Chem. Soc., Faraday Trans. 2* **74,** 1789–1801 (1978).

27. Doi, M. & Edwards, S. F. Dynamics of concentrated polymer systems. Part 2.—Molecular motion under flow. *J. Chem. Soc., Faraday Trans. 2* **74,** 1802–1817 (1978).

28. Doi, M. & Edwards, S. F. Dynamics of concentrated polymer systems. Part 3.—The constitutive equation. *J. Chem. Soc., Faraday Trans. 2* **74,** 1818–1832 (1978).

29. McLeish, T. C. B. Tube theory of entangled polymer dynamics. *Advances in Physics* **51,** 1379–1527 (2002).

30. Edwards, S. F. & Vilgis, T. A. The tube model theory of rubber elasticity. *Reports on Progress in Physics* **51,** 243–297 (1988).

31. Ball, R., Doi, M., Edwards, S. & Warner, M. Elasticity of entangled networks. *Polymer* **22,** 1010–1018 (1981).

32. Rubinstein, M. & Panyukov, S. Elasticity of Polymer Networks. *Macromolecules* **35,** 6670–6686 (2002).

33. Likhtman, A. E. Single-Chain Slip-Link Model of Entangled Polymers: Simultaneous Description of Neutron Spin-Echo, Rheology, and Diffusion. *Macromolecules* **38,** 6128–6139 (2005).

34. Ramírez-Hernández, A., Peters, B. L., Andreev, M., Schieber, J. D. & de Pablo, J. J. A multichain polymer slip-spring model with fluctuating number of entanglements for linear and nonlinear rheology. *The Journal of Chemical Physics* **143,** 243147 (2015).

35. Sgouros, A. P., Megariotis, G. & Theodorou, D. N. Slip-Spring Model for the Linear and Nonlinear Viscoelastic Properties of Molten Polyethylene Derived from Atomistic Simulations. *Macromolecules* **50,** 4524–4541 (2017).

36. Sussman, D. M. & Schweizer, K. S. Microscopic Theory of the Tube Confinement Potential for Liquids of Topologically Entangled Rigid Macromolecules. *Physical Review Letters* **107,** 078102 (2011).

37. Sussman, D. M. & Schweizer, K. S. Microscopic Theory of Entangled Polymer Melt Dynamics: Flexible Chains as Primitive-Path Random Walks and Supercoarse Grained Needles. *Physical Review Letters* **109,** 168306 (2012).

38. Sussman, D. M. & Schweizer, K. S. Entangled polymer chain melts: Orientation and deformation dependent tube confinement and interchain entanglement elasticity. *The Journal of Chemical Physics* **139,** 234904 (2013).

39. Dell, Z. E. & Schweizer, K. S. Segment-scale, force-level theory of mesoscopic dynamic localization and entropic elasticity in entangled chain polymer liquids. *The Journal of Chemical Physics* **146,** 134901 (2017).

40. Kirste, R., Kruse, W. & Ibel, K. Determination of the conformation of polymers in the amorphous solid state and in concentrated solution by neutron diffraction. *Polymer* **16,** 120–124 (1975).

41. Lieser, G., Fischer, E. W. & Ibel, K. Conformation of polyethylene molecules in the melt as revealed by small-angle neutron scattering. *Journal of Polymer Science: Polymer Letters Edition* **13,** 39–43 (1975).

42. Benoit, H. *et al.* Dimensions of a Flexible Polymer Chain in the Bulk and in Solution. *Nature Physical Science* **245,** 13–15 (1973).

43. Hsu, H.-P. Lattice Monte Carlo simulations of polymer melts. *The Journal of Chemical Physics* **141,** 234901 (2014).

44. Hsu, H.-P. & Kremer, K. Static and dynamic properties of large polymer melts in equilibrium. *The Journal of Chemical Physics* **144,** 154907 (2016).

45. Rubinstein, M. & Helfand, E. Statistics of the entanglement of polymers: Concentration effects. *The Journal of Chemical Physics* **82,** 2477–2483 (1985).

46. Kröger, M., Ramírez, J. & Öttinger, H. Projection from an atomistic chain contour to its primitive path. *Polymer* **43,** 477–487 (2002).

47. Everaers, R. *et al.* Rheology and microscopic topology of entangled polymeric liquids. *Science* **303,** 823–6 (2004).

48. Zhou, Q. & Larson, R. G. Primitive Path Identification and Statistics in Molecular Dynamics Simulations of Entangled Polymer Melts. *Macromolecules* **38,** 5761–5765 (2005).

49. Shanbhag, S. & Larson, R. G. Chain Retraction Potential in a Fixed Entanglement Network. *Physical Review Letters* **94,** 076001 (2005).

50. Foteinopoulou, K., Karayiannis, N., Mavrantzas, V. G. & Kröger, M. Primitive Path Identification and Entanglement Statistics in Polymer Melts: Results from Direct Topological Analysis on Atomistic Polyethylene Models. *Macromolecules* **39,** 4207–4216 (2006).

51. Tzoumanekas, C. & Theodorou, D. N. Topological Analysis of Linear Polymer Melts: A Statistical Approach. *Macromolecules* **39,** 4592–4604 (2006).

52. Shanbhag, S. & Kröger, M. Primitive Path Networks Generated by Annealing and Geometrical Methods: Insights into Differences. *Macromolecules* **40,** 2897–2903 (2007).

53. Likhtman, A. E. & Ponmurugan, M. Microscopic Definition of Polymer Entanglements. *Macromolecules* **47,** 1470–1481 (2014).

54. Caraglio, M., Micheletti, C. & Orlandini, E. Physical Links: defining and detecting inter-chain entanglement. *Scientific Reports* **7,** 1156 (2017).

55. Cates, M. & Deutsch, J. Conjectures on the statistics of ring polymers. *Journal de Physique* **47,** 2121–2128 (1986).

56. Müller, M., Wittmer, J. P. & Cates, M. E. Topological effects in ring polymers: A computer simulation study. *Physical Review E* **53,** 5063–5074 (1996).

57. Brown, S. & Szamel, G. Structure and dynamics of ring polymers. *The Journal of Chemical Physics* **108,** 4705–4708 (1998).

58. Brown, S. & Szamel, G. Computer simulation study of the structure and dynamics of ring polymers. *The Journal of Chemical Physics* **109,** 6184–6192 (1998).

59. Halverson, J. D., Lee, W. B., Grest, G. S., Grosberg, A. Y. & Kremer, K. Molecular dynamics simulation study of nonconcatenated ring polymers in a melt. I. Statics. *The Journal of Chemical Physics* **134,** 204904 (2011).

60. Tsalikis, D. G. *et al.* Microscopic Structure, Conformation, and Dynamics of Ring and Linear Poly(ethylene oxide) Melts from Detailed Atomistic Molecular Dynamics Simulations: Dependence on Chain Length and Direct Comparison with Experimental Data. *Macromolecules* **50,** 2565–2584 (2017).

61. Hur, K. *et al.* Chain Dynamics of Ring and Linear Polyethylene Melts from Molecular Dynamics Simulations. *Macromolecules* **44,** 2311–2315 (2011).

62. Lee, E., Kim, S. & Jung, Y. Slowing Down of Ring Polymer Diffusion Caused by Inter-Ring Threading. *Macromolecular Rapid Communications* **36,** 1115–1121 (2015).

63. Ge, T., Panyukov, S. & Rubinstein, M. Self-Similar Conformations and Dynamics in Entangled Melts and Solutions of Nonconcatenated Ring Polymers. *Macromolecules* **49,** 708–722 (2016).

64. Halverson, J. D., Lee, W. B., Grest, G. S., Grosberg, A. Y. & Kremer, K. Molecular dynamics simulation study of nonconcatenated ring polymers in a melt. II. Dynamics. *The Journal of Chemical Physics* **134,** 204905 (2011).

65. Kapnistos, M. *et al.* Unexpected power-law stress relaxation of entangled ring polymers. *Nature Materials* **7,** 997–1002 (2008).

66. Pasquino, R. *et al.* Viscosity of Ring Polymer Melts. *ACS Macro Letters* **2,** 874–878 (2013).

67. Doi, Y. *et al.* Melt Rheology of Ring Polystyrenes with Ultrahigh Purity. *Macromolecules* **48,** 3140–3147 (2015).

68. Smrek, J. & Grosberg, A. Y. Understanding the dynamics of rings in the melt in terms of the annealed tree model. *Journal of Physics: Condensed Matter* **27,** 064117 (2015).

69. Edwards, S. F. Statistical mechanics with topological constraints: I. *Proceedings of the Physical Society* **91,** 513–519 (1967).

70. Edwards, S. F. Statistical mechanics with topological constraints: II. *Journal of Physics A: General Physics* **1,** 303 (1968).

71. Frank-Kamenetskii, M. D., Lukashin, A. V. & Vologodskii, A. V. Statistical mechanics and topology of polymer chains. *Nature* **258,** 398–402 (1975).

72. Iwata, K. & Kimura, T. Topological distribution functions and the second virial coefficients of ring polymers. *The Journal of Chemical Physics* **74,** 2039–2048 (1981).

73. Tanaka, F. Osmotic pressure of ring-polymer solutions. *The Journal of Chemical Physics* **87,** 4201–4206 (1987).

74. Huang, Q. *et al.* Unexpected Stretching of Entangled Ring Macromolecules. *Physical Review Letters* **122,** 208001 (2019).

75. O'Connor, T. C., Ge, T., Rubinstein, M. & Grest, G. S. Topological Linking Drives Anomalous Thickening of Ring Polymers in Weak Extensional Flows. *Physical Review Letters* **124,** 027801 (2020).

76. Michieletto, D. & Turner, M. S. A topologically driven glass in ring polymers. *Proceedings of the National Academy of Sciences* **113,** 5195–200 (2016).

77. Michieletto, D., Nahali, N. & Rosa, A. Glassiness and Heterogeneous Dynamics in Dense Solutions of Ring Polymers. *Physical Review Letters* **119,** 197801 (2017).

78. Smrek, J., Chubak, I., Likos, C. N. & Kremer, K. Active topological glass. *Nature Communications* **11,** 26 (2020).

79. Halverson, J. D., Grest, G. S., Grosberg, A. Y. & Kremer, K. Rheology of Ring Polymer Melts: From Linear Contaminants to Ring-Linear Blends. *Physical Review Letters* **108,** 038301 (2012).

80. Tsalikis, D. G. & Mavrantzas, V. G. Threading of Ring Poly(ethylene oxide) Molecules by Linear Chains in the Melt. *ACS Macro Letters* **3,** 763–766 (2014).

81. Zhou, Y. *et al.* Effect of molecular architecture on ring polymer dynamics in semidilute linear polymer solutions. *Nature Communications* **10,** 1753 (2019).

82. Kreuzer, K. N. & Cozzarelli, N. R. Formation and resolution of DNA catenanes by DNA gyrase. *Cell* **20,** 245–254 (1980).

83. Mirkin, S. M. in *Encyclopedia of Life Sciences* (John Wiley & Sons, Ltd, Chichester, UK, 2001).

84. Vologodskii, A. & Rybenkov, V. V. Simulation of DNA catenanes. *Physical Chemistry Chemical Physics* **11,** 10543–10552 (2009).

85. Otto, M. & Vilgis, T. A. Topological Interactions in Multiply Linked DNA Rings. *Physical Review Letters* **80,** 881–884 (1998).

86. Otto, M. Topological interactions in systems of mutually interlinked polymer rings. *Journal of Physics A: Mathematical and General* **37,** 2881–2893 (2004).

87. Rubinstein, M. & Colby, R. *Polymer Physics* (Oxford University Press, New York, 2003).

88. Caraglio, M., Micheletti, C. & Orlandini, E. Mechanical Pulling of Linked Ring Polymers: Elastic Response and Link Localisation. *Polymers* **9,** 327 (2017).

89. Rane, S. S. & Mattice, W. L. Structure and internal dynamics of poly(ethylene oxide) catenanes in the melt. *Macromolecules* **38,** 3708–3712 (2005).

90. Sikorski, A. Monte Carlo study of catenated ring polymers. *Polymer* **35,** 3792–3794 (1994).

91. Vilgis, T. A. & Otto, M. Elasticity of entangled polymer loops: Olympic gels. *Physical Review E* **56,** R1314–R1317 (1997).

92. Ahmadian Dehaghani, Z., Chubak, I., Likos, C. N. & Ejtehadi, M. R. Effects of topological constraints on linked ring polymers in solvents of varying quality. *Soft matter* **16,** 3029–3038 (2020).

93. Wu, Z.-T. & Zhou, J.-J. Mechanical Properties of Interlocked-ring Polymers: A Molecular Dynamics Simulation Study. *Chinese Journal of Polymer Science* **37,** 1298–1304 (2019).

94. Kanaeda, N. & Deguchi, T. Universal Ratios in the Dynamics of Open and Closed Chains of Linked Ring Polymers in Solution via Brownian Dynamics. *Progress of Theoretical Physics Supplement* **191,** 146–153 (2011).

95. Natori, S. & Takano, H. Two-step relaxation mode analysis with multiple evolution times: Application to a single [n]polycatenane. *Journal of the Physical Society of Japan* **86** (2017).

96. Weidmann, J. L. *et al.* Poly[2]-catenanes containing alternating topological and covalent bonds. *Chemical Communications,* 1243–1244 (1996).

97. Hamers, C., Kocian, O., Raymo, F. M. & Stoddart, J. F. A Poly(bis[2]catenane) Containing a Combination of Covalent, Mechanical, and Coordinative Bonds. *Advanced Materials* **10,** 1366–1369 (1998).

98. Hamers, C., Raymo, F. M. & Stoddart, J. F. Main-Chain and Pendant Poly([2]catenane)s Incorporating Complementary π-Electron-Rich and -Deficient Components. *European Journal of Organic Chemistry* **1998,** 2109–2117 (1998).

99. Muscat, D. *et al.* Synthesis and characterization of poly[2]-catenanes containing rigid catenane segments. *Macromolecules* **32,** 1737–1745 (1999).

100. Watanabe, N., Ikari, Y., Kihara, N. & Takata, T. Bridged Polycatenane. *Macromolecules* **37,** 6663–6666 (2004).

101. Fustin, C. A. *et al.* Mechanically linked polycarbonate. *Journal of the American Chemical Society* **125,** 2200–2207 (2003).

102. Ahamed, B. N., Van Velthem, P., Robeyns, K. & Fustin, C. A. Influence of a Single Catenane on the Solid-State Properties of Mechanically Linked Polymers. *ACS Macro Letters* **6,** 468–472 (2017).

103. Endo, K., Shiroi, T., Murata, N., Kojima, G. & Yamanaka, T. Synthesis and characterization of poly(1,2-dithiane). *Macromolecules* **37,** 3143–3150 (2004).

104. Berrocal, J. A. *et al.* Ring-opening metathesis polymerization of a diolefinic [2]–catenane–copper(i) complex: An easy route to polycatenanes. *Macromolecules* **48,** 1358–1363 (2015).

105. Cao, P. F., Mangadlao, J. D., De Leon, A., Su, Z. & Advincula, R. C. Catenated Poly(ϵ-caprolactone) and Poly(L-lactide) via Ring-Expansion Strategy. *Macromolecules* **48,** 3825–3833 (2015).

106. Amabilino, D. B., Ashton, P. R., Reder, A. S., Spencer, N. & Stoddart, J. F. Olympiadane. *Angewandte Chemie International Edition in English* **33,** 1286–1290 (1994).

107. Iwamoto, H. *et al.* Synthesis of linear [5]catenanes via olefin metathesis dimerization of pseudorotaxanes composed of a [2]catenane and a secondary ammonium salt. *Chemical Communications* **52,** 319–322 (2016).

108. Amabilino, D. B. *et al.* The Five-Stage Self-Assembly of a Branched Heptacatenane. *Angewandte Chemie International Edition in English* **36,** 2070–2072 (1997).

109. Chichak, K. S. *et al.* Molecular Borromean rings. *Science* **304,** 1308–1312 (2004).

110. Danon, J. J. *et al.* Braiding a molecular knot with eight crossings. *Science* **355,** 159–162 (2017).

111. Dietrich-Buchecker, C. O., Sauvage, J. P. & Kintzinger, J. P. Une nouvelle famille de molecules : les metallo-catenanes. *Tetrahedron Letters* **24,** 5095–5098 (1983).

112. Wojtecki, R. J. *et al.* Optimizing the formation of 2,6–bis(*N*-alkyl-benzimidazolyl)pyridine–containing [3]catenates through component design. *Chemical Science* **4,** 4440–4448 (2013).

113. Burnworth, M. *et al.* Optically healable supramolecular polymers. *Nature* **472,** 334–337 (2011).

114. Wojtecki, R. J., Meador, M. A. & Rowan, S. J. Using the dynamic bond to access macroscopically responsive structurally dynamic polymers. *Nature Materials* **10,** 14–27 (2011).

115. Kumpfer, J. R. & Rowan, S. J. Thermo-, photo-, and chemo-responsive shape-memory properties from photo-cross-linked metallo-supramolecular polymers. *Journal of the American Chemical Society* **133,** 12866–12874 (2011).

116. Michal, B. T., McKenzie, B. M., Felder, S. E. & Rowan, S. J. Metallo-, thermo-, and photoresponsive shape memory and actuating liquid crystalline elastomers. *Macromolecules* **48,** 3239–3246 (2015).

117. Kramer, R., Lehn, J. M. & Marquis-Rigault, A. Self-recognition in helicate self-assembly: Spontaneous formation of helical metal complexes from mixtures of ligands and metal ions. *Proceedings of the National Academy of Sciences of the United States of America* **90,** 5394–5398 (1993).

118. Rowan, S. J. & Beck, J. B. Metal-ligand induced supramolecular polymerization: A route to responsive materials. *Faraday Discussions* **128,** 43–53 (2005).

119. Lewis, J. E., Galli, M. & Goldup, S. M. Properties and emerging applications of mechanically interlocked ligands. *Chemical Communications* **53,** 298–312 (2017).

120. Berendsen, H. J., van der Spoel, D. & van Drunen, R. GROMACS: A message-passing parallel molecular dynamics implementation. *Computer Physics Communications* **91,** 43–56 (1995).

121. Abraham, M. J. *et al.* Gromacs: High performance molecular simulations through multi-level parallelism from laptops to supercomputers. *SoftwareX* **1-2,** 19–25 (2015).

122. Jorgensen, W. L., Maxwell, D. S. & Tirado-Rives, J. Development and testing of the OPLS all-atom force field on conformational energetics and properties of organic liquids. *Journal of the American Chemical Society* **118,** 11225–11236 (1996).

123. McDonald, N. A. & Jorgensen, W. L. Development of an all-atom force field for heterocycles. Properties of liquid pyrrole, furan, diazoles, and oxazoles. *Journal of Physical Chemistry B* **102,** 8049–8059 (1998).

124. Jorgensen, W. L. & McDonald, N. A. Development of an all-atom force field for heterocycles. Properties of liquid pyridine and diazenes. *Journal of Molecular Structure: THEOCHEM* **424,** 145–155 (1998).

125. Jorgensen, W. L. & Tirado-Rives, J. Potential energy functions for atomic-level simulations of water and organic and biomolecular systems. *Proceedings of the National Academy of Sciences of the United States of America* **102,** 6665–6670 (2005).

126. Dahlgren, M. K., Schyman, P., Tirado-Rives, J. & Jorgensen, W. L. Characterization of biaryl torsional energetics and its treatment in OPLS all-atom force fields. *Journal of Chemical Information and Modeling* **53,** 1191–1199 (2013).

127. Allen, M. & Tildesley, D. *Computer Simulation of Liquids: Second Edition* (Oxford University Press, Oxford, 2017).

128. Darden, T., York, D. & Pedersen, L. Particle mesh Ewald: An N·log(N) method for Ewald sums in large systems. *The Journal of Chemical Physics* **98,** 10089–10092 (1993).

129. Essmann, U. *et al.* A smooth particle mesh Ewald method. *The Journal of Chemical Physics* **103,** 8577–8593 (1995).

130. Nosé, S. A molecular dynamics method for simulations in the canonical ensemble. *Molecular Physics* **52,** 255–268 (1984).

131. Hoover, W. G. Canonical dynamics: Equilibrium phase-space distributions. *Physical Review A* **31,** 1695–1697 (1985).

132. Parrinello, M. & Rahman, A. Polymorphic transitions in single crystals: A new molecular dynamics method. *Journal of Applied Physics* **52,** 7182–7190 (1981).

133. Markus, Y. *The Properties of Solvents* (Wiley, 1998).

134. Caleman, C. *et al.* Force field benchmark of organic liquids: Density, enthalpy of vaporization, heat capacities, surface tension, isothermal compressibility, volumetric expansion coefficient, and dielectric constant. *Journal of Chemical Theory and Computation* **8,** 61–74 (2012).

135. Hess, B., Bekker, H., Berendsen, H. J. C. & Fraaije, J. G. E. M. LINCS: A linear constraint solver for molecular simulations. *Journal of Computational Chemistry* **18,** 1463–1472 (1997).

136. Hess, B. P-LINCS: A parallel linear constraint solver for molecular simulation. *Journal of Chemical Theory and Computation* **4,** 116–122 (2008).

137. Van Gunsteren, W. F. & Berendsen, H. J. C. Computer Simulation of Molecular Dynamics: Methodology, Applications, and Perspectives in Chemistry. *Angewandte Chemie International Edition in English* **29,** 992–1023 (1990).

138. Frisch, M. *et al. Gaussian 09* Wallingford, CT, 2009.

139. Krishnan, R., Binkley, J. S., Seeger, R. & Pople, J. A. Self-consistent molecular orbital methods. XX. A basis set for correlated wave functions. *The Journal of Chemical Physics* **72,** 650–654 (1980).

140. Kendall, R. A., Dunning, T. H. & Harrison, R. J. Electron affinities of the first-row atoms revisited. Systematic basis sets and wave functions. *The Journal of Chemical Physics* **96,** 6796–6806 (1992).

141. Schüttelkopf, A. W. & Van Aalten, D. M. PRODRG: A tool for high-throughput crystallography of protein-ligand complexes. *Acta Crystallographica Section D: Biological Crystallography* **60,** 1355–1363 (2004).

142. Humphrey, W., Dalke, A. & Schulten, K. VMD: Visual molecular dynamics. *Journal of Molecular Graphics* **14,** 33–38 (1996).

143. Palmer, B. J. Transverse-current autocorrelation-function calculations of the shear viscosity for molecular liquids. *Physical Review E* **49,** 359–366 (1994).

144. Frenkel, M. & Marsh, K. *Densities of Halohydrocarbons* (Springer-Verlag, 2003).

145. Madelung, O. *Static Dielectric Constants of Pure Liquids and Binary Liquid Mixtures* (Springer-Verlag, 1991).

146. Lide, D. *CRC Handbook of Chemistry and Physics* 90th Editi (CRC Press, 2009).

147. Yaws, C. *Yaws' Handbook of Thermodynamic and Physical Properties of Chemical Compounds* (Knovel, 2003).

148. *Design Institute for Chemical Engineering, Project 801* (American Institute for Chemical Engineering, 2010).

149. Sivaramprasad, G., Rao, M. V. & Prasad, D. H. Density and Viscosity of Ethanol + 1,2-Dichloroethane, Ethanol + 1,1,1-Trichloroethane, and Ethanol + 1,1,2,2-Tetrachloroethane Binary Mixtures. *Journal of Chemical and Engineering Data* **35,** 122–124 (1990).

150. Li, P. & Merz, K. M. Metal Ion Modeling Using Classical Mechanics. *Chemical Reviews* **117,** 1564–1686 (2017).

151. Stote, R. H. & Karplus, M. Zinc binding in proteins and solution: A simple but accurate nonbonded representation. *Proteins: Structure, Function, and Genetics* **23,** 12–31 (1995).

152. Fan, X., Yuan, J., Bai, Y., Kong, J. & Wu, H. Bis[2,6-bis-(1-methyl-1H-benzimidazol-2-yl-kN 3)pyridine-kN]zinc dipicrate methanol disolvate. *Acta Crystallographica Section E: Structure Reports Online* **68,** m1072–m1072 (2012).

153. Youngs, T. G. A. & Hardacre, C. Application of Static Charge Transfer within an Ionic-Liquid Force Field and Its Effect on Structure and Dynamics. *ChemPhysChem* **9,** 1548–1558 (2008).

154. Schmidt, J. *et al.* Ionic charge reduction and atomic partial charges from first-principles calculations of 1,3-dimethylimidazolium chloride. *Journal of Physical Chemistry B* **114,** 6150–6155 (2010).

155. Beichel, W. *et al.* Charge-Scaling Effect in Ionic Liquids from the Charge-Density Analysis of *N*,*N*'-Dimethylimidazolium Methylsulfate. *Angewandte Chemie International Edition* **53,** 3143–3146 (2014).

156. Müller-Plathe, F. & Van Gunsteren, W. F. Computer simulation of a polymer electrolyte: Lithium iodide in amorphous poly(ethylene oxide). *The Journal of Chemical Physics* **103,** 4745–4756 (1995).

157. Lin, K. J. & Maranas, J. K. Does decreasing ion-ion association improve cation mobility in single ion conductors? *Physical Chemistry Chemical Physics* **15,** 16143–16151 (2013).

158. Savoie, B. M., Webb, M. A. & Miller, T. F. Enhancing Cation Diffusion and Suppressing Anion Diffusion via Lewis-Acidic Polymer Electrolytes. *Journal of Physical Chemistry Letters* **8,** 641–646 (2017).

159. De Gennes, P.-G. *Scaling Concepts in Polymer Physics* (Cornell University Press, Ithaca, 1979).

160. Pranami, G. & Lamm, M. H. Estimating Error in Diffusion Coefficients Derived from Molecular Dynamics Simulations. *Journal of Chemical Theory and Computation* **11,** 4586–4592 (2015).

161. Lee, H., Venable, R. M., MacKerell, A. D. & Pastor, R. W. Molecular dynamics studies of polyethylene oxide and polyethylene glycol: Hydrodynamic radius and shape anisotropy. *Biophysical Journal* **95,** 1590–1599 (2008).

162. Yeh, I. C. & Hummer, G. System-size dependence of diffusion coefficients and viscosities from molecular dynamics simulations with periodic boundary conditions. *Journal of Physical Chemistry B* **108,** 15873–15879 (2004).

163. Wang, M. D., Yin, H., Landick, R., Gelles, J. & Block, S. M. Stretching DNA with optical tweezers. *Biophysical Journal* **72,** 1335–1346 (1997).

164. Odijk, T. Notes: Stiff Chains and Filaments under Tension. *Macromolecules* **28,** 7016–7018 (1995).

165. Wyatt, P. J. Light scattering and the absolute characterization of macromolecules. *Analytica Chimica Acta* **272,** 1–40 (1993).

166. Liu, P., Kim, B., Friesner, R. A. & Berne, B. J. Replica exchange with solute tempering: A method for sampling biological systems in explicit water. *Proceedings of the National Academy of Sciences of the United States of America* **102,** 13749–13754 (2005).

167. Bussi, G. Hamiltonian replica exchange in GROMACS: a flexible implementation. *Molecular Physics* **112,** 379–384 (2014).

168. Edwards, S. & Vilgis, T. The effect of entanglements in rubber elasticity. *Polymer* **27,** 483–492 (1986).

169. Rouse, P. E. A Theory of the Linear Viscoelastic Properties of Dilute Solutions of Coiling Polymers. *The Journal of Chemical Physics* **21,** 1272–1280 (1953).

170. Kalathi, J. T., Kumar, S. K., Rubinstein, M. & Grest, G. S. Rouse Mode Analysis of Chain Relaxation in Homopolymer Melts. *Macromolecules* **47,** 6925–6931 (2014).

171. Kalathi, J. T., Kumar, S. K., Rubinstein, M. & Grest, G. S. Rouse mode analysis of chain relaxation in polymer nanocomposites. *Soft Matter* **11,** 4123–4132 (2015).

172. Hsu, H.-P. & Kremer, K. Detailed analysis of Rouse mode and dynamic scattering function of highly entangled polymer melts in equilibrium. *The European Physical Journal Special Topics* **226,** 693–703 (2017).

173. Pérez-Aparicio, R. *et al.* Chain dynamics of unentangled poly(ethylene-alt-propylene) melts by means of neutron scattering and fully atomistic molecular dynamics simulations. *Macromolecules* **44,** 3129–3139 (2011).

174. Tsolou, G., Stratikis, N., Baig, C., Stephanou, P. S. & Mavrantzas, V. G. Melt Structure and Dynamics of Unentangled Polyethylene Rings: Rouse Theory, Atomistic Molecular Dynamics Simulation, and Comparison with the Linear Analogues. *Macromolecules* **43,** 10692–10713 (2010).

175. Tsalikis, D. G., Mavrantzas, V. G. & Vlassopoulos, D. Analysis of Slow Modes in Ring Polymers: Threading of Rings Controls Long-Time Relaxation. *ACS Macro Letters* **5,** 755–760 (2016).

176. Papadopoulos, G., Tsalikis, D. & Mavrantzas, V. Microscopic Dynamics and Topology of Polymer Rings Immersed in a Host Matrix of Longer Linear Polymers: Results from a Detailed Molecular Dynamics Simulation Study and Comparison with Experimental Data. *Polymers* **8,** 283 (2016).

177. Reid, D. *et al.* DASH. *MiCCoM Codes,* http://miccomcodes.org (2016).

178. Ceriotti, M., Parrinello, M., Markland, T. E. & Manolopoulos, D. E. Efficient stochastic thermostatting of path integral molecular dynamics. *Journal of Chemical Physics* **133,** 124104 (2010).

179. Kreer, T., Baschnagel, J., Müller, M. & Binder, K. Monte Carlo simulation of long chain polymer melts: Crossover from rouse to reptation dynamics. *Macromolecules* **34,** 1105–1117 (2001).

180. Downey, J. P. Static and Dynamic Scaling Properties of Single, Self-Avoiding Polymer Chains in Two Dimensions via the Bond Fluctuation Method of Monte Carlo Simulation. *Macromolecules* **27,** 2929–2932 (1994).

181. Panja, D. & Barkema, G. T. Rouse modes of self-avoiding flexible polymers. *Journal of Chemical Physics* **131,** 154903 (2009).

182. De Gennes, P. G. Dynamics of Entangled Polymer Solutions. I. The Rouse Model. *Macromolecules* **9,** 587–593 (1976).

183. Ceperley, D., Kalos, M. H. & Lebowitz, J. L. Computer simulation of the dynamics of a single polymer chain. *Physical Review Letters* **41,** 313–316 (1978).

184. Ceperley, D., Halos, M. H. & Lebowitz, J. L. Computer Simulation of the Static and Dynamic Properties of a Polymer Chain. *Macromolecules* **14,** 1472–1479 (1981).

185. Richter, D. *et al.* From Rouse dynamics to local relaxation: A neutron spin echo study on polyisobutylene melts. *Journal of Chemical Physics* **111,** 6107–6120 (1999).

186. Bennemann, C., Baschnagel, J., Paul, W. & Binder, K. Molecular-dynamics simulation of a glassy polymer melt: Rouse model and cage effect. *Computational and Theoretical Polymer Science* **9,** 217–226 (1999).

187. Brodeck, M. *et al.* Study of the dynamics of poly(ethylene oxide) by combining molecular dynamic simulations and neutron scattering experiments. *Journal of Chemical Physics* **130,** 094908 (2009).

188. Pérez-Aparicio, R., Colmenero, J., Alvarez, F., Padding, J. T. & Briels, W. J. Chain dynamics of poly(ethylene-alt-propylene) melts by means of coarse-grained simulations based on atomistic molecular dynamics. *Journal of Chemical Physics* **132,** 024904 (2010).

189. Anderson, D. R. Thermal conductivity of polymers. *Chemical Reviews* **66,** 677–690 (1966).

190. Huang, C., Qian, X. & Yang, R. Thermal conductivity of polymers and polymer nanocomposites. *Materials Science and Engineering R: Reports* **132,** 1–22 (2018).

191. Mai, D. J. & Schroeder, C. M. Single polymer dynamics of topologically complex DNA. *Current Opinion in Colloid and Interface Science* **26,** 28–40 (2016).

192. Hsiao, K. W., Schroeder, C. M. & Sing, C. E. Ring Polymer Dynamics Are Governed by a Coupling between Architecture and Hydrodynamic Interactions. *Macromolecules* **49,** 1961–1971 (2016).

193. Miao, L., Young, C. D. & Sing, C. E. An iterative method for hydrodynamic interactions in Brownian dynamics simulations of polymer dynamics. *Journal of Chemical Physics* **147** (2017).

194. Kanaeda, N. & Deguchi, T. Diffusion of a ring polymer in good solution via the Brownian dynamics with no bond crossing. *Journal of Physics A: Mathematical and Theoretical* **41,** 145004 (2008).

195. Soh, B. W., Klotz, A. R., Robertson-Anderson, R. M. & Doyle, P. S. Long-Lived Self-Entanglements in Ring Polymers. *Physical Review Letters* **123** (2019).

196. Handa, M. & Biswas, P. Orientational relaxation of ring polymers in dilute solutions. *Soft Matter* **15,** 5896–5907 (2019).

197. Wang, Z. *et al.* Mechanism of Nonmonotonic Increase in Polymer Size: Comparison between Linear and Ring Chains at High Shear Rates. *Macromolecules* **52,** 8144–8154 (2019).

198. Liebetreu, M. & Likos, C. N. Hydrodynamic Inflation of Ring Polymers under Shear. *Communications Materials* **1,** 1–11 (2019).

199. Young, C. D., Qian, J. R., Marvin, M. & Sing, C. E. Ring polymer dynamics and tumbling-stretch transitions in planar mixed flows. *Physical Review E* **99,** 062502 (2019).

200. Peddireddy, K. R. *et al.* Unexpected entanglement dynamics in semidilute blends of supercoiled and ring DNA. *Soft Matter* **16,** 152 (2019).

201. Gruziel-Słomka, M., Kondratiuk, P., Szymczak, P. & Ekiel-Jeżewska, M. L. Stokesian dynamics of sedimenting elastic rings. *Soft Matter* **15,** 7262–7274 (2019).

202. Liebetreu, M., Ripoll, M. & Likos, C. N. Trefoil Knot Hydrodynamic Delocalization on Sheared Ring Polymers. *ACS Macro Letters* **7,** 447–452 (2018).

203. Kanaeda, N. & Deguchi, T. Universality in the diffusion of knots. *Physical Review E* **79,** 021806 (2009).

204. Weiss, L. B., Marenda, M., Micheletti, C. & Likos, C. N. Hydrodynamics and Filtering of Knotted Ring Polymers in Nanochannels. *Macromolecules* **52,** 4111–4119 (2019).

205. Soh, B. W., Klotz, A. R. & Doyle, P. S. Untying of Complex Knots on Stretched Polymers in Elongational Fields. *Macromolecules* **51,** 9562–9571 (2018).

206. Gruziel, M. *et al.* Periodic Motion of Sedimenting Flexible Knots. *Physical Review Letters* **121,** 127801 (2018).

207. Klotz, A. R., Soh, B. W. & Doyle, P. S. Equilibrium structure and deformation response of 2D kinetoplast sheets. *Proceedings of the National Academy of Sciences of the United States of America* **117,** 121–127 (2020).

208. Krajina, B. A., Zhu, A., Heilshorn, S. C. & Spakowitz, A. J. Active DNA Olympic Hydrogels Driven by Topoisomerase Activity. *Physical Review Letters* **121,** 148001 (2018).

209. Öttinger, H. C. *Stochastic Processes in Polymeric Fluids* (Springer-Verlag, Berlin, Heidelberg, 1996).

210. Rotne, J. & Prager, S. Variational Treatment of Hydrodynamic Interaction in Polymers. *Journal of Chemical Physics* **50,** 4831–4837 (1969).

211. Yamakawa, H. Transport properties of polymer chains in dilute solution: hydrodynamic interaction. *The Journal of Chemical Physics* **53,** 436–443 (1970).

212. Zylka, W. & Öttinger, H. C. A comparison between simulations and various approximations for Hookean dumbbells with hydrodynamic interaction. *The Journal of Chemical Physics* **90,** 474–480 (1989).

213. Zimm, B. H. Dynamics of polymer molecules in dilute solution: Viscoelasticity, flow birefringence and dielectric loss. *The Journal of Chemical Physics* **24,** 269–278 (1956).

214. Öttinger, H. C. Consistently averaged hydrodynamic interaction for Rouse dumbbells in steady shear flow. *The Journal of Chemical Physics* **83,** 6535–6536 (1985).

215. Öttinger, H. C. Generalized Zimm model for dilute polymer solutions under theta conditions. *The Journal of Chemical Physics* **86,** 3731–3749 (1987).

216. Magda, J. J., Larson, R. G. & Mackay, M. E. Deformation-dependent hydrodynamic interaction in flows of dilute polymer solutions. *The Journal of Chemical Physics* **89,** 2504–2513 (1988).

217. Liu, T. W. & Öttinger, H. C. Bead-spring rings with hydrodynamic interaction. *The Journal of Chemical Physics* **87,** 3131–3136 (1987).

218. Hearst, J. E. Effect of partial draining on the intrinsic viscosity of flexible macromolecules. *The Journal of Chemical Physics* **37,** 2547–2548 (1962).

219. Alexander-Katz, A. & Netz, R. R. Dynamics and instabilities of collapsed polymers in shear flow. *Macromolecules* **41,** 3363–3374 (2008).

220. Narros, A., Moreno, A. J. & Likos, C. N. Effects of knots on ring polymers in solvents of varying quality. *Macromolecules* **46,** 3654–3668 (2013).

221. Grosberg, A. Y. Critical exponents for random knots. *Physical Review Letters* **85,** 3858–3861 (2000).

222. Rauscher, P. M., Rowan, S. J. & de Pablo, J. J. Topological Effects in Isolated Poly[n]catenanes: Molecular Dynamics Simulations and Rouse Mode Analysis. *ACS Macro Letters* **7,** 938–943 (2018).

223. Rauscher, P., Schweizer, K., Rowan, S. & de Pablo, J. Dynamics of Poly[n]catenane Melts. *The Journal of Chemical Physics,* (Accepted) (2020).

224. Rauscher, P. M., Schweizer, K. S., Rowan, S. J. & de Pablo, J. J. Thermodynamics and Structure of Poly[n]catenane Melts. *Macromolecules* **53,** 3390–3408 (2020).

225. Bohn, M., Heermann, D. W., Lourenço, O. & Cordeiro, C. On the Influence of Topological Catenation and Bonding Constraints on Ring Polymers. *Macromolecules* **43,** 2564–2573 (2010).

226. Zimm, B. H. & Stockmayer, W. H. The dimensions of chain molecules containing branches and rings. *The Journal of Chemical Physics* **17,** 1301–1314 (1949).

227. Müller, M., Wittmer, J. P. & Cates, M. E. Topological effects in ring polymers. II. Influence of persistence length. *Physical Review E* **61,** 4078–4089 (2000).

228. Suzuki, J., Takano, A. & Matsushita, Y. Dimensions of catenated ring polymers in dilute solution studied by Monte-Carlo simulation. *The Journal of Chemical Physics* **149,** 204901 (2018).

229. Bohn, M. & Heermann, D. W. Topological interactions between ring polymers: Implications for chromatin loops. *The Journal of Chemical Physics* **132,** 044904 (2010).

230. Wittmer, J. P. *et al.* Long range bond-bond correlations in dense polymer solutions. *Physical Review Letters* **93,** 147801 (2004).

231. Wittmer, J. P. *et al.* Intramolecular long-range correlations in polymer melts: The segmental size distribution and its moments. *Physical Review E* **76,** 011803 (2007).

232. Zhao, S. R., Sun, C. P. & Zhang, W. X. Statistics of wormlike chains. I. Properties of a single chain. *The Journal of Chemical Physics* **106,** 2520–2529 (1997).

233. Hsu, H.-P., Paul, W. & Binder, K. Polymer chain stiffness vs. excluded volume: A Monte Carlo study of the crossover towards the worm-like chain model. *Europhysics Letters (EPL)* **92,** 28003 (2010).

234. Hsu, H.-P., Paul, W., Rathgeber, S. & Binder, K. Characteristic Length Scales and Radial Monomer Density Profiles of Molecular Bottle-Brushes: Simulation and Experiment. *Macromolecules* **43,** 1592–1601 (2010).

235. Messmer, D. *et al.* 3D Conformations of Thick Synthetic Polymer Chains Observed by Cryogenic Electron Microscopy. *ACS Nano* **13,** 3466–3473 (2019).

236. Halverson, J. D., Smrek, J., Kremer, K. & Grosberg, A. Y. From a melt of rings to chromosome territories: the role of topological constraints in genome folding. *Reports on Progress in Physics* **77,** 022601 (2014).

237. Dell, Z. E. & Schweizer, K. S. Intermolecular structural correlations in model globular and unconcatenated ring polymer liquids. *Soft Matter* **14,** 9132–9142 (2018).

238. Porod, G. Die Röntgenkleinwinkelstreuung von dichtgepackten kolloiden Systemen. *Kolloid-Zeitschrift* **124,** 83–114 (1951).

239. Ruland, W. Small-angle scattering of two-phase systems: determination and significance of systematic deviations from Porod's law. *Journal of Applied Crystallography* **4,** 70–73 (1971).

240. Sinha, S. K., Sirota, E. B., Garoff, S. & Stanley, H. B. X-ray and neutron scattering from rough surfaces. *Physical Review B* **38,** 2297–2311 (1988).

241. Wiest, J. M., Burdette, S. R., Liu, T. W. & Bird, R. B. Effect of ring closure on rheological behavior. *Journal of Non-Newtonian Fluid Mechanics* **24,** 279–295 (1987).

242. Schweizer, K. S. Microscopic theory of the dynamics of polymeric liquids: General formulation of a mode–mode-coupling approach. *The Journal of Chemical Physics* **91,** 5802–5821 (1989).

243. Guenza, M. Many chain correlated dynamics in polymer fluids. *Journal of Chemical Physics* **110,** 7574–7588 (1999).

244. Guenza, M. Cooperative Dynamics in Unentangled Polymer Fluids. *Physical Review Letters* **88,** 025901 (2002).

245. Farago, J. *et al.* Mode-coupling approach to polymer diffusion in an unentangled melt. I. the effect of density fluctuations. *Physical Review E* **85,** 051806 (2012).

246. Lodge, T. P. Reconciliation of the Molecular Weight Dependence of Diffusion and Viscosity in Entangled Polymers. *Physical Review Letters* **83,** 3218–3221 (1999).

247. Rosa, A., Orlandini, E., Tubiana, L. & Micheletti, C. Structure and Dynamics of Ring Polymers: Entanglement Effects Because of Solution Density and Ring Topology. *Macromolecules* **44,** 8668–8680 (2011).

248. Brás, A. R. *et al.* Compact structure and non-Gaussian dynamics of ring polymer melts. *Soft Matter* **10,** 3649–3655 (2014).

249. Tsalikis, D. G., Alatas, P. V., Peristeras, L. D. & Mavrantzas, V. G. Scaling Laws for the Conformation and Viscosity of Ring Polymers in the Crossover Region around Me from Detailed Molecular Dynamics Simulations. *ACS Macro Letters* **7,** 916–920 (2018).

250. Gooßen, S. *et al.* Molecular scale dynamics of large ring polymers. *Physical Review Letters* **113,** 168302 (2014).

251. Nahali, N. & Rosa, A. Nanoprobe diffusion in entangled polymer solutions: Linear vs. unconcatenated ring chains. *Journal of Chemical Physics* **148,** 194902 (2018).

252. Padding, J. T. & Briels, W. J. Time and length scales of polymer melts studied by coarse-grained molecular dynamics simulations. *Journal of Chemical Physics* **117,** 925–943 (2002).

253. Vladkov, M. & Barrat, J.-L. Linear and Nonlinear Viscoelasticity of a Model Unentangled Polymer Melt: Molecular Dynamics and Rouse Modes Analysis. *Macromolecular Theory and Simulations* **15,** 252–262 (2006).

254. Shaffer, J. S. Effects of chain topology on polymer dynamics: Configurational relaxation in polymer melts. *The Journal of Chemical Physics* **103,** 761–772 (1995).

255. Ediger, M. D., Angell, C. A. & Nagel, S. R. Supercooled Liquids and Glasses. *The Journal of Physical Chemistry* **100,** 13200–13212 (1996).

256. Kuhnhold, A. & Paul, W. Temperature dependent micro-rheology of a glass-forming polymer melt studied by molecular dynamics simulation. *Journal of Chemical Physics* **141,** 124907 (2014).

257. Kuhnhold, A. & Paul, W. Passive one-particle microrheology of an unentangled polymer melt studied by molecular dynamics simulation. *Physical Review E* **90,** 022602 (2014).

258. Lee, W. B. & Kremer, K. Entangled Polymer Melts: Relation between Plateau Modulus and Stress Autocorrelation Function. *Macromolecules* **42,** 6270–6276 (2009).

259. Likhtman, A. E., Sukumaran, S. K. & Ramírez, J. Linear Viscoelasticity from Molecular Dynamics Simulation of Entangled Polymers. *Macromolecules* **40,** 6748–6757 (2007).

260. Ramírez, J., Sukumaran, S. K., Vorselaars, B. & Likhtman, A. E. Efficient on the fly calculation of time correlation functions in computer simulations. *The Journal of Chemical Physics* **133,** 154103 (2010).

261. Liang, H., Grest, G. S. & Dobrynin, A. V. Brush-Like Polymers and Entanglements: From Linear Chains to Filaments. *ACS Macro Letters* **8,** 1328–1333 (2019).

262. Liang, H., Cao, Z., Wang, Z., Sheiko, S. S. & Dobrynin, A. V. Combs and Bottlebrushes in a Melt. *Macromolecules* **50,** 3430–3437 (2017).

263. Kröger, M. & Hess, S. Rheological Evidence for a Dynamical Crossover in Polymer Melts via Nonequilibrium Molecular Dynamics. *Physical Review Letters* **85,** 1128–1131 (2000).

264. Sheiko, S. S. & Dobrynin, A. V. Architectural Code for Rubber Elasticity: From Supersoft to Superfirm Materials. *Macromolecules* **52,** 7531–7546 (2019).

265. Banaszak, B. J. & de Pablo, J. J. A new double-rebridging technique for linear polyethylene. *The Journal of Chemical Physics* **119,** 2456–2462 (2003).

266. Auhl, R., Everaers, R., Grest, G. S., Kremer, K. & Plimpton, S. J. Equilibration of long chain polymer melts in computer simulations. *The Journal of Chemical Physics* **119,** 12718–12728 (2003).

267. Sliozberg, Y. R. & Andzelm, J. W. Fast protocol for equilibration of entangled and branched polymer chains. *Chemical Physics Letters* **523,** 139–143 (2012).

268. Subramanian, G. A topology preserving method for generating equilibrated polymer melts in computer simulations. *The Journal of Chemical Physics* **133,** 164902 (2010).

269. Berendsen, H. J. C., Postma, J. P. M., van Gunsteren, W. F., DiNola, A. & Haak, J. R. Molecular dynamics with coupling to an external bath. *The Journal of Chemical Physics* **81,** 3684–3690 (1984).